Technische Universität München

Department of Chemistry and Catalysis Research Center
Chair of Technical Electrochemistry

Operando and *In Situ* Characterizations of Fundamental Electrochemical Processes in Lithium- and Sodium-Ion Batteries

Fabian Linsenmann

Vollständiger Abdruck der von der Fakultät für Chemie der
Technischen Universität München zur Erlangung des akademischen Grades eines

Doktors der Naturwissenschaften (Dr. rer. nat.)

genehmigten Dissertation.

Vorsitzender:	Prof. Dr. Shigeyoshi Inoue
Prüfer der Dissertation:	1. Prof. Dr. Hubert A. Gasteiger
	2. Prof. Dr. Tom Nilges
	3. Assoc. Prof. Anne Co

Die Dissertation wurde am 26.11.2020 bei der Technischen Universität München eingereicht und durch die Fakultät für Chemie am 13.01.2021 angenommen.

Abstract

The elucidation of (electro)chemical processes in rechargeable batteries is a fundamental prerequisite for the development of new active materials with increased energy density and for prolonging the cycle life of battery cells. In many cases, the diagnostics of these processes is only possible in the environment of an assembled or even cycling cell, *i.e.*, *in situ* or *operando*, to assure that the system under investigation is representative of an operating battery and is not changing over time or by external influences. In the context of this thesis, two new analytical methods are presented which can be used to investigate active materials in lithium-ion batteries (LIBs) and sodium-ion batteries (SIBs).

The development of a novel micro-reference electrode (µ-RE) based on a sodiated tin wire allows the simultaneous measurement of the electrode impedances of cathode and anode in a SIB during cycling without the need for cell disassembly (*in situ*) and subsequent recombination of identical electrodes in the form of so called symmetrical cells. Electrochemical Impedance Spectroscopy (EIS) was used to monitor the change in electrode impedance of a hard carbon anode in a sodium-ion cell during cycling and as a function of state-of-charge (SOC). In a follow-up study, the obtained data were compared to the electrode resistances in case of the (de)lithiation of the same active material, and consequences for the fast-charging properties of hard carbon-based sodium- and lithium-ion cells were deduced.

In a second part of this thesis, a novel cell design for an *operando* measurement of the lithium concentration profile in a battery electrode using Neutron Depth Profiling (NDP) was developed. Hereby, the lithium transport during (de)intercalation of lithium in a graphite electrode could be visualized with high spatial resolution (≈0.5-3 µm), and it was possible to separate the lithium contributions of lithium-containing electrolyte, reversibly intercalated lithium, and lithium irreversibly bound in the solid electrolyte interphase (SEI). Furthermore, the respective lithium contributions could be quantified, which allowed for

determining the absolute lithium content in the SEI. Interestingly, it was found that only ≈61 % of the expected lithium amount from the irreversible capacity, assuming one lithium per electron of charge, can be detected in the SEI. A possible explanation for this is that a significant proportion of the lithium-containing compounds in the SEI dissolves in the electrolyte during formation. In a second study, the novel *operando* NDP cell design was employed to investigate lithium plating during fast-charging of a graphite electrode with high time and spatial resolution. While low charging rates resulted in approximately homogeneous lithium concentration profiles, a steep lithium concentration gradient across the depth of the graphite electrode was detected when lithium intercalation exceeded a threshold rate. The observed high lithium concentration towards the separator/electrode and the low concentration at the electrode/current collector interface, respectively, indicates a gradient in the lithiation degree of the graphite particles as a function of depth within the electrode. After fast-charging the graphite electrode, the lithium concentration equilibrates during potential relaxation within ≈20 min, resulting in an approximately homogeneous lithium distribution across the electrode, which underlines the importance of studying lithium plating on graphite using *operando* techniques.

Both of the novel analytical methods presented here offer great potential for usage as analytical tools to examine various electrochemical processes in lithium- and sodium-ion batteries in future studies.

Kurzfassung

Das Verständnis (elektro)chemischer Prozesse in wiederaufladbaren Batterien ist eine Grundvoraussetzung für die Entwicklung neuer Aktivmaterialien mit erhöhter Energiedichte und für die Verlängerung der Lebensdauer von Batteriezellen. In vielen Fällen ist die Diagnostik dieser Prozesse nur in der Umgebung einer assemblierten oder gar in Betrieb befindlichen Zelle möglich, d.h. *in situ* oder *operando*, da nur so sichergestellt werden kann, dass das zu untersuchende System repräsentativ für eine operierende Zelle ist und sich nicht zeitlich bzw. durch äußere Einflüsse verändert. Im Rahmen dieser Arbeit werden zwei neue analytische Methoden vorgestellt, mit denen Aktivmaterialien in Lithium-Ionen-Batterien (LIBs) und Natrium-Ionen-Batterien (SIBs) untersucht werden können.

Die Entwicklung einer neuartigen Mikroreferenzelektrode (µ-RE) auf der Basis eines sodiierten Zinndrahtes erlaubt die gleichzeitige Messung der individuellen Elektrodenimpedanzen von Kathode und Anode in einer Natriumionenbatterie während des Zyklisierens ohne die Notwendigkeit einer Zellöffnung (*in situ*) und anschließender Rekombination identischer Elektroden in Form sogenannter symmetrischer Zellen. Die Elektrochemische Impedanzspektroskopie (EIS) wurde verwendet, um die Änderung der Elektrodenimpedanz einer Hard Carbon Anode in einer Natriumionenzelle während des Zyklisierens und als Funktion des Ladezustands (SOC) zu bestimmen. In einer Folgestudie wurden die erhaltenen Daten mit den Elektrodenimpedanzen im Falle der (De)-Lithiierung des gleichen Aktivmaterials verglichen und Konsequenzen für die Schnellladung von Natrium- und Lithium-Ionen-Zellen auf Basis von Hard Carbon Anoden abgeleitet.

Der zweite Teil dieser Arbeit beschäftigt sich mit der Entwicklung eines neuartigen Zelldesigns zur Messung des Lithiumkonzentrationsprofils in einer Batterieelektrode mittels *operando* Neutronentiefenprofilierung (NDP). Hierdurch konnte der Lithiumtransport während der (De)-Interkalation von Lithium in einer Graphitelektrode ortsaufgelöst über die Dicke der Elektrode quantifiziert werden

und es war möglich, die Lithiumbeiträge des Elektrolyten, des reversibel interkalierten Lithiums und des irreversibel im Solid-Electrolyte-Interphase (SEI) gebundenen Lithiums zu unterscheiden. Darüber hinaus konnten die jeweiligen Lithiummengen quantifiziert werden, was die Bestimmung des absoluten Lithiumgehalts in der SEI ermöglichte. Interessanterweise wurde festgestellt, dass nur ≈61 % der aufgrund der irreversiblen Kapazität erwarteten Lithiummenge (unter der Annahme, dass ein Lithium/Elektron-Verhältnis von 1/1 vorliegt) in der SEI nachgewiesen werden kann. Eine mögliche Erklärung hierfür ist, dass sich ein signifikanter Anteil der lithiumhaltigen Verbindungen in der SEI während der Formierung im Elektrolyten auflöst. In einer zweiten Studie wurde das neuartige *operando* NDP-Zelldesign eingesetzt, um Lithium Plating während der Schnellladung einer Graphitelektrode zeit- und ortsaufgelöst zu untersuchen. Während niedrige Laderaten zu annähernd homogenen Lithiumkonzentrations-profilen führten, wurde ein steiler Lithiumkonzentrationsgradient entlang der Tiefe der Graphitelektrode festgestellt, wenn die Ladegeschwindigkeit einen Schwellenwert überschreitet. Die hohe Lithiumkonzentration in der Nähe der Grenzfläche zwischen Separator und Elektrode und die niedrige Konzentration an der Grenzfläche zwischen Elektrode und Stromabnehmer weist auf einen Gradienten im Lithiierungsgrad der Graphitpartikel als Funktion der Tiefe innerhalb der Elektrode hin. Darüber hinaus übersteigt die Lithiumkonzentration in der Nähe der Separator/Elektroden-Grenzfläche deutlich den für vollständig interkaliertes Graphit erwarteten Wert, was beweist, dass lokal Lithium Plating stattgefunden haben muss. Nach dem Schnellladen der Graphitelektrode gleicht sich der Lithiumkonzentrationsgradient während der Potentialrelaxation innerhalb von ≈20 min aus, was zu einer annähernd homogenen Lithiumverteilung entlang der Elektrodendicke führt.

Die beiden hier vorgestellten neuartigen Analysemethoden bieten großes Potential für den Einsatz als Untersuchungswerkzeuge zur Aufklärung verschiedener elektrochemischer Prozesse in Lithium- und Natriumionenbatterien in zukünftigen Studien.

Contents

1 INTRODUCTION 1

1.1 28 YEARS AFTER ITS COMMERCIALIZATION – THE NOBEL PRIZE FOR LITHIUM-ION BATTERIES 2019 1

1.2 A BRIEF HISTORY OF THE DEVELOPMENT OF ACTIVE MATERIALS FOR LITHIUM-ION BATTERIES 3

1.3 ACTIVE MATERIALS FOR SODIUM-ION BATTERIES 14

2 EXPERIMENTAL METHODS 20

2.1 ELECTROCHEMICAL IMPEDANCE SPECTROSCOPY (EIS) 20

2.2 NEUTRON DEPTH PROFILING (NDP) 26

2.2.1 NDP Working and Measuring Principle 26

2.2.2 NDP Data Processing 30

2.2.3 NDP for Lithium-Ion Battery Research 34

2.2.4 A Novel Operando NDP Cell Design 36

2.2.5 Operando NDP Cell Holder and Cooling Setup 40

2.3 FURTHER EXPERIMENTAL TECHNIQUES 43

3 RESULTS 47

3.1 ELECTROCHEMICAL IMPEDANCE SPECTROSCOPY USING MICRO-REFERENCE ELECTRODES 49

3.1.1 Development of a Micro-Reference Electrode for Impedance Measurements in SIBs 49

3.1.2 Comparing the Lithiation and Sodiation of a Hard Carbon Anode via Impedance Spectroscopy Using Micro-Reference Electrodes 59

3.2 *OPERANDO* NDP AS ANALYTICAL TECHNIQUE FOR LITHIUM-ION BATTERY RESEARCH 72

3.2.1 A Liquid Electrolyte-Based Lithium-Ion Battery Cell Design for Operando NDP 72

3.2.2 Spatially- and Time-Resolved Detection of Lithium Plating Using Operando NDP 90

4 CONCLUSIONS AND OUTLOOK 117

4.1 SUMMARY OF THE KEY DEVELOPMENTS OF THIS WORK 117

4.2 POTENTIAL FUTURE APPLICATIONS OF THE HERE DEVELOPED DIAGNOSTICS 120

5 APPENDIX 123

6 REFERENCES 129

7 SCIENTIFIC CONTRIBUTIONS 151

List of Abbreviations

Abbreviation	**Description**
AAM	anode active material
Al	aluminum
BET	Brunauer-Emmett-Teller
BYD	Build Your Dreams (Chinese car manufacturer)
CAM	cathode active material
CC	constant current
CCCV	constant current/ constant voltage
CE	counter electrode
CEI	cathode electrolyte interphase
Cu	copper
CV	constant voltage
EC	ethylene carbonate
EIS	electrochemical impedance spectroscopy
EMC	ethyl methyl carbonate
EV	electric vehicle
FEC	fluoroethylene carbonate
GHG	green house gas
GWRE	gold wire reference electrode
HEV	hybrid electric vehicle
HVS	high voltage spinel
ICE	internal combustion engine
LEDC	lithium ethylene dicarbonate
Li	lithium
$LiBF_4$	lithium tetrafluoroborate
LiDFOB	lithium difluoro(oxalato)borate
LNMO	lithium nickel manganese oxide ($LiNi_{0.5}Mn_{1.5}O_4$)
LP57	EC/EMC solvent (3:7, by mass) with 1 M $LiPF_6$
LSV	linear sweep voltammetry
Na	sodium
NCA	lithium nickel cobalt aluminum oxide ($LiNi_{0.8}Co_{0.15}Al_{0.05}O_2$)

NMCxyz	lithium nickel manganese cobalt oxide ($LiNi_xMn_yCo_zO_2$)
NMR	nuclear magnetic resonance
NMP	N-methyl-2-pyrrolidone
OCV	open-circuit voltage
OEMS	on-line electrochemical mass spectrometry
OEM	original equipment manufacturer
OER	oxygen evolution reaction
PBA	prussian blue analogue
PVDF	polyvinylidene difluoride
RE	reference electrode
SEI	solid electrolyte interface
SOC	state-of-charge
TGA	thermogravimetric analysis
VC	vinylene carbonate
WE	working electrode
XPS	x-ray photoelectron spectroscopy
ZEBRA	Zero Emission Battery Research Activities

List of Symbols

Symbol	Name	Unit
α	constant phase factor	-
ε	porosity	-
κ	conductivity	S/m
η	overpotential	V
Φ	phase shift	rad
ρ	density	kg/m^3
τ	tortuosity	-
ω	angular frequency	rad/s
Ω	solid angle	sr
A	surface area	m^2
C	capacitance	F
CO_2eq	carbon dioxide equivalent	t
d	length	m
f	frequency	1/s
j	imaginary number	-
i	current	A
I	intensity	counts/s
n	mols	mol
M	molar mass	g/mol
Q	charge/capacity	As
Q	constant phase element	$F \cdot s^{(\alpha-1)}$
R	resistance	Ω
$R_{contact}$	contact resistance	Ω
R_{CT}	charge transfer resistance	Ω
R_{el}	electrical resistance	Ω
R_{pore}	pore resistance	Ω
E	voltage	V
Z	complex impedance	Ω

1 Introduction

1.1 28 Years After Its Commercialization – The Nobel Prize for Lithium-Ion Batteries 2019

In October 2019, the Nobel Prize in Chemistry was awarded to John B. Goodenough, M. Stanley Whittingham, and Akira Yoshino "for the development of lithium-ion batteries".[1] In their reasoning, the Royal Swedish Academy of Sciences stated:

> "[…] This lightweight, rechargeable and powerful battery is now used in everything from mobile phones to laptops and electric vehicles. It can also store significant amounts of energy from solar and wind power, making possible a fossil fuel-free society. […]"

Since the commercialization of the first lithium-ion battery (LIB) by Sony in 1991,[2] this battery type has indeed had, and still has, a significant impact on our modern society, with many people carrying two or more devices powered by LIBs constantly with them, be it in form of a smart phone, a smart watch, wireless earbuds or a laptop. As a consequence, the inventors of the LIB had been ranked among the favorites for the Nobel Prize for years. What might have additionally tipped the scales in favor of the committee's decision in 2019 is the growing debate about climate change and global warming, bringing masses of people on the street demonstrating to demand climate action with the goal of radically reducing greenhouse gas (GHG) emissions in order to restrain the global temperature increase to no more than 2 °C above pre-industrial level, as ratified within the Paris Climate Agreement in 2015.[3] To reach this goal, a massive reduction in annual emissions of carbon dioxide equivalents (CO_2eq) is necessary, according to the UN Environment Programme Emissions Gap Report,[4] as illustrated in Figure 1. In order to even have a chance to accomplish the 2 °C goal until 2030, today's carbon emissions must be reduced by at least ≈27 % or even ≈50 % for the 1.5 °C goal.

However, projections show that by only implementing the commitments from the Paris Climate Agreement, it is at best possible to keep the emissions of ≈55 Gt CO_2eq in 2018 only roughly constant with the ≈53 Gt CO_2eq projected for 2030.

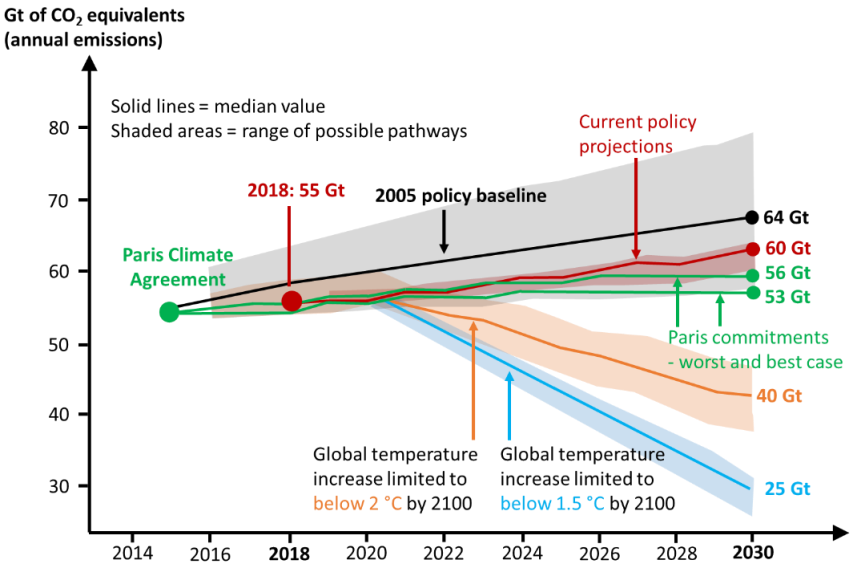

Figure 1. Global green house gas emissions under different scenarios and emissions gap by 2030 to keep the global temperature increase below 2 and 1.5 °C, respectively, redrawn according to [4].

Thus, the UN Environment Programme Emissions Gap Report stresses that actions to allow for the necessary transitions of the global energy sector have to be initiated by expanding renewable energy for electrification, phasing out coal for a rapid decarbonization of the energy system, and decarbonizing transport with a focus on electric mobility.[4] Further expanding the share of renewable energy sources requires the possibility of efficient energy storage to balance supply and demand of fluctuating energy sources, such as wind energy and photovoltaics. In 2018, the transportation sector was responsible for ≈24 % of direct CO_2 emissions from fuel combustion, of which ≈75 % were emitted by road vehicles.[5] Electrification of the transport sector, in order to switch from fossil fuel-based cars to electric vehicles (EVs), demands safe and long-lasting batteries with a sufficiently high energy density, which today can only be offered by lithium-ion-based systems. In recent years, virtually all major car manufacturers worldwide have committed to developing and releasing electrified vehicles (EVs). As an example, the Volkswagen Group (VW) has announced to invest 60 billion euros in electric mobility until 2024, and to launch approximately 75 new EV models and sell 28 million cars within the next 10 years.[6] In the European Union, the transition from internal combustion engines (ICE) to electric motor driven cars has been substantially accelerated by

the ratification of CO_2 emission regulations, which limit the average fleet emissions to 95 g CO_2/km by 2021, corresponding to ≈3.6 L of diesel or ≈4.1 L of gasoline per 100 km, and as decided in November 2018, emissions must be further decreased by 15 % (≈81 g CO_2/km) until 2025 and 37.5 % (≈59 g CO_2/km) by 2030.[7] With this legislation, the European CO_2 goals are the most rigorous in the world, *e.g.*, compared to CO_2 targets of the United States (121 g CO_2/km from 2020), China (117 g CO_2/km from 2020) or Japan (105 g CO_2/km from 2020). However, China introduced EV quotas for every car manufacturer starting in 2019 with 10 % and increasing each year by 2 %, *i.e.*, reaching 18 % in 2023.[8]

1.2 A Brief History of the Development of Active Materials for Lithium-Ion Batteries

In the mid-20th century, lithium came into focus of researches, having the lowest molecular mass of all metals (7 g/mol) and possessing a very low standard reduction potential (-3.05 *vs*. SHE), with the goal to increase the limited energy density of established battery types. Due to the low standard reduction potential, water could not be used as electrolyte and aprotic solvents, such as organic carbonates (*e.g.*, propylene carbonate), were identified as suitable solvents for electrolytes in combination with elemental lithium.[9] Further research efforts quickly resulted in the commercialization of lithium primary batteries, *i.e.*, non-rechargeable batteries, in the 1960s and 1970s.[10] Extensive investigations regarding rechargeable lithium-based electrochemical cells started in the early 1970s at Exxon and the Bell Laboratories in the US. Back then, the common opinion was that, just as in primary lithium batteries, elemental lithium should serve as anode material, and efforts were pursued to find a cathode material that could reversibly store lithium-ions at a sufficiently high potential.[11]

The fundamental working principle of LIBs is the shuttling of lithium-ions back and forth between two electrodes with different electrochemical potentials, which is why it is also referred to as “rocking chair battery”, a term coined by Armand in the 1970s.[12] Figure 2 shows a schematic setup of a typical LIB. Both the high potential electrode (cathode) and the low potential electrode (anode) active materials are typically coated on metal foil current collectors (typically aluminum

for the cathode and copper for the anode), forming porous electrodes which are separated by an electrically insulating porous material in order to avoid short-circuiting (referred to as separator).[13] Transfer of lithium-ions between the electrodes is assured by an ion-conducting aprotic electrolyte (most commonly ≈1 M $LiPF_6$ conductive salt dissolved in a mixture of organic carbonates, such as ethylene carbonate and ethyl methyl carbonate[14]) that is filling the pores of the separator and the porous electrodes. During discharging the cell, lithium-ions are extracted from the anode, transported through the electrolyte, and intercalated into the cathode material. In order to balance the separated charges, electrons are transferred through the external circuit and can be used to power an electrical device.

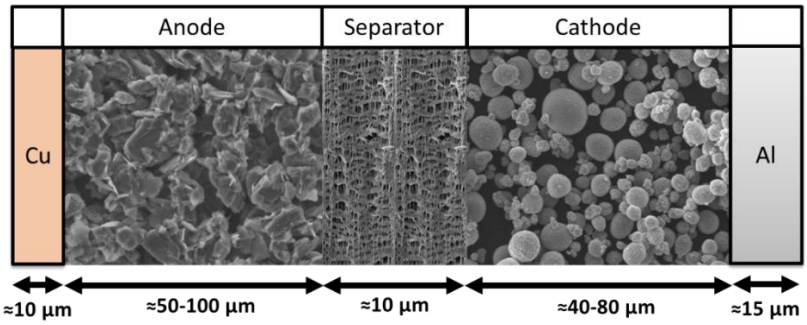

Figure 2. Schematic setup of a lithium-ion battery (LIB) cell with an NMC622 cathode (spherical particles, ≈10 µm) coated on an aluminum current collector, a graphite anode (flake-like particles, ≈20 µm) coated on a copper current collector, and a polyolefin-based porous separator.

Metal chalcogenides of the type MX_2 came into focus that had been shown to be able to host lithium-ions,[15] leading to the development of a TiS_2/Li cell by Whittingham and co-workers.[16,17] This cell still possessed a relatively low voltage of ≈2.5 V, but it was found that lithium could be reversibly (de)intercalated over the whole Li_xTiS_2 stoichiometry ($0 \leq x \leq 1$) within van der Waals slabs in the layered structure, offering a theoretical capacity of 239 mAh/g_{TiS2}. In 1977, Exxon then even demonstrated a 45 Wh cell prototype using lithium tetramethyl borate in dioxolane as electrolyte, allowing for more than 100 complete charge/discharge cycles.[11] Even though the use of elemental lithium as anode material brings advantages in terms of energy density, the lithium plating and stripping process was soon realized to be accompanied by the continuous chemical reaction of freshly formed lithium surfaces with electrolyte, and - more problematic - the inhomogeneous plating of lithium forms dendritic structures that may even grow through the separator and

lead to cell short-circuiting, posing severe safety issues. These safety problems proved impossible to be solved and finally stopped the commercialization efforts at Exxon.[18] The probably most prominent example of the early failure of the lithium metal electrode chemistry were explosion and fire accidents with MoS_2/Li cylindrical cells commercialized and sold in the million by Moli Energy in the 1980s, which led to a withdrawal of their cell from the market in 1989.[18,10] Since the working potential of the Li_xTiS_2 was relatively low, along with the development of the above mentioned commercial cells, efforts were taken to find other cathode materials with a higher mean discharge potential. A seminal discovery was achieved by Goodenough and co-workers in 1979/80 at Oxford University where they found that by substituting sulfur in the MX_2 chalcogenides structure with oxygen, a material class could be obtained offering a cathode potential beyond 4 V *vs.* Li^+/Li.[19, 20] The first compound of this class was $LiCoO_2$ (LCO), which should later on also serve as cathode material in the first commercial LIBs. The group of layered oxide cathode materials is to date the most widely used type of cathodes in commercial LIBs.

Due to the above described safety issues with metallic lithium electrodes, anode intercalation electrode concepts were investigated in parallel as a safer alternative.[21] Carbons were well known to intercalate lithium chemically[22, 23] with a maximum stoichiometry of LiC_6 in graphite, corresponding to a theoretical capacity of 372 $mAh/g_{graphite}$. However, at the beginning, the use of graphite as an intercalation material in an electrochemical cell was unsuccessful due to the lack of suitable electrolyte solvents. Besenhard and Eichinger[24] interpreted the observed exfoliation of graphite particles when using the commonly applied organic solvent propylene carbonate as solvent co-intercalation, with the accompanied graphite exfoliation resulting in the observed poor cycling performance.[25, 26] Reversible cycling could only be achieved using a solid polymer electrolyte at elevated temperatures.[27] In general, carbon materials can be classified into graphitizable or soft carbons[28] and into non-graphitizable or hard carbons (HCs). Soft carbons are turbostratic, *i.e.*, with random translations and rotations between adjacent layers, but already possess a certain degree of structural ordering of the crystallites, and therefore, can be transferred into the highly ordered graphitic state by a high-temperature treatment. Hard carbons that typically have a lower density, smaller

crystallites, and random orientation cannot be graphitized even at very high temperatures. The disordering of soft carbons compared to graphite reduces their specific capacity; however, it makes them compatible with a wide range of electrolytes, including propylene carbonate, since, in contrast to graphite, particle exfoliation does not occur.[29] The combination of Goodenough's $LiCoO_2$ cathode concept together with a soft carbon anode (petroleum coke) resulted in the first LIB purely based on intercalation electrodes, which was patented in 1985 by Yoshino and co-workers at Asahi Kasei in Japan.[30] Due to this patent filing, Akira Yoshino is considered the inventor of the LIB concept as we know it today.[31] Compared to a metallic lithium anode, the soft carbon anode possessed on average a 500 mV more positive potential, lowering the energy density of the cell. However, at the same time, issues such as dendrite growth and continuous electrolyte decomposition observed for metallic lithium anodes did not occur. A similarly designed battery based on $LiCoO_2$ and soft carbon (≈220 mAh/g_{SC}) was finally commercialized by Sony in 1991.[31] This first generation LIB by Sony had an energy density of ≈80 Wh/kg, which was considerably more than the back then widespread NiCd cells,[2, 32] and about as much as the NiMH battery by Ovonic Battery Company that had been at just about the same time commercialized.[33]

In a strive to increase the battery's energy density, the soft carbon anode was replaced by a hard carbon electrode (≈320 mAh/g_{HC}) already one year later, offering ≈120 Wh/kg.[2, 32] At the same time, Dahn and co-workers at Moli Energy showed that adding ethylene carbonate as a co-solvent to a propylene carbonate-based electrolyte prevented graphite exfoliation and continuous electrolyte decomposition, enabling reversible lithium (de)intercalation with excellent reversibility by protecting the graphite surface with a lithium-ion conducting but electronically insulating layer.[34] This concept of passivating a so-called solid electrolyte interphase (SEI) was first proposed by Peled in 1979 to be present on the surface of alkali and alkaline earth metals in non-aqueous battery electrolytes, suggesting that it is formed by a chemical reduction of the electrolyte on the metal;[35, 36, 37] it was further developed by Aurbach and others.[38, 39] The typical thickness of the SEI is in the order of nanometers.[40, 41] In 1991, Dahn, who had left Moli Energy one year earlier for Simon Fraser University (Canada), was the first to determine a phase diagram describing the electrochemical lithiation of

graphite, making use of *in situ* X-ray diffraction.[42] The formation of a stable SEI on graphite electrodes by ethylene carbonate was a breakthrough, since graphite exhibits a lower mean discharge potential and a capacity comparable to the HCs used before, resulting in an energy density of ≈155 Wh/kg in Sony's 3rd generation LIB.[43] Thus, artificial and natural graphites[44] became the almost exclusively used anodes in commercial LIBs.[45]

Even though the anode chemistry has barely changed over the past two decades, much progress was made in the development of new cathode active materials (CAMs). As a result, the specific cathode capacity of the first LIBs ($LiCoO_2$, ≈140 mAh/g_{LCO}) could be increased by ≈40 % to around 200 mAh/$g_{active\ material}$ for Ni-rich layered oxide materials commercialized today. Soon after the discovery of $LiCoO_2$, still at Oxford University, Thackeray, Goodenough, and co-workers developed $LiMn_2O_4$ (LMO), a spinel-type material with three-dimensional channels available for lithium transport, as a new class of cathode materials.[46] Compared to LCO, the material is significantly cheaper due to the substitution of the relatively expensive metal cobalt (≈30 €/kg_{Co}) by manganese (≈2 €/kg_{Mn}).[47] While LMO operates at a slightly higher potential than LCO, it has the drawback that its theoretical specific capacity is only ≈148 mAh/g_{LMO}, which results in a usable reversible capacity of merely ≈130 mAh/g_{LMO} due to lithium inventory losses during SEI formation in a full-cell against graphite. Moreover, it suffers from pronounced transition metal dissolution, especially at elevated temperatures.[48] Manganese dissolution and deposition on the graphite anode is known to cause accelerated lithium inventory loss, and is therefore detrimental for capacity retention.[49, 50] Nevertheless, mainly due to its low price, LMO was used in the Tesla Roadster from 2009, and in form of a blend with other CAMs (NMC111 and NCA) in the first BMW i3 vehicle from 2013 (60 Ah).[51] By means of substituting parts of the Mn in LMO by Ni, forming $LiNi_{0.5}Mn_{1.5}O_4$ (LNMO), the (de)intercalation potential of the resulting material can be increased from 4.0 to ≈4.7-4.75 V *vs.* Li^+/Li,[52] which significantly increases the specific energy. This so-called high voltage spinel (HVS) class of materials was discovered and first reported by Amine *et al.* in 1996.[53] In contrast to LMO, where the Mn oxidation state changes from an average +3.5 to +4 during delithiation, Mn remains at a valency of +4 in LNMO, which additionally lowers the tendency for Mn dissolution.[54] However, the very high mean cathode

potential leads to electrolyte oxidation, producing protic species which can in turn enhance transition metal dissolution by leaching metal ions from the cathode active material. An effective electrolyte or electrolyte additive suppressing oxidative decomposition at such high potentials has not yet been reported.

In the same year, Padhi and Goodenough discovered $LiFePO_4$ (LFP), crystallizing in an olivine structure with one-dimensional channels for lithium-ion transport, representing a third class of intercalation cathode materials.[55] LFP possesses a relatively high theoretical capacity of ≈170 mAh/g_{LFP}, but suffers from a very low electronic conductivity. Researchers around Michel Armand at Hydro Quebec[56] in Canada developed a carbon coating to increase the electronic conductivity which, together with the use of nanoparticle sized LFP, allows to cycle the material close to its theoretical capacity at room temperature and at high rate.[57] The material exhibits a relatively low (de)intercalation potential of ≈3.4 V *vs.* Li^+/Li. However, it is relatively cheap, environmentally benign, and shows good rate capability, which is why it is especially employed in applications such as grid storage or hybrid electric vehicles (HEVs), where energy density is not as crucial. Furthermore, it is used in electric buses and trucks, especially by the Chinese car manufacturer BYD.[58]

Layered oxide materials with the general composition $LiMO_2$, where M is one single or a mixture of multiple transition metals (M = Ni, Co, Mn), exhibit a theoretical capacity of ≈274 mAh/g_{CAM}. All types of stoichiometries have in common that only a limited amount of lithium can be extracted without causing irreversible changes to the crystal structure (O3 → P2 → O1 phase transformations,[59, 60] according to the lattice nomenclature by Delmas *et al.*[61]), going along with capacity fading during cycling. After Goodenough's discovery of the $LiCoO_2$ cathode active material, where ≈51 % of the lithium inventory are accessible,[19] efforts were made to find other layered oxide materials allowing for higher specific capacities. The first works date back to the early 1990s, when Dahn *et al.*[62, 63] and others[64] investigated $LiNiO_2$ (LNO) and found that lithium can be extracted at lower potentials compared to $LiCoO_2$ and $LiMn_2O_4$, thereby offering significantly higher capacities and at the same time avoiding electrolyte oxidation at high potentials. However, LNO suffered from many drawbacks, such as irreversible phase transitions occurring during cycling,[64] a low thermal stability in the discharged state,[65] and a high surface reactivity towards ambient air,[66, 67] and thus has not been commercialized until

today. Gradually, it was found that substituting a fraction of the Ni in LNO by Co (Delmas *et al*.[68]) or Co and Mn (Liu *et al*.,[69] Lu *et al*.,[70] and Ohzuku *et al*.[64]) increased on the one hand the capacity compared to LCO by suppressing the O3 → O1 phase transformation at high SOCs, and on the other hand improved the cycling stability compared to LNO. This led to the development of the well known compound $LiNi_{1/3}Mn_{1/3}Co_{1/3}O_2$ (NMC111) independently by Dahn[70] and co-workers, and Makimura[71] and co-workers in 2001, which has become one of the most used CAMs today (*e.g.*, employed in the BMW i3 EV from 2016).[72] Since then, interestingly, the trend has been going in the opposite direction, increasing the Ni content in the layered oxide CAMs, forming the class of Ni-rich NMCs. The idea here is to further increase the achievable capacity for the same cutoff potential by substituting Mn and Co by Ni, thereby reducing electrochemical electrolyte oxidation at high anodic potentials.

These material optimizations have yielded NMC523, NMC622, and NMC811, which by now all exhibit sufficient cycling stability for current or near-future applications in EV battery cells. A recent study by Harlow *et al*.[73] demonstrates that an advanced single crystal NMC523/graphite cell with an optimized electrolyte chemistry could achieve an EV driving range of > 1.6 million km. Using single crystalline (ca. 2-3 µm particles) instead of polycrystalline CAMs, where ca. 10-15 µm diameter secondary particles consist of ca. ≈200-500 nm primary particles,[74] has opened a new path to substantially enhance cycle life, as it largely eliminates the cracking of polycrystalline particles upon delithiation due to the anisotropic volume change of different primary particles. Upon particle cracking, the CAM surface area increases, which leads to more parasitic reactions between CAM and electrolyte.[75, 76, 77] As announced in January 2020, BMW has just extended its battery warranty from 8 years or 100,000 km to 160,000 km;[78] however, still far away from the projected range in the study from Harlow *et al*.

Apart from the NMC family, the currently most important CAM for EVs is NCA (*e.g.*, $LiNi_{0.8}Co_{0.15}Al_{0.05}O_2$)[79] due to its high capacity (≈200 mAh/g_{CAM}) and good cycling stability,[80] which is used in Tesla's Models S, X, and 3. NCA had been developed by substituting Ni in $LiNiO_2$ by Co and Al which resulted in a CAM with improved thermal stability and safety.[81, 82] The partial substitution is thought to

reduce Ni/Li cation mixing and to suppress phase transitions during cycling.[83] As recently published, Tesla sold ≈367,000 EVs of these models in 2019. According to a German engineering service company's report (PolarixPartner)[84] that dissected and analyzed a 75 kWh Tesla Model 3, the battery consists of 4416 cylindrical cells in the format 21700 (*i.e.*, 21 mm in diameter and 70 mm in length; the Model S and X used ≈8100 cells of the 18650 format; for a detailed comparison between the two cell formats s. Quinn *et al*.[85]) arranged in 100 battery modules which are connected in series and parallel to yield a power of 191 kW. Interestingly, the Co content in the NCA cathode chemistry was decreased to 2.8 %, and the battery material costs of the whole car were calculated to be ≈18,000 $. Adding estimated ≈10,000 $ of manufacturing costs, the analysis concludes that with an announced pricing of 35,000 $ (basic version), it is indeed possible to generate profit with this car, which many experts had doubted beforehand.

For the improvement of layered oxide CAMs, the development of ceramic coatings on the active particle surface, such as Al_2O_3, TiO_2 or ZrO_2,[86, 87] and the introduction of gradient materials with varying Ni-content along the particle radius, was crucial.[88, 89] Until today, the mechanistic understanding of the structural changes occurring upon high degree of delithiation has much improved. In 2017, Jung *et al*.[90] could for the first time conclusively demonstrate that the main reason for capacity fading when cycling different NMC/graphite cells (NMC = NMC111, NMC622, NMC811) to > ≈80 % SOC is a polarization on the cathode caused by oxygen release from the CAM surface lattice (detected by On-line Electrochemical Mass Spectrometry (OEMS)), leading to the formation of a thin oxygen-deficient resistive surface film on the particle surface (≈15 nm). The accompanied evolution of CO_2 and CO was explained by a chemical reaction of the released oxygen with electrolyte rather than by an electrochemical oxidation of electrolyte at these high potentials, as was often hypothesized in the literature.[90, 91, 92] These findings were supported by Wandt *et al*., [93] who could show that the evolved oxygen is at least in part highly reactive singlet oxygen. In this context, Pritzl *et al*. could very recently show that washing layered oxide CAMs with water, a standard procedure during production of *e.g.*, NCA, not only removes surface contaminants (Li_2CO_3 and LiOH), but also modifies the near-surface bulk structure by an H^+/Li^+-ion exchange which

upon a subsequent heat-treatment leads to an oxygen-depleted surface layer, and therefore reduces oxygen release during cycling.[94]

Due to its high price and problematic mining conditions,[95] current trends are going into the direction of further decreasing the Co share in CAMs. A recent publication from the Dahn group concludes that a complete substitution of Co in Ni-rich cathodes by other metal ions, such as Al, Mn, or Mg, is feasible.[83] Another approach to increase the capacity of CAMs is the development of so called "over-lithiated" or Li- and Mn-rich NCMs (LMR-NCMs, $x\,Li_2MnO_3 \bullet 1\text{-}x\,LiMO_2$, M = Ni, Co, Mn), first reported in 2001 by Lu *et al.*[70] and Thackeray *et al.*[96] This materials class features an extraordinarily high reversible capacity of ≈250 mAh/g_{CAM} and low material costs due to the high Mn and low Co content, but suffers from voltage fading, a large voltage hysteresis combined with a lower mean discharge potential compared to regular NMCs (≈3.4 $\bar{V}_{cell}$ and ≈3.8 $\bar{V}_{cell}$ in a full-cell *vs.* graphite), and structural instability during cycling, which is why it has not been commercialized so far.[97, 98, 99, 100]

Summing up some of the above discussed milestones in LIB development, Figure 3 shows a selection of the perhaps most relevant discoveries regarding LIB cathode materials research, which is not intended to be exhaustive.

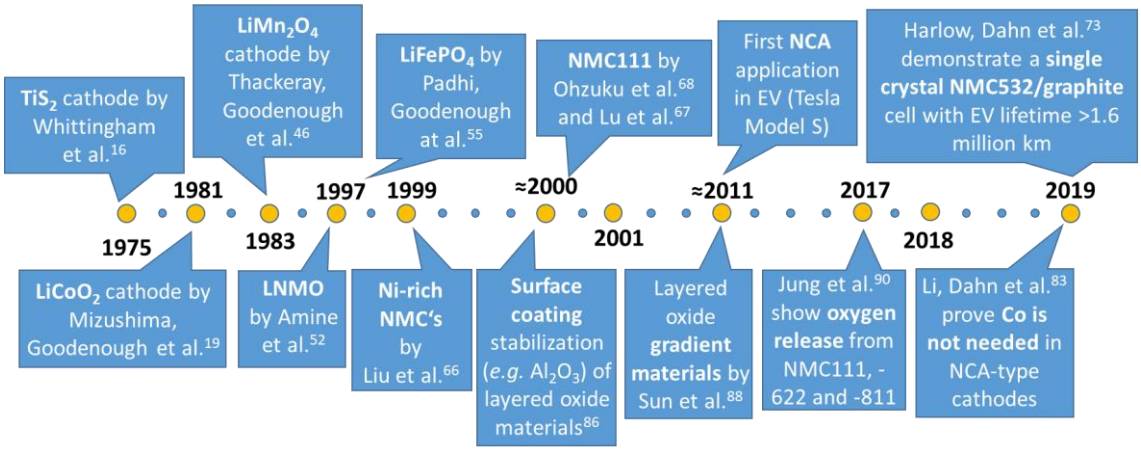

Figure 3. Important discoveries in the development of LIB cathode materials and understanding of fundamental electrochemical processes involved.

Since Sony's commercialization of the first graphite-based cell at the beginning of the 1990s, the anode chemistry has barely changed in commercial cells, and natural and synthetic graphites are almost exclusively used as AAMs. Natural graphites can be mined, whereas synthetic graphites are made from coke precursors by graphitizing them at temperatures up to 3000 °C which is why

natural graphite (≈8 €/kg) is considerably cheaper than synthetic graphite (≈13 €/kg).[101] Natural graphites have a higher degree of crystallinity and larger crystal sizes with a more ordered orientation, resulting in a slightly higher reversible capacity and lower irreversible capacity, but also in lower rate capability due to the smaller amount of edge sites that are needed for intercalation. Synthetic graphites have more edge sites due to the smaller, more randomly oriented crystallites, reducing the charge transfer resistance, but also presenting more reactive surface to the electrolyte, which slightly reduces first cycle reversibility.[102] However, the long-term cycling performance of synthetic graphites is typically better, which is believed to be related to its very high purity, lower thermal expansion, and higher thermal stability obtained through the graphitization process.[103] Introduction of additives, like vinylene carbonate[104] and others,[105] have increased the cycling stability of graphite anodes, but fundamentally new types of chemistries, such as alloy materials, could not yet prevail.

Silicon had already been considered as the future of anode materials, owing to its high theoretical capacity of ≈3579 mAh/g_{Si} ($Li_{15}Si_4$);[106] however, massive volume changes of ≈300 % during lithium (de)intercalation are leading to electrochemical milling (particle cracking), particle disintegration, continuous lithium inventory losses, and electrolyte consumption, all of which result in poor capacity retention.[107] In order to minimize structural degradation of particles and the electrode itself, an early approach was to employ nanometer-sized[108, 109, 110] or nano-structured[111] silicon, to protect the particles by shells[112, 113] or to embed silicon in a carbon matrix,[114, 115] which in turn again significantly decreases the energy density of the electrode. Even though these measures and the use of additives like fluoroethylene carbonate (FEC)[116, 117] improved the cycling stability, cycling in laboratory cells is often conducted *vs.* a lithium counter electrode (CE) and most of the time with excess electrolyte.[118] However, the transfer to commercial cell setups with both limited lithium inventory and limited electrolyte volume still remains challenging.[107] A different approach to avoid the high surface area of silicon nanoparticles and at the same time to minimize the particle volume expansion is partial utilization of micrometer-sized silicon particles, which can be produced very cost-effectively. Even though using only a limited fraction of the active material reduces the specific capacity, the achievable capacity is still higher

compared to graphite.[119] A recent publication by Jantke *et al.*[120] shows that with this method 250 cycles until 80 % of the initial capacity can be obtained in NMC622/silicon cells with a silicon usage of 30 %, allowing for an increase in anode volumetric capacity of ≈40 % (without calendering) compared to a state-of-the-art graphite electrode. Another advantage of silicon versus graphite could lie in better fast-charging capabilities, since the silicon lithiation potential is significantly more positive compared to graphite.

Since the recall of Moli Energy's metallic lithium-based cells, despite excessive research efforts,[121, 122, 123] no satisfactory solutions have yet been found to improve safety and longevity of lithium anodes to large-scale market readiness. Using a lithium anode would allow to increase the cell's energy density by 40-50 % compared to graphite.[124, 125] However, recent successes were reported using a slightly different approach, a so called "anode-free" LIB,[126, 127, 128] where the metallic lithium anode is formed *in situ* by plating lithium from the CAM on the anode copper current collector. Weber *et al.* demonstrated a dual-salt-based (LiDFOB/$LiBF_4$) liquid electrolyte exhibiting 80 % capacity retention after 90 charge–discharge cycles.[129]

Figure 4 summarizes some essential findings or conceptual discoveries with respect to LIB anodes, again, without the intention to be exhaustive.

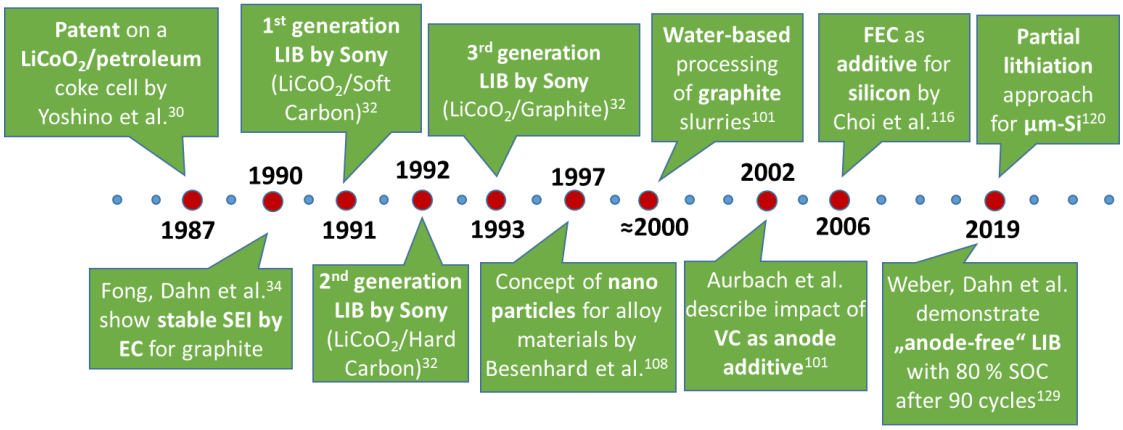

Figure 4. Important discoveries in the development of LIB anode materials and understanding of fundamental electrochemical processes involved.

In a nutshell, from the analysis above it can be concluded that the LIB cell specific capacity gains are gradually leveling off but that further gains are still possible in the future. Promising studies of long-lasting Ni-rich CAMs, potentially with Co contents close to zero, that could possibly be combined with silicon-based anodes or *in situ* plated metallic lithium anodes will very likely further increase cell capacity, and thus energy density to beyond 300 Wh/kg on a cell level. Economics of scale and further improvements regarding cell energy density and CAMs based on cheaper metal compositions will further reduce battery prices for EV packs. The price history of LIB cells between 2014 and 2019, and the expected prices in the years 2020 and 2022 are displayed in Figure 5,[130] showing that cell prices have already been reduced by ≈70 % between 2014 and 2019. The drop below 100 $/kWh, which is widely accepted as the tipping point where EVs have reached price parity with ICEs,[131] is expected to be reached in 2020. According to recent press information, VW has already managed to decrease its procurement prices for battery cells used in its first mass market EV, the model ID.3 (market launch mid 2020), to below 100 $/kWh.[132]

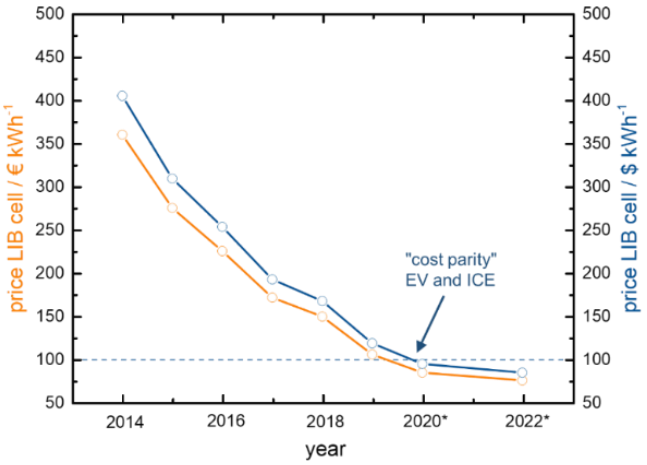

Figure 5. Globally averaged price history of LIBs on a cell level between 2014 and 2019 and expected prices for the years 2020 and 2022 in €/kWh (left y-axis) and $/kWh (right y-axis), produced from data from [130].

1.3 Active Materials for Sodium-Ion Batteries

To date, only very few smaller companies offer commercial SIBs (*e.g.*, Faradion, UK[133] or HiNa Battery Technology, China[134]) mainly advertised for the use in stationary applications or small electric vehicles (bicycles, small cars). Compared to LIBs, SIBs are still at an early stage of development since active materials combining

decent energy density with sufficient cycling stability are limited. Nevertheless, SIBs could indeed have advantages over LIBs. The fact that sodium does not form alloys with aluminum at typical anode potentials enables the substitution of Cu current collectors by Al with significant cost (≈factor of 3.4) and weight (≈factor of 3.3) saving potentials.[135] The standard reduction potential of Na^+/Na is only ≈330 mV higher than Li^+/Li; therefore, allowing for similarly high cell potentials. Sodium is not only by a factor of ≈1000 more abundant in the earth's crust than lithium,[136] but also far more evenly distributed; thus, reducing the current dependency on relatively few countries, *e.g.*, in South America, where lithium mining has also shown to come along with severe environmental and social issues. The molar mass of sodium (27 g/mol) is by a factor of ≈4 higher than lithium (7 g/mol), but compared on the practically relevant basis of the cathode active material itself, such as $LiCoO_2$ (98 g/mol, 274 mAh/g_{CAM}) and $NaCoO_2$ (114 g/mol, 235 mAh/g_{CAM}), the mass difference based on the cathode active material is only ≈14 %.

On the anode side, from the early beginnings in the late 1980s until today, the state-of-the-art materials are still hard carbons (HCs, ≈300 mAh/g_{AAM}); owing to the fact that sodium cannot be reversibly intercalated in graphite. This material class will be addressed in more detail in sections 3.1.1 and 3.1.2 of this PhD thesis.[137, 138] Since the first comprehensive investigation of HCs as anodes for SIBs by Dahn and co-workers in the early 2000s,[137, 139] hard carbons remain the most promising anode active material (AAM) today and probably also for the near future.[140] Other AAMs with reasonable specific capacities, such as Ti-based intercalation materials (*e.g.*, $Na_2Ti_3O_7$, ≈200 mAh/g_{AAM})[141] or alloying materials, such as the "p-block" elements (*e.g.*, Sn, Ge, P, and Sb)[140] suffer from very low cycling stabilities.

The classification of sodium-ion CAMs varies in the literature.[142, 143, 144, 145] The probably most prominent and most studied materials classes are oxides, especially the layered oxide family, polyanionic compounds, particularly the phosphate derivatives, and Prussian Blue analogue (PBA) materials.[146] After the discovery of the fast Na^+-conducting ceramic *β´´*-alumina by Kummer and Weber in 1967, the high-temperature (≈300 °C) liquid sodium based Na/S battery was already commercialized in the 1970s,[147] followed in the 1980s by the $Na/NiCl_2$ (ZEBRA)

battery.[148, 149] With promising discoveries in the field of layered oxide LIB materials, as summarized in detail in the previous chapter, similar $NaMO_2$-type cathodes came also into focus for SIB CAMs and were developed in tandem.[17, 150, 151, 152, 153, 154, 155, 156] According to the notation of Delmas *et al.*,[61] these compounds are termed On (n = 1, 2, 3) for sodium octahedrally coordinated by oxygen atoms (n denotes the repeat unit of the transition metal stacking) or Pn for a trigonal prismatic coordination. Similar to the lithium analogues, sodium metal oxides exist in a variety of polytypes, the most important being O3 (ABCABC), P2 (ABBA), and P3 (ABBCCA). In contrast to the lithium-based compounds, where lithium usually does not occupy prismatic sites due to its smaller ionic radius (0.76 Å *vs.* 1.02 Å), phase transitions between octahedrally and prismatically coordinated structures can occur during (de)intercalation *via* gliding of MO_2 sheets,[157, 142] which typically has negative effects on cycling stability and rate capability. However, advantageous could be that sodium-based layered oxides do not undergo irreversible spinel transformations upon high desodiation degrees (a capacity and cycle life limiting issue in lithium-based systems), which could enable stability over a larger range of sodium mole fraction.[145] In the 1970s and early 1980s, Delmas and co-workers performed pioneering work on the reversible (de)intercalation of sodium in Na_xCoO_2,[151] Na_xCrO_2,[158] Na_xMnO_2,[159] and Na_xFeO_2.[160] Main drawbacks of sodium-based layered oxides are the often occurring structural (multi)phase transitions (*e.g.*, P2 → O2 and P3 → O3) during cycling which results in poor cycle life[161] and characteristic stepwise voltage profiles.[162] Many reports showed that substituting parts of the transition metals by others forming binary, ternary, or quaternary compounds can improve the properties of the single-metal materials.[140] Examples for this approach are O3-$Na[Fe_{0.5}Co_{0.5}]O_2$[163] and O3-$Na[Ni_{0.33}Fe_{0.33}Co_{0.33}]O_2$[164] which, in contrast to the stepwise potential profile of $NaCoO_2$[162] and the low capacity of $NaFeO_2$,[165] exhibit a smooth potential curve, improved cyclability and comparatively high capacities of ≈160 mAh/g_{CAM}. Another interesting material is P2-$Na_{0.5}[Ni_{0.25}Fe_{0.13}Mn_{0.63}]O_2$[166] which has a very high capacity of ≈200 mAh/g_{CAM}, shows a good capacity retention, and an excellent rate capability. The high capacity, however, can only be obtained when cycling *vs.* a sodium CE, since sodium vacancies are filled during the first sodiation of the

material, which is of course only practically usable when employing sodium metal or sodium-containing anodes.

Polyanionic CAMs for SIBs stand out due to their high structural stability and tunable potential which can be adjusted by the inductive effect of anions in the lattice (*e.g.*, F^-).[167, 168] Important material classes are phosphates, pyrophosphates, fluorophosphates, and sulfates. The most studied structures include olivine, maricite, and NASICON compounds.[169] The sodium-analogue (≈154 mAh/g_{CAM} theoretical capacity) of the well known olivine-type $LiFePO_4$ (≈170 mAh/g_{CAM} theoretical capacity) exists in three polymorph structures, *i.e.*, olivine, maricite, and amorphous $NaFePO_4$. Above 450 °C, the open structured olivine-type $NaFePO_4$ transforms into the electrochemically poorly active maricite-type, where PO_4^{3-} tetrahedra isolate sodium-ions and block their diffusion paths,[170, 171] which makes synthesis of the pure olivine phase challenging. Another approach used by Oh *et al*. is to completely electrochemically delithiate $LiFePO_4$ and subsequently sodiate the $FePO_4$ in a half-cell *vs.* Na, yielding a reversible capacity of ≈125 mAh/g_{CAM}. Even though carbon-coated olivine $NaFePO_4$ can reach 100 cycles with a capacity retention of ≈90 %,[172] they are still very far from the excellent cycling stability of $LiFePO_4$. The most promising electrochemistry was reported using amorphous $NaFePO_4$ (a-$NaFePO_4$). Li *et al*.[173] showed that a-$NaFePO_4$ can reach ≈152 mAh/g_{CAM}, almost the theoretical capacity, and a capacity retention of ≈90 % over 300 cycles. The average potential of 2.4 V *vs.* Na^+/Na is, however, too low for a commercial application. The NASICON-type $Na_3V_2(PO_4)_3$ (NVP) exhibits an attractively flat potential profile at ≈3.4 V *vs.* Na^+/Na, but an only moderate theoretical capacity of ≈118 mAh/g_{CAM} (owing to 2 moles of cyclable sodium per formula unit); however, it demonstrates very good cycling stability of several 1000's of cycles (cycled *vs.* sodium metal) using carbon-coated NVP nanoparticles, obtained by rather complex synthesis routes.[174, 175] Another compound with very high cycling stability is the V-based *ortho*-disphosphate $Na_7V_4(P_2O_7)_4PO_4$ (VODP) with a flat potential plateau at 3.88 V *vs.* Na^+/Na and 78 % capacity retention after 1000 cycles without the requirement of a carbon-coating.[176] Also here, the drawback is the relatively low capacity of only ≈91 mAh/g_{CAM}. The average cathode potential can be increased by introducing F^--moieties in the crystal structure.[177] An example for a compound offering a comparatively high energy density is

$Na_3V_2(PO_4)_2F_3$ with two voltage plateaus at 3.7 and 4.2 V *vs.* Na^+/Na, a decent capacity of ≈120 mAh/g_{CAM}, and a good capacity retention.[178] However, the energy density of ≈507 Wh/kg_{CAM} is still relatively low, even lower than the ≈560 Wh/kg_{CAM} for $LiFePO_4$ (assuming 3.5 V *vs.* Li^+/Li and 160 mAh/g_{LFP}).[140] Nevertheless, carbon-coated nanoparticles of the same material showed a very long cycle life of 3000 cycles (cycled *vs.* sodium metal).[179]

A third interesting class of materials are Prussian Blue Analogues (PBA), *i.e.*, sodium-analogues of the original Prussian blue compound $KFe^{II}Fe^{III}(CN)_6$. Wang *et al*. reported on sodium iron hexacyanoferrate $Na_{1.92}FeFe(CN)_6$,[180] featuring two voltage plateaus at 3.3 and 3.0 V *vs.* Na^+/Na, a high capacity of 160 mAh/g_{CAM} and an attractive capacity retention of ≈80 % after 1000 cycles (cycled *vs.* sodium metal). Theses properties, together with the low cost of Fe, make Fe-based PBAs a very promising type of SIB cathode materials regarding a commercial use.[140]

In comparison, polyanionic compounds provide the highest potentials (> 3.75 V *vs.* Na^+/Na), while most layered-oxides are around ≈2.5-3 V *vs.* Na^+/Na and PBA materials are limited to ≈3.3 V *vs.* Na^+/Na.[140] Even though some of them show good cyclability (>1000 cycles), polyanionic compounds have low specific capacities (typically <120 mAh/g_{CAM}), whereas layered-oxides can provide higher capacities (up to ≈200 mAh/g_{CAM}), but are usually limited in cycling stability. In summary, with its high specific capacity (≈160 mAh/g_{CAM}), good cycling stability (≈1000 cycles), and decent potential (≈3 V *vs.* Na^+/Na), the PBA compound $Na_{1.92}FeFe(CN)_6$ provides a good trade-off between the necessary requirements on the way to a commercially viable CAM for SIBs. The other most promising cathode material for SIBs is $Na_3V_2(PO_4)_2F_3$, since it offers a decent capacity (120 mAh/g_{CAM}), a high potential (≈3.8 V *vs.* Na^+/Na), and very high cycle life (up to 3000 cycles cycled *vs.* sodium metal). In a SIB cell using a hard carbon anode, the combinations $Na_{1.92}FeFe(CN)_6$/HC and $Na_3V_2(PO_4)_2F_3$/HC can achieve an energy density of ≈310 Wh/kg on an active material based level (assuming 300 mAh/g_{HC} and 0.3 V *vs.* Na^+/Na as mean discharge potential for the HC anode[140]), which is already close to the ≈350 Wh/kg of a $LiMn_2O_4$/graphite cell (assuming 120 mAh/g_{LMO}, 355 mAh/$g_{graphite}$, and an average cell potential of 3.9 V[79]). However, compared to state-of-the-art material combinations in LIBs, such as NCA/graphite with ≈475 Wh/kg (assuming 200 mAh/g_{NCA}, 355 mAh/$g_{graphite}$, and an average cell

potential of 3.7 V[79]), the gap between LIBs and SIBs is still quite large, which underlines the necessity for SIB materials research and to achieve a better understanding of ageing mechanisms occurring during cycling.

2 Experimental Methods

2.1 Electrochemical Impedance Spectroscopy (EIS)

Detailed derivations of equations regarding the fundamental theory of Electrochemical Impedance Spectroscopy (EIS) can be found in Lazia,[181] Lvovich,[182] and Orazem.[183] Within this section, an overview on the most important and practically relevant correlations and equations for LIB analysis shall be given.

EIS is a non-destructive, *in situ* analytical technique which allows to simultaneously study electrochemical processes occurring at different time scales together with their associated resistances. The fundamental principle is to apply a sinusoidal current (galvanostatic, GEIS) or voltage (potentiostatic, PEIS) perturbation between the two electrodes under investigation and to measure the time-dependent voltage and current responses, respectively. Figure 6a exemplarily shows the schematic working principle of a PEIS measurement on a graphite/$LiFePO_4$ (LFP) battery cell where the potential perturbation with an amplitude of 10 mV is controlled between WE (graphite) and CE (LFP). The perturbation amplitude must be small, usually ≈5-20 mV for a PEIS, since for small excitations electrochemical systems show pseudo-linearity which results in an output signal with the same frequency as the input signal but that can be shifted in phase.

Let us assume the application of a small potential excitation signal E(t) of the form

$$E(t) = \widehat{E_0}\ \sin(\omega t) \tag{1}$$

where $\widehat{E_0}$ is the potential excitation amplitude and ω is the radial frequency in rad/s defined as:

$$\omega = 2\pi f \tag{2}$$

and f is the perturbation frequency in Hz.

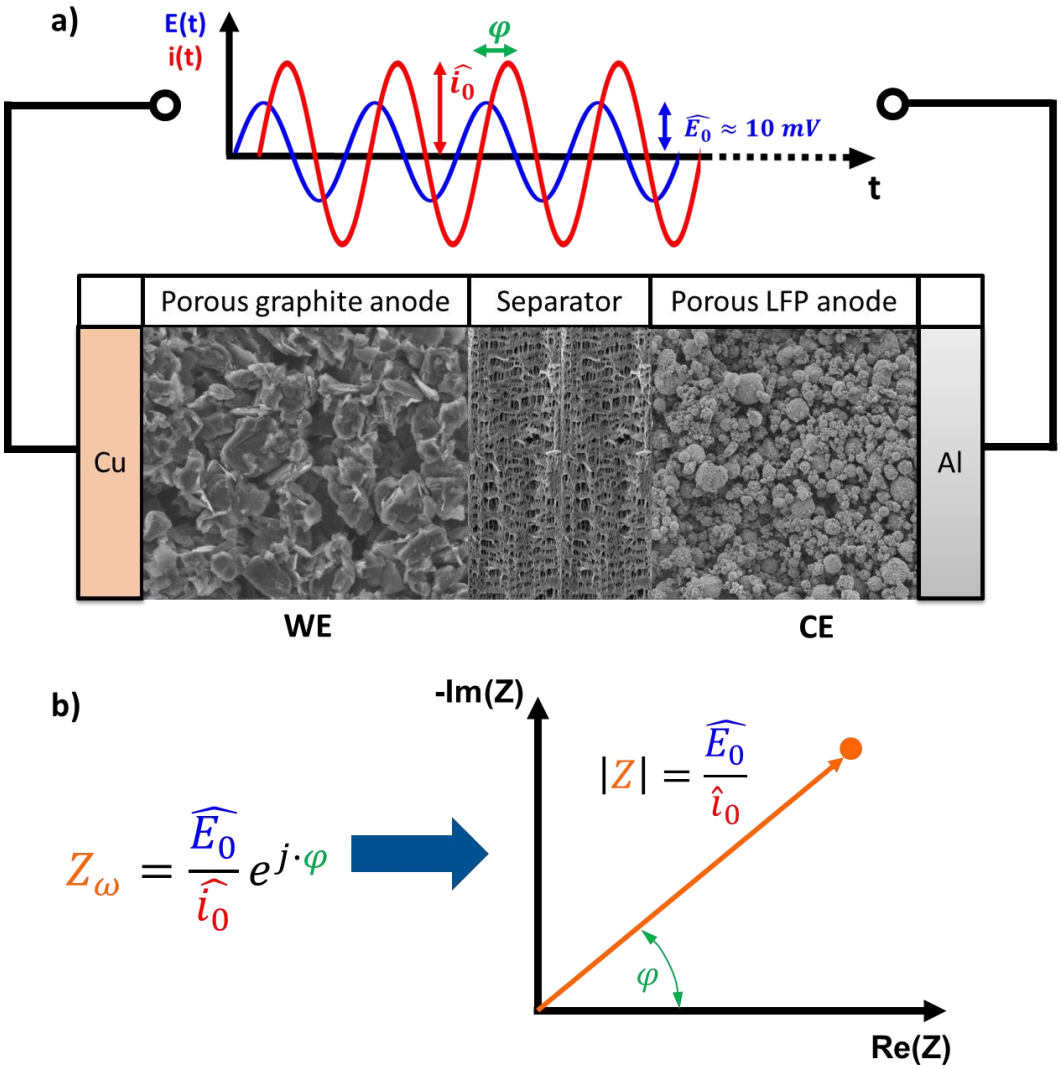

Figure 6. Working principle of an EIS measurement of a battery cell, exemplarily demonstrated for a graphite/$LiFePO_4$ (LFP) cell: **a)** a sinusoidal potential perturbation E(t) with an amplitude of 10 mV ($\hat{E}_0$) is applied between WE and CE; the current response i(t) is shifted in amplitude ($\hat{i}_0$)and phase (φ) with respect to the potential perturbation, **b)** definition of the complex impedance Z_ω and its depiction as a vector in a Nyquist representation.

In a linear system, the response will have the form:

$$i(t) = \hat{i}_0 \sin(\omega t - \varphi) \tag{3}$$

where $\hat{i}_0$ is the resulting current amplitude and φ is the resulting phase shift between the sinusoidal excitation signal and the response of the system. The total impedance Z_ω of the system is then defined as:

$$Z_\omega = \frac{E(t)}{i(t)} = \frac{\widehat{E_0}\, e^{j\omega t}}{\widehat{\imath_0}\, e^{j\omega t - j\varphi}} = \frac{\widehat{E_0}}{\widehat{\imath_0}} e^{j\varphi} = \widehat{Z_0}\, e^{j\varphi} \quad (4)$$

where E(t) and i(t) are the complex voltage and current, respectively, and j is the imaginary number $\sqrt{-1}$; $\widehat{Z_0}$ represents the amplitude ratio of $\widehat{E_0}$ and $\widehat{\imath_0}$. Z_ω is a function of frequency and composed of a real and an imaginary part, which can be illustrated by using Euler's formula:

$$e^{j\varphi} = \cos\varphi + j\sin\varphi \quad (5)$$

This yields:

$$Z_\omega = \widehat{Z_0}(\cos\varphi + j\sin\varphi) = Re\,(Z) + j \cdot Im(Z) \quad (6)$$

where $Re\,(Z)$ and $Im(Z)$ are the ω-dependent real and imaginary parts of the complex impedance. The complex impedance is typically represented in a Nyquist plot, where for every measured frequency ω the real part $Re(Z)$ is plotted on the x-axis and the negative imaginary part -$Im(Z)$ is plotted on the y-axis. Z_ω is therefore a vector in the x-y-plane with the length being the absolute value of $|Z|$ and the angle between the x-axis and the vector denoting the phase shift φ (s. Fig. 6b).

Table 1. Selection of typical equivalent circuit elements used to model electrochemical systems along with an expression to calculate their impedance.

Element	Impedance	
Resistor	R	
Capacitor	$\frac{1}{j\omega C}$	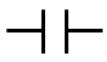
Constant Phase Element (CPE)	$\frac{1}{(j\omega)^\alpha Q}$	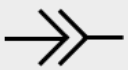
Warburg (finite)	$\frac{\sigma \cdot (1-j)}{\sqrt{\omega}}$	

The impedances of the most commonly used equivalent circuit elements are summarized in Table 1. These are: (i) a resistor, used to model the charge transfer resistance across an electrode interface (R_{CT}), a pore resistance (R_{pore}), an

electrical contact resistance between two materials ($R_{contact}$), or an electrolyte resistance ($R_{electrolyte}$); (ii) a capacitor (C) or constant phase element (Q), representing the double layer capacity of an electrode; and, (iii) a Warburg element (W), representing the impedance caused by diffusion of ionic species (*i.e.*, solid state diffusion of Li-ions in active material particles or liquid state diffusion of Li-ions in the electrolyte).

Figure 7a displays an equivalent circuit that can be used to model a graphite/LFP full-cell and Figure 7b shows a Nyquist plot representation of a graphite/LFP full-cell impedance measurement recorded in a Swagelok®-type T-cell.

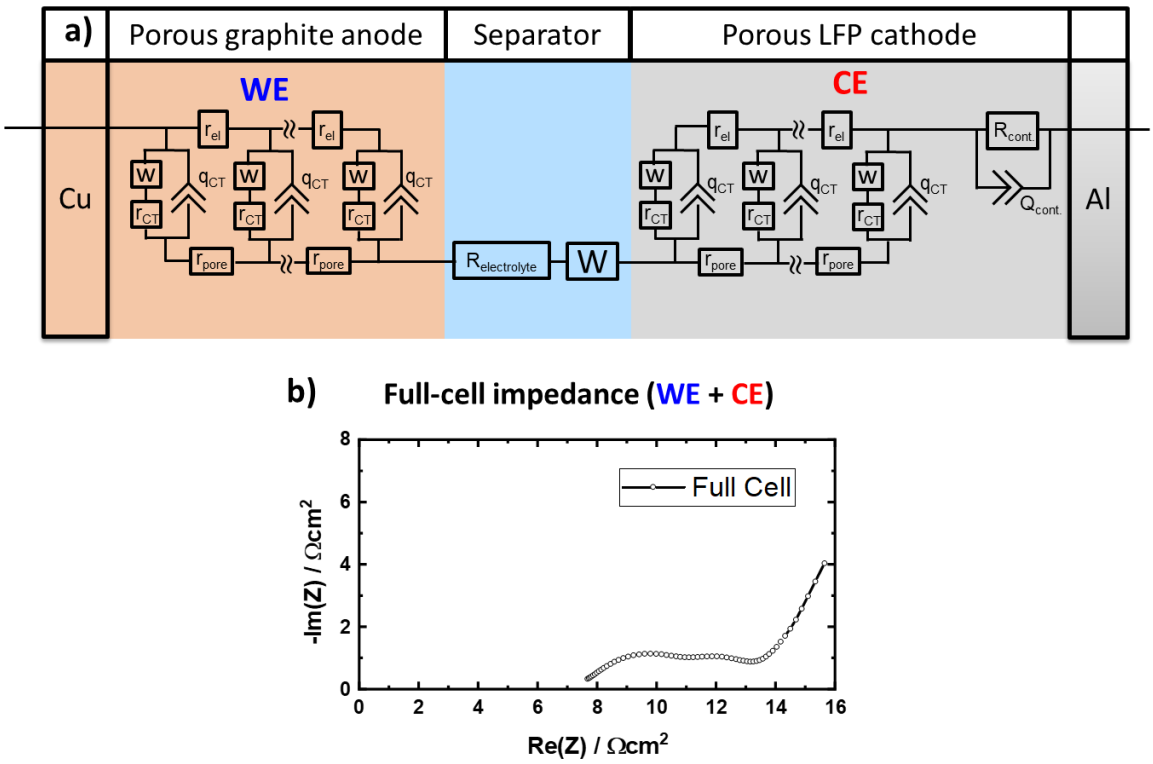

Figure 7. a) Equivalent circuit that can be used to model a graphite/LFP full-cell using a transmission line model (TLM) for both the porous graphite and the porous LFP electrode. Due to the very high electrical conductivity of graphite and copper, the contact resistance $\boldsymbol{R_{contact}}$ is only included in the cathode impedance. The Warburg impedance $\boldsymbol{w}$ included in the TLM reflects the resistance due to diffusion in the active material particles and the Warburg impedance $\boldsymbol{W}$ indicates the diffusion resistance due to Li-ion diffusion in the separator phase; **b)** Nyquist impedance plot (100 kHz-0.1 Hz) of a graphite/LFP full-cell impedance measurement recorded in a Swagelok®-type T-cell, representing the sum of the impedances of graphite anode and LFP cathode and the electrolyte resistance $\boldsymbol{R_{electrolyte}}$ (= high-frequency resistance, HFR).

Porous electrodes, such as the porous graphite anode or the porous LFP cathode, can be quite accurately modelled by a transmission line model (TLM), which is investigated in more detail in section 3.1.1 and 3.1.2 of this PhD thesis. In case of

the LFP cathode, a contact resistance $R_{contact}$ is included in the equivalent circuit, which was neglected in case of the graphite anode due to the very high electrical conductivity of copper and graphite. Additionally, the equivalent circuit contains a purely ohmic resistor representing the electrolyte resistance $R_{electrolyte}$ and Warburg diffusion elements. The Warburg impedance w included in the TLM reflects the resistance due to diffusion of Li-ions in the active material particles and the Warburg impedance W indicates the diffusion resistance due to Li-ion diffusion in the separator phase.

Since time constants for various electrochemical processes in LIBs can be similar, the resulting impedances often overlap making it difficult or even impossible to deconvolute anode and cathode contributions to the total cell impedance. A possibility to measure anode and cathode impedance simultaneously but separately within the same cell without opening the cell is to use a μ-reference electrode (μ-RE), which was also extensively used throughout this PhD thesis (s. section 3.1.1 and 3.1.2).

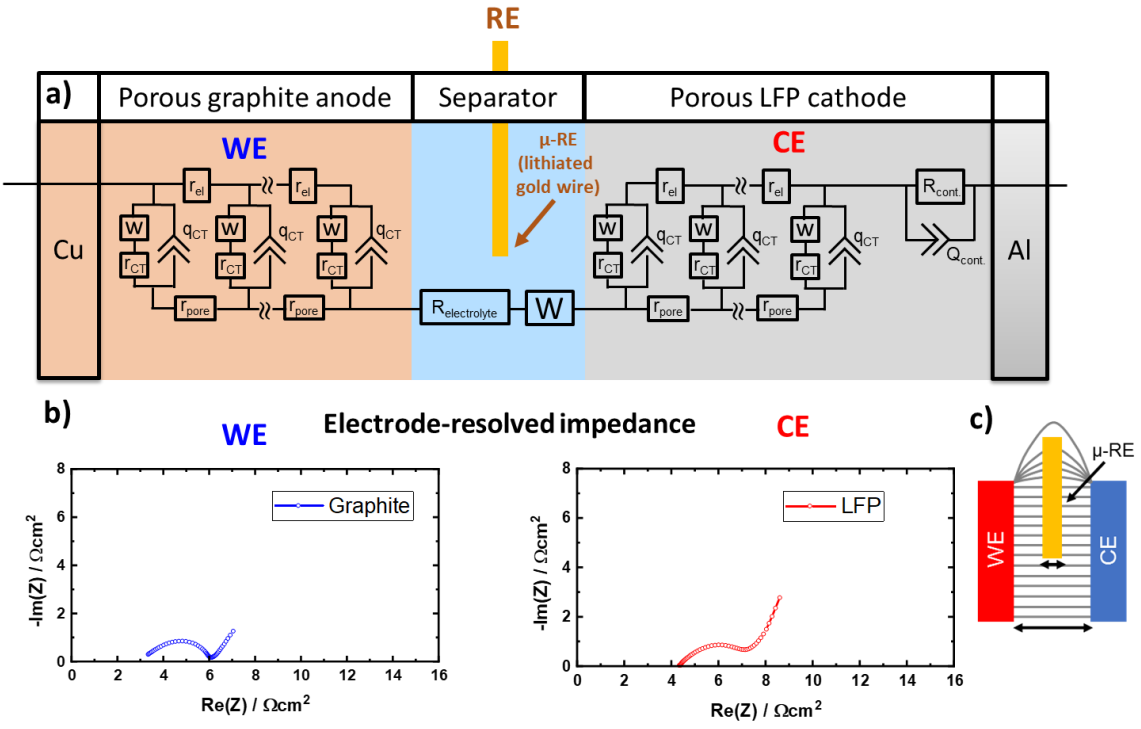

Figure 8. a) Schematic of an EIS measurement *via* a μ-RE, in this case an *in situ* lithiated 50 µm thick gold wire (μ-GWRE) placed between two glassfiber separators, which are indicated by the electrolyte resistance in the porous separators $\boldsymbol{R_{electrolyte}}$, and incorporated in a customized Swagelok® T-cell; **b)** electrode-resolved Nyquist impedance plots (100 kHz-0.1 Hz, measured in a T-cell) for the graphite WE (blue) and the LFP CE (red) which can be deconvoluted from the full-cell impedance (s. Fig.7b) using a μ-RE. Note that the high-frequency resistance (HFR) only equals the separator electrolyte resistance (the portion of the separator between µ-RE and the electrode) in

the case of the graphite electrode. In case of the LFP cathode, the HFR is ≈1 Ωcm² higher because the spectrum is shifted by a contact resistance $\boldsymbol{R_{contact}}$, which is not visible in the frequency range up to 100 kHz;[185] **c)** μ-RE placed centrally between WE and CE, where the electric field is homogeneous. The wire diameter must be small compared to the distance between the two electrodes.

In the case of a LIB, a 50 µm-thick insulated gold wire can be used as a μ-RE (μ-GWRE) which is incorporated centrally between the electrodes within a Swagelok® T-cell (s. Fig 8a). This technique was first reported by Solchenbach *et al*.[185] and later used extensively by Pritzl *et al*. and by Landesfeind *et al*. as a tool to study the impedance contributions of the individual electrodes in graphite/LNMO full-cells, which were then used to deconvolute the different impedance contributions (*e.g.*, R_{CT}, R_{pore}, and $R_{contact}$) of each of the electrodes.[184, 186] Pritzl *et al*. also investigated the impact of VC additive on the impedance of individual electrodes,[41] and quantified the growing contact resistances of LNMO cathodes during cycling.[187] To obtain a stable reference potential of the µ-GWRE, the gold wire is lithiated *in situ* using a very small lithiation current from the cathode (150 nAh, *i.e.*, <<1 ‰, and therefore negligible compared to the total capacity of the cathode) before cycling the cell. The thus lithiated gold wire exhibits a stable potential (≈310 mV *vs.* Li^+/Li[185]) after electrochemically alloying the gold with lithium, set by the $Li^+/AuLi_x$-alloy half-cell reaction. In order to be usable as μ-RE for EIS measurements, the RE must furthermore be located in the center between the two electrodes, where the electric field is homogeneous, and its diameter must be small with respect to the distance between the electrodes to order to minimize the potential gradient over the diameter of the wire (s. Fig. 8c). During a PEIS measurement using a RE, the potential is controlled *vs.* the μ-RE, and current and potential are measured between WE and CE. That way, the impedance of the WE, the CE, and the full-cell are recorded simultaneously, and it is possible to deconvolute the full-cell impedance into the impedance contributions from each individual electrode (s. Fig. 8b).

In this PhD thesis, a similar approach was used to develop a μ-RE for a SIB using an insulated tin-coated copper wire as RE.[188] The development and application of this μ-RE to measure the impedance of a hard carbon (HC) electrode in a sodium/hard carbon half-cell is given in detail in section 3.1.1.

2.2 Neutron Depth Profiling (NDP)

2.2.1 NDP Working and Measuring Principle

Neutron Depth Profiling is a non-destructive, near-surface nuclear analysis method for isotopes which undergo neutron-induced exoergic (energy releasing) charged particle reactions, producing either an α-particle through a so-called (n, α) reaction or a proton through a so-called (n, p) reaction, and a recoiling nucleus.[189] The method is suitable for certain light elements and based on measuring the energy loss of charged particles after exiting the specimen. Thus, depending on the sample matrix, depths up to ≈50 µm[190, 191, 192] with a maximal resolution around ≈20 nm[193] can be probed. The practically most relevant isotopes accessible *via* NDP (discarding radioactive species) are summarized in Table 2, together with their neutron capture characteristics.[191] Isotopes with high, medium, and low sensitivity are highlighted in green, orange, and red, respectively.

Table 2. Non-radioactive isotopes detectable *via* NDP, energy of the emitted charged particles, neutron cross sections, and resulting detection limits based on 0.1 cps, 0.013 sr detector solid angle, and a neutron intensity of 6×10^9 1/(cm²s) (obtained at the 20 MW NIST reactor, according to Downing *et al.*[191]). *E.g.*, the reaction ^{3}He(n,p)^{3}H denotes the neutron capture of a ^{3}He particle forming a proton (p) and a recoiling ^{3}H nucleus. The energy of the emitted particles given in column 4 refers to either the α-particle or the proton and the energy shown in column 5 refers to the recoiling nucleus.

Element	Reaction	Abundance (%)	Energy of emitted particles (keV)		Cross section (barns)	Detection limit (atoms/cm²)
He	^{3}He(n,p)^{3}H	0.00014	572	191	5333	1.5×10^{12}
Li	^{6}Li(n,α)^{3}H	7.4	2055	2727	940	9.0×10^{12}
B	^{10}B(n,α)^{7}Li	19.9	1472	840	3837	2.1×10^{12}
N	^{14}N(n,p)^{14}C	99.6	584	42	1.83	4.5×10^{15}
O	^{17}O(n,α)^{14}C	0.038	1413	404	0.24	3.5×10^{16}
S	^{33}S(n,α)^{30}Si	0.75	3081	411	0.19	6.0×10^{16}
Cl	^{35}Cl(n,p)^{35}S	75.8	598	17	0.49	1.7×10^{16}
K	^{40}K(n,p)^{40}Ar	0.012	2231	56	4.4	1.9×10^{15}

NDP was introduced as a method to detect the profile of boron impurities in p-type doped silicon wafers at IBM Research in the 1970s by Ziegler *et al.*,[193] taking advantage of the ^{10}B(n,α)^{7}Li reaction converting ^{10}B isotopes (≈20 % natural

abundance) to monoenergetic *α*-particles; before that time, the boron content was probed indirectly *via* electrical measurements. For the newly developed NDP analysis, a boron detection limit of 3 ppm and a depth resolution of ± 20 nm were reported. Later, NDP was used by Biersack *et al*.[194] to study the ^{3}He distribution, and by Fink *et al*.[195] to determine the ^{14}N concentrations in various solids after atom implantation. In order to enable a neutron capture reaction, the neutrons must be low in energy (<≈10 meV,[191] making use of thermal neutrons, with an energy distribution around ≈25 meV, or cold neutrons, whose energy is between 0-25 meV). The capture cross section is inversely proportional to the square root of the neutron energy, which means that lowering the neutron energy increases the reaction rate, so that using cold neutrons approximately doubles the reaction probability per neutron compared to thermal neutrons.[189] Besides that, the signal-to-noise ratio during a fixed measuring time of course also increases with the incident neutron flux, with higher fluxes enabling measurements on shorter time-scales. NDP experiments presented in this PhD thesis (s. sections 3.2.1 and 3.2.2), were therefore conducted at two neutron facilities offering very high neutron fluxes for NDP. These are the PGAA (Prompt Gamma Activation Analysis) beamline at the neutron reactor FRM2 (neutron source Heinz Maier-Leibnitz) [196, 197, 198] in Garching (Munich) offering a flux of 1.35×10^{9} $1/(cm^{2}s)$ and a mean cold neutron beam energy of 1.8 meV (6.7 Å), and the CNDP (Cold Neutron Depth Profiling) instrument[191] at the NIST Center for Neutron Research (NCNR) in Gaithersburg (MD, USA) with a flux of 1.22×10^{9} $1/(cm^{2}s)$ and a mean cold neutron beam energy of 8 meV (1.5 Å).

A schematic of the beamline setup of the N4DP (Neutron 4-Dimensional Depth Profiling) instrument at the PGAA beamline of the FRM2 is depicted in Figure 9a.

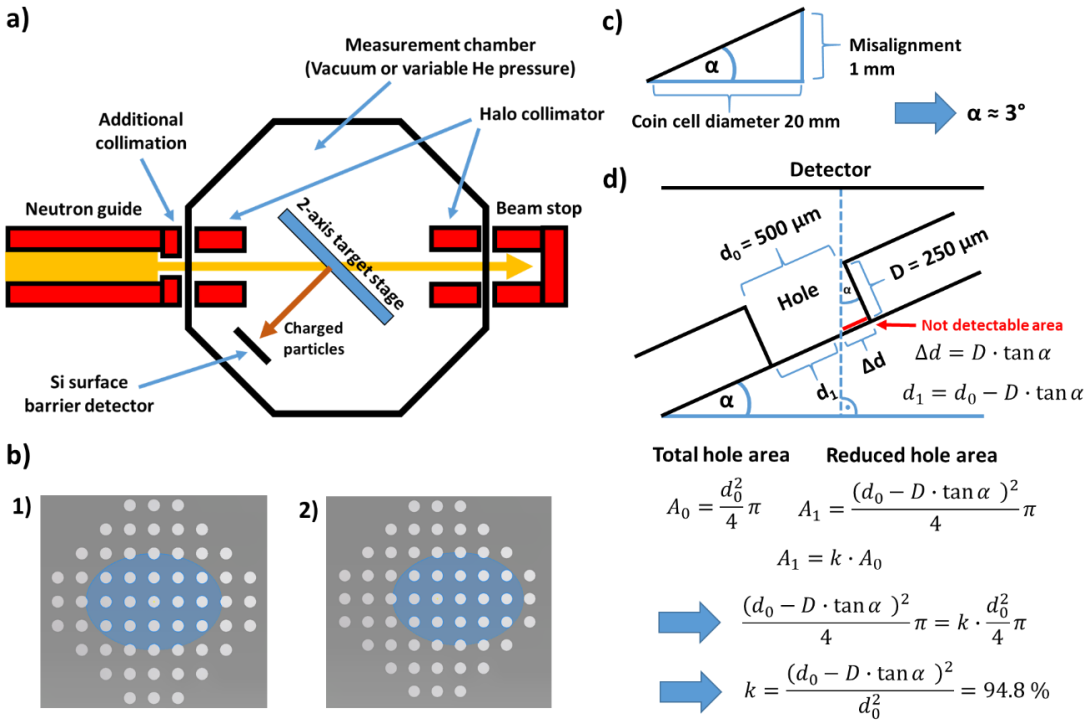

Figure 9. a) Top-view schematic of the N4DP instrument at the PGAA beamline of the FRM2 in Garching (Munich, Germany), adopted from Werner *et al.*[199] **b)** Superpositions of the neutron beam illuminated sample area (blue) with the 500 µm hole grid pattern of an *operando* NDP coin cell. 1) Illuminated area in the center of the pattern, and 2) shifted by 900 µm. **c)** Estimation of the coin cell tilt angle considering a 1 mm shift of one coin cell edge out of the sample holder plane. **d)** Estimation of an upper boundary for the effective hole area reduction assuming a tilt angle of 3° (D = 250 µm, d_0 = 500 µm).

The neutron beam is roughly circularly collimated by boron-containing shielding plates to an area of ≈12.6 mm² (Ø ≈4 mm),[197] enters the vacuum chamber (at a pressure of 10^{-4}-10^{-5} mbar for *ex situ* samples or a He atmosphere with adjustable pressure for *operando* samples)[198] *via* a 100 µm thick aluminum window and hits the sample at a 45° angle. Thus, the sample area illuminated by the neutron beam has the shape of an ellipse (≈17.8 mm²). For lithium concentration calibration, a reference sample with a well known ^{10}B concentration (^{10}B atoms/cm²) is used, which is explained in more detail below. In most cases, the illuminated area is identical for the reference sample and the specimen, which is why the shape and the size of the illuminated area do not have to be precisely known, as long as the sample sizes are larger than the projected beam area.

The latter is not anymore true for NDP experiments with the here newly developed NDP battery cell, where the charged particles can only reach the detector through the holes patterned onto the cap of a conventional coin cell. The pattern of 500 µm-wide holes and the projection of the neutron beam are shown in Figure 9b

(s. also section 3.2.1). In this case, the hole area illuminated by the neutron beam must be determined to allow for a lithium quantification by referencing the flux of charged particles to that obtained for the lithium standard reference. The total amount of hole area that is illuminated by the neutron beam and that contributes to the NDP signal depends on the relative alignment of the neutron beam with the hole grid pattern, which may vary according to the sketches 1) and 2) shown in Figure 9b. To determine the maximum and minimum possible active area, numerous superpositions of the projected elliptic beam area on the coin cell cap with the hole grid pattern were considered by shifting the beam area in multiple directions away from the grid pattern center between 0 mm and 1 mm in 100 µm steps, and by rotating the beam area by 0°, 22.5°, and 45°. This yields that the fractional hole area of the illuminated window area is between 20.2 % and 17.8 %. If the coin cell is not in an ideal plane-parallel alignment with the detector, the effective hole area might be further reduced, since a small fraction of the charged particles emanating would then be blocked by the stainless steel casing (s. Figure 9d). The maximum tilt angle was estimated by assuming that the coin cell is lifted by 1 mm at one edge (the maximum estimated misalignment), resulting in an angle of ≈3° (s. Figure 9c). Together with a hole diameter of d = 500 µm and a thickness of the coin cell cap of D = 250 µm, this yields an additional area reduction of 5.2 % (s. Figure 9d). Note, that this approach underestimates the active area, since the resulting projection has an elliptic shape and is not a circular area, and therefore, the 5.2 % area reduction is an upper boundary. As a result, the maximum accessible fraction of the total hole area remains at 20.2 % (perfect angular alignment) and the minimum would become 16.9 % (3 ° angular displacement). The obtained range of hole area fractions must be applied as a correction to all of the NDP signals from the *operando* coin cell when referenced to a lithium concentration standard. The average of these min/max values for the active area fraction is ≈(18.6 ± 1.6) %, resulting in a relative uncertainty due to geometric considerations of ± 9.0 %.

As shown in Figure 9a, the detector is placed normal to the sample surface (a second detector can be placed normal to the rear surface of the sample; which is useful if charged particles can exit to both sides of the sample) in order to maximize

the viewing depth into the sample, since the particle emission is isotropic.[191] The sample-detector distance is usually 96 mm, however, needs to be adjusted if samples with different thicknesses are to be compared. In case the signal rates increase to beyond 1 kHz, which induces pile-up effects inside the detector, the neutron beam intensity can be reduced by different attenuators (5.9 %, 16 %, and 47 %).[198]

2.2.2 NDP Data Processing

NDP can be very favorably used in the field of LIBs since lithium possesses a high sensitivity, and thus very low detection using NDP (s. Table 2). The underlying nuclear reaction ^{6}Li(n,α)^{3}H is explicitly written in equation (7):

$$^{6}Li + n \rightarrow \ ^{4}He(2055\ keV) + \ ^{3}H(2727\ keV) \qquad (7)$$

The specific energy of the emitted particles is defined by the Q-value of the nuclear reaction, *i.e.*, the amount of energy absorbed or released during the reaction, and is hence characteristic for a given element.[191] In case of lithium, a double positively charged $^{4}He^{2+}$ (α-particle) with an energy of 2055 keV and a single positively charged particle $^{3}H^{+}$ (*triton* particle) with an energy of 2727 keV is formed. The charged particles travel across the sample and lose energy by electrostatic interactions with the matrix atoms.[191] Since these interactions are proportional to the square of the particle charge, α-particles lose their kinetic energy much faster compared to *triton* particles, which is why they can only exit from the surface near region (≈10 µm). Figure 10 shows two simulated NDP spectra for $^{3}H^{+}$ particles formed in a 10 µm thick sample consisting of 1.35×10^{21} Li atoms/cm^{3} homogeneously distributed in a carbon matrix. The black curve represents the energy distribution simulated by using the mean residual energy function E(x) (s. inset) determined by the SRIM stopping range tables for $^{3}H^{+}$ in carbon, and thus shows sharp intensity changes. The red curve includes (simulated) statistical variations in the energies, described by a normalized Gaussian, due to intrinsic noise of the detector, electronic noise of the signal readout chain, and particle dependent broadening, such as statistical processes in the detector (charge carrier

statistics of electron-hole pair production and energy straggling in the dead-layer of the detector).[198]

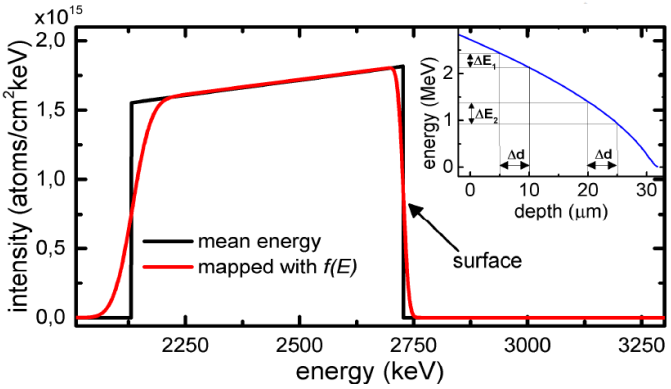

Figure 10. Two simulated NDP spectra for $^3H^+$ from a 10 µm thick sample consisting of 1.35×10^{21} Li atoms/cm^3 homogeneously distributed in a carbon matrix. The black curve represents the energy distribution simulated by using the mean residual energy function $E(x)$ (s. inset). The mean residual energy $E(x)$ was determined by the SRIM stopping range tables for $^3H^+$ in carbon. The red curve includes statistical variations in the energies due to intrinsic noise of the detector, electronic noise of the signal readout chain, and particle dependent broadening, such as statistical processes in the detector. Reprinted from Materials Characterization, Volume 146, December 2018, Trunk *et al.*, Pages 127-134, Copyright (2020), with permission from Elsevier.[199]

The slope in the simulated NDP spectra originates from the non-linear relation between energy loss and travelled distance within the sample (s. inset in Figure 10), since the energy loss is a function of the particle energy. As can be seen from the simulated spectrum in Figure 10 (red line), the NDP spectrum resolution is higher at the surface, where the signal broadening is dominated by intrinsic uncertainties of the detector and the readout chain, and reduced towards lower energies due to additional statistical scattering processes in the sample material.[198]

Figure 11 outlines a typical procedure to determine the lithium concentration profile from an NDP measurement. First, the ADC (analog-to-digital converter) channels of the detector have to be calibrated for the energies of the charged particles. Typically, this is achieved using one or two energy standard materials, *e.g.*, LiF, $LiNbO_3$ or B_4C films, with a very low thickness to minimize the particle energy loss within the sample. From the characteristic signals in the NDP spectra of the references which occur at well defined energies a correlation between ADC channel and particle energy can be obtained.

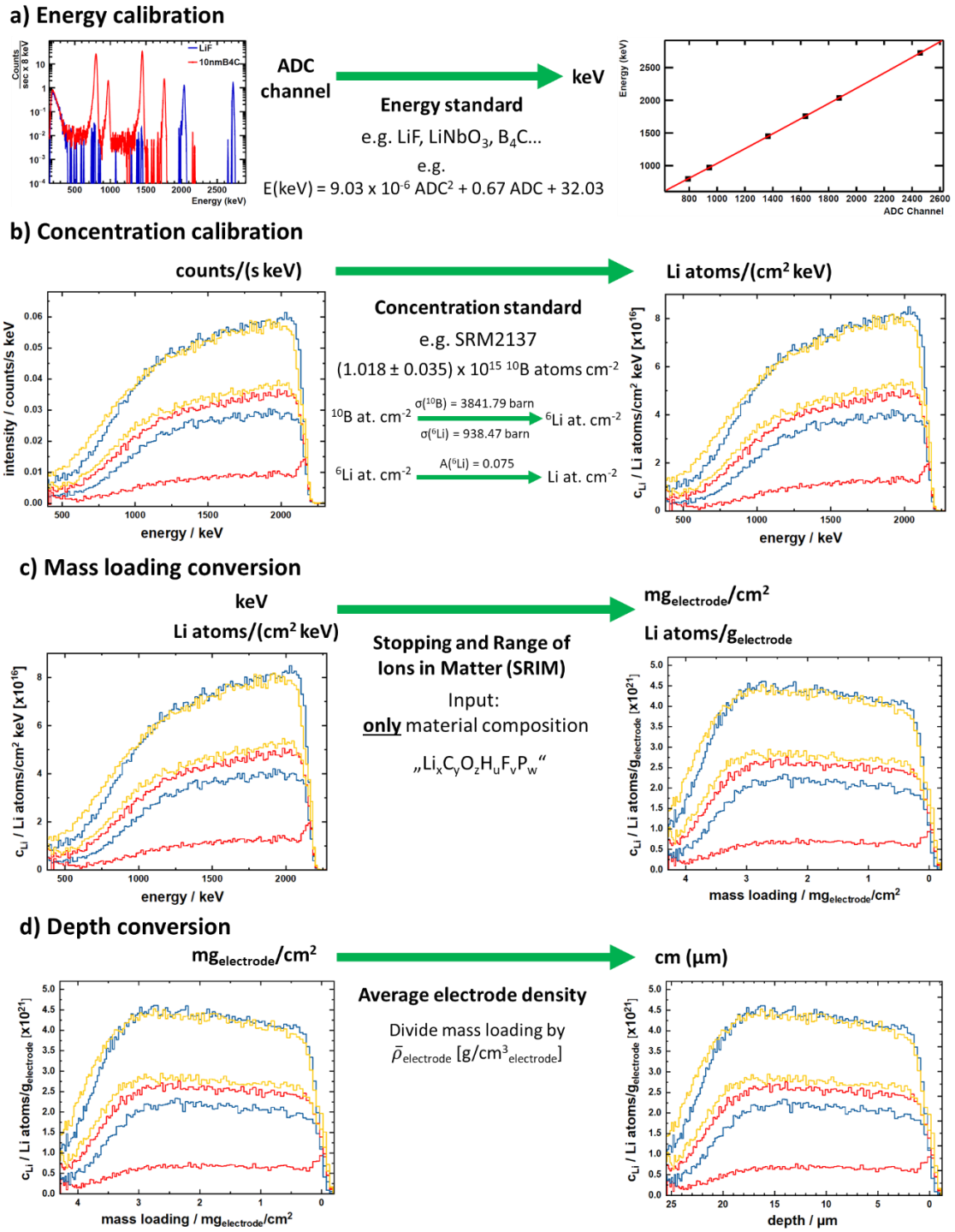

Figure 11. Typical procedure to determine a lithium concentration profile from NDP raw data: **a)** energy calibration using an energy standard (*e.g.*, thin layer of LiF);[200] **b)** concentration calibration by means of a concentration standard (*e.g.*,^{10}B doped Si wafer); **c)** conversion into mass loading using the SRIM software; and **d)** conversion of mass loading into a depth profile assuming an average electrode density $\bar{\rho}_{electrode}$.

As explained above, the reaction ^{6}Li(n,α)^{3}H yields two signals, one from an *alpha* (2055 keV) and one from a *triton (*2727 keV) particle. The reaction ^{10}B(n,α)^{7}Li produces four signals, since ^{10}B nuclei can decay *via* two reaction pathways, in each

case forming ^{7}Li and *alpha* particles but with varying energies, 94 % ^{7}Li* (849 keV, where * denotes that the ^{7}Li nucleus is in excited state, which decays afterwards releasing γ-radiation) and *alpha* (1470 keV) and 6 % ^{7}Li (1010 keV) and *alpha* (1770 keV) particles, respectively (s. red and blue spectra in Figure 11a). Thus, we obtain NDP spectra showing counts per second *vs.* particle energy.

By means of a concentration standard, the count rate can be transformed into a "lithium loading per unit area", *i.e.*, Li atoms/cm^{2} (where the area refers to a geometrical sample area and not a BET area). Here, usually certified standard samples are used, such as a silicon crystal with well defined ^{10}B implantation (*e.g.*, SRM2127 with 1.018 ± 0.035× 10^{15} ^{10}B atoms/cm^{2}). Provided that the active areas (= sample area illuminated by the neutron beam) of the reference and the NDP sample are identical, the sample count rate can be directly converted into a corresponding ^{10}B concentration (^{10}B atoms/cm^{2}), from which a respective equivalent number of ^{nat}Li atoms/cm^{2} is accessible *via* the neutron capture cross sections of ^{10}B (3841.79 barn) and ^{6}Li (938.47 barn) together with the natural abundance of ^{6}Li (≈7.4 %) (s. Figure 11b).[201] If the active areas are not identical, as is the case in *operando* NDP studies with the above described hole grid patterned coin cell, the ratio between the active areas of sample and reference have to be determined as precisely as possible. This can be done by estimating the active area of the sample *via* geometrical superpositions of the projected incident neutron beam and the hole grid pattern of the *operando* NDP cell, as demonstrated in Figure 9b, which was done in the NDP study conducted at FRM2 in Garching (s. section 3.2.1). Alternatively, a lithium standard (*e.g.*, LiF-foil) can be mounted inside the coin cell cap, which is the most accurate approach to determine the active area, and which was used in the NDP study performed at the NCNR in Gaithersburg (MD, USA) (s. section 3.2.2).

The energy loss of the charged particles (*alpha* or *triton*) moving through a matrix can be simulated rather precisely. To calculate the depth of formation of a charged particle from its energy loss requires knowledge of the characteristic stopping power of the matrix material, which was compiled by Ziegler *et al*.[202] and Janni *et al*.[203] in form of tables for a huge number of elements during the early days of NDP. Nowadays their data are provided by the software tool SRIM (**S**topping and **R**ange of **I**ons in **M**atter) that was written by Ziegler *et al*. in 1985 and that has been

updated regularly since.[204] The SRIM program predicts the energy loss of a charged particle when traveling across a homogeneous material matrix consisting of different elements with a defined composition. Therefore, the only input parameter is the elemental material composition and the SRIM program relates a given energy loss to a certain amount of mass loading (in terms of mg_{matix}/cm^2) the particle has traversed, thereby converting the particle energy on the NDP x-axis to a mass loading of sample and the lithium atom areal loading (Li atoms/cm^2) on the NDP y-axis to a lithium concentration (Li atoms/g_{matrix}) (s. Figure 11c). Note, that the density of the sample material is not required for these transformations. For the energy loss of the charged particles, it is irrelevant how closely packed the matrix atoms are, only the total mass of matrix that was passed determines the energy loss, while the traversed distance does not matter. However, in many cases, it is favorable to know the spatial lithium distribution, *i.e.*, to obtain a lithium concentration depth profile. In this case, the mass loading can easily be converted into a depth *via* dividing the mass loading by an average material density $\bar{\rho}_{electrode}$ (s. Figure 11d). This of course presupposes that the material matrix can be approximated by a homogeneous density, as it is the case for an electrolyte-filled LIB electrode at a certain SOC.

2.2.3 NDP for Lithium-Ion Battery Research

The exploitation of NDP as lithium-sensitive analytical technique in the field of LIBs was first reported in 2003 by Lamaze *et al*., who employed NDP to determine the distribution of lithium (*via* $^6Li(n,\alpha)^3H$) and nitrogen (*via* $^{14}N(n,p)^{14}C$), in the ion beam deposited solid electrolyte lithium phosphorus oxynitride (LiPON) under various fabrication conditions.[205] Between 2009 and 2014, Whitney *et al*.[206, 207] and Nagpure *et al*.[208, 209, 210] published several *ex situ* studies where they *post-mortem* investigated the lithium profiles in the near surface area of electrodes from aged cells. *E.g.*, Whitney *et al*.[206] studied the graphite SEI growth rate in commercial LFP/graphite cells after storing the cells for different times at 50 °C. In a second study,[207] they benchmarked two different NDP facilities by testing the very same samples (an aged graphite anode and an aged NMC111 cathode), which showed high reproducibility, and determined the depth resolution for the *triton* particles in

graphite to be 0.44 µm. However, neither of the studies commented on the *post-mortem* treatment of the cycled electrodes, such as washing to remove lithium-containing electrolyte salt residuals, which are indistinguishable from lithium bound in the SEI, since NDP detects lithium independently from its chemical environment.[191] Therefore, some type of washing procedure seems indispensable, even though there remains the risk that parts of the SEI might dissolve in the washing solvent.

A more quantitative analysis on the amount of lithium-containing electrolyte decomposition products was reported by Wetjen *et al*. and by Trunk *et al*. who *post-mortem* investigated the buildup of inactive lithium-containing SEI decomposition products in cycled silicon-graphite composite electrodes *via* NDP.[198, 211] Trunk *et al*.[198] introduced a mathematical method to separate the signal contribution from *αlpha*- and *triton* particles, which overlap in samples with mass loadings typical for practical LIB electrodes (>≈20 µm). Thereby, the commonly used approach to insert thin separation foils (*e.g.*, a 7.5 µm Kapton® foil) impermeable for *αlpha*-particles can be avoided, thereby increasing the viewing depth into the sample. Furthermore, Wetjen *et al*.[211] demonstrated by *ex situ* NDP measurements that the accumulation of lithium-containing electrolyte decomposition products is most pronounced during the first 60 cycles and occurs uniformly over the thickness of the SiG electrode, underlining that the Si nanoparticle active material is utilized completely. It was further shown that the massive expansion of the electrode thickness (≈3-fold) over extended cycling, leading to a ≈2.5-fold increase in void volume, together with electrolyte consumption would dry out a commercial cell very quickly, posing severe problems for a commercial deployment of Si nanoparticles.

The first *in situ*, or more precisely, *operando* study was reported by Oudenhoven *et al*. in 2011 on a thin film solid-state microbattery.[192] However, the application of *operando* NDP to conventional LIBs is very challenging since a window is required to prevent electrolyte evaporation and because the limited escape depth of the charged particles for a porous electrode is already intrinsically limited to a few tens of micrometers. This would additionally be strongly diminished by the current collector (≈10 µm copper or ≈15 µm aluminum in commercial cells) and the cell

casing, which for all types of battery cell hardware would be impermeable even for *triton* particles. Therefore, very thin current collectors and cell windows are required for *operando* NDP cells. Furthermore, NDP experiments are typically performed in high vacuum (≈10^{-4} mbar), significantly below the vapor pressure of an LIB electrolyte, which would lead to a bulging of the window and to an inhomogeneous compression of the cell stack. Several approaches were performed in the literature to deal with the limited depth penetration and the electrical contacting issues with regard to liquid electrolyte-based cells. Wang *et al*. and Liu *et al*. used a tin foil as WE studying the lithium intercalation into tin in a half-cell *vs*. lithium, protecting the lithiated tin anode by a thin Kapton® window. Zhang *et al*. used a ≈10 µm thick Al current collector serving at the same time as window in order to study lithium transport in porous ≈12 µm thick LFP electrodes.[212] While Zhang *et al*. did not further specify the exact cell setup used in their study, Liu *et al*. used a coin cell setup with a circular hole within the cap casing that was sealed by a Kapton® tape. Even though the diameter of the hole was not specified, one would expect electrical contacting issues when using a non-rigid window, such as a current collector metal or metal-coated polymer foil, especially when operating the NDP sample chamber at pressures below the vapor pressure of the electrolyte. This would limit such a design, at best, to very slow cycling rates. Whether this is the case, cannot be ascertained, since none of the published *operando* NDP studies we are aware of reports the specific capacity they could achieve, therefore lacking the proof that the material under study is really subject to conditions that are comparable to a commercial cell, since otherwise the measured effects may have little implications for commercial batteries.

2.2.4 A Novel *Operando* NDP Cell Design

For the above outlined reasons, one goal of this PhD thesis, was to design and validate an improved *operando* NDP lithium-ion battery cell setup aiming at: 1) an electrochemical performance comparable to a standard laboratory cell, ideally also at high C-rates; 2) maximizing the viewing depth by minimizing thickness and density of the cell window and current collector; and, 3) allowing operation at

reduced pressure in the NDP sample chamber, keeping it, however, above the vapor pressure of the electrolyte to avoid electrolyte gassing.

The focus was to study a graphite electrode since graphite has a much lower crystallographic density (≈2.2 g/cm^3) compared to cathode active materials, so that thicker electrodes can be probed, and as graphite is still the most relevant anode active material in commercial LIB cells. Even for graphite electrodes, however, the viewing depth is limited to a maximum of ≈20-30 µm. To prepare such thin electrodes, commercial graphites were unsuitable, as their d_{50} particle diameters are already ≈20 µm (s. Figure 12a), which would not allow for the preparation of a homogeneous 20-30 µm thick electrode. Therefore, we employed a sieved artificial commercial graphite with a narrow particle size distribution around ≈6 µm in length and ≈1 µm in height of the flake-like particles (s. Figure 12a), such that the resulting electrode would serve as a more homogeneous model electrode with a significant amount of particles being stacked on top of each other (s. inset in Figure 12a). In order to reduce the stopping power of current collector and window as much as possible, a copper-sputtered (100 nm) Kapton® foil (7.5 µm) was used, on top of which circular graphite electrodes were doctor-blade coated through a ≈80 µm thick PTFE-coated fiberglass mask. For detailed information regarding electrode and cell fabrication s. section 3.1.1.

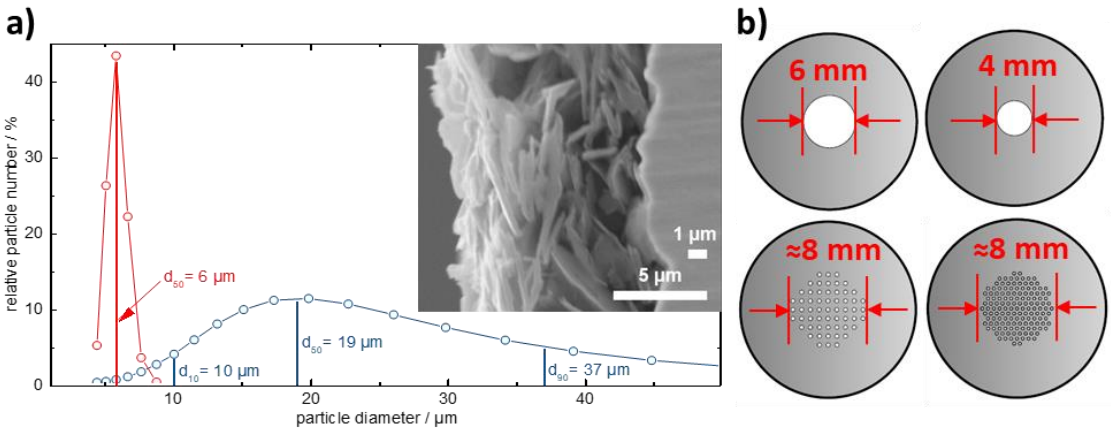

Figure 12. a) Particle size distribution for a commercial artificial graphite (blue) and the same active material obtained after sieving to lower the d_{50}-value to ≈6 µm (red); the inset shows an SEM cross-section of an uncompressed electrode coated with ≈6 µm particles on a copper current collector. **b)** Coin cell cap designs used over the course of the *operando* NDP cell development: a 6 mm (≈28.3 mm^2) and a 4 mm (≈12.6 mm^2) circular hole, 57 x 500 µm holes (≈11.2 mm^2) in a square arrangement, and 139 x 300 µm holes (≈9.8 mm^2) in a hexagonal arrangement.

A first attempt was the adoption of the coin cell setup with one hole in the cap studying the effect of the hole size on the cycling performance. The two single-hole diameters that were examined are shown in the upper part of Figure 12b. Since the neutron beam at the PGAA beamline at the MLZ (Garching, Munich) is collimated to a circular shape with a diameter of ≈4 mm, a 6 mm wide window would be ideal to compensate for minor alignment inaccuracies, to maximize signal intensity, and to minimize background radiation (β- and γ-radiation) from neutron interaction with the cell's stainless steel casing. As it is well known that uneven pressure distribution and lack of contact pressure on a cell stack can lead to increased local overpotentials,[213] we performed cell tests to benchmark the NDP cell *vs.* a conventional coin cell without hole(s) and used compressible glassfiber separators (six pieces) in order to somewhat improve the pressure distribution in the hole area. The complete setup of the NDP coin cell is displayed in Figure 13a. First cycling tests using a 6 mm wide hole yielded significantly less reversible capacity than the expected ≈355 mAh/$g_{graphite}$ (cycled *vs.* a capacitively oversized LFP electrode), even at a slow cycling rate of C/15. Thus, we narrowed the hole size to a diameter of 4 mm hoping that this might provide a finite and more homogeneous contact pressure. In this case, the cell obtained a reversible capacity of ≈349 mAh/$g_{graphite}$, which could still be within the weighing error of the electrode. However, disassembling the cell in fully charged state, *i.e.*, with the graphite anode being lithiated, revealed that the center of the hole still showed the black color of unlithiated graphite, whereas the golden color of LiC_6 was present everywhere else on the active material. This can be seen in the left panel of Figure 13b showing a photograph of the decrimped coin cell opened in the fully charged state. This clearly illustrates that even an only 4 mm diameter hole is too large to provide a sufficient compression of the cell stack, resulting in an utterly inhomogeneous extent of the lithiation reaction over the electrode area. As the area under the 4 mm diameter hole is only ≈10 % of the overall area, this effect is not so apparent in the overall capacity of the cell. However, the Li-NDP signal obtained from the 4 mm diameter hole region would by no means reflect the lithium concentrations in the majority of the electrode area, and thus any correlation between the Li-NDP signal and the cell performance would be utterly flawed.

Based on the above observations, a new *operando* cell design approach was taken, considering two constraints: 1) the need for a sufficiently large hole area in order to obtain sufficient charged particle counts; 2) the need for very small hole diameters in order to maintain sufficient local compression on the cell stack. This was accomplished by replacing the single-hole design by a hole grid pattern based on either 500 µm or 300 µm diameter holes (s. lower parts of Figure 12b). Lithiating the graphite electrode using the coin cell cap with the 500 µm diameter hole grid pattern, now resulted in a perfectly homogeneous lithiation across the entire electrode area (s. right panel in Figure 13b) Obviously, the stiffness of the 7.5 µm Kapton® window is sufficient to provide enough cell stack compression across the entire hole patterned region to allow for a complete lithiation of the graphite particles. The cap design was subsequently optimized by using 139 holes with an even smaller diameter of 300 µm to further improve the rate capability of the *operando* cell. A high rate capability of the cell design is important when studying lithium intercalation during fast-charging of graphite electrodes, which is a topic of great interest among EV manufacturers, since fast recharging (at least partly) of a car battery could afford smaller battery pack sizes, and therefore holds significant cost saving potential, without triggering driving range issues. Fast-charging of graphite electrodes studied by means of *operando* NDP is addressed in section 3.2.2 of this PhD thesis.

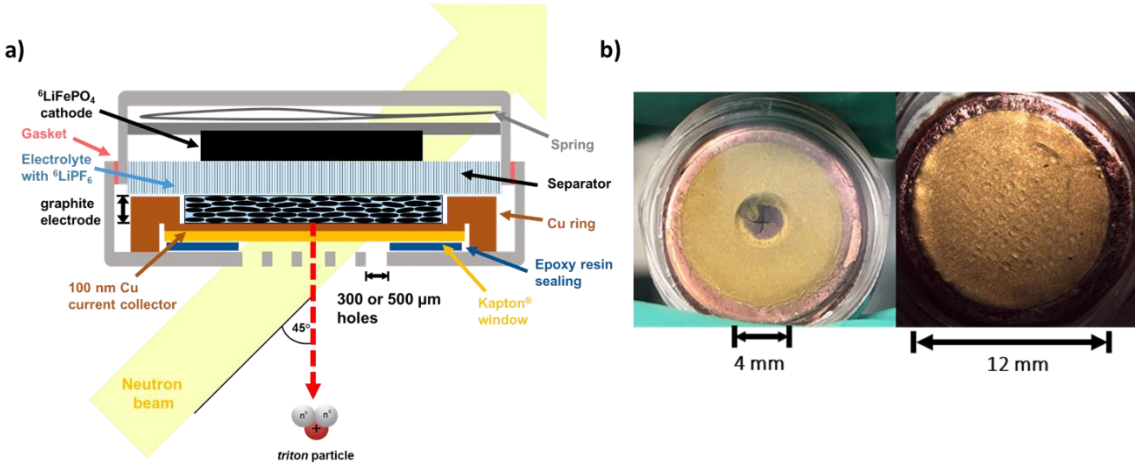

Figure 13. a) Cross-sectional schematic of the *operando* NDP coin cell setup with 300 or 500 µm-sized holes, which was analogously used during cell development with one large circular hole with different diameters (s. Fig 12b), **b)** photographs of graphite electrodes from decrimped coin cells opened in their fully charged state with one 4 mm-wide hole (left) and 500 µm holes in the coin cell cap (right). The center of the 4 mm hole is clearly not completely lithiated to LiC_6 (missing golden color), whereas the 500 µm holes show complete lithiation.

Next, we will compare the cycling performance of a conventional T-cell with that of a coin cell with a cap that is patterned with 300 µm holes, which is depicted in Figure 14. For this, three formation cycles were conducted at a rate of C/10. The cells consisted of a graphite WE (≈1 mAh/cm², 1.13 cm² for the NDP, and 0.95 cm² for the T-cell), a capacitively oversized LFP CE (≈3.5 mAh/cm², 0.78 cm² for the NDP, and 0.95 cm² for the T-cell), six glassfiber separators, and 270 µL LP57 electrolyte (EC:EMC = 30:70 wt% + 1 M $LiPF_6$). The voltage profile of the *operando* NDP cell follows closely the one obtained from the T-cell and both cells deliver a reversible capacity of ≈360 mAh/$g_{graphite}$ during the first three formation cycles. The first cycle coulombic efficiency is ≈80 %, which is due to the high BET surface area (≈15 m²/g) of the sieved graphite particles.

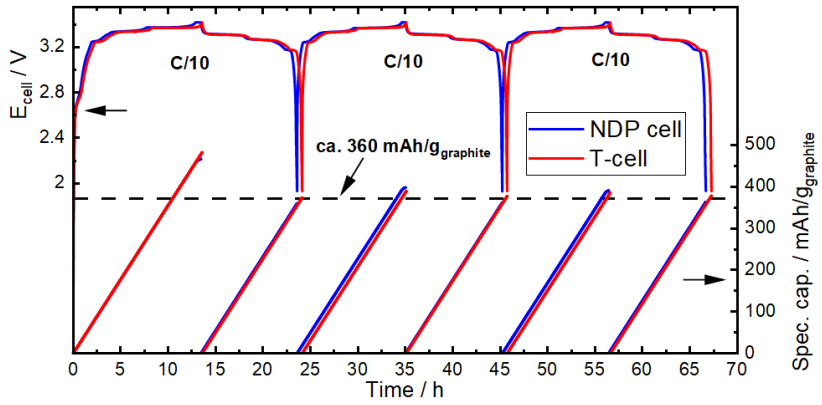

Figure 14. Comparison of the cycling performance of the *operando* NDP coin cell (blue) with 300 µm holes (cycled at ambient pressure) and a Swagelok® T-cell (red) with an analogous setup, *i.e.*, graphite WE (≈1 mAh/cm²), a capacitively oversized LFP CE (≈3.5 mAh/cm²), six glassfiber separators, and 270 µL LP57 electrolyte. The only differences are the geometric electrode areas, which are 1.13 cm² (NDP cell) and 0.95 cm² (T-cell) for the graphite WE, and 0.78 cm² (NDP cell) and 0.95 cm² (T-cell) for the LFP CE, respectively. This comparison proves that the *operando* NDP and the T-cell show a comparable performance.

2.2.5 *Operando* NDP Cell Holder and Cooling Setup

For the cycling of the *operando* NDP cells during beamtimes, an SP300 potentiostat (Biologic, France) was used. The cables were hooked up using BNC lead-throughs into the NDP sample chamber. The chamber atmosphere was exchanged to ≈400-150 mbar of He by alternatingly evacuating and flushing with He gas. To position and electrically connect the cells within the chamber, a special cell holder was designed. The first prototype, an aluminum metal plate (Al is used to reduce background radiation as much as possible) with four cell mounting spots

electrically insulated from the rest of the holder (where four cells could be connected *via* a metal contact pressing onto the cell casing) is depicted in Figure 15a. An optimized cell mount using gold pins as connectors, which eliminates contact resistance issues encountered with the first prototype, is displayed as a single unit in Figure 15b.

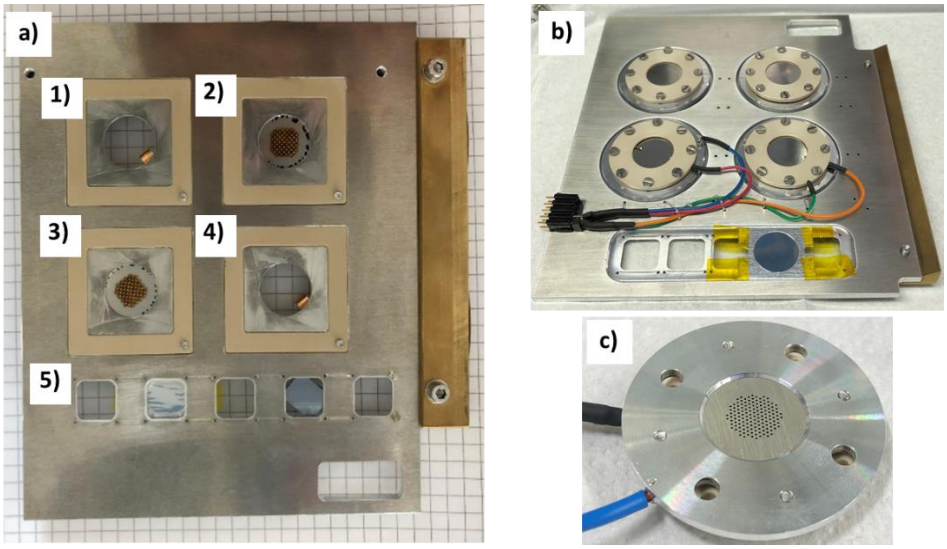

Figure 15. a) First generation NDP cell holder with four mounting slots (1-4, two cells are mounted) for *operando* NDP coin cells connected with copper clamps, and, additionally, six slots (5) where reference samples can be attached. **b)** Second generation optimized NDP cell holders mounted on an aluminum stage. This setup additionally allows for cooling *via* connecting a cooling unit (displayed in Figure 16). **c)** Photograph of a single cell mount that can be attached to the NDP holder from b), which uses gold pins contacting negative and positive poles of the battery.

Each of these individual cell mount units can be prepared inside a glovebox and afterwards connected to an aluminum plate (s. Fig. 15b), which is then positioned and fixed inside the NDP chamber. This stage can be remotely moved inside the chamber, allowing for the individual illumination of each cell with the neutron beam. Furthermore, the aluminum stage can be coupled with a cooling unit, a metallic vessel connected to a cooling fluid circulator (Julabo GmbH, Germany), thus, allowing to cool the NDP cells to ≈-20 °C. The technical drawings of the cell holder, aluminum stage, cooling unit, and an evacuation chamber (used to test cell cycling under reduced pressure in a laboratory environment) can be found in the Appendix of this thesis. The stage together with four mounted cells and the cooling vessel are depicted in Figure 16.

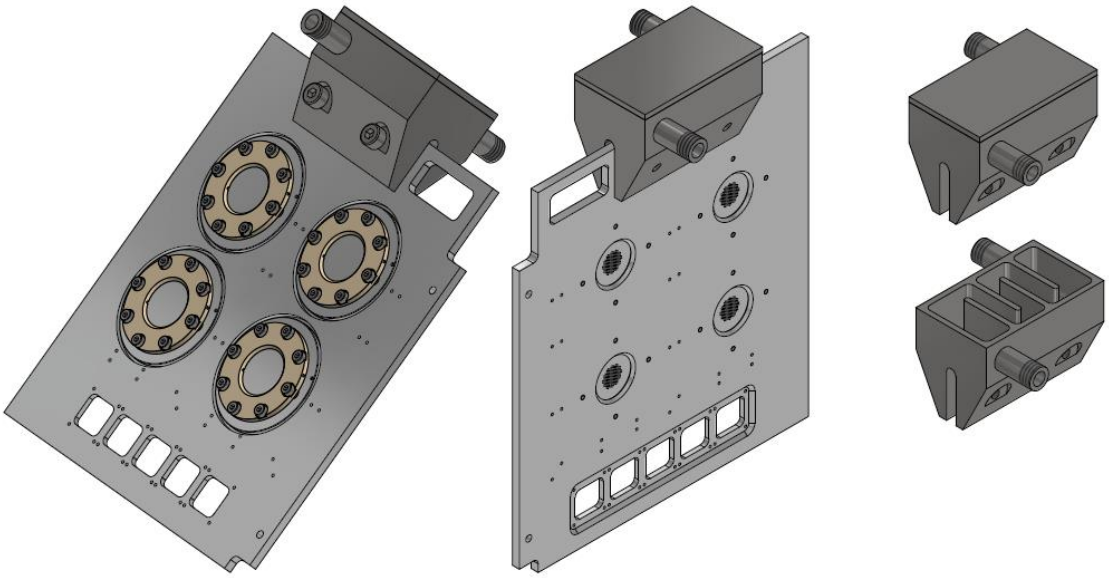

Figure 16. Aluminum stage connected to an aluminum cooling unit through which a cooling fluid can be circulated in order to operate the NDP cells at a user-defined temperature down to ≈-20 °C.

The temperature on the aluminum surface next to the mounted cells can be tracked *via* four individual thermocouples (not shown). In order to electrically separate the cells from the aluminum plate and at the same time assure a good heat transfer to cool the cells, a ≈500 µm-thick plastic pad with high thermal conductivity (silicon rubber, ≈5 W/mK) is placed between the stage and the cell mount. The cooling stage can for example be employed to study lithium plating during low-temperature operation, which, however, was not anymore in the scope of this PhD thesis. To perform electrochemical cycling tests in the laboratory prior to an experiment in a neutron reactor, a polycarbonate cylinder with an O-ring sealing was designed, which can be connected to a vacuum pump. This offers the possibility to, a) adjust the pressure to below ambient pressure, and b) purge the chamber with nitrogen in order to avoid water condensation on the surface of cell holder and cell at low-temperature operation.

2.3 Further Experimental Techniques

^{6}Li enrichment of a LIB electrolyte and $LiFePO_4$ cathode

In order to increase the signal-to-noise ratio during NDP measurements, and thus to largely reduce the acquisition time for one spectrum to 2 min, the natural abundance of ^{6}Li of ≈7 at% was enriched to ≈95 at%. This was achieved by using ^{6}Li-enriched $LiPF_6$ as conductive salt, which can be purchased at Sigma Aldrich (95at%). The as-delivered salt was dried in a glass oven (drying oven 585, Büchi, Switzerland) at 80 °C for 16 h under dynamic vacuum and then tested via ^{1}H, ^{31}P, and ^{19}F NMR for impurities. To assure that also impurities that cannot be traced by NMR but could affect cycling performance, an electrolyte was prepared with $^{6}LiPF_6$ (EC:EMC = 30:70 wt% + 1 M $^{6}LiPF_6$), and its quality was verified by performing long-term cycling tests at 1 C using NMC622/graphite T-cells and by benchmarking these data with data from nominally identical cells with a commercial LP57 electrolyte (EC:EMC = 30:70 wt% + 1 M conventional $^{7}LiPF_6$). The cycling performance is shown in Figure 17.

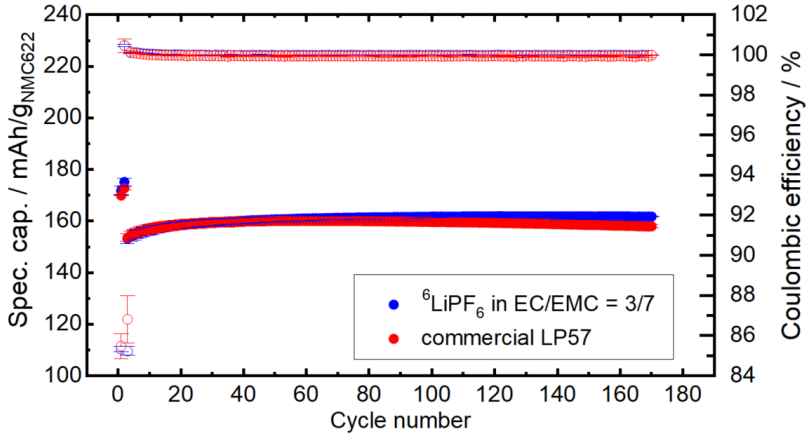

Figure 17. Cycling performance of nominally identical NMC622/graphite cells cycled with a commercial LP57 (red symbols), and a self-mixed EC/EMC electrolyte with 1 M $^{6}LiPF_6$ (blue symbols). The obtained specific discharge capacities shown by the solid symbols (left y-axis) and the coulombic efficiencies by the open symbols (right y-axis). The error bars represent the deviation from the average of two nominally identical cells.

The capacity fading and the coulombic efficiencies are similar for both the $^{6}LiPF_6$-containing electrolyte and the commercial LP57, from which we conclude that the electrolyte does not contain impurities in a significant amount.

During formation a significant amount of primarily ^{7}Li from the commercial LFP electrode will be mixed with the electrolyte, which requires that also the lithium in

the LFP cathode active material is enriched to the same level as the lithium in the electrolyte. Thus, a single-layer pouch cell with a ≈30 x 30 mm LFP electrode was assembled *vs.* a metallic ^{7}Li foil (450 µm, 99.8 %, Rockwood Lithium) using a glassfiber separator, and 1 mL of LP57 electrolyte (1 M $LiPF_6$ in EC:EMC = 3:7 by weight, BASF SE) in a half-cell setup to completely delithiate the cathode (C/10, CC until 4 V_{cell} and CV until a current cutoff of C/100). The pouch cell setup is in detail described by Buchberger *et al.*[214] Afterwards, the LFP cathode is harvested, washed with DMC, and reassembled in a similar pouch cell now using metallic ^{6}Li foil, which was rolled from ^{6}Li chunks (99.8 %, 95 at% enrichment, Sigma Aldrich) after washing it with dried hexane, a 2500 Celgard® separator, and 100 µL of $^{6}LiPF_6$-containing electrolyte. The voltage profiles for the delithiation and relithiation steps are depicted in Figure 18.

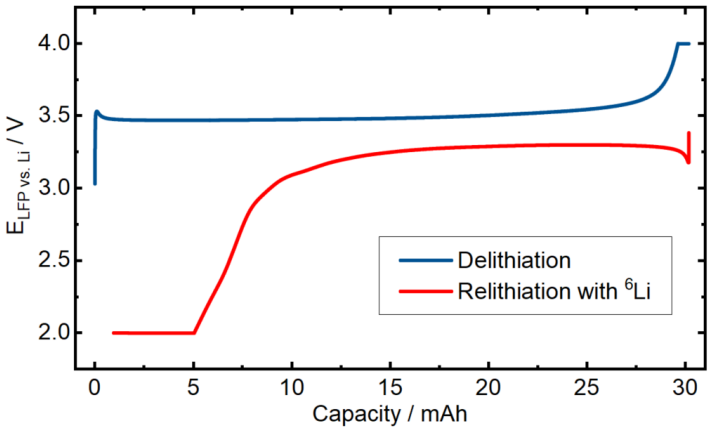

Figure 18. Complete delithiation of an $LiFePO_4$ (LFP) electrode in an LFP/^{7}Li pouch cell (blue), and subsequent relithiation of the harvested $FePO_4$ (FP) electrode in a second FP/^{6}Li pouch cell (red) with the $^{6}LiPF_6$-containing electrolyte (1 M $^{6}LiPF_6$ in EC:EMC = 3:7 by weight)

X-Ray Photoelectron Spectroscopy (XPS)

The surface-analytical technique X-ray photoelectron spectroscopy (XPS) was used in order to quantify the lithium diffusion into the copper metal of the anode current collector in a LIB (section 3.2.1). All experiments were performed using an Axis Supra spectrometer (Kratos, UK). The sample preparation was carried out in an argon-filled glovebox (<0.1 ppm O_2 and H_2O, MBraun, Germany), and then the sample was transferred into the XPS with an air-tight sample loading device from Kratos. The samples were mounted on a sample holder with an adhesive tape. The transfer vessel was connected to the flexi-lock of the XPS without any exposure to air, and the antechamber evacuated to a pressure of ≈10^{-8} torr before transferring

the sample to the sample analysis chamber (SAC), where the pressure was kept below $<3 \times 10^{-8}$ torr during the measurement. The spectra were acquired with monochromatic Al-K_α radiation ($h\upsilon$ = 1487 eV) with an emission current of 15 mA, a pass energy of 20 eV, a step size of 0.1 eV, a dwell time of 300 ms, and a measured spot size of 800 x 300 μm. The measurement was performed in hybrid lens mode with turned on charge neutralizer, averaging over 4 scans (Cu 1s, Li 1s, Cu 3p, N 1s). Data treatment was done using Kratos' ESCApe software (version 1.1). Binding energies (BE) were referenced to the adventitious carbon peak at 284.8 eV in the C 1s spectrum, and fitting done by employing a mixture of 30 % Laurentzian and 70 % Gaussian functions with a Shirley background subtraction. The ratio between copper and lithium atoms was determined based on the fitted spectra of Li 1s and Cu 3p. Sputtering the sample surface was performed with an Ar^+-ion gun at an energy of 5 keV. The sputter time was 10 s in the first step and 30 s in all subsequent cycles (raster size 2 x 1 mm). Conversion of the sputtering time into a depth rate was done by completely sputtering through a pristine 100 nm thick copper layer on top of the Kapton® foil, using the N 1s signal from the Kapton® polyimide as indicator for a total penetration of the copper layer.

3 Results

The following chapter contains two published studies and two manuscript drafts of which one was recently submitted to a peer-reviewed journal and is currently under review. The chapter is topically divided into *in situ* studies using Electrochemical Impedance Spectroscopy (EIS) by means of μ-REs (section 3.1), and studies performed by means of *operando* Neutron Depth Profiling (NDP) (section 3.2).

In section 3.1.1, a novel μ-RE is presented based on an *in situ* sodiated tin wire that can be used to deconvolute the contributions of anode and cathode impedances to the full-cell impedance in a sodium-ion battery (SIB) cell. This method eliminates the need to build and age multiple identical cells for combining pairs of anodes or cathodes in so-called symmetrical cells in order to obtain electrode-resolved impedance data. The approach of inserting a μ-RE in a T-cell based battery hardware was transferred from the well-known gold wire reference electrode (GWRE), which was also developed at the Chair of Technical Electrochemistry by Solchenbach *et al*.,[185] using an *in situ* lithiated, insulated 50 µm thick gold wire as RE. In this study, the new micro-tin wire reference electrode (µ-TWRE) is first validated and afterwards used to measure the impedance of a hard carbon (HC) anode in a Na/HC half-cell. In the second manuscript (section 3.1.2), we employ the μ-TWRE to compare the impedance evolution during (de)sodiation of a HC anode with the impedances obtained during (de)lithiation of the very same active material as a function of state-of-charge (SOC) and over extended cycling.

Section 3.2.1 deals with the development of an *operando* NDP coin cell setup that can be used to record NDP spectra of battery electrodes during operation, while at the same time delivering a cell performance comparable to a standard laboratory cell. Here, the lithium concentration depth profile across a graphite anode is measured during formation of an LFP/graphite cell. In a second study

(section 3.2.2), the *operando* NDP method is used to monitor lithium plating spatially-resolved across the thickness of a graphite electrode at a high time resolution (≈2 min/spectrum) during fast-charging. Here, we could show that lithium plating upon fast-charging does not occur homogenously across the thickness of the graphite electrode, but that it initiates on graphite particles in the vicinity to the separator. As soon as the charging process is stopped, plated lithium dissolves and lithium redistributes across the electrode thickness by lithium diffusion/migration and subsequent intercalation into the graphite particles that are at a lower SOC, *i.e.*, those located near the electrode/current collector interface. Unfortunately, the NDP data presented in this study include a low energy peak which is already visible before starting the *operando* cycling experiment, strongly suggesting the presence of metallic or SEI-bound lithium near the separator/electrode interface. The unexplained lithium enrichment at this interface must have formed during cell formation or sample transport from Germany to the US and most likely originates from increased SEI formation on graphite particles adjacent to the separator. We believe that the origin of this inhomogeneously formed SEI might be related to impurities in the $^{6}LiPF_6$-based electrolyte, even though this was not apparent from the validation experiments conducted with the $^{6}LiPF_6$ electrolyte (s. section 2.3). Thus, we intend to reproduce the NDP experiment using a purified electrolyte which is why the manuscript was not yet submitted to a peer-reviewed journal. Due to the shutdown of the neutron reactor FRM2 in Garching from March 2020 and the unavailability of beamtime in the US because of the corona pandemic, it was unfortunately not yet possible to repeat the experiment and data shown in the manuscript of section 3.2.2 should be considered preliminary.

3.1 Electrochemical Impedance Spectroscopy Using Micro-Reference Electrodes

3.1.1 Development of a Micro-Reference Electrode for Impedance Measurements in SIBs

This section presents the article "*A Reference Electrode for In Situ Impedance Measurements in Sodium-Ion Batteries*".[188] The manuscript was submitted to the peer-reviewed Journal of the Electrochemical Society in September 2019 and was published in November 2019. The article is published open access and distributed under the terms of the Creative Commons Attribution 4.0 License. The permanent web link is: https://iopscience.iop.org/article/10.1149/2.0741915jes/meta. A summary of the article was presented by Fabian Linsenmann as Paper 146 at the Dallas, Texas, Meeting of the Electrochemical Society, May 26–May 30, 2019.

In the literature, impedance data of individual electrodes for sodium-ion battery (SIB) active materials are very rare. Most of the publications simply provide full-cell impedance data, mostly measured *vs.* a sodium metal electrode, and often ascribe changes in full-cell impedance to changes in the impedance of the HC WE;[215, 216, 217, 218, 219] thereby, neglecting the impedance change of the sodium metal CE. Since the magnitude of a sodium metal electrode can be on the order of several hundreds of Ωcm^2,[220, 221] and has been found to change drastically during cycling,[222] the assumption that the CE impedance contribution can be neglected is very likely not valid in most cases. Therefore, the use of reference electrodes for impedance measurements is indispensable to deconvolute the individual impedance contributions in half-cells or full-cells, as has also been shown in the case of LIBs.[41, 185, 184, 186] Moreover, this technique saves tremendous experimental effort compared to the symmetrical cell approach[223, 224] and furthermore prevents possible artifacts that could be introduced by cell disassembly and reassembly of (aged) electrodes into so-called symmetrical cells.

In this study, we present an easily reproducible technique based on a tinned copper wire that was insulated manually using polyurethane spray with a total thickness of ≈100 µm. A sufficiently stable reference potential allowing for

high-quality EIS measurements over extended cycling is assured by *in situ* sodiating the tip of the tin wire from a sodium source inside the cell, such as a sodium CE or a sodium-containing cathode. Furthermore, the validity of the obtained EIS spectra is proven by a comparison with data recorded *via* a symmetrical cell approach. To present a first application of the newly developed diagnostic technique, the impedance of a HC electrode is tracked during cycling in a Na/HC half-cell. It has been recently shown that artefact-free impedance measurements using high-impedance μ-REs, such as a μ-TWRE or μ-GWRE, are not possible if the impedances of WE and CE differ strongly,[225] as it is the case for a high surface area HC electrode (with a roughness factor of rf ≈150 cm^2_{BET}/cm^2_{geo}) compared to a sodium or lithium metal electrode (rf ≈1 cm^2_{BET}/cm^2_{geo}). However, attaching a free-standing electrode, *e.g.*, a porous carbon paper, on top of the metal electrode reduces the CE impedance to an extent that electrode-resolved EIS measurements can be performed without artefacts.

The impedance technique presented in this publication will be a useful tool for all researchers working on the development of new cathode or anode active materials for SIBs, enabling them to characterize impedance changes during long-term cycling in full- or half-cells.

Author contributions

F.L. and D.P. developed the use of an insulated tin-coated copper wire as μ-reference electrode in a sodium-ion battery. FL performed the insulation of the wire and all electrochemical experiments. The data was analyzed by F.L. and D.P., and the manuscript was written by F.L. and H.A.G. All authors discussed the data and commented on the results.

Journal of the Electrochemical Society

The Electrochemical Society
Advancing solid state & electrochemical science & technology

OPEN ACCESS

A Reference Electrode for In Situ Impedance Measurements in Sodium-Ion Batteries

To cite this article: Fabian Linsenmann *et al* 2019 *J. Electrochem. Soc.* **166** A3668

View the article online for updates and enhancements.

This content was downloaded from IP address 37.201.5.1 on 07/01/2021 at 12:04

A Reference Electrode for In Situ Impedance Measurements in Sodium-Ion Batteries

Fabian Linsenmann, *,z **Daniel Pritzl,** * **and Hubert A. Gasteiger****

Chair of Technical Electrochemistry, Department of Chemistry and Catalysis Research Center, Technische Universität München, 85748 Garching, Germany

In this work, we introduce a newly developed micro-reference electrode (μ-RE) for sodium-ion batteries (SIBs). This μ-RE is based on a 50 μm-sized tin-coated copper wire, manually insulated using polyurethane (PU) spray, such that only the cross-sectional area of the wire tip is in contact with the electrolyte. The tin-coating allows for facile in situ electrochemical sodiation, resulting in a stable potential of the wire that enables in situ Electrochemical Impedance Spectroscopy (EIS). We will show that reliable single-electrode impedance data from SIB cells can be obtained with this new tin wire μ-RE (μ-TWRE) concept, validated by comparing μ-RE-based single-electrode impedance data with those acquired by a symmetrical cell approach. As hard carbons are currently the most promising anode material for SIBs, we evaluate the impedance evolution of a hard carbon anode over extended charge/discharge cycles in a half-cell vs. sodium metal, comparing its impedance measured at the same state-of-charge (SOC) over 50 cycles. Thus, we demonstrate that EIS using a μ-TWRE can be used as a convenient tool to quantify the impedance evolution of SIB anodes and cathodes.

© The Author(s) 2019. Published by ECS. This is an open access article distributed under the terms of the Creative Commons Attribution 4.0 License (CC BY, http://creativecommons.org/licenses/by/4.0/), which permits unrestricted reuse of the work in any medium, provided the original work is properly cited. [DOI: 10.1149/2.0741915jes]

Manuscript submitted September 5, 2019; revised manuscript received October 21, 2019. Published November 5, 2019. This was Paper 146 presented at the Dallas, Texas, Meeting of the Society, May 26–May 30, 2019.

The demand for lithium-ion batteries (LIBs) used in portable electronics and automotive applications has strongly increased within the last ten years. In 2018, for the first time in history, more than 2 million fully electric vehicles (FEVs) were sold worldwide.[1] As recently decided by the European Union, the maximum average fleet CO_2 emission target of 95 g/km (from 2021) must be even further reduced to ≈60 g/km by 2030, which forces original equipment manufacturers (OEMs) to strongly increase their share of hybrid and fully electric vehicles (EVs). This is one reason why more and more OEMs announce the release of new electric vehicles with increasing battery pack sizes, with alone the Volkswagen group stating that they are planning to sell 22 million EVs by 2030.[2] Therefore, a rapid acceleration of the battery demand is to be expected within the next years, which will likely affect the demand for lithium and its cost. In order to become independent from lithium, cheaper and more sustainable alternatives to LIBs are getting into focus. Since sodium is ≈1000 more abundant in the earth's crust and less locally concentrated compared to lithium,[3] sodium-ion battery (SIB) research has attracted considerable attention in recent years.[4–7] Particularly, applications such as grid storage where high volumetric and gravimetric energy density are less critical could provide an interesting use case for SIBs.[8]

In order to advance the fundamental materials characterization for SIBs, it is desirable to adapt the electrochemical and analytical techniques established in the field of LIB research to sodium-based systems. Electrochemical impedance spectroscopy (EIS) is a fast and non-invasive technique to provide valuable insights into intercalation kinetics, interfacial processes, and/or the effect of additives via monitoring of the associated resistances, so that it is used intensively for LIB studies.[9–15] However, the measurement of cell impedance data does not allow for the deconvolution of cathode and anode impedances, and for in situ impedance analysis of individual electrodes a reference electrode (RE) is required.[9,16–18] Without a RE, the only possibility to independently quantify the anode and/or cathode impedance is the disassembly of multiple cells and the recombination of identical anode or cathode pairs in symmetrical cells.[13,19–22] In the latter case, monitoring the evolution of the electrode impedance as a function of state-of-charge (SOC) and/or over extended cycling requires dis- and reassembly of numerous cells, so that artefacts due to cell opening and electrode transfer may be introduced. On the other hand, when using μ-REs, the design and placement of the μ-RE with respect to working (WE) and counter electrode (CE) in a three-electrode setup is crucial in order to obtain artefact-free impedance spectra.[9,16,17,23] The μ-RE has to fulfill the following requirements: a) its potential has to be stable within the measuring duration of the impedance spectrum (typically <20 min); b) it has to be located centrally between anode and cathode, where the electric field is homogeneous; and, c) its cross-sectional dimensions have to be small compared to the distance between the electrodes in order to minimize the potential gradient across the diameter of the μ-RE. In general, it is advantageous to use μ-REs with a well-defined reference potential, as simple metal wire *pseudo*-REs frequently exhibit too large potential drifts, as was shown by Dollé et al. for copper and silver wires;[24] in some cases, however, the potential of *pseudo*-REs is sufficiently stable to enable EIS analysis down to frequencies of ≈0.1 Hz.[14,25]

For EIS studies in LIBs, Solchenbach et al.[9] incorporated a 50 μm thick insulated gold wire into a standard Swagelok T-cell, whereby the wire tip that exposes the gold to the electrolyte was located centrally between cathode and anode, separated from each electrode by a ≈200 μm thick glass fiber separator. To obtain a stable reference potential, the gold wire tip was electrochemically lithiated in situ from a lithium source within the cell (a metallic lithium electrode or a conventional LIB cathode), producing an Li-Au alloy with a well-defined potential of ≈0.31 V vs. Li^+/Li. As the Au-Na phase diagram shows several intermetallic phases such as AuNa and $AuNa_3$,[26] we were hoping that the same gold wire μ-RE concept could be utilized for SIB studies. Unfortunately, tests performed in our group to electrochemically alloy gold with sodium were unsuccessful, since the intercalation kinetics of sodium in gold seem to be significantly slower compared to lithium. However, there are other metals known for facile alloying with sodium, such as barium, lead, zinc, and tin.[27] Tinned copper wires are standard materials used for electrical leads and therefore can be purchased with diameters down to 25 μm. Abraham et al.[18] successfully used an insulated 25 μm thick tinned copper wire as μ-RE for EIS measurements in a LIB, which was also lithiated in situ to form an Li_xSn alloy for which one expects to obtain a stable potential.

In the present study, we demonstrate that a commercially available tinned copper wire can be easily (and even reversibly) sodiated, ultimately yielding a tin wire μ-RE (referred to as μ-TWRE) with a relatively stable reference potential. We will show that reliable single-electrode impedance data from sodium-ion battery cells can be obtained with this new μ-TWRE concept, validated by comparing μ-TWRE based single-electrode impedance data with those obtained by the symmetrical cell approach. Due to their low cost and comparably good capacities, hard carbon materials are to date the almost

*Electrochemical Society Student Member.
**Electrochemical Society Fellow.
zE-mail: fabian.linsenmann@tum.de

ubiquitously used and most promising anodes for SIBs.[28–31] Despite their central importance for SIBs, very few impedance data on sodiated hard carbon electrodes have been published and, to the best of our knowledge, there is no publication analyzing the evolution of the hard carbon impedance over extended cycling that is based on electrode-resolved EIS analysis, i.e., without being compromised by the impedance contribution from the counter electrode, such as a sodium metal electrode. Therefore, we will here track the evolution of the impedance of a hard carbon electrode in a half-cell setup over extended cycling by means of an in situ impedance measurement with a μ-TWRE.

Experimental

Electrode and electrolyte preparation.—Hard Carbon electrodes were composed of hard carbon (Kuranode, BET surface area 5.2 m^2/g, Kuraray, Japan), sodium carboxymethyl cellulose (CMC, Sunrose, NPI, Japan), and styrene-butadiene rubber (SBR, emulsion in water, solid content 40 wt%, Zeon, Japan) at a weight ratio of 97:1.5:1.5. Na-CMC was first mixed with highly pure water (18 MΩcm, Merck Millipore, Germany) using a planetary mixer (Thinky, USA; at 2000 rpm for 15 min). Hard carbon powder was added in three steps in order to reach a final solid content of 50 wt% with 2 min mixing in between at 2000 rpm. SBR was added to the slurry and mixed at 500 rpm for 2 min. The ink was coated onto aluminum foil (MTI, United States) using a 100 μm gap size four-way film applicator (Erichsen, Germany) and dried at room temperature for 5 h, resulting in an average loading of 3 ± 0.3 mg/cm^2 ($\equiv 0.87 \pm 0.087$ mAh/cm^2, based on a specific capacity of 290 mAh/g_{HC}); hard carbon electrodes were then punched out at a diameter of 11 mm. Together with glass fiber separators (11 mm diameter, VWR, Germany), the electrodes were dried under dynamic vacuum at 120°C for 12 h in a glass oven (drying oven 585, Büchi, Switzerland) and transferred into an argon-filled glove box (MBraun, Germany) without exposure to air. The as-used uncompressed hard carbon electrodes had a thickness of 59 ± 2 μm (Al current collector 15 ± 1 μm) and a porosity of ≈60%. Note that the home-made Swagelok T-cell setup is designed in a way that only a pressure of ≈2 bar is exerted on the cell stack by the compression spring. By compressing a hard carbon electrode using a strain/compression testing machine (Zwick, Germany) with a defined pressure of 2 bar, the thickness change was found to be +/−1 μm, which is within the error of the thickness gauge (Mitutoyo, Japan). Sodium disks (11 mm diameter, thickness ≈500 μm) were punched out from sodium foil that was prepared from sodium ingots (99.95%, Sigma Aldrich) within an argon-filled glove box (O_2 and H_2O <0.1 ppm). The electrolyte was prepared by mixing 50 vol% ethylene carbonate (EC, ≥99%, Sigma Aldrich) and 50 vol% dimethyl carbonate (BASF SE, Germany) with 1 M $NaPF_6$ (99.9%, Kishida Chemicals, Japan).

Cell assembly and electrochemical testing.—Swagelok T-cells were assembled inside an argon-filled glove box with hard carbon working electrodes (WE) and sodium counter electrodes (CE), 60 μL electrolyte, two glass fiber separators, and a tinned copper wire (diameter = 50 μm, Eurowire, Great Britain) with a manually applied insulation as reference electrode (μ-TWRE). Unfortunately, as demonstrated recently by Morasch et al.,[32] this cell configuration would not allow for the acquisition of single-electrode EIS data by means of a μ-RE, since the resistances of WE and CE have to be within the same order of magnitude when using a high-impedance μ-RE (i.e., a μ-TWRE or a lithiated gold wire μ-RE). They showed, however, that the attachment of a freestanding high-surface area carbon electrode to a metallic lithium electrode reduces its impedance to the extent that artefact-free half-cell EIS data can be acquired with a high-impedance RE.[32] Following their recommendation, we sandwiched a high-surface area carbon fiber paper (H1410 type from Freudenberg (Germany), cut to 10 mm diameter, with a thickness of 150 μm and a BET area of ≈14 m^2/g) between the separator and the sodium metal CE (s. Figure 1a), which effectively reduces the impedance of the latter by means of chemical interaction of the metallic sodium with the carbon matrix, resulting in a mixed potential of the carbon paper/sodium composite anode that is within less than 0.5 mV of that of a pure metallic sodium electrode after 5 h (s. Figure 1b).

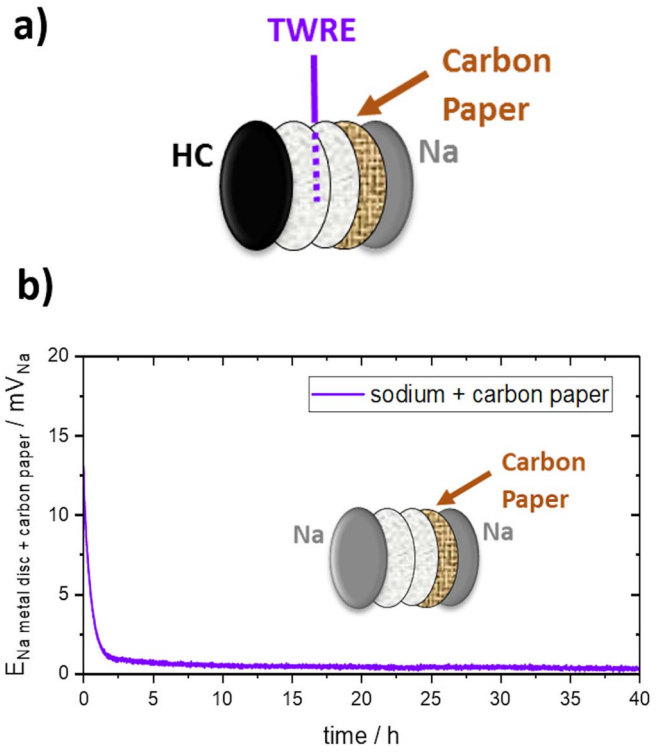

Figure 1. a) Electrode stack exemplarily shown for the in situ EIS measurement of an HC electrode in a Swagelok T-cell using a μ-TWRE that is located centrally between two glass fiber separators. A carbon paper freestanding electrode is put on top of the sodium metal disk in order to decrease the resistance of the sodium CE;[32] b) mixed potential of the carbon paper/sodium composite measured at OCV vs. sodium metal.

Impedance spectra analysis.—In order to compare the impedance responses measured via the μ-RE with those collected using a symmetrical cell, the spectra were fitted with a MATLAB-based application ("EIS Breaker" written by J. Landesfeind),[14] which applies a *fminsearch* MATLAB function using a Nelder-Mead simplex algorithm and modulus weighing. The underlying equivalent circuit is depicted in Figure 5c and consists of a high-frequency resistance R_{HFR} and a mono-rail transmission-line incorporating a pore resistance R_{pore} and a charge transfer resistance R_{CT} in parallel to a constant phase element Q, similar to the one used by Landesfeind et al.[14] The transmission line is simplified by neglecting the resistance rail through the active material due to the high electronic conductivity of the carbon electrode and is therefore called mono-rail TLM (mTLM).

The tinned copper wire was insulated using polyurethane spray (Urethan 71, Kontakt Chemie, Germany), resulting in a total thickness of ≈100 μm (s. Figure 2). The incorporation of the μ-RE in the Swagelok T-cell was done according to Solchenbach et al.[9]

Prior to cell cycling, the μ-TWRE was electrochemically sodiated in situ from the sodium CE by applying a charging current of 50 nA until a potential cutoff of 10 mV vs. Na^+/Na is reached, requiring several tens of hours (see later). At the end of the charging process, the potential was found to relax to ≈110 mV vs. Na^+/Na within 5 h and then remained relatively stable over more than 100 h. The hard carbon half-cells were cycled galvanostatically at C/10 (referenced to a hard carbon capacity of 290 mAh/g_{HC}) within a cell potential range of +1.5 V_{cell} and +10 mV_{cell}. For impedance measurements, the cell was charged at C/10 to 100 mV_{cell} where it was switched to OCV for 30 min, followed by potential-controlled EIS (referred to as

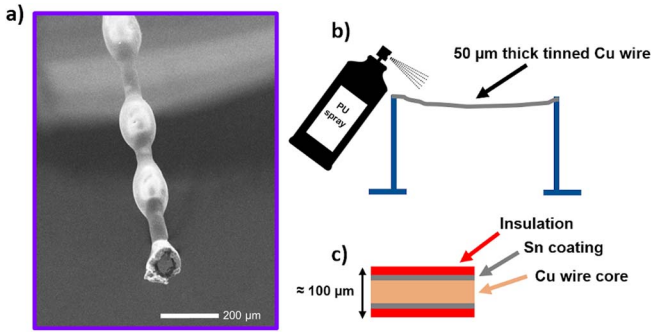

Figure 2. a) SEM image of the tinned copper wire coated with polyurethane (PU); b) insulation process of the µ-RE wire using PU spray; c) schematic representation of the µ-RE consisting of a copper wire core, a Sn layer coating, and PU insulation, with a total thickness of the insulated µ-TWRE of ≈100 µm.

PEIS) at OCV using the µ-TWRE and a perturbation amplitude of 20 mV between 100 kHz and 0.1 Hz. For validating EIS measurement results performed with the µ-TWRE, the impedance response of a freshly assembled cell after ca. 24 h rest at OCV was compared to EIS measurements using the symmetrical cell approach. All experiments (cycling and impedance) were performed in temperature-controlled chambers (Binder, Germany) at 25°C.

Results and Discussion

In situ sodiation of the µ-TWRE.—As experimentally shown by Solchenbach et al., the use of a pseudo-µ-RE (in that case a non-lithiated gold wire µ-RE, s. Figure 3b and c in Reference 9) can lead to artefacts in the impedance spectra in the low-frequency region if the potential drift is too large relative to the perturbation amplitude. Thus, while in some instances pseudo-µ-RE can be used to produce high-quality impedance spectra down to even 0.1 Hz,[14,25] µ-REs with an electrochemically well-defined potential are preferable. For this reason, Solchenbach et al.[9] had lithiated their gold wire µ-RE, and we will explore the in situ sodiation of the tip of the polyurethane coated tin-shroud that surrounds the copper wire of the here presented µ-RE (s. Figure 2). Figure 3 shows the potential profile during the in situ galvanostatic sodiation and desodiation of the tin phase of the µ-RE (total diameter ≈100 µm, assembled in a Swagelok T-cell) using sodium metal disks as WE and CE. The (de)-sodiation was performed with a constant current of 50 nA, with a lower cutoff potential of 10 mV vs. Na^+/Na, and an upper cutoff potential of 1.5 V vs. Na^+/Na,

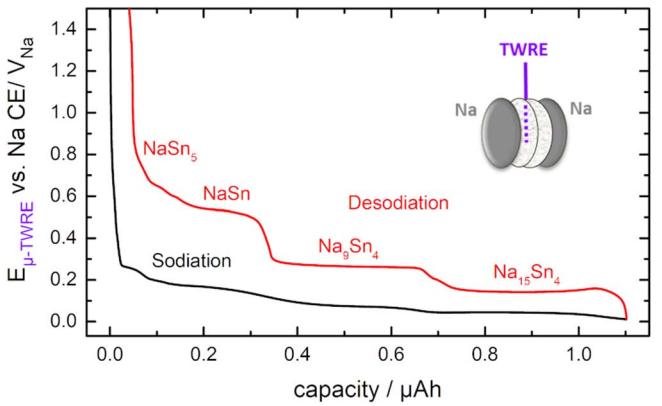

Figure 3. Potential profile during the reversible in situ (de)-sodiation of the tip of the Sn coating of the µ-TWRE recorded from the sodium metal WE in a T-cell with two sodium metal electrodes (s. inset scheme). During desodiation, four potential plateaus can be distinguished, most likely assignable to Na-Sn-phases with the compositions $Na_{15}Sn_4$, Na_9Sn_4, NaSn and $NaSn_5$ according to Ellis et al.[33]

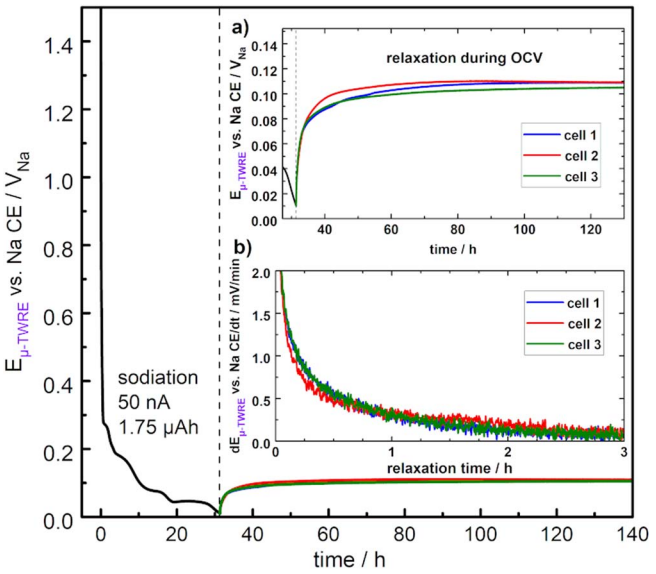

Figure 4. Potential profile during the galvanostatic (50 nA) in situ sodiation of one of the µ-TWRE to a cutoff potential of 10 mV vs. a sodium CE (requiring ≈35 h), followed by the potential relaxation during the subsequent OCV phase, shown for three independently assembled Swagelok T-cells. a) Magnification of the µ-TWRE potential during the OCV relaxation phase, demonstrating the highly reproducible behavior for three different cells; b) potential drift rate (in mV/min) of these three µ-TWREs during the first 3 h of the OCV relaxation phase (i.e., after the end of the sodiation procedure).

requiring roughly 22 h per half-cycle. During sodiation (black line in Figure 3), four potential plateaus can be discerned, whereby the last three plateaus are very distinctly visible during the desodiation half-cycle (red line). Comparing the voltage profile shown in Figure 3 with the combined cycling and X-ray diffraction (XRD) experiments conducted on sputtered tin film electrodes by Ellis et al.[33] (with an areal sodiation capacity of ≈1 mAh/cm^2), the desodiation plateaus in Figure 3 can most likely be assigned to four different sodium-tin phases, namely $Na_{15}Sn_4$, Na_9Sn_4, NaSn, and $NaSn_5$.

In a next step, the stability of the µ-TWRE after sodiation to a cutoff potential of 10 mV vs. Na^+/Na was evaluated. Figure 4 shows the first galvanostatic (50 nA) sodiation of a µ-TWRE to 10 mV vs. Na^+/Na (requiring ≈35 h) and the subsequent relaxation phase over ≈100 h at open circuit voltage (OCV) for three µ-TWRE cells. During sodiation, a total charge of ≈1.75 µAh is passed from the sodium WE to the µ-TWRE. Assuming a typical capacity for a SIB cathode electrode of 2 mAh/cm^2 (corresponding to ≈2 mAh for the here used 11 mm diameter electrodes), the total charge required for the sodiation of the µ-TWRE would be <0.1% of the cathode capacity and can therefore be considered negligible. The magnification of the OCV relaxation phase in inset of Figure 4a clearly shows the highly reproducible potential vs. time profiles for the three µ-TWREs, all relaxing toward a stable potential of ≈100–110 mV vs. Na^+/Na. As we want to use the sodiated µ-TWRE to obtain electrode-resolved EIS data down to low frequencies, a sufficiently small µ-TWRE potential drift over the duration of an EIS experiment is required. For a more convenient assessment of the potential drift of the µ-TWRE, the inset of Figure 4b shows the time dependence of its potential ($dE_{\mu\text{-TWRE}}/dt$) over the course of the OCV relaxation phase: approximately 2.5 h after the sodiation of the µ-TWRE, the potential drift rate decreases to below ≈0.1 mV/min, and remains at such low values for another ≈100 h until the end of the experiment (with a total drift of ≈2 mV over this period). Considering that the acquisition time for a typical impedance experiment between 100 kHz and 0.1 Hz is at most 20 min, the maximum potential drift of the µ-TWRE with a drift rate of ≤0.1 mV/min is ≤2 mV. Therefore, for the potential perturbation amplitude of 20 mV used for our PEIS measurements, the total potential drift of the

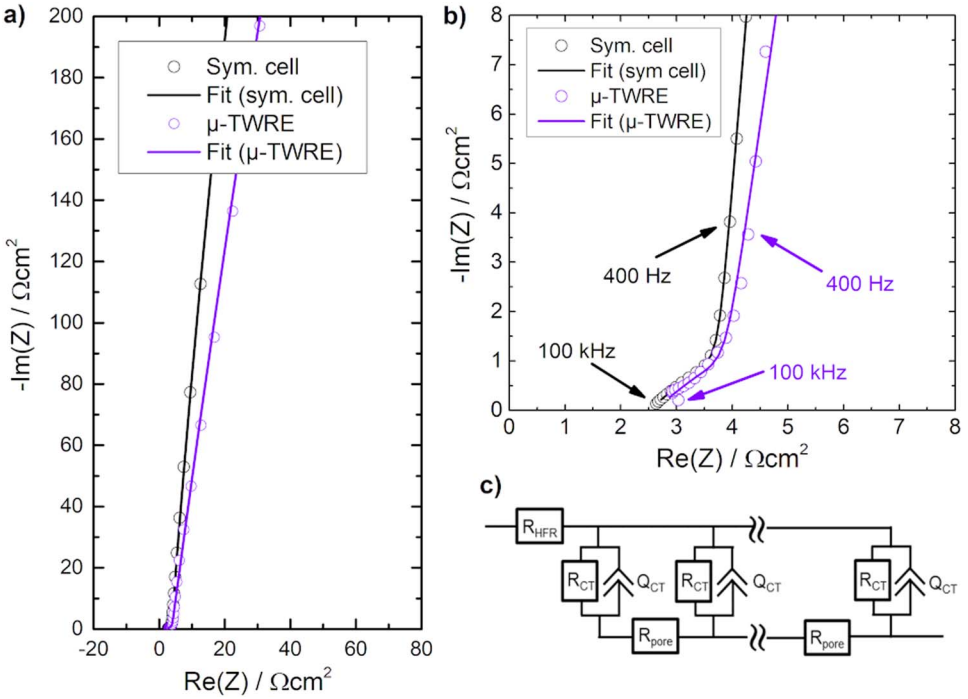

Figure 5. a) Comparison of the Nyquist impedance spectra of the pristine HC anode in an HC/Na half-cell with a μ-TWRE (purple line/symbols) with that of the pristine HC anode in a symmetrical HC/HC cell (black line/symbols), whereby the real and imaginary impedance values of the latter were divided by two in order to represent one single HC electrode. The PEIS data at OCV (taken between 100 kHz and 0.1 Hz with a perturbation amplitude of 20 mV) were recorded directly after a 24 h wetting period. The symbols represent the measured, and the lines the fitted PEIS data (shown between 30 kHz and ≈7 Hz); b) magnification of the high frequency (HFR) region; c) equivalent circuit used to fit the impedance spectra, consisting of a high-frequency resistance (R_{HFR}) and a transmission line model with a parallel R_{CT}/Q_{CT} element, a negligible electronic resistance rail, and a pore resistance (R_{pore}) that represents the ionic conduction resistance in the electrolyte phase within the HC electrode pores (referred to as mTML circuit; s. Experimental section).

μ-TWRE is only ≈10%, satisfying the requirement that the potential drift of the RE must be small with respect to the perturbation amplitude over the duration of the PEIS experiment. This means that after an OCV relaxation time of ≈2.5 h, reliable PEIS data can be obtained with our μ-TWRE for the above specified experimental conditions.

Validation of the μ-TWRE impedance data.—In order to confirm the validity of the impedance response measured with the here developed μ-TWRE, the in situ EIS measurements of the HC anode in an HC/Na half-cell are compared with ex situ data collected using an HC/HC symmetrical cell. For this purpose, two out of three hard carbon electrodes from the same coating were used to build a symmetrical HC/HC T-cell. The third electrode was incorporated into a T-cell equipped with a μ-TWRE (setup depicted in Figure 1a). For each cell, EIS data were acquired at OCV after a 24 h wetting phase. The resulting Nyquist plots are displayed in Figures 5a and 5b, reflecting the so-called blocking conditions (i.e., conditions where the charge transfer resistance (R_{CT}) depicted in the transmission line model shown in Figure 5c is very large), as one would expect for pristine HC electrodes far above the potential where a charge transfer reaction can occur. The black curves show the impedance response of the symmetrical HC/HC cell, whereby the real and imaginary values were divided by 2 in order to represent one of the two nominally identical hard carbon electrodes. The purple lines show the EIS data of the HC electrode collected from an HC/Na half-cell equipped with the μ-TWRE. While the high-frequency intercepts for the data sets shown in Figures 5a and 5b is very similar, as one would expect, one needs to note that differences up to ≈1 Ωcm² have been observed in repeat experiments with different cells, which originates from slightly different compressions of the two easily compressible 250 μm thick glass fiber separators that is due to the slight variations in the compression of the T-cells, which are equipped with a compression spring.[9] Furthermore, the impedance spectrum of the HC/Na half-cell with the μ-TWRE displays a downward pointing bend at frequencies above ≈30 kHz (s. Figure 5b), which is a well-known artefact of high impedance REs, that was also observed before.[14,34] Therefore, only impedance values at frequencies below ≈30 kHz should be taken into account when using the μ-TWRE.

The impedance spectra feature a 45°-line at high frequencies, originating from the ionic conduction resistance in the electrolyte phase within the porous electrode (R_{pore}) that is nicely visible under blocking conditions; at lower frequencies, this transitions into an almost purely capacitive behavior (i.e., a nearly vertical line in the Nyquist plot). As outlined by Landesfeind et al.,[14] the impedance responses shown in Figures 5a and 5b can be fitted with the simple transmission line model depicted in Figure 5c, consisting of an ionic conduction rail represented by R_{pore}, of parallel circuit elements of a charge transfer resistance (R_{CT}) and a constant phase element (Q_{CT}) that represents the double-layer capacitance, and of an electronic conduction rail with a negligible electronic resistance in the case of the highly conductive hard carbon electrode (referred to here as mTLM circuit). Fitting the data in Figures 5a and 5b to the circuit in Figure 5c, the obtained R_{pore} values are 4.1 ± 0.3 Ωcm² for a single HC electrode in the symmetrical HC/HC cell (based on two repeat experiments) and 4.5 ± 0.3 Ωcm² for the HC electrode in the HC/Na half-cell with the μ-TWRE (based on three repeat experiments). Therefore, within the error of measurement, the impedance analysis for the HC/HC symmetrical cells and the HC/Na half-cells with the μ-TWRE agrees very well, and thus validates the accuracy of the μ-TWRE approach (similarly good agreement was observed previously for a lithiated gold wire μ-RE[14]). From the pore resistances, the tortuosities of the electrodes can be calculated:[35] taking into account an electrolyte conductivity of 8.2 mS/cm (at 25°C), an electrode thickness of ≈44 μm, a porosity of 60%, and an electrode area of 0.95 cm², this equates to electrode tortuosities of 4.4 ± 0.3 and 4.8 ± 0.3 for the HC/HC symmetrical cell and the HC/Na half-cell measurements, respectively. In comparison, tortuosities measured for flake-like graphite electrodes using the same technique were found to be around 5.[35]

Hard carbon impedance evolution during cycling.—As already described above, a major advantage of the in situ impedance measurement method with a μ-TWRE for SIBs is the possibility to very easily monitor the impedance of an individual electrode (in the present case the HC electrode) during (long-term) cycling of a cell. In the literature, impedance data on sodiated hard carbon electrodes are quite rare. If provided, the measured impedances are often not normalized to the electrode area,[29,36–38] which makes a quantitative comparison between different studies difficult. More problematic, however, is that most studies simply monitor the change in cell impedance and ascribe this to a change in the hard carbon impedance,[29,36–40] i.e., neglecting possible changes in the impedance of the CE, which in most of these studies was sodium metal. For example, Väli et al.[39] present impedance data between 300 kHz and 10 mHz of a glucose-derived hydrothermal hard carbon in an HC/Na half-cell in EC/DMC + 1 M $NaPF_6$ electrolyte, measured after cycling to different cell potentials (1.0, 0.6, 0.37, and 0.04 V), analyzing the change in cell impedance, i.e., the sum of the impedance of the hard carbon WE and of the sodium CE. Since the surface area of the sodium counter electrode is likely to change substantially during cycling, especially during the half-cycles where sodium plating occurs, the impedance of the sodium electrode is expected to also change over the course of cycling; this is well known for lithium metal electrodes,[41,42] where the impedance change of a graphite electrode in graphite/Li half-cell impedance measurements is often mistakenly ascribed to the change in the impedance of the graphite electrode.[43] There is clear evidence in the literature that the same uncertainties are present in the case of impedance measurements of cells with a sodium metal electrode, particularly as the charge transfer resistance of a typical sodium metal electrode is rather large (several hundreds of Ωcm^2, with the exact value depending on the sodium metal roughness[44,45]). Moreover, in a recent study, Dugas et al.[45] point out that the SEI formed on a sodium metal electrode is not stable and that therefore also the impedance of the Na electrode changes drastically over time, which was measured in an Na/Na symmetrical cell in EC/DMC + (50v%/50v%) + 1 M $NaPF_6$ over 290 h. Here, the charge transfer resistance roughly doubled from ≈150 Ωcm^2 to ≈300 Ωcm.[2] Due to the fact that the impedance of the sodium counter electrode cannot be deconvoluted from the overall cell impedance, no precise information on the evolution of the hard carbon impedance can be gained from the overall impedance of HC/Na half-cells, unless the hard carbon impedance would be significantly larger than the estimated several hundreds of Ωcm^2 expected for the Na electrode.

As already discussed above, one way to eliminate the impedance contribution from the sodium metal CE would be the use of symmetrical cells. Unfortunately, hardly any published study determines the impedance of the hard carbon electrode with symmetrical cells or even with a reference electrode. An exception is a study by Ding et al.,[46] who use the symmetrical cell approach in order to deconvolute the contributions from the sodium metal CE. Here, they investigate the electrochemical performance of a hard carbon anode for ionic-liquid based SIBs in a temperature range of 10–90°C using Na/Na and HC/HC symmetrical cells. As a conclusion, they stress that the R_{CT} value for the Na electrode is much larger than that for the HC electrode, which again demonstrates that overall cell impedance data on SIB half-cells can easily be misinterpreted if the sodium metal impedance contribution is not taken into account.

To the best of our knowledge, there are no data on the impedance evolution of a hard carbon anode over extended cycling of an HC/Na half-cell, neither measured in symmetrical cells nor employing a μ-RE. Figure 6a shows the hard carbon impedance spectra of a hard carbon electrode cycled vs. sodium metal (as shown in Figure 1a). PEIS was measured during cycling at a cell potential of 100 mV_{cell} during the sodiation cycle after an OCV relaxation phase of 30 min (measured at OCV). Depicted are the EIS spectra recorded during cycle 1 (purple symbols) and cycle 2 (cyan symbols). Both hard carbon impedance spectra feature a large semi-circle at low frequencies, with an apex frequency of ≈25 Hz, presumably representing the charge transfer resistance of the hard carbon anode, as well as a short 45°-line at high frequencies, which reflects R_{pore}. The impedance spectra were fitted

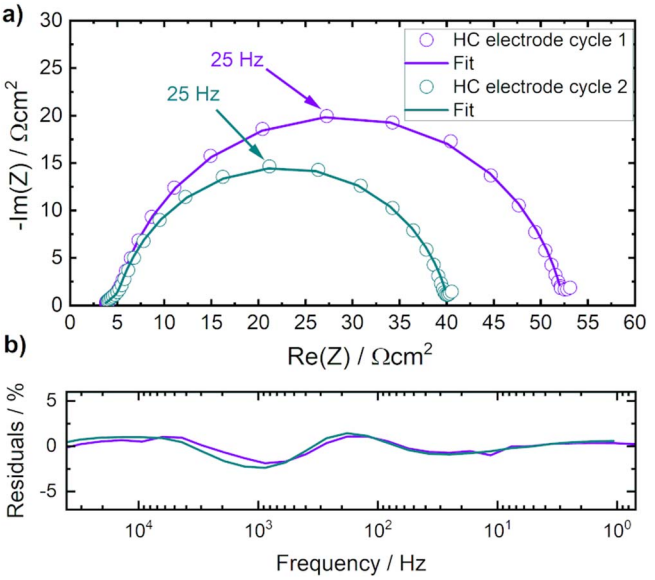

Figure 6. a) Nyquist impedance plot of the hard carbon electrode impedance measured in an HC/Na half-cell using the μ-TWRE (for the cell setup s. Figure 1a) during cycling at rate of 0.1 C at 25°C for the first cycle (purple line/symbols) and for the second cycle (cyan line/symbols). For the impedance measurements, the cell was cycled to a cell potential of 100 mV_{cell} during the sodiation cycle, then held at OCV for 30 min, after which time a PEIS was acquired at OCV between 100 kHz and 0.1 Hz and with an amplitude of 20 mV. The impedance data are depicted by symbols and the fit to the equivalent circuit shown in Figure 5c is given by the lines (for fitting parameter, s. Table I); b) residuals between the impedance data and the equivalent circuit fit, demonstrating the good description of the impedance data by the simple equivalent circuit depicted in Figure 5c.

using the equivalent circuit shown in Figure 5c, whereby the ionic resistance R_{pore} was fixed to the value of 4.5 Ωcm^2 that was determined from the fit under blocking conditions (s. discussion of Figure 5); to obtain a stable fit, the electronic resistance of the electronic rail (s. Figure 5c) was set to a very small value of 0.001 Ωcm^2, which essentially means that the resistance of the electronic rail is negligible. The resulting fit is shown by the solid lines in Figure 6a and the error between the fit and the data is depicted in Figure 6b, demonstrating that the simple equivalent circuit shown in Figure 5c with only one R_{CT}/Q_{CT} element is sufficient to describe the impedance response of the HC electrode. The resulting fitting parameters to describe the hard carbon electrode impedance in the first and second cycle are summarized in Table I. For the obtained α_{CT} values that are reasonably close to 1, the magnitudes of the constant phase elements (Q_{CT}) can be approximated with a capacitance, which in turn can be normalized by the actual surface area of the hard carbon electrodes of ≈150 cm^2_{HC}/cm^2 (from ≈3 mg_{HC}/cm^2 loading and ≈5 m^2_{HC}/g_{HC} BET), yielding a surface area normalized capacitance of ≈1.7 $\mu F/cm^2_{HC}$. This is consistent

Table I. Summary of the fitting parameter and the obtained parameter values for the hard carbon impedance spectra shown in Figure 6a, using the equivalent circuit depicted in Figure 5c. Here, R_{HFR} is the high frequency resistance, R_{CT} is the charge transfer resistance of the hard carbon electrode, Q_{CT} is the constant phase magnitude, and α_{CT} is the constant phase exponent.

	Cycle 1		Cycle 2	
parameter	value	error/%	value	error/%
$R_{HFR}/\Omega cm^2$	3.4	2.2	3.3	2.3
$R_{CT}/\Omega cm^2$	47.6	0.3	35.3	0.5
$Q_{CT}/mF \cdot s^{(\alpha_{CT}-1)}/cm^2$	0.25	1.9	0.26	2.8
a_{CT} /	0.9	0.4	0.9	0.6

with a typical double-layer capacitance in aprotic electrolytes[47] and therefore confirms that the semi-circle feature in Figure 6a represents the charge-transfer resistance of the hard carbon electrode.

The charge transfer resistance R_{CT} of the hard carbon anode in the first cycle is on the order of 50 Ωcm^2 (s. Table I), i.e., much smaller than the above estimated charge transfer resistance of a typical sodium metal electrode. Thus, its value could not be obtained from the overall HC/Na cell impedance without the use of a reference electrode. The hard carbon R_{CT} also significantly decreases from cycle 1 to cycle 2. Other carbon-based intercalation materials, such as graphite, do not exhibit a decreasing charge transfer resistance in the first two cycles, but rather show a monotonously increasing anode impedance with time,[9,15] usually explained by SEI growth and a subsequent increase in SEI resistance. A plausible reason for the decrease in R_{CT} for the hard carbon anode in an SIB could be that the surface area of the hard carbon electrode is increasing during the first cycle(s), owing perhaps to the opening of pores or other as yet unknown phenomena.

Figure 7a shows the voltage profiles for cycle 1, 2, and 52 of a hard carbon anode cycled at 0.1 C and 25°C vs. sodium metal in an HC/Na half-cell with a μ-TWRE, with the inset depicting the evolution of the specific desodiation capacity and the coulombic efficiency vs. cycle number. The hard carbon cell exhibits a high first-cycle coulombic efficiency of ≈92%, which is close to values that have been reported for this type of HC.[44] After the second cycle in which a coulombic efficiency of >99.5% has been reached, the capacity fading of the hard carbon electrode is minor, retaining a specific reversible capacity of 265 mAh/g_{HC} or ≈94% after 52 cycles.

Figure 7b shows Nyquist impedance plots, each measured during sodiation at a cell potential of 100 mV vs. Na CE and a 30 min relaxation phase at OCV during cycle 1, 2, and afterwards during every 10th cycle between 100 kHz and 10 mHz. As already explained for the impedance spectra of cycle 1 and 2 in detail above, within the first two cycles, two regions can be distinguished within the impedance spectra. A large semi-circle at mid and low frequencies, which we attribute to a charge transfer resistance (R_{CT}, ≈48 Ωcm^2 for cycle 1 and ≈36 Ωcm^2 for cycle 2), and a short line with a 45°-slope at high frequencies (visible in a magnification of Figure 6a, not shown) originating from a pore resistance (R_{pore}), which we also identified in the impedance spectrum of the blocking hard carbon electrode (0% SOC) in Figure 5. This pore resistance at high frequencies and the semi-circle at mid frequencies is also visible during all other cycles. However, roughly starting at cycle 22, a second semi-circle at higher frequencies compared to the first semi-circle is evolving and growing in magnitude with increasing cycle number, which is most apparent in cycle 52. This second semi-circle might be due to the SEI resistance that is hidden underneath the large semi-circle during the first cycles. With ongoing cycling, the SEI resistance is likely to increase which could be the reason that this process becomes more and more visible as a second semi-circle for higher cycle numbers.

The total magnitude of the hard carbon electrode impedance, which we define as the difference of the real part of the low frequency resistance at 0.1 Hz (R_{LFR}) and the real part of the high frequency resistance at 30 kHz (R_{HFR}), is plotted in Figure 7b (s. inset). As already mentioned above, Figure 7b shows that the total, real part of the electrode resistance first decreases during initial cycling (at least in the second cycle, however, most likely within the first couple of cycles) and afterwards slowly increases. Taking into account the processes that we assigned to the features in the impedance spectra above, we speculate that the increase in electrode impedance for longer cycling (>cycle 22), is related to aging effects of the electrode, most likely due to a growth of the SEI. This hypothesis is supported by the fact that the diameter of the second, larger semi-circle stays roughly constant from cycle 22 and the increase of the total resistance seems to originate from the second, smaller semi-circle that we attributed to an SEI resistance.

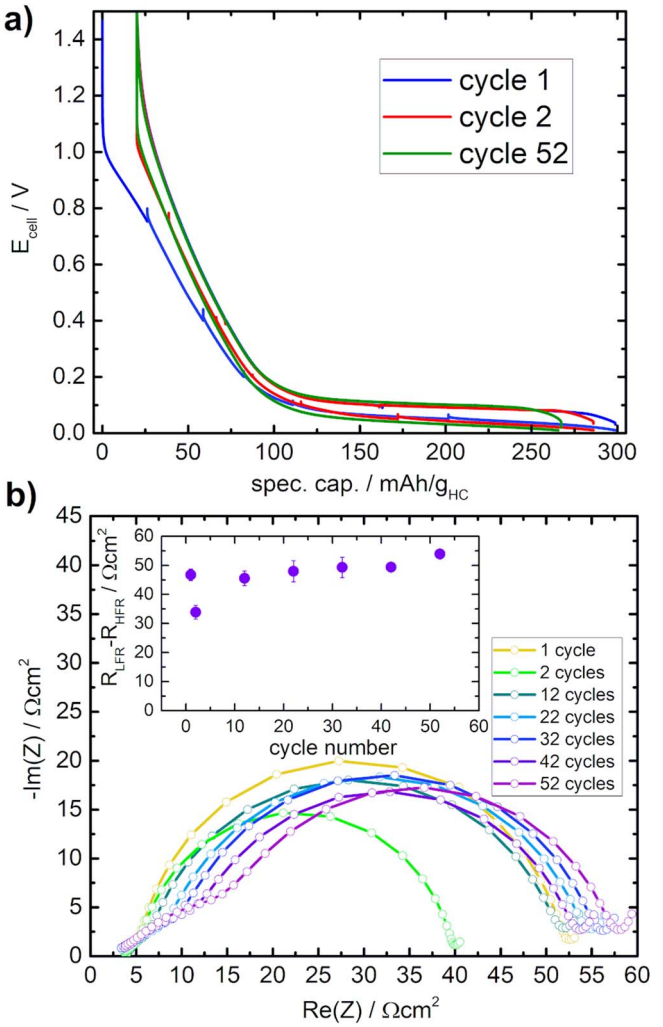

Figure 7. a) Voltage profiles of cycle 1, 2, and 52 for the (de)-sodiation of a hard carbon anode cycled between 1.5 and 0.01 V_{cell}. The inset shows the specific desodiation capacity and the coulombic efficiency vs. cycle number; b) Nyquist plot of the impedance response of a hard carbon electrode in an HC/Na half-cell obtained with a sodiated μ-TWRE and measured during the first, second, and thereafter every 10th sodiation cycle at a potential of 100 mV_{cell} (data for cycle 1 and 2 are the same as in Figure 6). The inset depicts the overall electrode impedance obtained by subtracting the high-frequency resistance recorded at 30 kHz (R_{HFR}) from the low-frequency resistance recorded at 0.1 Hz (R_{LFR}). Conditions: 25°C, EC/DEC (50v%/50v%) + 1 M $NaPF_6$ electrolyte, cycling at a rate of 0.1 C, PEIS with 20 mV amplitude after an OCV phase of 30 min, frequency range 100 kHz-0.1 Hz.

Conclusions

In this work, we introduce a new method that enables in situ impedance measurements in sodium-ion battery cells, which allows for separating single-electrode contributions to the overall cell impedance. The newly developed technique is based on a μ-RE consisting of a ≈100 μm thick tinned copper wire with a polyurethane insulation, referred to as tin-wire micro-reference electrode (μ-TWRE) that can be easily incorporated into a Swagelok type T-cell. By in situ sodiating the tip of the tinned wire from a sodium source within the cell, e.g., from a sodium metal counter electrode or a sodium containing cathode active material, it is possible to alloy sodium with tin, yielding Na-Sn-phases that exhibit a reference electrode potential, which is stable enough in order to perform high-quality impedance measurements. The validity of the data obtained from the μ-TWRE was evaluated by comparing them to measurements performed in symmetrical cells, which were in very good agreement.

The use of this newly developed μ-RE makes it possible to easily monitor the impedance evolution of an individual electrode in sodium-ion battery cells over extended cycling, thereby saving experimental effort compared to the use of symmetrical cells and eliminating

possible artefacts introduced by cell assembly and disassembly required for symmetrical cell measurements. As a first application, we measured the impedance of a hard carbon anode cycled vs. a sodium metal counter electrode at a rate of 0.1 C over 50 cycles. Interestingly, the impedance of the electrode decreases during the first cycles, a phenomenon not known for the intercalation of lithium in graphite, and afterwards increases steadily. We assume that the decreasing impedance might stem from a surface area increase of the active material particles during SEI formation. The herein presented μ-TWRE based EIS method could be used in future studies to characterize novel anode and cathode materials for sodium-ion batteries over long-term cycling and to identify cross-talk phenomena between working and counter electrode.

Acknowledgment

We gratefully acknowledge the funding by the BMBF (Federal Ministry of Education and Research, Germany) for its financial support under the auspices of the ExZellTUM II project, grant number 03XP0081. The authors would like to thank Tim-Patrick Fellinger for providing the hard carbon samples from Kuraray as well as Robert Morasch for his development of a procedure which allowed to obtain EIS data with capacitively strongly imbalanced electrodes and Bharat Suthar for his advice on EIS fitting.

ORCID

Fabian Linsenmann https://orcid.org/0000-0001-8788-2584
Daniel Pritzl https://orcid.org/0000-0002-9029-107X

References

1. McKinsey, "Electric Vehicle Index 2019," can be found under https://www.mckinsey.de/branchen/automobil-zulieferer/electric-vehicle-index, accessed on 09/04/2019.
2. VW, "Volkswagen plans 22 million electric vehicles in ten years," can be found under https://www.volkswagen-newsroom.com/en/press-releases/volkswagen-plans-22-million-electric-vehicles-in-ten-years-4750, accessed on 09/04/2019.
3. D. L. Anderson, *Theory of the Earth*, Blackwell Scientific Publications 1989.
4. L. Chen, M. Fiore, J. E. Wang, R. Ruffo, D.-K. Kim, and G. Longoni, *Adv. Sustain. Syst.*, 1 (2018).
5. B. L. Ellis and L. F. Nazar, *Curr. Opin. Solid State Mater. Sci.*, **16**, 168 (2012).
6. K. Kubota and S. Komaba, *J. Electrochem. Soc.*, **162**, A2538 (2015).
7. N. Yabuuchi, K. Kubota, M. Dahbi, and S. Komaba, *Chem. Rev.*, **114**, 11636 (2014).
8. M. I. Jamesh and A. S. Prakash, *J. Power Sources*, **378**, 268 (2018).
9. S. Solchenbach, D. Pritzl, E. J. Y. Kong, J. Landesfeind, and H. A. Gasteiger, *J. Electrochem. Soc.*, **163**, A2265 (2016).
10. J. C. Burns, N. N. Sinha, G. Jain, H. Ye, C. M. VanElzen, W. M. Lamanna, A. Xiao, E. Scott, J. Choi, and J. R. Dahn, *J. Electrochem. Soc.*, **159**, A1095 (2012).
11. M. Klett, J. A. Gilbert, S. E. Trask, B. J. Polzin, A. N. Jansen, D. W. Dees, and D. P. Abraham, *J. Electrochem. Soc.*, **163**, A875 (2016).
12. N. Ogihara, S. Kawauchi, C. Okuda, Y. Itou, Y. Takeuchi, and Y. Ukyo, *J. Electrochem. Soc.*, 159 (2012).
13. R. Petibon, C. P. Aiken, N. N. Sinha, J. C. Burns, H. Ye, C. M. VanElzen, G. Jain, S. Trussler, and J. R. Dahn, *J. Electrochem. Soc.*, **160**, A117 (2013).
14. J. Landesfeind, D. Pritzl, and H. A. Gasteiger, *J. Electrochem. Soc.*, **164**, A1773 (2017).
15. D. Pritzl, S. Solchenbach, M. Wetjen, and H. A. Gasteiger, *J. Electrochem. Soc.*, **164**, A2625 (2017).
16. M. Ender, J. Illig, and E. Ivers-Tiffée, *J. Electrochem. Soc.*, **164**, A71 (2017).
17. J. Costard, M. Ender, and M. Weiss, *J. Electrochem. Soc.*, **164**, 80 (2017).
18. D. P. Abraham, S. D. Poppen, A. N. Jansen, J. Liu, and D. W. Dees, *Electrochim. Acta*, **49**, 4763 (2004).
19. J. C. Burns, L. J. Krause, D.-B. Le, L. D. Jensen, A. J. Smith, D. Xiong, and J. R. Dahn, *J. Electrochem. Soc.*, **158**, A1417 (2011).
20. R. Petibon, N. N. Sinha, J. C. Burns, C. P. Aiken, H. Ye, C. M. Vanelzen, G. Jain, S. Trussler, and J. R. Dahn, *J. Power Sources*, **251**, 187 (2014).
21. R. Petibon, E. C. Henry, J. C. Burns, N. N. Sinha, and J. R. Dahn, *J. Electrochem. Soc.*, **161**, A66 (2014).
22. C. H. Chen, J. Liu, and K. Amine, *J. Power Sources*, **96**, 321 (2001).
23. M. Ender, E. Ivers-Tiffé, and A. Weber, *J. Electrochem. Soc.*, **159**, 128 (2012).
24. M. Dollé, F. Orsini, A. S. Gozdz, and J.-M. Tarascon, *J. Electrochem. Soc.*, **148**, A851 (2002).
25. D. Pritzl, J. Landesfeind, S. Solchenbach, and H. A. Gasteiger, *J. Electrochem. Soc.*, **165**, A2145 (2018).
26. A. D. Pelton, *J. Phase Equilibria*, **7**, 228 (1986).
27. J. I. Kroschwitz and A. Seidel, *Kirk-Othmer Encyclopedia of Chemical Technology*, Wiley, 2006.
28. H. Hou, X. Qiu, W. Wei, Y. Zhang, and X. Ji, *Adv. Energy Mater.*, **7**, 1 (2017).
29. C. Bommier, D. Leonard, Z. Jian, W. F. Stickle, P. A. Greaney, and X. Ji, *Adv. Mater. Interfaces*, **3**(19), 1600449 (2016).
30. S. Komaba, W. Murata, T. Ishikawa, N. Yabuuchi, T. Ozeki, T. Nakayama, A. Ogata, K. Gotoh, and K. Fujiwara, *Adv. Funct. Mater.*, **21**, 3859 (2011).
31. E. Irisarri, A. Ponrouch, and M. R. Palacin, *J. Electrochem. Soc.*, **162**, A2476 (2015).
32. R. Morasch, B. Suthar, and H. A. Gasteiger, *to be submitted*.
33. L. D. Ellis, T. D. Hatchard, and M. N. Obrovac, *J. Electrochem. Soc.*, **159**, A1801 (2012).
34. S. Solchenbach, *PhD Thesis*, Technical University of Munich, 2018.
35. J. Landesfeind, J. Hattendorff, A. Ehrl, W. A. Wall, and H. A. Gasteiger, *J. Electrochem. Soc.*, **163**, A1373 (2016).
36. C. Bommier, W. Luo, W. Y. Gao, A. Greaney, S. Ma, and X. Ji, *Carbon N. Y.*, **76**, 165 (2014).
37. W. Lv, F. Wen, J. Xiang, J. Zhao, L. Li, L. Wang, Z. Liu, and Y. Tian, *Electrochim. Acta*, **176**, 533 (2015).
38. A. Ponrouch, A. R. Goñi, and M. R. Palacín, *Electrochem. Commun.*, **27**, 85 (2013).
39. R. Väli, A. Jänes, T. Thomberg, and E. Lust, *Electrochim. Acta*, **253**, 536 (2017).
40. R. Väli, A. Jänes, T. Thomberg, and E. Lust, *J. Electrochem. Soc.*, **163**, A1619 (2016).
41. D. Aurbach, E. Zinigrad, Y. Cohen, and H. Teller, *Solid State Ionics*, **148**, 405 (2002).
42. G. A. Umeda, E. Menke, M. Richard, K. L. Stamm, and B. Dunn, *Journal of Materials Chemistry*, **4**, 1593 (2011).
43. J. Y. Song, H. H. Lee, Y. Y. Wang, and C. C. Wan, *J. Power Sources*, **111**, 255 (2002).
44. M. Dahbi, T. Nakano, N. Yabuuchi, S. Fujimura, K. Chihara, K. Kubota, J. Y. Son, Y. T. Cui, H. Oji, and S. Komaba, *ChemElectroChem*, **3**, 1856 (2016).
45. R. Dugas, A. Ponrouch, G. Gachot, R. David, M. R. Palacin, and J. M. Tarascon, *J. Electrochem. Soc.*, **163**, A2333 (2016).
46. C. Ding, T. Nohira, R. Hagiwara, A. Fukunaga, S. Sakai, and K. Nitta, *Electrochim. Acta*, **176**, 344 (2015).
47. D. Pritz, A. E. Bumberger, M. Wetjen, J. Landesfeind, S. Solchenbach, and H. A. Gasteiger, *J. Electrochem. Soc.*, **166**, A582 (2019).

3.1.2 Comparing the Lithiation and Sodiation of a Hard Carbon Anode via Impedance Spectroscopy Using Micro-Reference Electrodes

In the following section, the manuscript *"Comparing the Lithiation and Sodiation of a Hard Carbon Anode Using In Situ Impedance Spectroscopy"* is presented. The manuscript was submitted to the peer-reviewed Journal of the Electrochemical Society in November 2020 and was published in January 2021. The article is published open access and distributed under the terms of the Creative Commons Attribution 4.0 License. The permanent web link can be found under: https://iopscience.iop.org/article/10.1149/1945-7111/abd64e. The scope of this work is a detailed analysis of the electrode impedance of a commercial hard carbon (HC) during lithiation and sodiation, and a comparison of the impedance change as a function of state-of-charge (SOC) and during cycling. The article was submitted recently to a peer-reviewed journal and is currently under review.

Prior to the discovery of SEI-stabilizing additives, such as ethylene carbonate in the early 1990s,[34] amorphous carbons were used as anode active materials in LIBs. The first generation LIB commercialized by Sony in 1991 employed a soft carbon (SC) anode which was replaced by a hard carbon (HC) anode one year later.[32] Even though there are reports on very high specific (de)lithiation capacities that can be obtained for certain HC materials in lithium-ion batteries, this type of material suffers from drawbacks, such as a lower volumetric energy density compared to graphite and from the fact that its in principle large specific capacities that exceed the theoretical capacity of graphite (372 mAh/g_{AAM}) are only accessible at anode potentials very close to 0 V *vs.* Li^+/Li; rendering them not usable in full-cell applications due to the hazard of lithium plating.[226] This is the reason why HC anodes were gradually substituted by graphite, which is today the almost exclusively used anode chemistry. However, concerning SIBs, HCs are still the most promising anode active material, since sodium does not intercalate into graphite.

Thus, in this study, we provide electrode-resolved EIS data obtained using μ-REs, namely a lithiated μ-GWRE in the case of (de)lithiation and a sodiated μ-TWRE in the case of (de)sodiation, measured for varying SOCs and upon extended cycling. By

fitting the obtained EIS spectra with a simple electrochemical equivalent circuit model, we can separate and quantify the charge transfer resistance (R_{CT}) and the pore resistance (R_{pore}) of HC electrodes in Na/HC and in Li/HC half-cells. For both, R_{CT} decreases/increases reversibly with increasing/decreasing SOC, as also is the case for graphite anodes in LIBs. Interestingly, for (de)sodiation of the hard carbon electrode, R_{CT} is ≈10-fold larger compared to (de)lithiation. The higher electrode impedance, which is dominated by the charge transfer resistance, results in larger overpotentials during fast sodiation, *i.e.*, fast-charging in a respective full-cell, which was confirmed in HC sodiation and lithiation rate tests, respectively. The reduced rate capability for HC-based SIBs is an important performance indicator when it comes to assessing SIBs regarding a commercial use.

Author contributions

F.L. performed all cycling and impedance measurements. The data was analyzed by F.L. and D.P. The manuscript was written by F.L. and H.A.G. All authors discussed the data and commented on the results.

Journal of The Electrochemical Society, 2021 **168** 010506

Comparing the Lithiation and Sodiation of a Hard Carbon Anode Using In Situ Impedance Spectroscopy

Fabian Linsenmann,*,z Daniel Pritzl, and Hubert A. Gasteiger**

Chair of Technical Electrochemistry, Department of Chemistry and Catalysis Research Center, Technische Universität München, 85748 Garching, Germany

We present *in situ* electrochemical impedance spectroscopy data measured during (de)sodiation and (de)lithiation of a commercial hard carbon (HC) anode material. For this purpose, two different systems of *micro*-reference electrodes (μ-RE) were used: a gold-wire reference electrode (μ-GWRE) for Li/HC half-cells and a tin-wire reference electrode (μ-TWRE) for Na/HC half-cells. We show that for both (de)sodiation (using EC/DMC + 1 M $NaPF_6$ electrolyte) and (de)lithiation (using EC/EMC + 1 M $LiPF_6$ electrolyte) the impedance spectra are dominated by a charge transfer resistance (R_{CT}) which is reversibly decreasing/increasing with increasing/decreasing state-of-charge. The contributions to the HC electrode resistance (R_{anode}), i.e., charge transfer (R_{CT}), pore (R_{pore}), and separator resistance (R_{HFR}), were obtained by fitting the impedance spectra using a representative equivalent circuit. We conclude that the R_{CT} associated with sodiation of HC is ≈10-fold higher compared to the lithiation of HC at 100% SOC. Furthermore, we compare the evolution of R_{anode} measured *in situ* over 52 cycles at the same SOC. We find that the higher electrode resistances for sodiated HC result in a considerably reduced rate capability for HC sodiation. For a potential future commercialization of sodium-ion batteries, the fast-charging properties (=HC sodiation) would be a crucial performance indicator.
© 2021 The Author(s). Published on behalf of The Electrochemical Society by IOP Publishing Limited. This is an open access article distributed under the terms of the Creative Commons Attribution 4.0 License (CC BY, http://creativecommons.org/licenses/by/4.0/), which permits unrestricted reuse of the work in any medium, provided the original work is properly cited. [DOI: 10.1149/1945-7111/abd64e]

Manuscript submitted November 18, 2020; revised manuscript received December 18, 2020. Published January 7, 2021. *This was paper 146 presented at the Dallas, Texas, Meeting of the Society, May 26–May 30, 2019.*

Until today, graphite is the almost exclusively used anode active material (AAM) in commercial lithium-ion batteries (LIBs) owing to its high capacity (≈350–360 $mAh/g_{graphite}$) and low average discharge potential,[1,2] resulting in a relatively high energy density. In 2016, the market share of anode active materials for commercial LIBs was 89% graphite (43% artificial and 46% natural graphite), 7% amorphous carbon, 2% lithium titanate (LTO) and 2% silicon or tin-based materials.[3] Interestingly, the very first LIB introduced by Sony in 1991 used an amorphous (disordered) carbon anode, more precisely a soft carbon (SC) with a specific capacity of ≈220 mAh/g_{SC}.[4,5] This cell with an $LiCoO_2$ cathode yielded an energy density of ≈80 Wh kg^{-1},[4,5] considerably more than the back then used nickel-cadmium cells (≈50 Wh kg^{-1}).[6] Two classes of amorphous carbons are typically distinguished: hard carbons (HC) that exhibit a high degree of cross-linking between graphitic domains and therefore cannot be graphitized even at very high temperatures, and soft carbons with little cross-linking where neighboring graphitic domains have a tendency to lie in almost parallel pre-orientation, so that they can be transformed into the graphitic state by pyrolysis at temperatures between 2000 °C–3000 °C.[7] The SC anode in Sony's first generation LIB was substituted already one year later by a HC anode with a higher capacity of ≈320 mAh/g_{HC}, resulting in an energy density of ≈120 Wh kg^{-1} with a $LiCoO_2$ cathode.[4] While graphite is known to undergo a volume expansion of ≈10% during lithium intercalation,[8] with the d-spacing between neighboring graphene layers increasing from 0.335 to ≈0.37 nm,[9] HCs typically show higher d-spacings already in their delithiated state (>0.38 nm), so that they, contrary to graphite, do not undergo volume expansion upon lithiation.[4,5] Nishi et al.[4,5] explain the very high full-cell cycling stability of HC based LIBs by the absence of volume change upon lithiation/delithiation, which is supposed to decrease lithium inventory losses induced by cracking of the solid electrolyte interphase (SEI) caused by volume changes, a well-known aging mechanism of graphite anodes during long-term cycling, especially at elevated temperatures.[10,11] However, the lower density of HCs[7,12] (≈1.45–1.55 g cm^{-3} vs 2.2 g cm^{-3} for graphite) and their relatively high first-cycle irreversible capacity losses of ≈20%[4,5,13] (vs <10% for graphite[14,15]) significantly reduce the energy density of the cell. Therefore, the development of new electrolytes based on ethylene carbonate[16] that enabled the application of graphite as anode active material, gradually led to the replacement of HC anodes by graphite in LIBs.[5] Furthermore, the fact that the graphite potential for lithium (de) intercalation is close to that of metallic lithium (≈100 mV vs Li^+/Li) over nearly the entire charge/discharge curve increases the energy density compared to HCs that typically feature sloping voltage profiles.[17] Consequently, while in 1997 the market shares of HC and graphite were still 52% and 43%,[18] respectively, today artificial and natural graphites are dominating the anode material market, as mentioned above.[2,3]

In the literature, it is often argued that some HCs can incorporate lithium-ions in ratios higher than the well-known LiC_6 stoichiometry found for fully intercalated graphite,[1] which should allow for practical reversible capacities above the theoretical capacity of graphite of 372 $mAh/g_{graphite}$. In fact, high reversible capacities for lithium insertion into HCs are reported in the literature.[5,13,19–23] However, since the voltage profiles at higher state-of-charge (SOC) become very flat for HCs, a considerable fraction of their capacity is obtained at potentials significantly below 100 mV vs Li^+/Li[13,19] and can typically only be accessed by constant voltage holds at the end of the charging phase at very low potentials of ≈10 mV vs Li^+/Li. Additionally, the thus obtained high reversible capacities are often accompanied by high irreversible capacity losses[21] and a large voltage hysteresis.[13] Novak et al.[24] therefore point out that even though some HCs do show reversible capacities above the theoretical specific capacity of graphite, the actually usable capacity is restricted in practical applications. In summary, the main issues related to a commercial use of HCs are[24]: a) the risk of lithium plating at potentials close to 0 V vs Li^+/Li at the end of charge, if high lithiation capacities are to be utilized; b) an often observed coulombic efficiency (CE) decrease when charging to such low voltages; and c) the flat potential profile that makes it difficult to properly control the cutoff cell voltage during charging in order to prevent overcharging.

While graphite is now used almost exclusively in LIBs, it cannot be used as anode active material in sodium-ion batteries (SIBs), as it is widely accepted that graphite cannot reversibly intercalate sodium-ions when using standard organic carbonate-based electrolytes.[25] The reason for this is believed to be the thermodynamic instability of the resulting Na-C-phases.[26] On the other

*Electrochemical Society Student Member.
**Electrochemical Society Fellow.
zE-mail: fabian.linsenmann@tum.de

hand, electrochemical sodium insertion reactions into disordered carbons have been observed and reported already in the late 1980s,[27] and probably some of the first experiments on rechargeable sodium-ion cells were published by Doeff et al. in 1993,[28] who demonstrated cycling of a sodium-ion battery consisting of a HC anode (petroleum coke), a solid polymer electrolyte, and a sodium cobalt bronze cathode ($Na_{0.6}CoO_2$). For the petroleum coke, a maximum stoichiometry of NaC_{15} could be obtained, which would correspond to a specific capacity of ≈149 mAh/g_{HC}.

The storage mechanism of both lithium and sodium in disordered carbonaceous materials, such as HCs, is still not completely understood and under ongoing discussion in the literature.[29] The first studies where the intercalaction mechanism of lithium and sodium in HCs was investigated and directly compared were reported by Stevens and Dahn in 2000 and 2001.[17,30] These authors conclude from *in situ* wide angle and small angle X-ray scattering (WAXS and SAXS) that the insertion mechanisms for lithium and sodium in HCs seem to be similar. At higher anode potentials (i.e., at low SOCs), the insertion between approximately parallel graphene sheets, described by Liu and Dahn[22] as a "house of cards" structure, was attributed to giving rise to the sloping voltage profile in the low SOC region. Additionally, during the flat, low-voltage plateau found at higher SOC, lithium and sodium fill nanopores in an adsorption-like process occurring at chemical potentials close to that of the metals themselves. Stevens and Dahn could confirm interlayer intercalation at low SOCs also by *in situ* X-ray diffraction (XRD) measurements of the d-spacing increase during lithium or sodium insertion.[17] These results were confirmed by Komaba et al. through *ex situ* XRD and Raman spectroscopy.[31] Evidence for the pore filling mechanism in the high SOC region was obtained from small-angle X-ray spectroscopy (SAXS) data,[17] later on confirmed by Gotoh et al.[32] and Chevallier et al.[33] for lithium via ^{7}Li solid state NMR and by Stratford et al.[34] and Morita et al.[35] in the case of sodium via ^{23}Na solid state NMR.

In summary, while HC anodes have been replaced by graphite in commercial LIBs, the HC material family is until today still the most promising anode material for SIBs. Therefore, in this study, we want to shed light on the impedance evolution of a commercial HC anode during (de)sodiation in the very first formation cycle and over extended cycling, and compare it with the associated impedance changes in the case of (de)lithiation of the same HC anode material. To the best of our knowledge, SOC-dependent anode impedance data of a HC anode have not been reported in the literature in the case of sodium. As discussed in former studies from our group,[36,37] electrode-specific impedances, i.e., without superposition of the counter electrode (CE) impedance, are only accessible by means of *in situ* impedance measurements using a micro-reference electrode (μ-RE) or via harvesting electrodes and assembling them into symmetrical cells.[38] In this study, we directly compare the evolution of the charge transfer resistance R_{CT} during the first cycle (de) sodiation and (de)lithiation of the same hard carbon active material. We show that the *in situ* obtained impedance spectra collected using μ-REs, namely a micro-tin wire reference electrode (μ-TWRE) in the case of sodium and a micro-gold wire reference electrode (μ-GWRE) in the case of lithium, can be fitted with a simple electrical equivalent circuit to extract R_{CT}, the ionic conduction resistance in the electrolyte phase of the electrode R_{pore}, and the high frequency resistance R_{HFR}. Furthermore, we evaluate the change in anode impedance R_{anode} over the course of 52 cycles and determine the rate capability for sodiation and lithiation of the HC anode, respectively.

Experimental

Electrode and electrolyte preparation.—Hard carbon (HC) electrodes consisted of hard carbon (Kuranode, BET surface area = 5.2 m^2 g^{-1}, Kuraray, Japan), sodium carboxymethyl cellulose (Na-CMC, Sunrose, NPI, Japan), and styrene-butadiene rubber (SBR, emulsion in water, solid content 40 wt%, Zeon, Japan) at a weight ratio of 97:1.5:1.5. First, Na-CMC was mixed with highly pure water (18 MΩcm, Merck Millipore, Germany) using a planetary mixer (Thinky, USA) at 2000 rpm for 30 min. HC powder was then added in three consecutive steps such as to reach a final solid content of 50 wt% with 2 min mixing in between at 2000 rpm. Finally, SBR was added to the slurry and mixed at 500 rpm for 2 min.

For the electrodes used in Li/HC half-cells, the ink was coated onto copper foil (10 ± 1 μm thickness, MTI, United States) using a 100 μm gap size four-way film applicator (Erichsen, Germany), and then dried at room temperature for 5 h, resulting in electrodes with an average loading of 3.0 ± 0.3 mg_{HC}/cm^2 (≡0.66 ± 0.07 mAh cm^{-2}, based on a nominal specific capacity of 220 mAh/g_{HC}). Electrodes were punched out at a diameter of 11 mm and dried under dynamic vacuum at 120 °C for 12 h in a glass oven (drying oven 585, Büchi, Switzerland) together with glass fiber separators (diameter = 11 mm, VWR, Germany), and then transferred into an argon-filled glovebox (MBraun, Germany) without exposure to ambient air. The thickness of the as-used uncompressed HC electrodes was 59 ± 2 μm and the porosity was ≈60%. The electrolyte consisted of 1 M lithium hexafluorophosphate ($LiPF_6$) in a mixture of ethylene carbonate (EC, ⩾99%, Sigma Aldrich) and ethyl methyl carbonate (EMC, BASF SE, Germany) at a weight ratio of 3:7 (LP57, BASF SE, Germany). Lithium disks (diameter = 11 mm, thickness ≈450 μm) were punched from commercial lithium foil (99.9%, Albermarle, USA) inside an argon-filled glovebox (O_2 and H_2O < 0.1 ppm).

The electrodes used in Na/HC half-cells were obtained using the same preparation procedure as described above, but casting the HC ink onto aluminum foil (15 ± 1 μm thickness, MTI, United States). The electrode loading was also 3.0 ± 0.3 mg_{HC}/cm^2 (≡0.84 ± 0.08 mAh cm^{-2}, based on a specific capacity of 280 mAh/g_{HC}). The thickness of the as-used uncompressed HC coating was 59 ± 2 μm and the porosity was ≈60%, i.e., identical with the HC electrodes for the Li/HC half-cells. The sodium electrolyte was prepared by mixing 50 vol% ethylene carbonate (EC, ⩾99%, Sigma Aldrich) and 50 vol% dimethyl carbonate (DMC, BASF SE, Germany) with 1 M $NaPF_6$ (99.9%, Kishida Chemicals, Japan). Sodium disks (diameter = 11 mm, thickness ≈500 μm) were punched out from a sodium foil that was prepared from sodium ingots (99.95%, Sigma Aldrich) inside an argon-filled glovebox (O_2 and H_2O < 0.1 ppm).

A conductivity meter (LF 1100+, SI Analytics, Germany, with a custom made ground-glass fitting) with a built-in temperature sensor was used to measure the conductivity of the used electrolytes at 25 °C.

Assembly and cycling of cells for impedance measurements.—For electrochemical impedance spectroscopy (EIS) measurements, three-electrode Swagelok® T-cells were assembled inside an argon-filled glovebox with a hard carbon working electrode (WE), a lithium or sodium metal counter electrode (CE), and a micro-reference electrode (μ-RE) sandwiched between glass fiber separators; the specially designed connection for μ-REs was described in detail by Solchenbach et al.[36] The cell setup is depicted in Fig. 1a. For the Li/HC half-cells, four glass fiber separators and 120 μl electrolyte were used, whereas two glass fiber separators and 60 μl electrolyte were used for the Na/HC half-cells; the lithium and sodium electrolytes were composed as specified above. Note that the number of separators employed only influences the magnitude of the high-frequency resistance (R_{HFR}) and does not impact the cell performance of the cells reported in this study. In the case of Li/HC half-cells, the μ-RE was a Kapton®-coated μ-gold-wire reference electrode (μ-GWRE) with an overall diameter of 64 μm, as described earlier.[36] In the case of Na/HC half-cells, a sodiated tinned copper wire (diameter = 50 μm, Eurowire Ltd., United Kingdom) with a polyurethane insulation (resulting in a total diameter of ≈100 μm) was used as reference electrode (μ-TWRE); preparation and setup were described in detail by Linsenmann et al.[37] The μ-GWRE cannot be employed in SIB cells because the kinetics for lithium-gold alloy formation are too sluggish to allow for an in situ

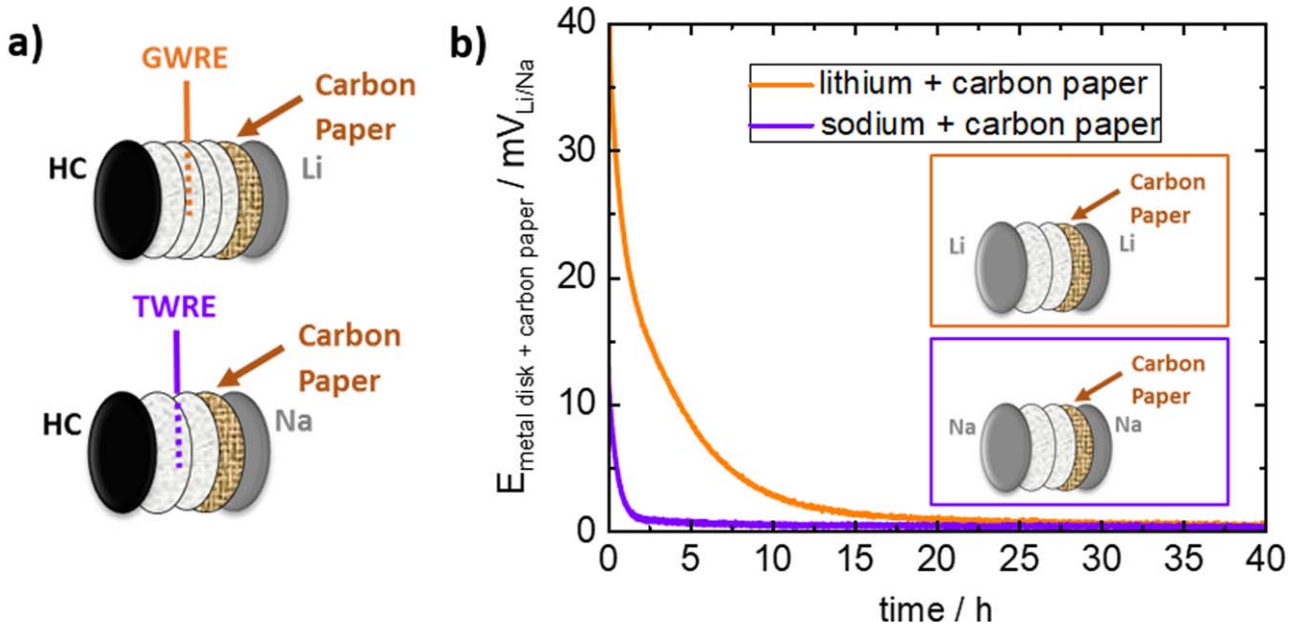

Figure 1. (a) Electrode stack configuration for the *in situ* EIS measurements of a hard carbon (HC) electrode in a Li/HC half-cell with a μ-GWRE (upper sketch) and in a Na/HC half-cell with a μ-TWRE (lower sketch), assembled in three-electrode Swagelok® T-cells.[36] The μ-RE is located centrally between four or two glass fiber separators. A porous carbon paper free-standing electrode is attached to the lithium/sodium metal CE in order to decrease the CE impedance, which is required to obtain artefact-free EIS data. (b) Open circuit voltage (OCV) of the carbon paper + lithium electrode (orange line) or of the carbon paper + sodium electrode (purple line) vs a metallic lithium or sodium CE, respectively. The cell setup is shown in the insets of Fig. 1b.

lithiation of the high-impedance gold wire (diameter only ≈50 μm) in a LIB cell, which would be necessary to obtain a stable wire potential allowing for artefact-free EIS measurements.

Unfortunately, recording EIS data with capacitively strongly imbalanced electrodes (i.e., in this case, a high capacity hard carbon WE with low impedance and a low capacity lithium or sodium metal CE with high impedance) leads to artefacts when using a high-impedance μ-RE, as demonstrated recently by Morasch et al.[39] However, attaching a free-standing high-surface area carbon electrode to a metal electrode reduces its impedance, thereby enabling artefact-free half-cell EIS data acquisition.[37,39] Thus, we sandwiched a high-surface area carbon fiber paper (H1410 type from Freudenberg, Germany), cut to 10 mm diameter (150 μm thickness and BET area of ≈14 m^2 g^{-1}), between the separator and the metal CE (s. Fig. 1a), thereby reducing the impedance of the latter by means of the gradually occurring chemical lithiation or sodiation of the carbon matrix. In order to determine the mixed potential of the resulting metal/carbon paper composite CE, Swagelok® T-cells were assembled with a metal/carbon paper composite WE, two glass fiber separators, and a metal CE (s. insets in Fig. 1b). Tracking the open circuit voltage (OCV) of these cells reveals that the mixed potential of the metal/carbon paper composite electrode approaches the reversible potential of the pure metal (within <0.5 mV) after ≈25 h in the case of lithium and after ≈5 h in case of sodium (s. Fig. 1b).

Prior to cell cycling, the μ-REs were sodiated/lithiated *in situ*. This was done by applying a lithiation current of 150 nA for 1[40] in the case of Na/HC half-cells, a constant sodiation current of 50 nA was applied to the μ-TWRE until a potential +10 mV vs the sodium CE was reached.[37] For the SOC-dependent EIS measurements, the Li/HC and the Na/HC half-cells were cycled galvanostatically. The C-rate was C/10 (based on a hard carbon capacity of 280 mAh/g_{HC} for (de)sodiation and of 220 mAh/g_{HC} for (de)lithiation) and cycling was done within a cell potential range of +1.5 V_{cell} and +10 mV_{cell} using a VMP3 potentiostat (Biologic, France). Prior to the EIS measurements, the cell was cycled to different cell potentials (750, 400, 200, 100, 50, and 10 mV_{cell} during lithiation/sodiation as well as 100, 400, and 1500 mV_{cell} during delithiation/desodiation), followed by a 30 min relaxation phase at OCV. Subsequently, potential-controlled electrochemical impedance spectroscopy (PEIS) was recorded, controlling the voltage perturbation vs the μ-GWRE or the μ-TWRE. The perturbation amplitude was 20 mV and the frequency range 30 kHz–0.1 Hz. All experiments were performed in temperature-controlled chambers (Binder, Germany) at 25 °C.

Assembly and cycling of Li/HC and Na/HC half-cells for rate testing.—Rate-tests for the HC electrodes (3.0 ± 0.3 mg_{HC}/cm^2) were performed in conventional three-electrode Swagelok® T-cells with a lithium or sodium metal CE and with a lithium or sodium metal RE, respectively, using four glass fiber separators to avoid cell short-circuiting by metallic dendrites at high cycling rates, and 120 μl of the respective lithium or sodium electrolyte specified above. Cell testing was done using a battery cycler (Series 4000, Maccor, USA). Constant-current lithiation/sodiation rates of 0.1, 0.2, 0.5, 1, 2, 3, 4, 5, and 10 C were used, with a lower cutoff voltage of +10 mV vs the lithium/sodium RE potential; the constant-current delithiation/desodiation to an upper cutoff voltage of +1.5 V vs the lithium/sodium RE potential was conducted at a rate that equaled the lithiation/sodiation rate for the two lowest rates (0.1 and 0.2 C) and was then kept constant at 0.2 C for higher lithiation/sodiation rates in order to assure complete delithiation/desodiation of the electrode at the end of each cycle. Three cycles were conducted for each lithiation/sodiation rate, and for the evaluation of the lithiation/sodiation rate performance of the HC electrodes, the third cycle at every C-rate was used. Contrary to the above described impedance experiments, the C-rate is referenced to the same nominal capacity of 280 mAh/g_{HC} for both the Li/HC and the Na/HC half-cells, so that a C-rate of 1 C corresponds to the same current density (0.88 mA cm^{-2}). This was done to allow for a fair comparison of the fast-charging capability (lithiation vs sodiation), as this is known to strongly depend on the geometric current density, as long as the electrode thickness and porosity are kept constant.[41] All experiments were performed in temperature-controlled chambers (Binder, Germany) at 25 °C.

Impedance spectra analysis.—In order to fit the Nyquist impedance spectra of the HC electrodes, an equivalent circuit model was used, which is depicted in Fig. 3c. It consists of a high-frequency resistance element (R_{HFR}) as well as of a mono-rail

transmission line that includes a pore resistance (R_{pore}), representing the ionic conduction resistance of the electrolyte within the pores of the HC electrodes, and a charge transfer resistance R_{CT} in parallel to a constant phase element Q_{CT}, similar to the circuit used by Landesfeind et al.[42] The transmission line is simplified by neglecting the electronic resistance rail through the electrode due to the high electronic conductivity of the carbon electrode; for this reason, it will be referred to furtheron as mono-rail transmission line model (mTLM). Fitting of the impedance spectra was performed with a MATLAB-based application ("EIS Breaker" written by J. Landesfeind),[42] which applies an fminsearch MATLAB function using a Nelder-Mead simplex algorithm and modulus weighing.

The pore resistance was determined by fitting the impedance spectrum obtained at the initial OCV prior to the first lithiation/sodiation of the HC electrodes (i.e., at 0% SOC) in Li/HC and Na/HC half-cells. At this condition, the charge transfer resistance of the HC electrode is orders of magnitude larger than R_{pore}, so that the impedance response closely resembles that obtained under so-called blocking conditions. Here, only points measured within a frequency range between ≈30 kHz and ≈25 Hz were taken into account in order to improve the goodness of the fit. The R_{pore} value obtained under these conditions was then fixed during the fitting of R_{CT}, Q_{CT}, and R_{HFR} for the impedance spectra measured over the course of the first (de)lithiation/(de)sodiation cycle. For these fits, frequencies between ≈30 kHz and ≈1 Hz were considered in order to exclude Warburg-like impedance responses at low frequencies and artefacts stemming from the wire-shaped RE geometry at frequencies >30 kHz.[43] The evolution of the hard carbon electrode impedance over extended cycling at C/10 was followed in terms of the high-frequency resistance (R_{HFR}) corrected low-frequency resistance (R_{LFR}), corresponding to the approximate impedance contribution a hard carbon anode would have in a battery cell (i.e., $R_{anode} = R_{LFR} - R_{HFR}$). This was done by subtracting the real part of the high-frequency resistance (R_{HFR}) taken at 30 kHz from the low-frequency resistance (R_{LFR}), which was defined as the real part of the impedance at the impedance minimum in the low-frequency region of each spectrum, i.e., the transition from the large semi-circle into the Warburg-like linear impedance increase (s. double arrows in Figs. 8a and 8b).

Results and Discussion

First-cycle (de)sodiation and (de)lithiation of a hard carbon electrode.—As already discussed in the literature, the cell impedance of half-cells with a carbon working electrode (WE) and a lithium or sodium counter electrode (CE) is often used to deduce the carbon electrode impedance behavior, neglecting the contribution of the CE,[37,44] even though the impedance of metal electrodes can be quite significant and furthermore changes substantially over the course of cycling.[39] Therefore, in order to study the hard carbon (HC) working electrode impedance *in situ* during the first formation cycle, Na/HC half-cells with 1 M $NaPF_6$ in EC/DMC (1/1 by volume) and Li/HC half-cells with 1 M $LiPF_6$ in EC/EMC (3/7 by weight) were built with micro-reference electrodes to deconvolute the WE and the CE impedance. For the Na/HC half-cells, a tin-wire (μ-TWRE) was used, while a gold-wire reference electrode (μ-GWRE) was used for the Li/HC half-cells. A carbon paper was placed between the lithium or the sodium metal CE and the adjacent separator in order to reduce the impedance of the CE which was shown to be necessary to allow for artefact-free impedance measurements.[39]

Figure 2a shows the cell voltage profiles for the first sodiation and desodiation of a HC electrode in a Na/HC half-cell as a function of the specific capacity of the HC active material obtained for a constant-current (de)sodiation rate of 0.1 C (referenced to a nominal HC (de)sodiation capacity of 280 mAh/g_{HC}) and with a lower cell cutoff potential of 10 mV_{cell}. The voltage was controlled vs the metal CE and the cycling of the cell was interrupted at cell voltages

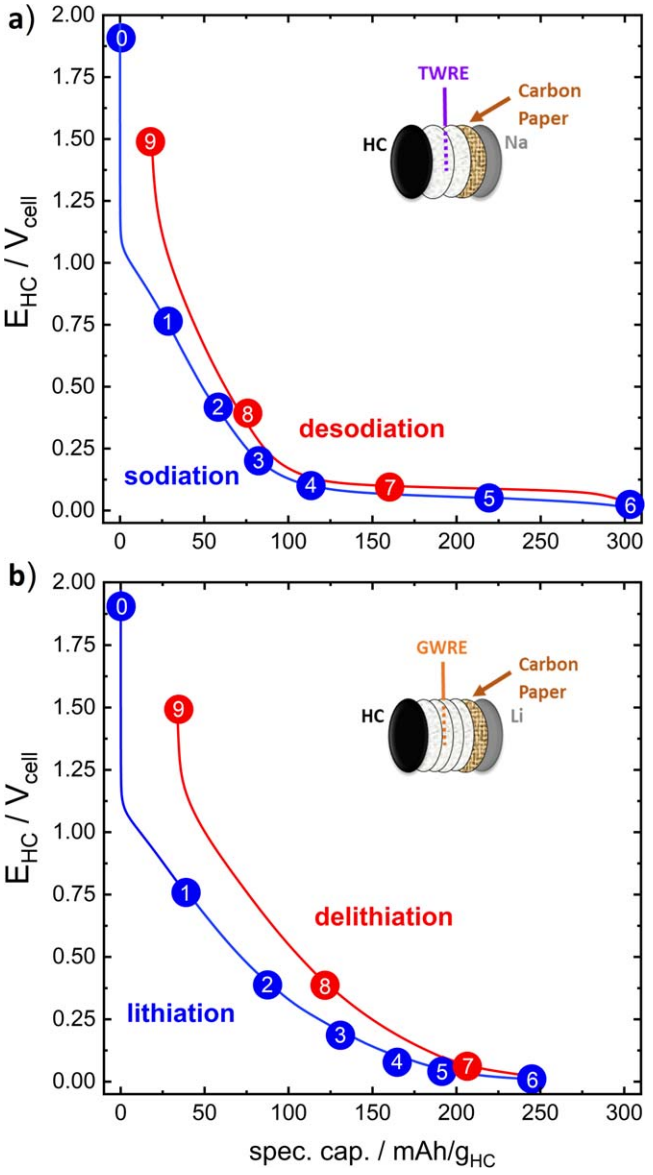

Figure 2. (a) Cell voltage (E_{cell}) of a Na/HC half-cell vs capacity during the first-cycle (de)sodiation at a rate of 0.1 C in EC/DMC (1/1 by volume) with 1 M $NaPF_6$ and with a lower cell voltage cutoff potential of 10 mV_{cell}. The experiment is conducted in a Swagelok®-type T-cell equipped with a μ-TWRE that is placed in between two glass fiber separators and a carbon paper that is placed between the sodium metal CE and the adjacent separator (see scheme in the inset). At the cell potentials labelled from 1–9 in the graph, the cycling procedure was stopped and potential-controlled electrochemical impedance (PEIS) spectra were acquired after an OCV period of 30 min; the point labeled 0 marks the initial OCV prior to the first sodiation. (b) Analogous measurements for a Li/HC half-cell with 1 M $LiPF_6$ in EC/EMC (3/7 by weight), using a μ-GWRE placed between two glass fiber separators (s. inset).

of 750, 400, 200, 100, 50, and 10 mV_{cell} during sodiation and at 100, 400, and 1500 mV_{cell} during desodiation. At each of these voltage setpoints, the cell was rested for 30 min at OCV, followed by an *in situ* potential-controlled electrochemical impedance (PEIS) measurement, whereby the voltage perturbation amplitude was controlled vs the μ-TWRE. For the Na/HC half cell (Fig. 2a), the cell voltage curves during sodiation (blue line/symbols) and during desodiation (red line/symbols) exhibit a sloping profile that transitions into a nearly flat low-voltage region at cell voltages below ≈100 mV and that extends over roughly two thirds of the total (de)

sodiation capacity. These types of voltage profiles are commonly observed for the (de)sodiation of HC electrodes. The first-cycle coulombic efficiency (CE) for the Na/HC half-cell is ≈92%.

The analogous experiment at 0.1 C was conducted for a Li/HC half-cell equipped with a μ-GWRE (Fig. 2b), whereby the C-rate in the case of lithium is referenced to the nominal HC (de)lithiation capacity of 220 mAh/g_{HC}. Currently, we do not know the reason why the (de)sodiation capacities are relatively high compared to the (de)lithiation capacities. However, since this is a commercial product (Kuraray, Japan), it might be that the carbon material was developed with a focus on its application in SIBs.

In contrast to the Na/HC half-cell, the cell voltage curve during lithiation (blue line/symbols) and delithiation (red line/symbols) does not show an extended low-voltage plateau, as it was observed for the Na/HC half-cell between ≈100–300 mAh/g_{HC}, and the sloping voltage region extends almost all the way to the lower cutoff potential of 10 mV_{cell}. The reason for this difference is currently not known and might be a specific property of this type of hard carbon. The first-cycle lithiation capacity of ≈260 mAh/g_{HC} is lower than that observed for the Na/HC half-cell (≈300 mAh/g_{HC}), as is the first-cycle coulombic efficiency of ≈84% (≈92% for the Na/HC half-cell).

Determining the pore resistance R_{pore} of hard carbon electrodes in Na/HC and Li/HC half-cells.—The ionic resistance in the electrolyte phase within the pores of the hard carbon electrodes (R_{pore}) used in the Na/HC and Li/HC half-cells was determined at OCV prior to any sodiation/lithiation of the HC electrodes, i.e., at the initial 0% SOC condition, corresponding to the points labeled with 0 in Figs. 2a and 2b. As the charge transfer resistance (R_{CT}) in this case should be very large, these conditions should closely approach the so-called blocking conditions, which allow for the most precise evaluation of R_{pore} from a fit of the hard carbon electrode impedance data (recorded by PEIS at OCV) to the equivalent circuit depicted in Fig. 3c, as was demonstrated by Landesfeind et al.[42] and Linsenmann et al.[37] The equivalent circuit consists of a mono-rail transmission line model (mTLM) composed of an ionic conduction rail represented by R_{pore}, of parallel circuit elements of a charge transfer resistance (R_{CT}) and a constant phase element (Q_{CT}) that represents the double-layer capacitance, and of an electronic conduction rail with a negligible electronic resistance corresponding to the highly conductive hard carbon particles. A single resistance element is added to the electronic rail of the mTLM to represent the high frequency resistance (R_{HFR}) that describes the sum of the external electronic contact resistance of the HC anode electrode and of the effective ionic resistance in the separator between the μ-RE and the HC electrode.

The measured impedance data of the hard carbon electrode (symbols) and the corresponding equivalent circuit fit (dashed lines) for a Na/HC and a Li/HC cell are depicted in Figs. 3a and 3b, respectively. In order to obtain a stable fit, rather than setting the electronic resistance of the electronic rail (s. Fig. 3c) to zero, it was set to a very small value of 0.001 Ωcm^2, which, as will be shown, is negligible compared to the measured R_{pore} values. For the hard carbon electrodes prepared in this study (s. Experimental section), we obtain a HC electrode pore resistance of 4.8 ± 0.5 Ωcm^2 in the Na/HC half-cells and of 4.6 ± 0.6 Ωcm^2 in the Li/HC half-cells (each based on two repeat experiments, whereby the error was obtained by including both the error of the cell-to-cell variability and the fitting error (s. Table I)), which are essentially identical within the error of measurement (the values obtained for the impedance data fit shown in Figs. 3a and 3b are given in Table I). As the HC electrodes for all the cells are nominally identical with regards to thickness and porosity, equal R_{pore} values of the HC electrode measured in Na/HC and in Li/HC half-cells would suggest equal conductivities of the two electrolytes. The latter is indeed the case, with an electrolyte conductivity of 8.2 mS cm^{-1} for the sodium electrolyte and of 8.3 mS cm^{-1} for the lithium electrolyte at 25 °C. The other fitting parameters are summarized in Table I for one data set each for both cell types (that shown in Figs. 3a and 3b), showing that the charge transfer resistance (R_{CT}) is indeed orders of magnitude larger than R_{pore}, so that blocking conditions are closely met; furthermore, the values of the constant phase element exponents α_{CT} are still reasonably close to 1, as is observed for most LIB electrodes.[42,45]

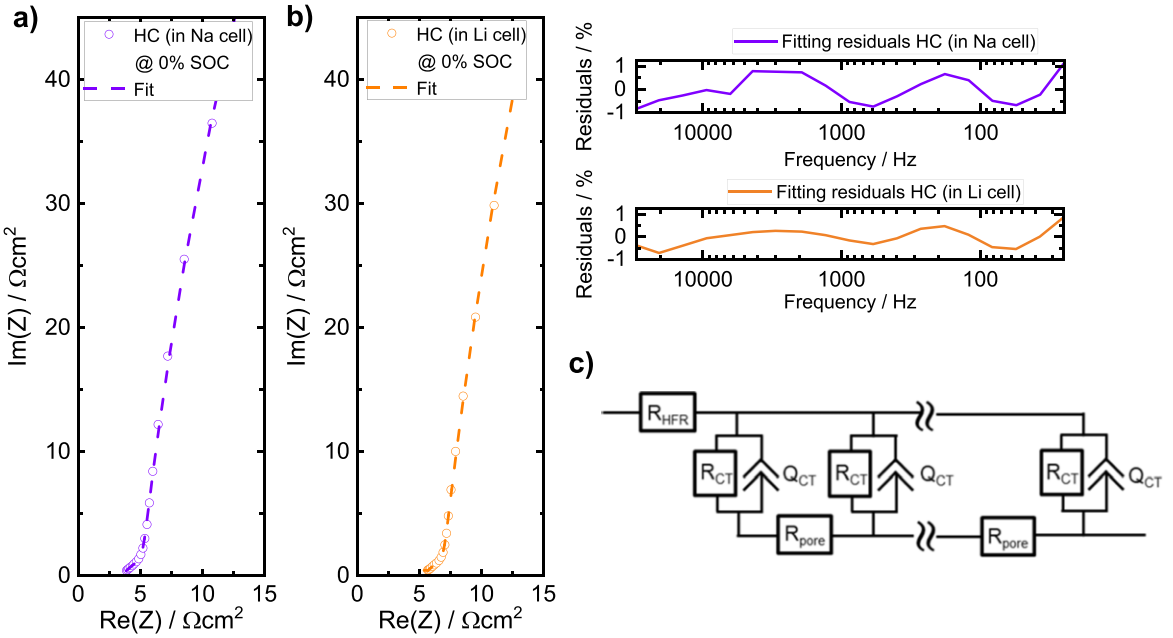

Figure 3. (a) Nyquist plot (purple symbols) of the hard carbon electrode impedance in a Na/HC half-cell with a μ-TWRE (s. inset of Fig. 2a at 0% SOC prior to the first sodiation (≡point 0 in Fig. 2a); (b) Nyquist plot (orange symbols) of the hard carbon electrode impedance in a Li/HC half-cell with a μ-GWRE (s. inset of Fig. 2b) at 0% SOC prior to the first lithiation (≡point 0 in Fig. 2b). The plotted PEIS data (symbols) were acquired at OCV and range from ≈30 kHz to ≈25 Hz. The fit to the equivalent circuit depicted in panel (c) (dashed lines) was performed in the same frequency range, whereby the residuals of the fit vs frequency are given in the panels next to the Nyquist plots. (c) The equivalent circuit used for fitting consists of a high-frequency resistance element (R_{HFR}), a mono-rail transmission line model (mTLM) with R/Q-elements (in parallel) that are composed of a charge transfer resistance (R_{CT}) and a constant phase element (Q_{CT}), and pore resistance elements (R_{pore}) that represent the ionic conduction resistance in the electrolyte phase in the pores of the electrode.

Table I. Fitting parameters and their obtained values for the hard carbon impedance spectra at 0% SOC prior to sodiation (from Fig. 3a) or lithiation (from Fig. 3b), using the equivalent circuit depicted in Fig. 3c. Here, R_{HFR} is the high-frequency resistance, R_{CT} is the charge transfer resistance of the hard carbon electrode, Q_{CT} is the constant phase element magnitude, and α_{CT} is the constant phase exponent. The errors (in %) are the fitting errors obtained by the least-squares minimization fitting method. Note that four glass fiber separators were used in the case of the Li/HC half-cell, compared to only two that were used in the Na/HC cell, explaining the nearly 2-fold higher R_{HFR} value.

	Na/HC Half-cell		Li/HC Half-cell	
Parameter	Value	Error/%	Value	Error/%
$R_{HFR}/\Omega cm^2$	3.5	4.2	5.3	9.5
$R_{pore}/\Omega cm^2$	4.5	10	4.6	13
$R_{CT}/k\Omega cm^2$	1.0	24	1.8	13
$Q_{CT}/mF{\cdot}s^{(\alpha_{CT}-1)}/cm^2$	0.18	5.2	0.22	2.6
α_{CT}/	0.92	1.0	0.92	0.6

The nearly 2-fold higher R_{HFR} value obtained for the Li/HC cell is due to the fact that four glass fiber separators were used in this case, compared to only two that were used in the Na/HC cell. Considering the almost identical conductivities of the sodium and of the lithium ion electrolyte (s. above), one would expect a close to 2-fold higher R_{HFR} for the Li/HC compared to the Na/HC half-cells. However, also earlier studies[37,40] have shown that the compression of multiple glass fiber separators can vary significantly from cell to cell due to minor differences in cell stack compression.

Note that the errors given in Table I represent the fitting error determined by the MATLAB-based fitting script (using an fminsearch MATLAB function, applying a Nelder-Mead simplex algorithm and modulus weighing), and therefore represents the error induced by fitting and not a cell-to-cell variation; both errors are included in the above given average R_{pore} values of the HC electrodes in the Na/HC and the Li/HC half-cells.

SOC-dependent evolution of the hard carbon electrode impedance in Na/HC and HC/Li half-cells.—The Nyquist spectra of the HC electrode impedances recorded at the OCV points labelled 0–9 (s. Figs. 2a and 2b) are displayed in Figs. 4 and 5. Figure 4 shows the spectra for sodiation (a) and desodiation (b) recorded for the Na/HC half-cell, and Fig. 5 for lithiation (a) and delithiation (b) in the Li/HC half-cell. For both half-cells, the HC electrode impedance decreases with increasing SOC during the first sodiation/lithiation half-cycle and then increases again during the subsequent desodiation/delithiation half-cycle. For all the Nyquist plots of the hard carbon electrodes, three distinct features can be distinguished: i) an x-axis intercept of the high-frequency part of the spectra, marking the high frequency resistance (R_{HFR}); ii) a short ≈45°-line at high frequencies that originates from the pore resistance (R_{pore})[42] already described above (s. Fig. 3); and, iii) a semi-circle at mid and low frequencies that is caused by the charge transfer process and whose diameter decreases with decreasing charge transfer resistance. As already discussed in the context of Table I, the higher R_{HFR} value in the Li/HC half-cell is due to the fact that four glass fiber separators were used in Li/HC half-cells compared to only two glass fiber separators in the Na/HC half-cells.

The data in Figs. 4 and 5 suggest that the HC electrode impedance decreases continuously with decreasing cell potential, i.e., with decreasing HC potential or with increasing hard carbon SOC (a quantitative analysis will be presented in the next section). Unfortunately, to the best of our knowledge, no data on the impedance of hard carbon anodes upon (de)sodiation exist in the literature (there are some full-cell impedance measurements,[46] but these do not allow for a deconvolution of the anode impedance).

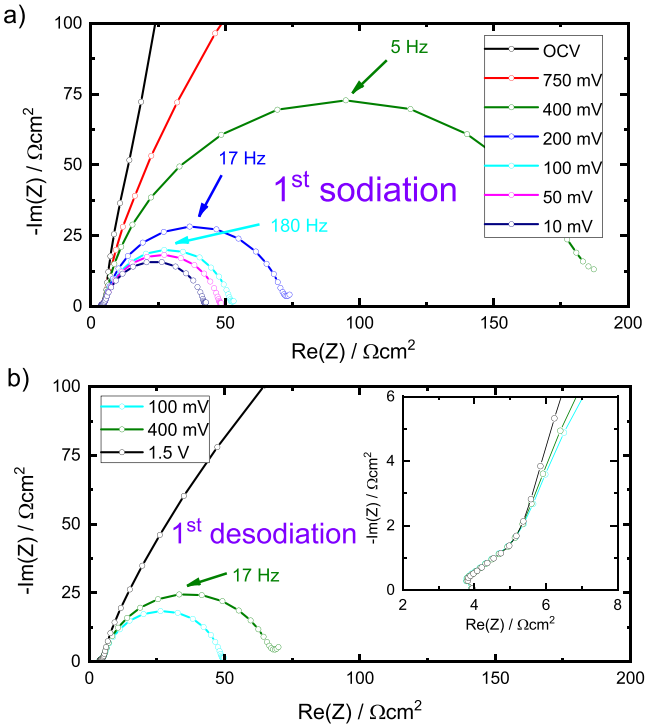

Figure 4. Nyquist plots of the HC impedance in Na/HC half-cells recorded during the first-cycle (de)sodiation at the OCV points labeled with 0–9 that are shown in Fig. 2a, using a frequency range between 30 kHz and 0.1 Hz: (a) sodiation, (b) desodiation. The inset in (b) shows the magnification of the high-frequency region, depicting the short ≈45°-line part of the spectra. The experiments were conducted at 25 °C with an EC/DEC (1/1 by volume) + 1 M $NaPF_6$ electrolyte.

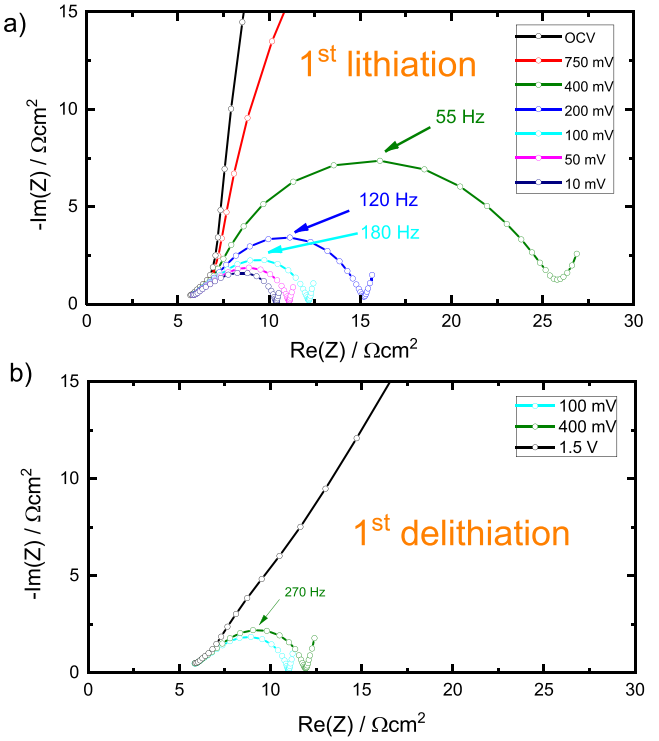

Figure 5. Nyquist plots of the HC impedance in Li/HC half-cells recorded during the first-cycle (de)lithiation at the OCV points labeled with 0–9 that are shown in Fig. 2b, using a frequency range between 30 kHz and 0.1 Hz: (a) lithiation, (b) delithiation. The experiments were conducted at 25 °C with an EC/EMC (3/7 by mass) + 1 M $LiPF_6$ electrolyte.

Even in the case of carbon based anodes in lithium-ion batteries, very few studies exist where the impedance of carbon based anodes is measured *in situ* as a function of SOC during the first lithiation. For example, Dollé et al.[47] used an LFP-based RE for *in situ* measurements of the impedance of an MCMB-type graphite anode, reporting that the graphite electrode impedance is increasing with SOC between 0.55 and 0.02 V vs Li^+/Li. On the contrary, Song et al.[44] show that the impedance of their graphite electrode measured with a Li μ-RE first decreases with increasing SOC, reaching a minimum at 0.094 V vs Li^+/Li, and then increases again. They, however, employ a mixture of ethylene carbonate (EC) and γ-butyrolactone as electrolyte in contrast to Dollé et al.,[47] who use EC and ethylmethyl carbonate (EMC). To the best of our knowledge, the only *in situ* impedance study of a HC anode as a function of SOC during the electrode formation vs lithium was published by Barsoukov et al.[48] Here, the authors analyzed impedance spectra of an MCMB, a graphite, and a hard carbon electrode recorded during the first lithiation by means of a Li μ-RE placed within a custom-made LIB cell. They find that for both graphite and hard carbon the electrode impedance first decreases upon lithiation and then continuously grows with increasing SOC. However, the reliability of the cell setup is questionable, since the MCMB shows an irreversible capacity of 47% in the first cycle and only a specific capacity of 221 mAh g^{-1}, whereas coulombic inefficiencies of <10% and capacities of ≈330 mAh g^{-1} [49] are generally reported for MCMB active materials in the literature.[50,51] In so far unpublished EIS experiments on (de)lithiation of artificial graphite electrodes performed in our group, we also find the trend that the electrode impedance decreases with increasing SOC during the first cycle (measured in half-cells using a μ-GWRE). In the following section, we will fit the hard carbon impedance spectra shown in Figs. 4 and 5 to the equivalent circuit model shown in Fig. 3c in order to extract the charge transfer resistance and to determine its first-cycle variation with SOC.

Charge transfer resistance (R_{CT}) of HC electrodes vs SOC in Na/HC and Li/HC half-cells.—By comparing the Nyquist impedance spectra in Figs. 4 and 5, it becomes clear that the magnitude of the hard carbon electrode impedance is significantly larger for the Na/HC compared to the Li/HC half-cell. In order to precisely evaluate the value of the charge transfer resistance (R_{CT}) and to compare the obtained values for (de)sodiation and (de)lithiation, the impedance spectra in Figs. 4 and 5 were fitted using the equivalent circuit shown in Fig. 3c. In this case, the pore resistance R_{pore} was fixed to the value obtained from the spectra in blocking conditions (for one set of experiments, these are shown in Table I, while their average values are 4.8 ± 0.5 Ωcm^2 and 4.6 ± 0.6 Ωcm^2 for the Na/HC and the Li/HC half–cell). Exemplary fits for the spectra recorded after the first sodiation/lithiation of a Na/HC and a Li/HC half-cell to a cell potential of 10 mV are depicted in Fig. 6a (purple symbols (data) and dashed line (fit)) and 6b (orange symbols (data) and dashed line (fit)), respectively. Especially in the case of the HC impedance in the Li/HC half-cell (s. Fig. 3b), it becomes clear that the true value of R_{CT} can only be determined by a fit of the impedance data to a transmission line model since the ≈45°-part at high frequencies, that reflects the contribution from R_{pore}, is partially overlapping with the semi-circle that originates from the charge transfer resistance.

The thus determined R_{CT} values of the HC electrode during the first cycle in both the Na/HC (purple symbols/lines in Fig. 6c) and the Li/HC (orange symbols/lines) half-cell rapidly decrease upon the initial sodiation/lithiation to ≈100 mAh/g_{HC}, after which they gradually decrease until the lower cutoff potential of 10 mV_{cell} is reached. During the subsequent desodiation/delithiation, the R_{CT} values closely follow those during sodiation/lithiation. The absolute R_{CT} values of the hard carbon electrodes at 100% SOC are ≈10-fold higher for (de)sodiation compared to (de)lithiation. For example, at 100% SOC (i.e., at a cell potential of 10 mV), R_{CT} is 37.4 ± 0.1 Ωcm^2 for the Na/HC half-cell compared to only 3.5 ± 0.03 Ωcm^2 for the Li/HC half-cell. As one would expect, the high-frequency resistance R_{HFR} (lower panel of Fig. 7c) remains constant throughout this cycle. In Table II, the fitting parameters for the fits shown in Figs. 6a and 6b are tabulated together with the fitting errors.

HC electrode impedance evolution over the course of cycling of Na/HC and Li/HC half-cells.—Figure 7a shows the specific desodiation/delithiation capacities and the coulombic efficiencies of Na/HC (purple symbols) and Li/HC half-cells (orange symbols) over extended cycling at a rate of 0.1 C between 1.5 and 0.01 V_{cell}. The slow cycling rate was chosen due to the additional resistance added to the electrode stack by the carbon paper free-standing electrode attached to the metallic CE (s. Fig. 1a), which was necessary to allow for *in situ* EIS measurements with μ-REs (i.e., the μ-TWRE and the μ-GWRE), as was discussed in the Experimental section.[39] Cycling the cells at higher C-rates would lead to increased ohmic potential drops that negatively affect the cycling capacity of the cell and would thus artificially reduce the HC electrode capacity from its intrinsic value in the absence of this added resistive element (i.e., the carbon fiber paper) in the cell. For both the Na/HC and the Li/HC half-cells, the HC electrode shows a fairly stable cycling behavior over 52 cycles. In case of the Li/HC half-cells, the formation of an effective SEI seems to be somewhat slower, since the coulombic efficiency over the first ≈4 cycles is significantly lower that that observed for Na/HC half-cells. For both cell types, the cycling stability is very similar, with desodiation/delithiation capacity losses of ≈18 mAh/g_{HC} between cycle 1 and 52, corresponding to a relative capacity loss of ≈6% for the Na/HC half-cells and of ≈8% for the Li/HC half-cells.

Figures 8a and 8b show the evolution of HC impedance spectra over extended cycling (cycle 1, 2, 12, and 52), measured in Na/HC and Li/HC half-cells at OCV after sodiation/lithiation to a cell voltage of 100 mV_{cell}, followed by a relaxation phase of 30 min (for the first cycle, this would correspond to point 4 in Figs. 2a and 2b). In the case of the Li/HC half-cell (Fig. 8b), the shape of the hard carbon impedance spectra, consisting of a pore resistance R_{pore} indicated by a ≈45°-line which transitions into a large semi-circle originating from a charge transfer resistance R_{CT}, does not vary over cycling; however, the diameter of the semi-circle, and therefore the magnitude of R_{CT} is changing. In contrast, in the case of the Na/HC half-cell, the large semi-circle starts to split into a smaller one at higher frequencies and a larger one at lower frequencies after ≈30 cycles (shown for cycle 52 in Fig. 8a). Unfortunately, we currently do not know the origin of this additional impedance feature; as it is reproducible and evolves only upon extended (de)sodiation, we believe that it reflects a hitherto unknown ageing mechanism of HC anodes upon extended sodiation/desodiation cycles. Because of the appearance of this second semi-circle, the HC spectra in the Na/HC half-cell cannot be fitted by the equivalent circuit depicted in Fig. 3c, which is the reason why the evolution of R_{CT} could not be evaluated over long-term cycling. Instead, we evaluated the approximate impedance contribution of a HC anode in a battery cell, defined as $R_{anode} = R_{LFR} - R_{HFR}$ (s. purple/orange double arrow in Figs. 8a/8b), whereby R_{HFR} is approximated by the real part of the impedance at 30 kHz and R_{LFR} is approximated by the real part of the impedance at the transition from the large low-frequency semi-circle to the Warburg-like linear impedance increase. Thereby, the impedance of the separator (closely corresponding to the impedance at 30 kHz) and contributions from the Warburg-like impedance response at rather low frequencies are excluded, so that the remaining impedance should be a reasonable approximation of the impedance contribution of a hard carbon anode in a battery cell. The thus determined R_{anode} values of the HC electrode are plotted as a function of cycle number in Fig. 8c for the Na/HC half-cells (purple symbols) and the Li/HC half-cells (orange symbols). For both the Na/HC and the Li/HC half-cells, R_{anode} decreases by ≈25% after the first cycle, which could be explained by an increase of the specific surface area of the HC active material during the first cycles via opening of initially inaccessible pores in the material, which in

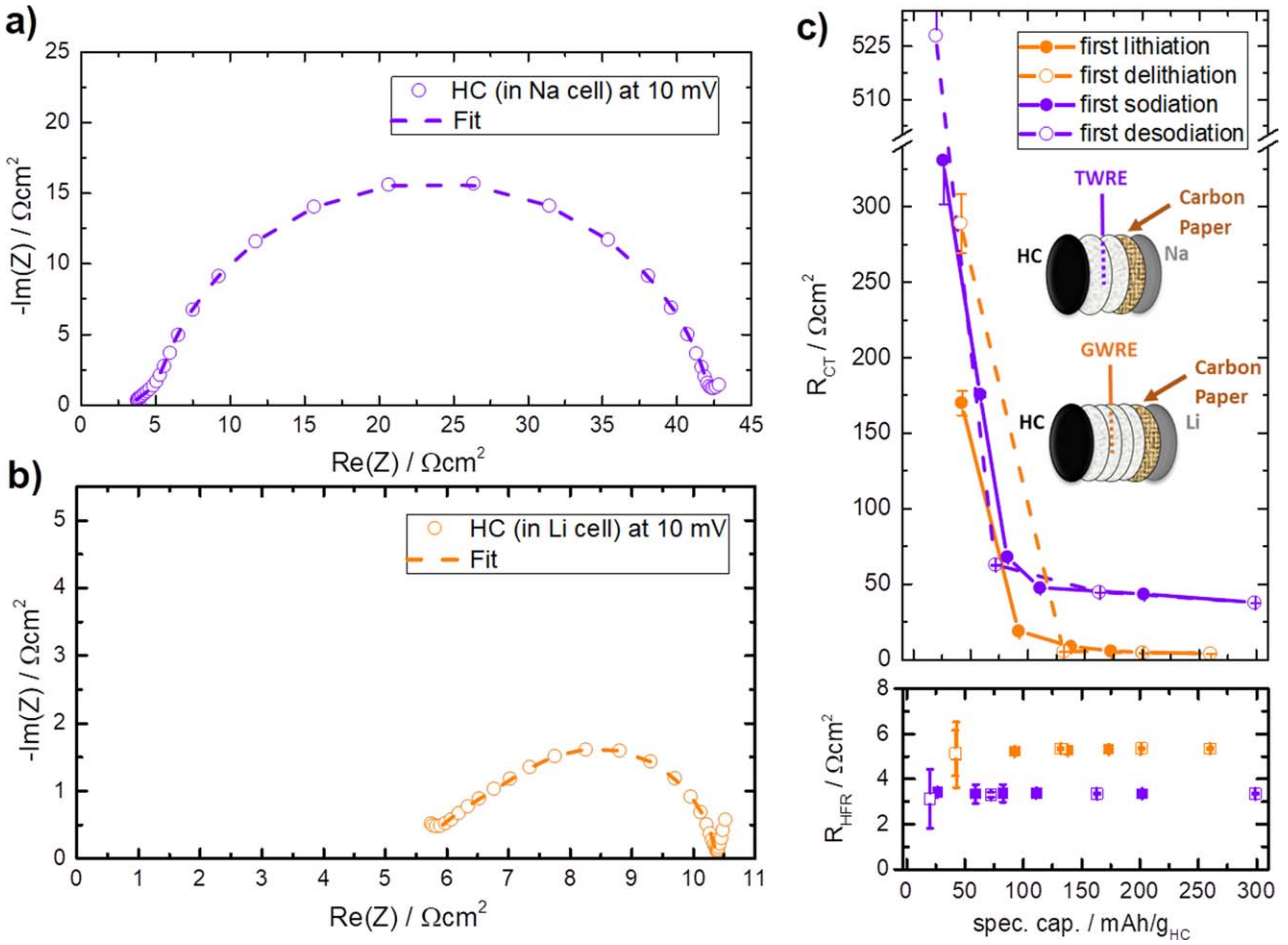

Figure 6. Analysis of the hard carbon electrode impedance data for the first-cycle sodiation/lithiation at 0.1 C and 25 °C (the corresponding voltage profiles and impedance spectra are shown in Fig. 2 as well as in Figs. 4 and 5). The left panels show a fit (dashed lines) of the HC electrode impedance data (symbols) acquired at 10 mV_{cell} after a 30 min OCV phase (≡ points 6 in Fig. 2), using the equivalent circuit model depicted in Fig. 3c: (a) for the Na/HC half-cell using the μ-TWRE; (b) for the Li/HC half-cell using the μ-GWRE. The thus obtained fitting parameters are given in Table II. (c) Area normalized charge transfer resistance (R_{CT}) and high-frequency resistance (R_{HFR}) vs SOC in the first cycle, determined by fitting the HC impedance spectra recorded for the Na/HC half-cell (purple symbols/lines; spectra shown in Fig. 4) and for the Li/HC half-cell (orange symbols/lines; spectra shown in Fig. 5) to the equivalent circuit model shown in Fig. 3c; the R_{pore} values were set to those determined in blocking conditions (s. Table I). The error bars represent the fitting errors obtained by the least square fitting method.

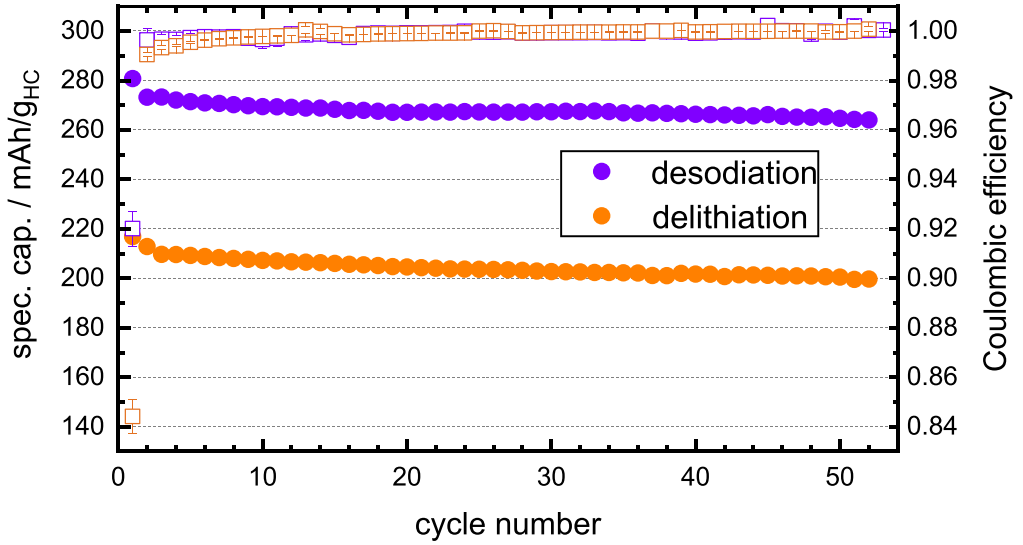

Figure 7. Specific desodiation (purple symbols) and delithiation (orange symbols) capacities as well as coulombic efficiencies vs cycle number of Na/HC and Li/HC half-cells, respectively, cycled at 0.1 C between 1.5 and 0.01 V_{cell}.

Table II. Fitting parameters and their obtained values for the hard carbon impedance spectra shown in Figs. 6a and 6b, measured after the first sodiation of Na/HC and the first lithiation of Li/HC half-cells to a cell potential of 10 mV_{cell} (≡ 100% SOC), using the equivalent circuit depicted in Fig. 3c. Here, R_{HFR} is the high-frequency resistance, R_{CT} is the charge transfer resistance of the hard carbon electrode, Q_{CT} is the constant phase magnitude, and α_{CT} is the constant phase exponent. R_{pore} was fixed to the values obtained in blocking conditions (s. Table I), based on the impedance spectra shown in Figs. 3a and 3b. The error is based on the fitting errors obtained by the least square fitting method.

	HC/Na Half-cell		HC/Li Half-cell	
Parameter	Value	Error/%	Value	Error/%
$R_{pore}/\Omega cm^2$ (from Table I)	4.5	10	4.6	13
$R_{HFR}/\Omega cm^2$	3.4	1.0	5.4	0.5
$R_{CT}/\Omega cm^2$	37.4	0.2	3.5	0.9
$Q_{CT}/mF{\cdot}s^{(\alpha_{CT}-1)}/cm^2$	0.25	1.1	0.3	5.5
α_{CT}/	0.89	0.2	0.89	1.0

turn would facilitate charge transfer into the active material particles.[37] As was already noted in the discussion of the data in Fig. 6c, the HC impedance, dominated by a charge transfer resistance, is significantly higher for the Na/HC compared to the Li/HC half-cells. Over the course of cycling, the hard carbon anode impedance values for both cell types gradually increase, and after 52 cycles the hard carbon impedance R_{anode} is still ≈5-fold higher for the Na/HC than for the Li/HC half-cells.

Sodiation/lithiation rate capability of HC electrodes in Na/HC and Li/HC half-cells.—The higher hard carbon charge transfer resistances in Na/HC vs Li/HC half-cells (s. Figs. 6 and 7) are expected to result in higher kinetic overpotentials of the hard carbon electrode in Na/HC half-cells. Since the kinetic overpotential lowers the hard carbon electrode potential during sodiation (or lithiation), the hard carbon electrode potential will decrease below 0 V vs Na^+/Na (or Li^+/Li) at lower and lower SOC values, as the C-rate and thus the current density is increased. Therefore, the sodiation (or lithiation) capacity at which the hard carbon electrode potential decreases below 0 V vs Na^+/Na (or Li^+/Li) marks the maximum accessible capacity that can be reached under constant-current charging conditions without risking sodium (or lithium) plating, which is detrimental to cycle-life and safety. The relationship between the thus defined maximum accessible capacity of a hard carbon electrode vs C-rate, however, cannot be determined by simply monitoring the cell voltage, since the overpotentials of a sodium or lithium metal counter electrode can be very high at high current densities.[39] Therefore, the hard carbon electrode cutoff potential during the following rate tests in Na/HC and Li/HC half-cells was controlled to +10 mV vs a metallic sodium or lithium RE, respectively, rather than vs the cell voltage, analogous to the procedure described by Landesfeind et al.[52] Since kinetic as well as transport-related overpotentials in general increase with current density, the C-rates in these experiments were referenced to the same nominal capacity of 280 mAh/g_{HC}, allowing for a direct comparison of the rate capability for sodiation and lithiation in Na/HC and Li/HC half-cells, respectively. In this case, a rate of 1 C corresponds to a current density of 0.88 mA cm^{-2}. In order to avoid cell short-circuiting by sodium/lithium dendrites originating from the sodium/lithium metal counter electrode (expected to occur for current densities larger than ≈1 mA cm^{-2},[53] i.e., at rates larger than ≈1.15 C in our case), the distance between WE and CE was increased to ≈800 μm by using four glass fiber separators (compared to the more commonly employed two glass fiber separators).

Figure 9a shows the C-rate dependence of the accessible specific capacity for sodiation (purple symbols/line) and lithiation (orange symbols/lines) of Na/HC and Li/HC half-cells, respectively, using a lower cutoff potential of +10 mV vs Li^+/Li and Na^+/Na, respectively. For the Na/HC half-cell, the capacity drops rapidly beyond a rate of 1 C, which can be explained by the high charge transfer resistance R_{CT} of the HC electrode for sodiation (≈50 Ωcm^2, s. Fig. 6c). For example, at a current density of 1.76 mA cm^{-2} (≡2 C), this equates to a kinetic overpotential of ≈90 mV. The consequence of this can be estimated by considering the voltage vs capacity curve shown in Fig. 2a that was recorded at only 0.1 C corresponding to only ≈0.09 mA cm^{-2}, in which case the overpotentials of both the Na and the HC electrode can be considered negligible, so that the cell voltage should be close to the HC electrode potential vs the Na^+/Na reference potential. Shifting this voltage profile negative by ≈90 mV, *viz.*, by the projected kinetic overpotential at 2 C, means that point 4 in Fig. 2a (at ≈115 mAh/g_{HC}) that marks a cell voltage of 100 mV (corresponding to also ≈100 mV vs Na^+/Na) would be expected to drop to ≈10 mV vs Na^+/Na, corresponding to the cutoff potential of our Na/HC half-cell in the rate test shown in Fig. 8a, where a sodiation capacity of ≈150 mAh/g_{HC} was obtained at 2 C. Considering this rough estimate, this is reasonably close to the projected ≈115 mAh/g_{HC} based on the data at 0.1 C, suggesting that the high R_{CT} of the hard carbon electrode in the Na/HC half-cell is the origin for the rapid drop in capacity between 1 and 2 C. This suggests that based on kinetic overpotential constraints, the sodiation rate capability of the here used hard carbon material would be limited to somewhere between ≈1–2 C, even in the absence of mass-transport limitations (these would become more important for higher, more application-relevant HC areal capacities, resulting in thicker electrodes and higher current densities for a given C-rate[41]).

On the other hand, for the Li/HC half-cell, the lithiation capacity decreases more gradually and does not show such a rapid capacity drop, consistent with its ≈10-fold lower charge transfer resistance (s. Fig. 6c). This becomes more apparent when normalizing the capacity to the capacity at 0.1 C, as shown in Fig. 9b.

Conclusions

In the present work, we utilized *in situ* electrochemical impedance spectroscopy (EIS) to investigate the impedance change of a commercial hard carbon (HC) active material in Na/HC and Li/HC half-cells. For the Na/HC half-cells, a sodiated tin-wire reference electrode (μ-TWRE) was employed, whereas in the case of the Li/HC half-cells, a lithiated gold wire reference electrode (μ-GWRE) was used to acquire electrode-resolved impedance data. Both in the case of Na/HC and Li/HC, we determined the pore resistance (R_{pore}) of the anode prior to the first sodiation/lithiation, where so-called blocking electrode conditions are observed. Subsequently, we monitored the charge transfer resistance R_{CT} as a function of the state-of-charge (SOC) and potential during the first cycle (de)sodiation and (de)lithiation by fitting the impedance spectra with a simple equivalent circuit consisting of a mono-rail transmission line model (mTML) and a high-frequency resistance (R_{HFR}). R_{CT} clearly dominates the total electrode impedance for both (de)sodiated and (de)lithiated HC and it reversibly decreases/increases with increasing/decreasing SOC during the first cycle. At the end of the first sodiation/lithiation half-cycle, i.e., at 100% SOC, R_{CT} was found to be a factor of ≈10 larger for sodiation compared to lithiation of the same hard carbon active material. Note that other types of electrolytes, especially when using additives, might affect

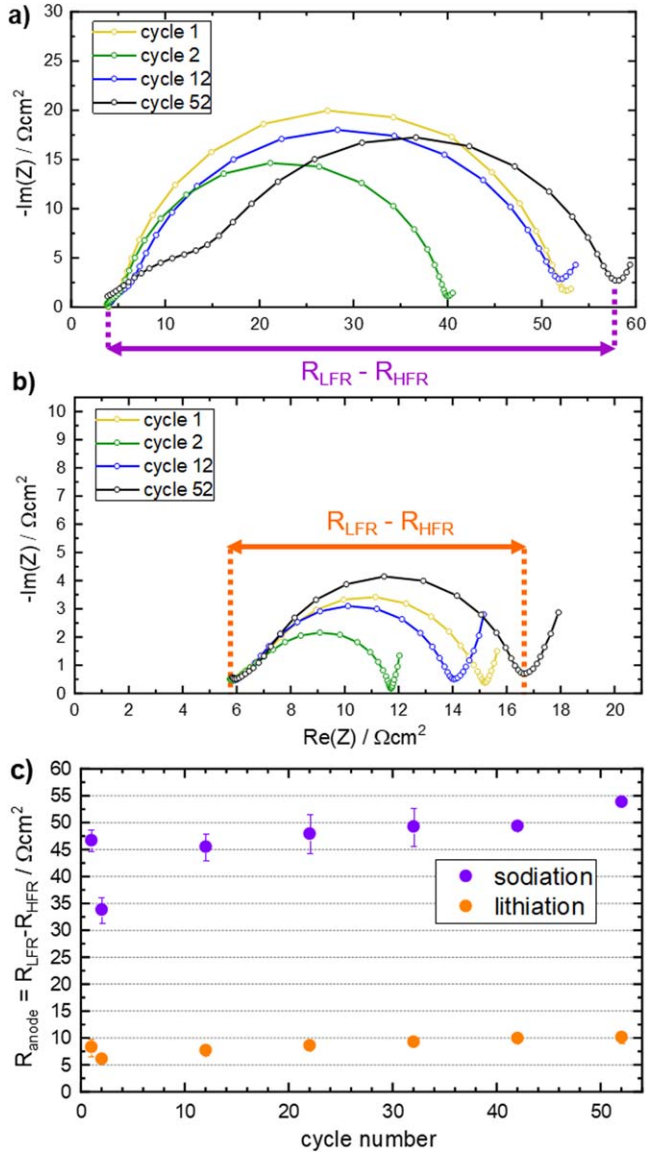

Figure 8. (a) Nyquist plots of the HC impedance in a Na/HC half-cell recorded during sodiation (measured at OCV after cycling to a cell voltage of 100 mV_{cell}) for cycle 1 (yellow), 2 (green), 12 (blue), and 52 (black) within a frequency range between 30 kHz and 0.1 Hz, (b) Nyquist plots of the HC impedance in a Li/HC half-cell using the same cycling and EIS measurement procedure, (c) hard carbon electrode impedance R_{anode} evolution during cycling at a rate of 0.1 C between 1.5 and 0.01 V_{cell} (s. Fig. 7) for sodiation (purple) and lithiation (orange). Here, we defined the approximate impedance contribution of a HC anode in a battery cell as $R_{anode} = R_{LFR} - R_{HFR}$ (s. purple/orange double arrows in Figs. 8a/8b), where R_{LFR} is taken as the real part of the impedance at the impedance minimum in the low-frequency region, i.e., the transition from the large semi-circle to the Warburg-like linear impedance increase, and R_{HFR} is taken as the real part of the impedance value measured at 30 kHz. The error bars represent the deviation from the average impedance of two nominally identical cells.

the observed electrode resistances. However, the electrolytes used in this study, i.e., EC/DMC + 1 M $NaPF_6$ and EC/EMC + 1 M $LiPF_6$, were chosen to be very similar in order to assure reasonable comparability between the Na/HC and Li/HC cells.

Furthermore, we traced the impedance evolution of the HC electrode ($R_{anode} = R_{LFR} - R_{HFR}$), defined as the difference of a low-frequency resistance R_{LFR} (real part of the impedance in the low-frequency region where the transition from the large semi-circle into the Warburg-like linear impedance occurs) and a high-frequency resistance R_{HFR} (real part of the impedance at 30 kHz), over

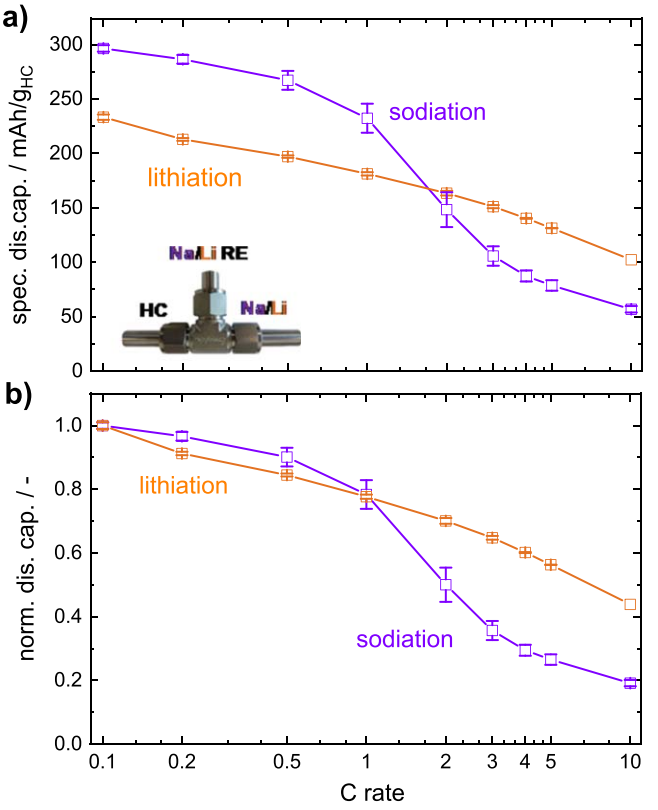

Figure 9. (a) Peukert plot for the sodiation (purple) and lithiation (orange) capacity vs C-rate of hard carbon electrodes in Na/HC and Li/HC half-cells, whereby the capacity values are determined once the HC electrode potential reaches 10 mV vs a sodium and a lithium reference electrode, respectively. The sodiation/lithiation rates were 0.1, 0.2, 0.5, 1, 2, 3, 4, 5 and 10 C for three cylces each, plotting the capacity for the third cycle. The desodiation/delithiation rate was fixed to 0.2 C, except for the sodiation/lithiation rate of 0.1 C, where it was fixed to 0.1 C. For both sodiation and lithiation the C-rate is referenced to 280 mAh/g_{HC}, such that a C-rate of 1 C corresponds to the same current density for sodiation and lithiation (0.88 mA cm^{-2}). (b) Data from (a) normalized by the specific sodiation/lithiation capacity obtained at 0.1 C.

52 cycles via EIS measurements at a constant cell potential of ≈100 mV_{cell}. For both the Li/HC and the Na/HC half-cells, R_{anode} first decreases after the first cycle and then gradually increases during long-term cycling (52 cycles) and at this potential (corresponding to mid-SOC values) is on average a factor of ≈5 higher for the Na/HC cells compared to the Li/HC cell.

The larger R_{anode} values of the latter are reflected in the lower rate performance of the HC electrode towards sodiation when compared to lithiation, which was demonstrated in three-electrode rate tests. For C-rates of ≈2 C and beyond, the specific capacity obtained for sodiation drops below the capacity accessible for lithiation of the hard carbon anode, which can be explained by the higher HC anode resistance. Since currently hard carbons are the most promising anode material for sodium-ion batteries (SIBs), their relatively high electrode impedance upon (de)sodiation could be another challenge for a future commercialization of SIBs apart from the lower energy density and/or reduced cycling performance with respect to state-of-the-art lithium-ion batteries.

Acknowledgments

We gratefully acknowledge funding by the BMBF (Federal Ministry of Education and Research, Germany) for its financial support under the auspices of the ExZellTUM II project, grant number 03XP0081 and ExZellTUM III project, grant number 03XP0255. The authors would like to thank Tim-Patrick Fellinger

for providing the hard carbon samples from Kuraray as well as Bharat Suthar for his advice on EIS fitting.

ORCID

Fabian Linsenmann https://orcid.org/0000-0001-8788-2584
Hubert A. Gasteiger https://orcid.org/0000-0001-8199-8703

References

1. J. R. Dahn, *Phys. Rev. B*, **44** (1991).
2. J. Asenbauer, T. Eisenmann, M. Kuenzel, A. Kazzazi, Z. Chen, and D. Bresser, *Sustain. Energy Fuels*, 1 (2020).
3. G. E. Blomgren, *J. Electrochem. Soc.*, **164**, A5019 (2017).
4. Y. Nishi, *J. Power Sources*, **100**, 101 (2001).
5. Y. Nishi, *Interface Mag.*, **25**, 71 (2016).
6. P. Kurzweil and J. Garche, *Overview of Batteries for Future Automobiles* (Elsevier B.V) (2017).
7. R. E. Franklin, *Proc. R. Soc. A Math. Phys. Eng. Sci.*, **209**, 196 (1951).
8. M. Winter, G. H. Wrodnigg, J. O. Besenhard, W. Biberacher, and P. Novák, *J. Electrochem. Soc.*, **147**, 2427 (2002).
9. M. Winter and J. O. Besenhard, *Handb. Batter. Mater.*, 383 (2007).
10. V. Agubra and J. Fergus, *Materials (Basel).*, **6**, 1310 (2013).
11. A. J. Smith, J. C. Burns, X. Zhao, D. Xiong, and J. R. Dahn, *J. Electrochem. Soc.*, **158**, A447 (2011).
12. Encyclopedia of Electrochemical Power Sources, "Secondary batteries - Lithium rechargeable systems- Lithium ion." *Negative Electrodes: Graphite* (2009).
13. T. Zheng, Y. Liu, E. W. Fuller, S. Tseng, U. von Sacken, and J. R. Dahn, *J. Electrochem. Soc.*, **142** (1995).
14. H. Buqa, D. Goers, M. Holzapfel, M. E. Spahr, and P. Novák, *J. Electrochem. Soc.*, **152**, A474 (2005).
15. H. Buqa, M. Holzapfel, F. Krumeich, C. Veit, and P. Novák, *J. Power Sources*, **161**, 617 (2006).
16. R. Fong, U. von Sacken, and J. R. Dahn, *J. Electrochem. Soc.*, **137**, 2009 (1990).
17. D. A. Stevens and J. R. Dahn, *J. Electrochem. Soc.*, **148**, A803 (2001).
18. M. Endo, C. Kim, K. Nishimura, T. Fujino, and K. Miyashita, *Carbon N. Y.*, **38**, 183 (2000).
19. K. Tatsumi, T. Kawamura, S. Higuchi, T. Hosotubo, H. Nakajima, and Y. Sawada, *J. Power Sources*, **68**, 263 (1997).
20. H. Azuma, H. Imoto, S. N. I. Yamada, and K. Sekai, *J. Power Sources*, **81–82**, 1 (1999).
21. S. Flandrois and B. Simon, *Carbon N. Y.*, **37**, 165 (1999).
22. Y. Liu, J. S. Xue, T. Zhen, and J. R. Dahn, *Carbon N. Y.*, **34**, 193 (1996).
23. K. Sato, M. Noguchi, A. Demachi, N. Oki, and M. Endo, *Science*, **264**, 556 (1994).
24. P. Novak, D. Goers, and M. E. Spahr, *Carbons for Electrochemical Energy Storage and Conversion Systems*, ed. F. Beguin and E. Frackowiak (Crc Press) Chap. 7, p. 263 (2009).
25. B. Jache and P. Adelhelm, *Angew. Chemie - Int. Ed.*, **53**, 10169 (2014).
26. K. Nobuhara, H. Nakayama, M. Nose, S. Nakanishi, and H. Iba, *J. Power Sources*, **243**, 585 (2013).
27. P. Ge and M. Fouletier, *Solid State Ionics*, **28–30**, 1172 (1988).
28. M. M. Doeff, Y. Ma, S. J. Visco, and L. C. De Jonghe, *J. Electrochem. Soc.*, **140**, 169 (1993).
29. D. Saurel, B. Orayech, B. Xiao, D. Carriazo, X. Li, and T. Rojo, *Adv. Energy Mater.*, **8**, 1 (2018).
30. D. A. Stevens and J. R. Dahn, *J. Electrochem. Soc.*, **147**, 1271 (2002).
31. S. Komaba, W. Murata, T. Ishikawa, N. Yabuuchi, T. Ozeki, T. Nakayama, A. Ogata, K. Gotoh, and K. Fujiwara, *Adv. Funct. Mater.*, **21**, 3859 (2011).
32. K. Gotoh, M. Maeda, A. Nagai, A. Goto, M. Tansho, K. Hashi, T. Shimizu, and H. Ishida, *J. Power Sources*, **162**, 1322 (2006).
33. M. Letellier, F. Chevallier, F. Béguin, E. Frackowiak, and J. N. Rouzaud, *J. Phys. Chem. Solids*, **65**, 245 (2004).
34. J. M. Stratford, P. K. Allan, O. Pecher, P. A. Chater, and C. P. Grey, *Chem. Commun.*, **52**, 12430 (2016).
35. R. Morita et al., *J. Mater. Chem. A*, **4**, 13183 (2016).
36. S. Solchenbach, D. Pritzl, E. Jia, Y. Kong, J. Landesfeind, and H. A. Gasteiger, *J. Electrochem. Soc.*, **163**, 2265 (2016).
37. F. Linsenmann, D. Pritzl, and H. A. Gasteiger, *J. Electrochem. Soc.*, **166**, A3668 (2019).
38. R. Petibon, C. P. Aiken, N. N. Sinha, J. C. Burns, H. Ye, C. M. VanElzen, G. Jain, S. Trussler, and J. R. Dahn, *J. Electrochem. Soc.*, **160**, A117 (2013).
39. R. Morasch, B. Suthar, and H. A. Gasteiger, *J. Electrochem. Soc.*, **167**, 100540 (2020).
40. S. Solchenbach, D. Pritzl, E. J. Y. Kong, J. Landesfeind, and H. A. Gasteiger, *J. Electrochem. Soc.*, **163**, A2265 (2016).
41. K. G. Gallagher et al., *J. Electrochem. Soc.*, **163**, A138 (2016).
42. J. Landesfeind, D. Pritzl, and H. A. Gasteiger, *J. Electrochem. Soc.*, **164**, A1773 (2017).
43. S. Solchenbach, *PhD Thesis*, Technical University of Munich (2018).
44. J. Y. Song, H. H. Lee, Y. Y. Wang, and C. C. Wan, *J. Power Sources*, **111**, 255 (2002).
45. S. Oswald, D. Pritzl, M. Wetjen, and H. A. Gasteiger, *J. Electrochem. Soc.*, **167**, 100511 (2020).
46. C. Bommier, W. Luo, W. Y. Gao, A. Greaney, S. Ma, and X. Ji, *Carbon N. Y.*, **76**, 165 (2014).
47. M. Dollé, F. Orsini, A. S. Gozdz, and J.-M. Tarascon, *J. Electrochem. Soc.*, **148**, A851 (2002).
48. E. Barsoukov, J. H. Kim, C. O. Yoon, and H. Lee, *J. Electrochem. Soc.*, **145**, 2711 (2006).
49. J. Yao, G. X. Wang, J. H. Ahn, H. K. Liu, and S. X. Dou, *J. Power Sources*, **114**, 292 (2003).
50. N. Paul, J. Wandt, S. Seidlmayer, S. Schebesta, M. J. Mühlbauer, O. Dolotko, H. A. Gasteiger, and R. Gilles, *J. Power Sources*, **345**, 85 (2017).
51. F. M. Courtel, S. Niketic, D. Duguay, Y. Abu-Lebdeh, and I. J. Davidson, *J. Power Sources*, **196**, 2128 (2011).
52. J. Landesfeind, A. Eldiven, and H. A. Gasteiger, *J. Electrochem. Soc.*, **165**, A1122 (2018).
53. D. Aurbach, E. Zinigrad, H. Teller, and P. Dan, *J. Electrochem. Soc.*, **147**, 1274 (2002).

3.2 *Operando* NDP as Analytical Technique for Lithium-Ion Battery Research

3.2.1 A Liquid Electrolyte-Based Lithium-Ion Battery Cell Design for *Operando* NDP

This section presents the article "*A Liquid Electrolyte-Based Lithium-Ion Battery Cell Design for Operando Neutron Depth Profiling"* which was submitted to the peer-reviewed Journal of the Electrochemical Society in February 2020 and published in May 2020. The article is published open access and distributed under the terms of the Creative Commons Attribution 4.0 License. The permanent web link is available under: https://iopscience.iop.org/article/10.1149/1945-7111/ab9b20/meta. The article was presented by Fabian Linsenmann as Paper 268 at the Atlanta, Georgia, Meeting of the Electrochemical Society, October 13-October 17, 2019.

In the following study, a novel cell design for *operando* Neutron Depth Profiling (NDP) of lithium-ion batteries with liquid electrolyte is presented. NDP is a non-destructive nuclear analytical technique which is suitable to measure lithium concentrations as a function of depth. The method takes advantage of the $^{6}Li(n,^{3}H)^{4}He$ reaction, *i.e.*, the emission of an *alpha* ($^{4}He^{2+}$) and a *triton* particle ($^{3}H^{+}$) with very defined energies after neutron capture of a ^{6}Li nucleus (≈7.6 at% of the natural abundance of lithium). The produced charged particles lose energy on their way through the sample matrix, and their residual energy can be correlated to depth and amount of lithium, by which a lithium depth profile of the sample can be obtained.

The here developed novel cell design uses a thin 7.5 µm thick exit window (Kapton® foil) for charged particles, the inner surface of which is sputter-coated with a 100 nm thick copper film that serves as current collector. This allows to minimize the energy loss through the window and the current collector, thereby maximizing the viewing depth into the cell. Furthermore, a homogeneous compression of the window area is assured by utilizing a coin cell containing a dense pattern of 500 µm diameter holes that were laser-cut into the stainless steel cell cap of a conventional coin cell. It is shown that the graphite electrode active

material underneath these holes is completely lithiated during the charging process, whereas this was not the case for a single 4 mm diameter hole, the latter represents the *operando* NDP cell design that had been described in the literature. Owing to the homogeneous compression, afforded by the pattern of only 500 µm diameter holes, this newly designed *operando* NDP cell performs similar to a standard laboratory cell, contrary to what is observed for large single-hole designs. Therefore, the electrochemical processes probed *via* NDP with the new cell design are indeed representative for the entire cell, not only for the processes probed underneath the window regions, and thus properly represent the cell electrochemistry. In contrast to *ex situ* NDP setups, the measurement chamber is not under high vacuum but filled with He gas at a pressure of ≈400 mbar to avoid bulging of the window that would occur if the NDP sample chamber pressure goes below the vapor pressure of the electrolyte.

As a first application, we recorded NDP data during formation of a graphite electrode, visualizing the lithium concentration across the electrode with a time resolution of ≈1 h. Together with reference measurements of the pristine cell before starting cell cycling, it was possible to distinguish between lithium in the electrolyte, reversibly intercalated lithium in graphite, and irreversibly bound lithium in the solid electrolyte interphase (SEI). A pronounced lithium peak was detected at the interface of the 100 nm thick copper current collector coated on the Kapton® window and the graphite electrode, which could be confirmed by means of X-ray photoelectron spectroscopy (XPS) to be due to the formation of a Cu-Li alloy during cycling. The amount of alloyed lithium corresponds to only ≈0.1 % of the reversibly intercalated lithium, which makes it virtually non-detectable by electrochemical charge/discharge measurements. Furthermore, it was possible to quantify the lithium concentrations in the graphite electrode, and thus to determine the absolute amount of lithium bound in the SEI. The amount of reversibly intercalated lithium detected by NDP, $(3.78 \pm 0.51) \times 10^{21}$ Li atoms/$g_{electrode}$, matched very well with the amount estimated from the reversible capacity, $(3.86 \pm 0.29) \times 10^{21}$ Li atoms/$g_{electrode}$. Interestingly, the amount of lithium in the SEI was found to be significantly smaller than predicted from the irreversible capacity measured electrochemically, when assuming an electrolyte decomposition mechanisms with an average ratio of 1 lithium/electron (Li/e^-). Here, a ratio of

(0.61 ± 0.08) Li/e^- was measured using NDP. We believe that the most likely reason for this is that soluble components of the SEI dissolve in the electrolyte during formation, and are thus not detectable in the *operando* NDP experiment.

Author contributions

The cell design was developed by F.L., M.T., R.G., and H.A.G. All electrochemical tests, such as NDP cell evaluation and benchmarking were performed by F.L. and P.R. NDP experiments were conducted by M.T., L.W., F.L., and P.R. XPS analysis was performed by F.L. Data treatment was done by M.T., F.L., and P.R. The manuscript was written by F.L., M.T., and H.A.G. All authors discussed the data and commented on the results.

Journal of The Electrochemical Society

The Electrochemical Society
Advancing solid state & electrochemical science & technology

OPEN ACCESS

A Liquid Electrolyte-Based Lithium-Ion Battery Cell Design for *Operando* Neutron Depth Profiling

To cite this article: Fabian Linsenmann *et al* 2020 *J. Electrochem. Soc.* **167** 100554

View the article online for updates and enhancements.

This content was downloaded from IP address 88.130.59.146 on 24/11/2020 at 10:20

Journal of The Electrochemical Society, 2020 **167** 100554

A Liquid Electrolyte-Based Lithium-Ion Battery Cell Design for *Operando* Neutron Depth Profiling

Fabian Linsenmann,[1,=,*,z] Markus Trunk,[2,=] Philip Rapp,[1] Lukas Werner,[2] Roman Gernhäuser,[3] Ralph Gilles,[4] Bastian Märkisch,[2] Zsolt Révay,[4] and Hubert A. Gasteiger[1,]**

[1]*Chair of Technical Electrochemistry, Department of Chemistry and Catalysis Research Center, Technische Universität München, 85748 Garching, Germany*
[2]*Particle Physics at Low Energies, Physics Department, Technische Universität München, 85748 Garching, Germany*
[3]*Central Technology Lab, Physics Department, Technische Universität München, 85748 Garching, Germany*
[4]*Heinz Maier-Leibnitz Zentrum, Technische Universität München, 85748 Garching, Germany*

In this study, we present a novel cell design for liquid electrolyte-based lithium-ion batteries (LIBs) to detect the lithium distribution across an electrode by neutron depth profiling (NDP). This newly developed cell design allows to obtain electrochemical data comparable to a standard laboratory cell making use of 500 μm diameter holes to assure a homogeneous compression over the entire electrode area. We present *operando* NDP data recorded during the formation of a porous graphite electrode where we can both distinguish between irreversibly bound lithium within the solid electrolyte interphase (SEI) and reversibly intercalated lithium into graphite, and quantify the lithium concentration profile across the electrode. The amount of lithium reversibly intercalated into the graphite electrode ($\approx LiC_6$), based on one lithium per electron of charge (1 Li/e$^-$), was found to corroborate well with the lithium amount quantified using *operando* NDP. However, comparing the irreversible capacity with the amount of lithium detected as SEI within the graphite anode, a significantly smaller Li/e$^-$ ratio was observed. Furthermore, we confirm that small amounts of lithium alloy into the copper current collector, using NDP and complementary *ex situ* X-ray photoelectron spectroscopy (XPS).

© 2020 The Author(s). Published on behalf of The Electrochemical Society by IOP Publishing Limited. This is an open access article distributed under the terms of the Creative Commons Attribution 4.0 License (CC BY, http://creativecommons.org/licenses/by/4.0/), which permits unrestricted reuse of the work in any medium, provided the original work is properly cited. [DOI: 10.1149/1945-7111/ab9b20]

Manuscript submitted February 6, 2020; revised manuscript received May 12, 2020. Published June 25, 2020. *This was Paper 268 presented at the Atlanta, Georgia, Meeting of the Society, October 13–17, 2019.*

Neutron depth profiling (NDP) is a non-destructive nuclear analytical technique, which enables the *in situ*/*operando* monitoring of the lithium concentration during charging/discharging of lithium-ion batteries (LIBs) across the thickness of the electrode with a (sub-) micrometer spatial resolution. The sample is homogeneously illuminated using a cold neutron beam, whereby the ^{6}Li(n,^{3}H)^{4}He reaction produces two types of charged species with well-defined initial energies, namely a $^4He^{2+}$ particle (*alpha* particle) and a $^3H^+$ particle (*triton* particle).[1] When traveling through any sample material (e.g., through an electrode), the $^4He^{2+}$ and $^3H^+$ particles lose part of their energy, and a measurement of their energy distribution allows to quantify the lithium concentration distribution as function of depth.[2] Chemical bonds of the investigated ^{6}Li nuclei with the surrounding material do not alter the reaction cross-section or the energy of the produced daughter nuclei, which are in the keV regime. Since NDP is thus not sensitive to the chemical environment, it probes the local sum of active lithium, irreversibly attached lithium, and lithium salt in the electrolyte in the same manner; therefore, to distinguish between these different lithium species, suitably chosen reference measurements are required, as will be outlined in this study.

Within the field of battery research, NDP can be utilized to measure fresh or *post-mortem* electrode samples *ex situ* with relatively little experimental effort. For *ex situ* samples measured in a typical NDP chamber under reduced pressure (10^{-5} mbar) the viewing depth is only limited by the density and elemental composition of the sample itself. For example, a graphite electrode with a porosity of 30% has a viewing depth of $\approx$45 μm, owing to the relatively low crystallographic density of graphite ($\approx$2.2 g/cm^3).[3] Thus, Whitney et al.[4] and Nagpure et al.[2] used *ex situ* NDP to study the growth of the solid electrolyte interphase (SEI) layer on graphite electrodes that underwent different cyclic and calendaric ageing processes. In a recent publication by Wetjen et al.,[5] the lithium from electrolyte decomposition products in silicon-graphite composite electrodes that accumulates around the active material particles was probed by *ex situ* NDP after cycling the material for different cycle numbers. The homogeneous lithium concentration across the electrode thickness after extensive cycling suggested a homogeneous active material utilization across the electrode thickness, and it was shown that the cumulative irreversible capacity is in good agreement with the total lithium accumulated in the SEI.

The non-destructive nature of the NDP technique can be much more favorably exploited when performing *operando* experiments. In this case, however, the viewing depth into the sample is naturally diminished by the additional energy loss of the charged particles as they travel through the current collector, the cell containment, and the electrolyte in the electrode pores. The so-called stopping power, which determines the accessible depth into the sample, depends on the thickness, the density, and the chemical composition of all the materials through which the charged particles travel before reaching the detector. Therefore, in order to maximize the viewing depth into the electrode under study, the cell window and the current collector must be as thin as possible. The usual approach found in the literature is the use of either a thin plastic foil (e.g., a 7.5 μm Kapton® film[6]) or the current collector itself (e.g., a 10–16 μm aluminum (Al)[7–9] or 10 μm copper (Cu) foil[10]) as cell window; in one case, where the lithiation of tin was studied,[11] a tin foil served at the same time as active material and as cell window. However, we found that the poor mechanical rigidity of these very thin windows generally results in an inhomogeneity or lack of mechanical compression of the cell stack underneath the window. This problem is even more pronounced when studies are performed in NDP sample chambers held under reduced pressure (typically in the sub-mbar range) in order to minimize the energy loss of the charged particles in the atmosphere as they travel between the sample window and the detector. Unfortunately, inhomogeneous compression can lead to differences in local overpotentials and even to local lithium plating during the charging of a graphite anode.[12] Besides

=These authors contributed equally to this work.
*Electrochemical Society Student Member.
**Electrochemical Society Fellow.
zE-mail: fabian.linsenmann@tum.de

this, the use of thin and non-rigid windows can also result in an incomplete capacity utilization of the part of the electrode located directly underneath the window, limiting the charge/discharge rate capability to very low rates and/or requiring very long constant voltage phases at the end of charge/discharge in order to achieve a homogeneous state-of-charge (SOC) across the entire electrode area. This must be considered when analyzing *operando* NDP cell data (i.e., data taken under potentially inhomogeneous compression), as these artefacts caused by inhomogeneous cell compression may not at all relate to the processes occurring in commercial cells (i.e., taken under comparably homogeneous compression). Therefore, it is to show that the specific capacity obtained from the active materials under study (in terms of $mAh/g_{active\ material}$), and thus the electrochemical processes probed are indeed representative of the entire cell, i.e., whether the electrochemical processes of the electrode segment underneath the window probed by NDP occur homogeneously over the entire window and/or cell area, as would be required for a rigorous comparison with conventional cells.

In order to attain a sufficiently homogeneous cell compression, so as to avoid the above described artefacts, we developed a coin cell based *operando* NDP cell, where the coin cell cap was perforated with a pattern of closely spaced 500 μm diameter holes (prepared via laser cutting) onto which a 7.5 μm Kapton® foil was placed as a window for the emitting *triton* particles. On one hand, the overall ca. 2.2% perforation of the cell cap allowed for a substantial emission of *triton* particles from inside the cell; on the other hand, the diameter of the holes is small enough to still provide a homogeneous compression of the electrodes within the cell for the given bending stiffness of the 7.5 μm Kapton® foil window. Nevertheless, the liquid electrolyte in the cell was found to cause problems (e.g., bulging of the window caused by gas formation) whenever the vacuum level in the NDP chamber was substantially below the vapor pressure of the electrolyte. Therefore, we used a helium gas atmosphere at a pressure of about 400 mbar in the NDP sample chamber, which was high enough to circumvent this problem and still low enough to sufficiently reduce the interaction of the *triton* particles with the helium atoms within the NDP sample chamber.

Previous studies focused on a variety of different electrode materials, like observing the lithium (de-)intercalation in a lithium titanate (LTO) anode with a very low areal capacity and loading ($\approx$0.15 mAh/g_{LTO} and $\approx$0.9 mg_{LTO}/cm^2), presumably to limit the electrode thickness.[9] Here, we focus on graphite-based anodes, which are nowadays the most frequently used anode materials in industry because of their high energy density and good cycling stability; to allow for complete penetration of the NDP signal, the areal capacity also had to be restricted to $\approx$0.6 $mAh/g_{graphite}$, which is $\approx$4-fold lower than in industrial applications. Due to their low density, anode active materials such as graphite or silicon allow for a higher accessible NDP viewing depth compared to, e.g., cathode active materials. In order to compromise the viewing depth in an *operando* NDP cell as little as possible, the mass density of the metal current collector has to be minimized. While low-density aluminum can be used as current collector for LIB cathodes, a copper current collector with an unfortunately $\approx$3-fold higher density must be used for graphite and silicon anodes, since lithium alloys with Al at potentials below $\approx$0.3 V vs. Li^+/Li.[13] Therefore, in order to maximize the viewing depth, we use a very thin copper layer (100 nm-thick) as anode current collector, which was deposited on a 7.5 μm-thick Kapton® foil acting as cell window. While the latter is permeable for *triton* particles, the Kapton® foil of this thickness is impermeable to *alpha* particles,[14] which therefore could not be detected and not used for a higher depth resolution analysis of the lithium profile near the interface between the electrode and the current collector. Taking into account the *triton* stopping power of the helium atmosphere in the NDP chamber (at $\approx$400 mbar), of the Cu/Kapton® foil assembly, and of the electrolyte-filled graphite electrode (assuming an electrolyte-filled pore volume fraction of $\approx$47%, which then equates to an effective density of $\approx$1.7 $g/cm^3_{electrode}$), the NDP viewing depth into the graphite anode mounted in the *operando* coin cell in the presented NDP setup can be estimated to be $\approx$26 μm.[15] Even though this physical limitation confines the general application of *in situ*/*operando* NDP to graphite anodes with a $\approx$3–4 times lower thickness and areal capacity compared to commercially used graphite anodes, it still allows to study fundamental electrochemical processes. This restriction, however, does not apply in the case of silicon-based anodes, since their thickness is much lower at industrially relevant areal capacities due to the high specific capacity of silicon. E.g., Jantke et al. used anodes based on a composite of micrometer-sized silicon and conductive carbon, which had an areal capacity of $\approx$2.5 mAh/cm^2 at an anode thickness of only $\approx$25 μm[16]; similarly, Wetjen et al. investigated nanosilicon/graphite composite-based electrodes, which had an areal capacity of $\approx$2 mAh/cm^2 at an anode thickness of only $\approx$20 μm.[5] In both cases, the complete electrode depth could be probed by *in situ*/*operando* NDP.

In the here presented study, we aimed for a pristine graphite anode thickness of only $\approx(17 \pm 2)$ μm in order to: (1) assure a still precise quantification of *triton* particles emitted near the anode/separator interface (i.e., farthest away from the NDP cell window); (2) avoid a superposition of low energy *triton* particles (i.e., those emitting near the anode/separator interface) with the strong NDP background signal at low energies; and, (3) allow for a possible swelling of the graphite anode during operation. With the optimized *operando* NDP cell design presented in this study, we could demonstrate that the compression of the graphite anode is sufficiently homogenous to attain a homogeneous lithiation across the entire graphite anode and to extract its full capacity at a rate of $\approx$C/16. For the here examined graphite electrodes, the evolution of the lithium profile across the entire thickness of the anode could be quantitatively followed over the course of charge/discharge, further proving the utility of our cell design for *operando* NDP studies. The NDP data corroborate well with the lithium concentration derived from the electrochemically observed reversible capacity based on one lithium per electron of charge (1 Li/e^-). However, a significantly lower ratio of (0.61 ± 0.08) was observed when comparing the lithium amount in the graphite electrode SEI to the electrochemically measured irreversible capacity. A possible explanation could be either electrolyte decomposition mechanisms with an average Li/e^- ratio of <1 or a subsequent dissolution of lithium-containing SEI compounds during/after formation, which is currently subject of further investigation. Moreover, consistent with previous *operando* NDP studies, our *operando* NDP and *ex situ* XPS (X-ray photoelectron spectroscopy) data also show that during the slow lithiation of a graphite electrode small amounts of lithium can diffuse into the copper current collector, forming a Li-Cu alloy.

Experimental

Electrode preparation.—Due to the short range of the *triton* particles in NDP and to assure that the lithium profile can be obtained across the entire electrode thickness, a graphite anode electrode with a thickness of only $\approx(17 \pm 2)$ μm was prepared, which is less than the typical size of commercial graphite particles with a d_{50} value of $\approx$20 μm. Therefore, in order to obtain a homogeneously thin graphite electrode, commercially available artificial graphite particles (Sigracell SG3, SGL Carbon, Germany) with a BET area of 4 $m^2\ g^{-1}$ ($d_{50} = 19$ μm, $d_{90} = 37$ μm) were sieved to obtain graphite particles with a small and narrow particle size distribution around 6 μm ($d_{50} = 5.8$ μm, $d_{90} = 8.5$ μm) and a BET area of $\approx$15 $m^2\ g^{-1}$. The resulting graphite particle size distribution is shown in Fig. 1 (red line) in comparison to the original graphite material (blue line).

Electrode inks were prepared by mixing the sieved artificial graphite and polyvinylidene difluoride (PVDF, Kynar HSV 900, Arkema, France) at a mass ratio of 91:9 with N-methyl-pyrrolidone (NMP, anhydrous, 99.5%, Sigma-Aldrich, Germany) at a solid content of 28 wt% in a planetary mixer (Thinky, USA) for 15 min. The resulting ink was then doctor blade-coated onto a 100 nm-thick

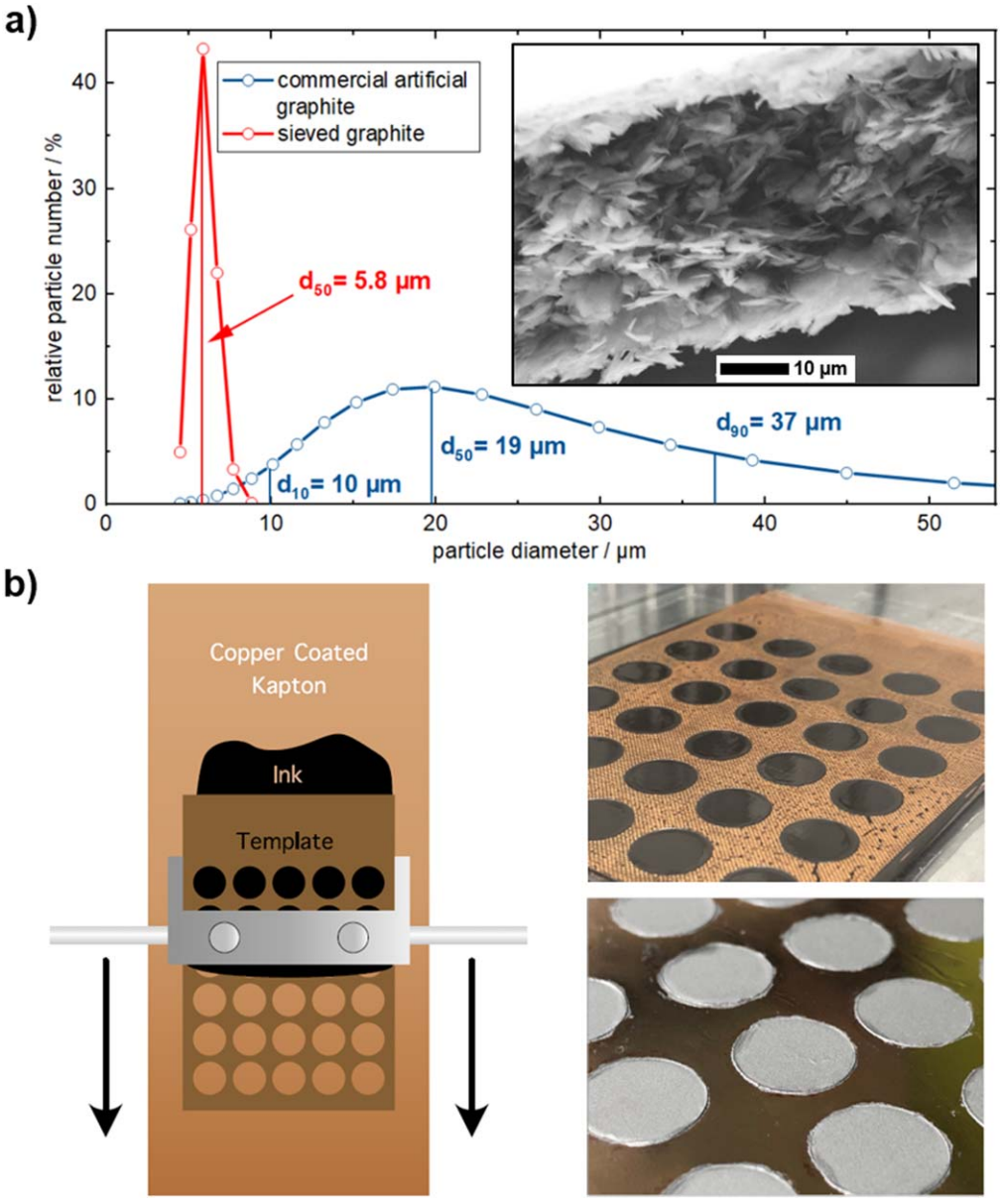

Figure 1. (a) Particle size distribution for a commercial artificial graphite (blue) and the same active material, which was sieved to remove particles larger than ≈10 μm (red); the inset shows an SEM cross-section of an NDP electrode before compression. (b) Illustration of the doctor blade mask-assisted coating procedure of the graphite electrode ink onto the copper coated Kapton® foil serving as window for the *operando* NDP coin cell (left), and photos of the coated electrodes (right top) and of the uncompressed electrodes after drying (right bottom).

copper layer serving as current collector that had been sputter-coated (Movatec, Germany) onto a 7.5 μm Kapton® (DuPont, USA) foil, serving as anode current collector and window for the *operando* NDP cell. The 12 mm diameter graphite electrodes were obtained by coating through an 80 μm-thick mask made from a PTFE coated fiberglass film (Fiberflon, Fiberflon GmbH & Co. KG, Germany) that contained holes with 12 mm diameter (s. Fig. 1b). The coating including the mask was dried at 50 °C in a convection oven for 10 min. The mask was then removed and the coating dried for another 3 h at 50 °C. To allow electrical contacting of the current collector in the coin cell assembly (s. below), the electrodes were punched out with a larger diameter of 15 mm, so that an outer 1.5 mm wide rim of the non-coated copper current collector remained (s. Fig. 2a). Finally, the electrodes were compressed to a porosity of ≈(47 ± 6)% using a KBr press (PE-011, Mauthe, Germany), as determined by areal weight and thickness measurements, considering uncertainties of ±0.034 mg for the coating mass, and ±2 μm for the coating thickness, where the error in mass determination originates mainly from variations in the current collector weight (standard deviations of ten current collector samples). This procedure yielded an electrode loading of (1.99 ± 0.03) $mg_{graphite}$ (≡1.76 ± 0.03 $mg_{graphite}/cm^2$) with a nominal areal capacity of 0.62 mAh/cm^2 (based on a reversible capacity of 350 $mAh/g_{graphite}$) and with an electrode thickness of ≈(17 ± 2) μm.

Cell assembly and cell cycling.—The electrodes were glued into a commercial CR2032 coin cell cap (Hohsen Corp., Japan) using epoxy resin (UHU Plus Endfest, Bolton Group S.r.l., Italy) applied onto the copper rim area (s. Fig. 2b). For this work, two different types of specially designed coin cell caps were used. For initial experiments, a hole with 4 mm diameter (0.13 cm^2 open window area) was laser-cut into the cap. As this design resulted in a poor compression of the electrode and a very inhomogeneous current distribution (s. below discussion), an improved cap design was devised, containing a grid of 57 laser-cut holes with individual diameters of 500 μm arranged in a quadratic pattern and with a

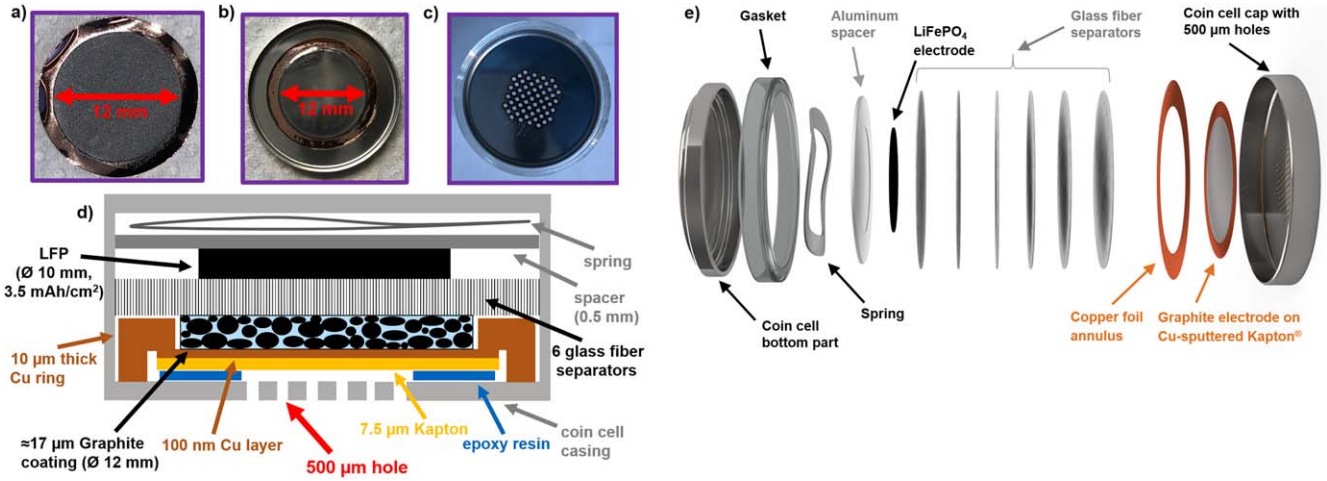

Figure 2. (a) Graphite electrode (12 mm diameter, uncompressed) mask-coated onto a 100 nm Cu film that was sputter-deposited onto a 7.5 μm-thick Kapton foil (the final assembly was punched out at 15 mm diameter, leaving a 1.5 mm wide Cu perimeter for electrical contacting); (b) graphite electrode glued into the inside of a CR2032 coin cell cap; (c) top-view of a CR2032 coin cell cap containing 57 laser-cut holes with a diameter of 500 μm; (d) cross-sectional schematic of the *operando* NDP cell setup; (e) *operando* NDP cell setup in exploded view.

center-to-center distance of 1 mm (extending over a roughly circular area with a diameter of ≈10 mm), amounting to a similar total open window area of 0.11 cm^2 (s. Fig. 2c). The electrode glued into the coin cell cap was dried overnight at 80 °C under dynamic vacuum in a glass oven (drying oven 585, Büchi, Switzerland) and then transferred into an argon-filled glovebox without exposure to ambient atmosphere.

To assure electrical contact between the copper current collector and the stainless steel coin cell cap, a 10 μm thick copper foil ring with an inner diameter of 13 mm and an outer diameter of 19 mm was positioned around the graphite working electrode (WE), as shown by the thick orange marked element in the cell cross sectional sketch in Fig. 2d and the orange marked ring in the exploded view shown in Fig. 2e. The coin cell was assembled using six glass fiber separators with a diameter of 17 mm (VWR, Germany), each with an uncompressed thickness of 250 μm (s. Figs. 2d and 2e; the compressed thickness is ≈200 μm each), which were soaked with 270 μl of 1 M $LiPF_6$ in a mixture of ethylene carbonate and ethyl methyl carbonate (EC:EMC = 30:70 wt%; LP57, BASF, Germany). The use of multiple thick glass fiber separators was chosen in order to improve the homogeneity of the pressure distribution as well as to facilitate gas diffusion away from the graphite electrode surface. As counter electrode (CE), a capacitively oversized $LiFePO_4$ (LFP) (LFP High Energy, Custom Cells Itzehoe GmbH, Germany) electrode with a diameter of 10 mm and an areal capacity of ≈3.5 mAh/cm^2 was used. A 0.5 mm-thick aluminum spacer containing a 100 μm × 10.1 mm circular milled slot was used to precisely center the LFP CE during cell assembly and to adjust the height of the electrode stack to yield a calculated cell pressure of ≈3 bar.

The *operando* NDP cell with the optimized cap design containing the 500 μm holes used during beamtime was cycled between 3.43 and 1.93 V_{cell} at a C-rate of ≈C/16 (≡39 $\mu A/cm^2$) using an SP300 potentiostat (Biologic, France). The cell was first charged to 3.43 V_{cell} (CCCV charge with a C/32 current cutoff to end the CV phase) and then discharged to 1.93 V_{cell} (CCCV charge with a C/80 current cutoff to end the CV phase), followed by a 2 h rest phase at open circuit voltage (OCV). Afterwards, the cell was again charged to 3.43 V_{cell} (CCCV charge with a C/32 current cutoff to end the CV phase). The cell with one large 4 mm hole and the *operando* cell with 500 μm holes for the visual lithiation determination during cell development were cycled accordingly, but at a C-rate of C/15 (CCCV charge with a C/30 current cutoff to end the CV phase, CC discharge

For the later described *in situ* experiment to study the lithium intercalation into the Cu current collector, an uncoated anode current collector (i.e., a 100 nm Cu on 7.5 μm Kapton® foil without the graphite electrode) was used as WE and a 16 mm diameter and 450 μm-thick lithium disk was used as CE. One set of these coin cells was not charged, but simply stored at 25 °C and OCV for 16 h. The other set of cells were cycled such that the WE potential was first scanned from OCV (≈3 V vs. Li^+/Li) to 250 mV vs. Li^+/Li within 2 h (corresponding to a scan rate of ≈0.38 mV/s), and then further reduced to 20 mV vs. Li^+/Li within 14 h at ≈0.0045 mV s^{-1}. For the *ex situ* XPS measurements, coin cells with a standard cell cap were assembled, also with a Cu-coated Kapton® foil as WE, a 2500 Celgard® polyolefin separator (Celgard, USA) with 50 μl of LP57 electrolyte, and a Li disk CE. The same cycling procedure was used for the *ex situ* NDP cells.

Neutron depth profiling (NDP) and quantification of the NDP signal.—NDP measurements were conducted using the N4DP setup at the PGAA instrument of the Heinz Maier-Leibnitz Zentrum (MLZ) in Garching, Germany.[17,18] The cold neutron beam exhibits a flux of 1.35 × 10^9 cm^{-2} s^{-1} and is collimated to a circular-shaped beam profile with a diameter of 4 mm using boron-containing plastic plates.[14] The NDP chamber was filled with helium gas at a pressure of about 400 mbar, well above the vapor pressure of the liquid electrolyte in the cell while keeping the additional energy loss of the charged particles by interaction with the helium on their way from the cell window to the detector (placed at a distance of 9.6 cm) low. The coin cell was mounted on a specially designed *operando* sample holder, shown in Fig. 3. Here, four different *operando* cells can be mounted together with several *ex situ* reference samples. The sample holder is mounted at an angle of 45° with respect to the incoming neutron beam, with the cap of the coin cell containing the window holes facing and aligned in a normal direction to the charged particle detector (ORTEC).

The measured signal intensities were converted to absolute quantities by comparing them to the signal obtained from the boron-containing reference sample SRM2137.[19] It consists of a well-defined ^{10}B concentration profile implanted into a silicon wafer and the boron content within the total implantation is known with a precision of ±3.4%.[19] Within a calibration measurement, the integrated signal intensity, representing the total ^{10}B amount within the SRM2137 reference, was determined with a systematic uncertainty of ±0.9%. In order to relate the measured signals to lithium, the ratio of the thermal neutron capture cross sections of ^{10}B (≈3840 b) and ^6Li (≈940 b) was taken into account together with the natural abundance of ^6Li (≈7.6%).

While these aspects must be considered for the quantification of *ex situ* NDP data from harvested electrodes, *operando* NDP

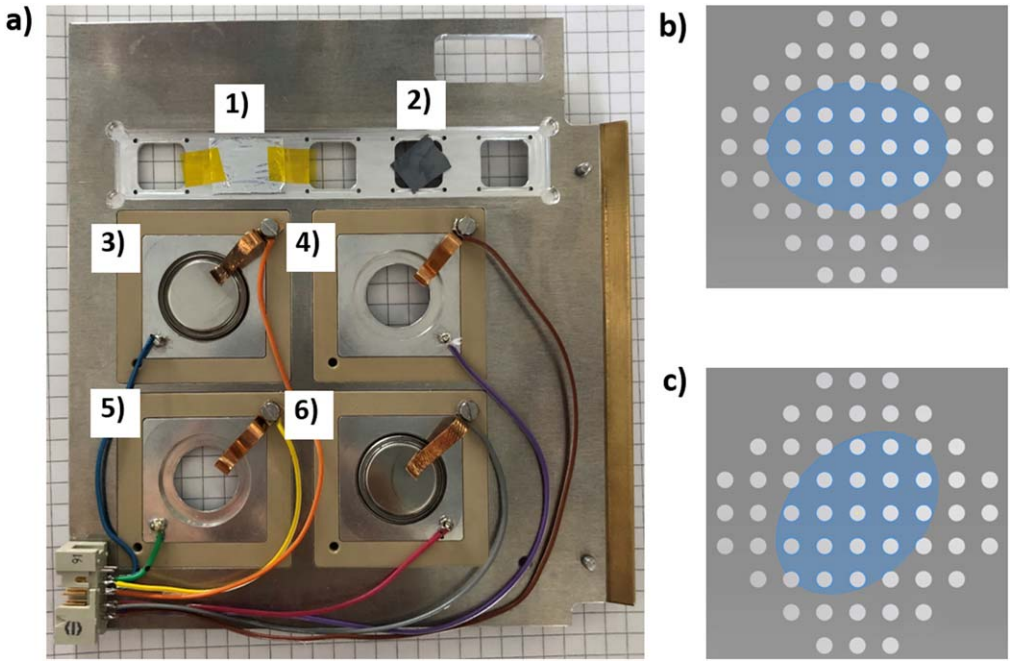

Figure 3. (a) NDP cell holder with five reference sample slots, used for elemental quantity and energy calibration, of which two are mounted: (1) LiF-coated Mylar® foil, and (2) ^{10}B-doped silicon wafer (SRM2137). (3)–(6) show four mounting slots for *operando* NDP coin cells (in this picture, (3) and (6) are mounted). (b) + (c) Drawings of the 500 μm diameter hole grid on the front-side of the coin cells, superimposed with the area illuminated by the neutron beam (blue area, ≈17.77 mm^2 ellipse), shown for either a perfect alignment of the center and the central axes of the incident neutron beam with the center and the central axes of the hole grid (b) or for the case where the neutron beam area is rotated by an angle of 45° (c). From these kind of drawings, the maximum and minimum hole area/beam area ratio were calculated by considering rotation angles of 0°, 22.5°, and 45° as well as in-plane offsets of the neutron beam area from the hole grid center by distances between 0 mm and 1 mm in 100 μm steps.

measurements with the here presented *operando* coin cell must also take into account the reduced area from where the emanating charged particles can reach the detector. Since the SRM2137 reference sample is larger than the neutron beam area hitting the sample, charged particles from the whole illuminated area can reach the detector. On the other hand, this is not true for the *operando* coin cell, because the 0.25 mm-thick stainless-steel cap is impermeable for the charged particles and so they can only emanate from the area defined by the processed grid of holes with individual diameters of 500 μm, as discussed in the following. The circularly collimated, ≈4 mm diameter neutron beam hits the sample at an angle of 45°, resulting in an illuminated area in form of an ellipse (≈17.77 mm^2) on the window area with the hole pattern. As shown in Figs. 3b and 3c, the fraction of illuminated holes depends on the positioning of the coin cell within the elliptic beam area, which was considered by calculating the variation of the fraction of illuminated hole areas when moving the beam center in multiple directions away from the grid pattern center between 0 mm and 1 mm in 100 μm steps and a rotation of the coin cell by 0°, 22.5°, and 45° (s. Figs. 3b and 3c) was taken into account. Based on the maximum displacement error of the illuminated neutron beam area with respect to the grid pattern of the holes of 1 mm in all directions on the window plane, the maximum and minimum fractional hole area of the illuminated window area is 20.2% and 17.8%, respectively. In addition, further uncertainties might arise from a slight angular misalignment of the coin cell out of the ideal plane-parallel alignment with the detector, which would reduce the hole area fraction that is in line-of-sight with the detector. Based on our experimental setup, we estimate a maximum angular displacement of 3° between the coin cell window and the detector plane, caused by a maximum of 1 mm misalignment over the 20 mm coin cell diameter. This would lead to a further reduction of the hole area fraction by a maximum of 5.2% of the above stated value due to in-plane alignment of beam and grid pattern. Therefore, the maximum accessible hole area fraction of the illuminated window area would remain at 20.2% (perfect angular alignment) and the minimum would become 16.9% (3° angular displacement). Thus, the reduced NDP sampling area due to the given hole pattern and the above geometrical considerations can be estimated to be (18.6 ± 1.7)% of the original beam area. This uncertainty of the reduced beam area based on the here discussed min/max considerations therefore induces a systematic uncertainty of ±9.1%.

In summary, it is important to state that the systematic uncertainty originating from the geometrical setup of the *operando* coin cell is larger (±9.1%) than the errors of the calibration that are the ±3.4% of the SRM2137 standard and the ±0.9% of the reference calibration measurement. Therefore, while NDP is a rather precise quantitative technique for samples larger than the incident neutron beam, its precision is somewhat compromised for the here presented cell design due to the 500 μm diameter hole pattern. However, as will be shown, this processed grid is critical for assuring a homogenous compression of the cell stack and good electrical contact. Considering all three uncertainties, given by the error in the SRM2137 standard (±3.4%), an uncertainty of ±0.9% arising from the reference sample calibration procedure, and the relative geometrical min/max error (±9.1%), the total systematic uncertainty of the lithium concentration measurement was determined to be ±9.8% assuming Gaussian error propagation for errors with independent origins. It is to note that this systematic uncertainty scales all *operando* NDP spectra in the same manner, i.e., it is independent of the SOC.

NDP was recorded continuously (event-based) during cycling (*operando*) and the data were later averaged over 1 h to achieve sufficient statistics. Thus, the NDP spectra represent the lithium concentrations averaged over ΔSOC = ≈6−8%, except for spectrum 5 in Figs. 6 and 7 which was recorded during a 2 h OCV phase. The additional energy losses caused by the fact that the *triton* particles pass through different materials before hitting the detector, i.e., the 100 nm-thick Cu current collector, the 7.5 μm-thick Kapton® foil, and the helium atmosphere were taken into account when translating the energy spectra to depth profiles. For the conversion of

the energy spectra to depth profiles, the stopping power of the *triton* particles provided by the SRIM software was used.[15,20] Since the elemental anode composition influences the material stopping power for the *triton* particles, the change of the composition was also taken into account.[9,14] Here, the anode composition was estimated using the pristine anode composition and the fully electrolyte-filled pores of the anode. During cell operation, lithium-ions are accumulated in the anode, leading to a change of the anode composition. Here, the lithium accumulated in the anode at the different SOCs was determined by integration of the NDP energy spectra and the composition was corrected for it. Upon operation, also SEI formation will occur by reduction of the electrolyte. Hereby, only electrolyte, which was previously present within the anode pores, is transformed into an SEI layer, and thus the change of the elemental composition due to SEI formation was assumed to be negligible. An overview of the anode compositions modeled for the different SOC states is shown in Table I.

X-ray photoelectron spectroscopy (XPS).—For the *ex situ* XPS measurements, the coin cells were decrimped inside an argon-filled glovebox. Small pieces (3 × 3 mm) were cut-out from the WE with a scalpel and mounted on a stainless steel stub (Ø = 15 mm), which was then transferred from the glovebox into the load-lock of the XPS system without air exposure using a transfer vessel (Kratos, UK). With an Axis Supra system (Kratos, UK), XPS spectra were recorded using monochromatic Al-K_α radiation ($h\upsilon$ = 1487 eV) at a base pressure of $<3 \times 10^{-8}$ torr, a pass energy of 20 eV, a step size of 0.1 eV, a dwell time of 300 ms, and a measured spot size of 800 × 300 μm. The measurement was performed in hybrid lens mode with turned on charge neutralizer. Regional spectra were averaged from 4 scans (Cu 1s, Li 1s, Cu 3p, N 1s). The obtained spectra were processed and fitted using the Kratos ESCApe software (version 1.1). Binding energies (BE) were corrected based on the C–C/C–H peak of adventitious carbon at 284.8 eV in the C 1s spectrum. A mixture of 30% Laurentzian and 70% Gaussian functions was employed for the fitting procedure together with a Shirley background subtraction. The ratio between copper and lithium atoms was done based on the fitted spectra of Li 1 s and Cu 3p. Etching was performed using Ar^+ ions with an energy of 5 keV. The etching time was 10 s in the first step and in the subsequent steps always 30 s. The raster size was 2 × 1 mm. The etching time was converted into a depth rate by completely etching through the 100 nm-thick Cu layer on top of the Kapton® foil. The N 1s signal from the Kapton® polyimide was used as indicator for a total penetration of the Cu layer. From that, an etching rate of ≈1.8 nm/30 s was calculated.

Results and Discussion

Cycling performance of a coin cell with a 4 mm window.—First, the electrochemical performance of a coin cell with a single 4 mm diameter hole laser-cut into its cap is tested. Similar to previous works,[11] this configuration would be favorable for NDP, since it maximizes the signal from the charged particles produced by the $^6Li(n,^3H)^4He$ reaction inside the cell. Figure 4 displays the voltage profile of a graphite/LFP coin cell with a 4 mm hole that was cycled inside a glovebox at a rate of C/15. During the first cycle, a reversible capacity of 349 mAh/$g_{graphite}$ and a coulombic efficiency of ≈73%, corresponding to a first-cycle irreversible capacity of ≈27% are obtained. These numbers are reasonably close to the reversible capacity of ≈355 mAh/$g_{graphite}$ and the first-cycle irreversible capacity of ≈22% measured in a standard coin cell (without a window hole and using the same graphite electrode coated on a 10 μm-thick copper current collector foil). They indicate a good electrochemical performance of the cell and that this cell setup would be representative of a standard cell. However, upon opening the cell at 100% SOC after the second charging cycle revealed that even during charging at C/15, the central part of electrode in the middle of the 4 mm diameter window hole does not show the golden color expected from a pure LiC_6 phase[21] (s. inset in Fig. 4). This clearly indicates that even during relatively slow charging at C/15, full lithiation does not occur in the center of the window hole, so that a large fraction of the area probed by NDP would not at all be

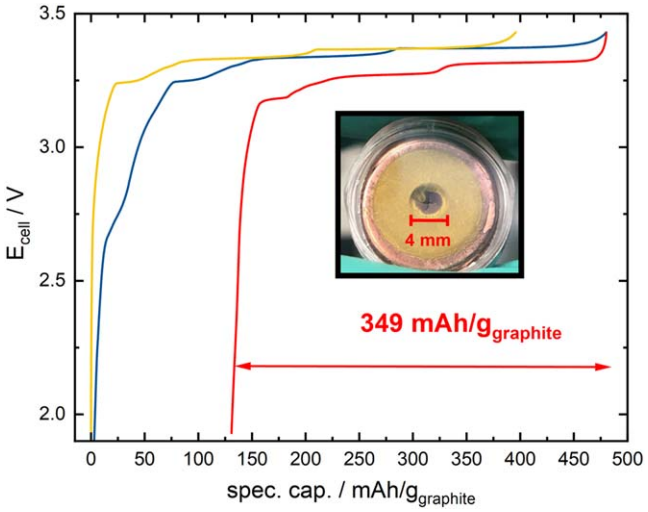

Figure 4. Cell potential profiles for the 1st charge/discharge (blue/red lines) and for the second charge (yellow line) of a graphite electrode cycled vs. an LFP cathode in a coin cell with a 4 mm window hole that was sealed by the 7.5 μm Kapton® foil. The Kapton® foil was sputter-coated with a 100 nm-thick Cu layer onto which the graphite electrode was coated (s. Fig. 2a). The charge was conducted at C/15 with a CV hold at 3.43 V_{cell} (with a C/30 cutoff) and discharged to 1.93 V_{cell} at C/15. The inset shows a decrimped coin cell that was disassembled after the second complete charge to 100% SOC at C/15 and the CV hold at 3.43 V_{cell}. Here, it is clearly visible that the graphite active material within the window hole region was not completely lithiated across the entire window area due to the absence of the golden LiC_6 phase.

Table I. Elemental composition of the graphite anode estimated for different SOCs. For the pristine graphite anode, the composition of the graphite anode layer (graphite + PVDF) is well known and it can be assumed that the pores in the anode layer (47% porosity) are completely filled with the LP57 electrolyte. Upon operation, the composition change induced by the (de−)intercalated of lithium-ions in the graphite active material was considered. The lithium additionally accumulated in the anodes was determined via integration of the NDP energy spectra and is taken into account to model the anode composition as a function of SOC.

Anode SOC (spectrum #)	H (mol%)	Li (mol%)	C (mol%)	O (mol%)	F (mol%)	P (mol%)
Pristine (1)	22.0	0.3	64.8	9.1	3.6	0.3
50% (2)	21.3	3.5	62.7	8.8	3.5	0.3
100% (3)	20.5	6.9	60.5	8.5	3.3	0.3
50% (4)	21.1	4.3	62.2	8.7	3.4	0.3
0% (5)	21.8	1.4	64.1	9.0	3.5	0.3
50% (6)	21.0	4.6	62.0	8.7	3.4	0.3
100% (7)	20.5	6.9	60.5	8.4	3.3	0.3

representative for the whole electrode. This inhomogeneous lithiation might be caused by increased intercalation overpotentials in the poorly compressed central region of the window hole.

As shown in the photograph in Fig. 4, the clearly under-lithiated central region extends only over a diameter of ≈3 mm (i.e., over an area of ≈0.071 cm^2), which corresponds to only ≈6% of the entire graphite electrode (1.13 cm^2), explaining why the overall capacity of the coin cell with the 4 mm window is very close to that of a standard coin cell (s. ≈355 $mAh/g_{graphite}$). Of concern, however, is the fact that this under-lithiated central region with an area of ≈0.071 cm^2 constitutes ≈55% of the overall window area (4 mm diameter or 0.13 cm^2) over which the NDP data are collected. Therefore, an NDP measurement obtained entirely from this region would not properly represent the undisturbed cell chemistry in the coin cell. The observation that the golden color of the LiC_6 phase is only present in a region of ≈0.5 mm within the 4 mm diameter hole (s. inset of Fig. 4) suggests that this is the maximum distance over which the local cell compression remains in an acceptable range.

Optical appearance of a lithiated graphite anode cycled in a coin cell with 500 μm holes.—These findings suggest that in a ≈0.5 mm-thick ring inside the perforated hole a LiC_6 phase is still present and thus a hole with a ≈1 mm diameter might be sufficient to exclude inhomogeneous lithiation. However, in order to assure a sufficient cell compression, we decreased the hole diameter itself to ≈0.5 mm. At the same time, the overall sampling area for the *triton* particles should be maintained in order to maximize the NDP signal. These two requirements resulted in our improved *operando* NDP cell design shown in Fig. 2c in which the single 4 mm window hole (≈0.13 cm^2) was replaced by a pattern of 57 holes with individual diameters of 500 μm, while the total hole area could almost be maintained (≈0.11 cm^2). The validity of this improved design was demonstrated by an analogous experiment as that discussed in the previous section, whereby a coin cell with 500 μm holes (s. Fig. 2c) was cycled accordingly (CCCV charge to a cutoff voltage of 3.43 V_{cell} at a rate of C/15 with a CV hold until C/30), so that the graphite anode is expected to be at its fully lithiated state. Figure 5a shows a photograph of a graphite electrode extracted from this fully lithiated decrimped coin cell with an array of 500 μm holes, which are visible by little indentations in the graphite electrode coating where the electrode was slightly pressed into the window holes due to the compressive force on the cell stack. The golden color in the magnification in Fig. 5b is even present in the indentations of the electrode, and it clearly indicates that full lithiation occurred homogeneously over the entire surface of the electrode. These findings indicate that the region of interest (i.e., within the holes) is representative of the entire graphite electrode, contrary to what we had concluded for the cell design with the single 4 mm window hole (s. inset of Fig. 4). The array of 500 μm window holes in the coin cell cap thus maximizes the net area accessible for the NDP signal (i.e., for *triton* particle emission) while assuring a homogeneous electrochemical behavior across the entire electrode area. This improved setup was used for the further discussed *operando* NDP measurements.

Cycling performance and NDP energy spectra of a graphite electrode obtained in an operando NDP cell with 500 μm holes.—Figure 6a shows the voltage profiles of the graphite/LFP *operando* NDP cell mounted within the NDP chamber under reduced helium pressure (≈400 mbar). Displayed are the first charging (blue) and discharging (red) half-cycles as well as the second charging half-cycle (yellow), conducted at a rate of C/16 with a CCCV charge to 3.43 V_{cell} (until C/32) and a CC discharge. The obtained reversible capacity of the capacity-limiting graphite electrode is ≈348 $mAh/g_{graphite}$, which agrees well with the ≈355 $mAh/g_{graphite}$ obtained in a conventional coin cell, as does the first-cycle irreversible capacity of ≈22% (this high value can be explained by the very high BET surface area of the here used graphite active material).

Figure 6b shows the acquired NDP energy spectra during the three half-cycles. The points labelled with numbers 1–7 in Fig. 6a indicate the SOC regions during which the NDP spectra shown in Fig. 6b were recorded *operando* (the spectra were averaged over 2 h for point 1 and over 1 h for all other points). Thereby, the NDP spectra were averaged over an SOC range of Δcap ≈30 $mAh/g_{graphite}$. The spectrum labelled with 1 was measured on the pristine cell, i.e., during an OCV rest phase before starting cell cycling. The spectra consist of signals from the *triton* particles of the

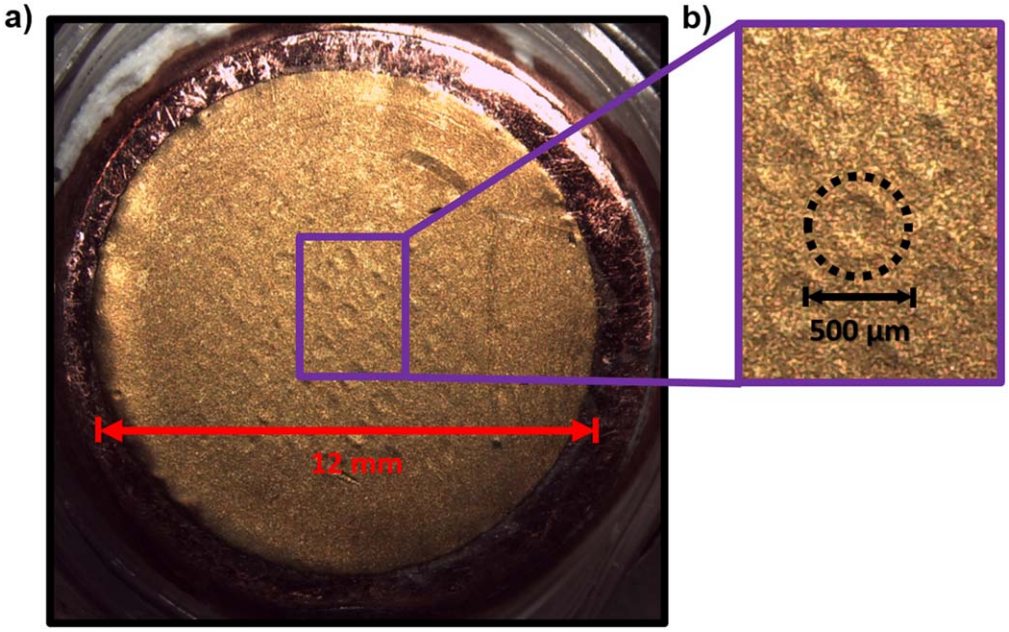

Figure 5. (a) Post mortem photograph of a graphite electrode that was lithiated in the improved *operando* NDP coin cell design with an array of 500 μm holes in the coin cell cap (s. Fig. 2d). The graphite in this graphite/LFP cell was charged at C/15 with a CV hold at 3.43 V_{cell} (with a C/30 cutoff). Subsequently, the cell was decrimped in a fully charged state. The golden color indicates a complete LiC_6 formation over the complete electrode area. (b) Magnification of the center part of the electrode. The slight imprints of the 500 μm diameter holes in the coin cell cap are visible in the graphite electrode. This magnified image clearly shows that the lithiation of the graphite electrode occurred completely also in the regions which are located within the center of the window holes.

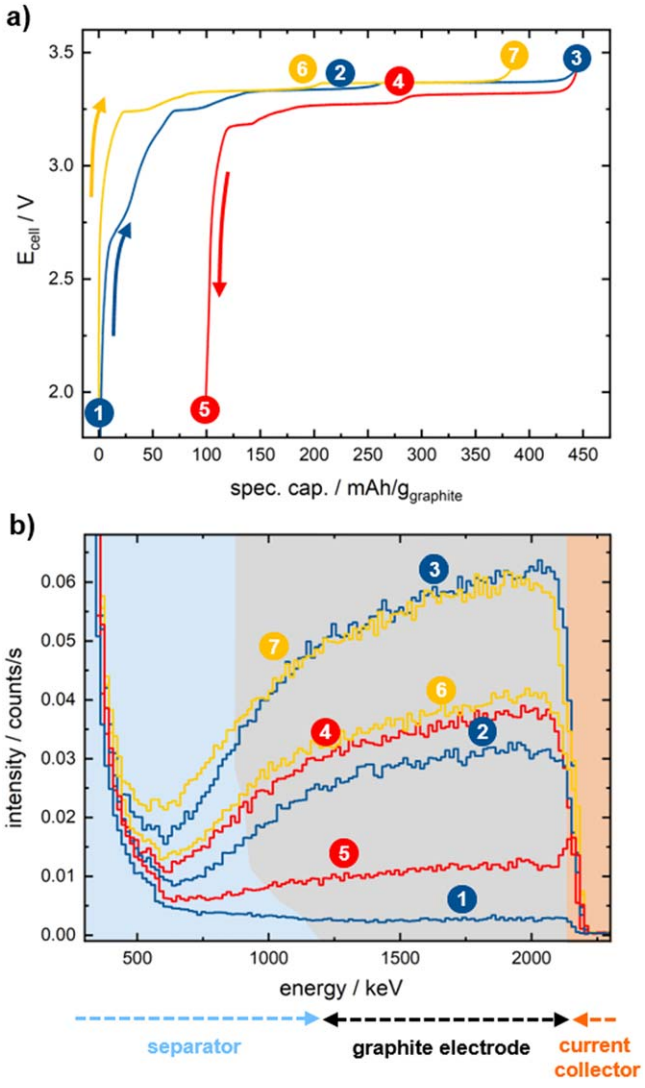

Figure 6. (a) Cell potential profiles of the *operando* NDP graphite/LFP cell with the 500 μm diameter hole array design (s. Fig. 2c) for the first charging (blue), the first discharging (red), and the second charging (yellow) half-cycles. The cell was charged at a rate of C/16 (≡39 μA/cm^2) followed by a CV hold at 3.43 V_{cell} (until C/32) and discharged to 1.93 V_{cell} at C/16. The colored dots indicate SOC regions where an NDP spectrum was recorded over the course of 1 h, corresponding to a Δcap = ≈30 mAh/$g_{graphite}$. (b) Measured NDP signal intensity as a function of the *triton* particle energy, plotted for various SOC regions (always averaged over 1 h). The differently colored backgrounds indicate the approximate energy ranges for NDP signals stemming from the graphite electrode (gray), from a part of the separator region (blue), and from a part of the Cu current collector/Kapton® foil assembly (orange); as described in the text, these were obtained from the inflection points of the NDP profiles.

^{6}Li(n,^{3}H)^{4}He reaction and are dominated below ≈600 keV by an exponentially-shaped background signal stemming from *beta*- and *gamma*-radiation.[10,17] The *alpha* particles, which are also produced during neutron capture of ^{6}Li, are not observed here, as they do not penetrate through the Kapton® foil window.[5] The *triton* particles, however, also lose part of their initial energy of 2727 keV during their passage through the measurement setup before hitting the detector, and thus the signals at (2163 ± 10) keV (s. Fig. 6b) correspond to *triton* particles emitted from inside the coin cell at the interface between the graphite anode and the Cu current collector. The energy loss in the 100 nm-thick copper current collector was roughly estimated to ≈11 keV.[15] Using reference measurements, the energy loss caused by the Kapton® foil could be determined to be (301 ± 0.6) keV. The remaining energy loss before hitting the detector was assigned to the helium atmosphere and it can be used as a precise measure for the gas pressure within the NDP chamber. The energy loss of (248 ± 10) keV correlates to a helium mass loading of (0.72 ± 0.03) mg/cm^2.[15] It can be translated to a helium gas pressure of (420 ± 18) mbar, when taking into account the sample-detector distance of 9.6 cm, consistent with the nominal helium pressure of ≈400 mbar. At energies higher than ≈2163 keV, i.e., the material before the current collector, the signal intensity rapidly drops to zero at all SOCs, which indicates that no lithium diffuses into the Kapton® window during the experiment showing the stability of the foil. Signals from lower energies correspond to lithium present at greater depth inside the anode electrode, i.e., towards the interface between the graphite electrode and the separator interface (s. Fig. 2d). An intensity decrease towards lower energies (i.e., towards a greater depth into the electrode) is typical for NDP spectra and mainly originates from the curvature of the energy-to-depth relation.[14]

The NDP signal of the pristine graphite anode prior to the first charging (spectrum number 1 in Fig. 6b) solely originates from the lithium-ions in the 1 M $LiPF_6$ based electrolyte that is filling the pores of the graphite electrode; however, the NDP signal is superimposed by the signal from background radiation which steeply increases below ≈600 keV. Around a depth corresponding to ≈1200 keV, a small kink in the intensity is observed, which we believe corresponds to the transition region between the graphite electrode and the separator (blue/gray interface), i.e., to the anode/separator interface; the NDP signal is higher in the glass fiber separator, as its pore volume fraction that is filled with the $LiPF_6$ electrolyte is ≈90% compared to a pore volume fraction of only ≈47% in the graphite electrode. This shows that the lithium distribution within the complete anode can be probed via NDP. During cell charging (blue spectra in Fig. 6b), the NDP signal intensity increases, which indicates a lithium enrichment across the whole graphite anode. Since NDP detects lithium regardless of its chemical state, three at first indistinguishable contributions to the lithium NDP signal are now present: (1) lithium from the $LiPF_6$ salt present in the liquid electrolyte located only in the pores of the anode and it is assumed to be constant for all SOCs (at a signal level equal to spectrum 1 in Fig. 6b); (2) lithium reversibly intercalated into the graphite particles; and, (3) irreversibly lost active lithium, bound within the SEI formed on the surface of the graphite particles. The maximum NDP signal intensity is reached at the end of the first charge (i.e., at 100% SOC), where a complete anode lithiation to LiC_6 is expected (spectrum number 3 in Fig. 6b). Upon the subsequent discharge (red voltage profile in Fig. 6a), the NDP signal intensity decreases, reaching its minimum at the end of the first discharge (spectrum number 5). At this point, the graphite anode is completely delithiated and the NDP signal can be assigned to the sum of lithium in the electrolyte pores and the lithium stored irreversibly in the SEI that was formed during the first cycle. The SEI, according to a study by Schwenke et al., that was based on graphite electrodes harvested after formation and subjected to a washing with DMC (dimethyl carbonate), mainly consists of LiF, lithium ethylene dicarbonate (LEDC), lithium methyl carbonate (LMC), and lithium ethyl carbonate (LEC).[22] At the transition between the different phases, namely between the separator and the graphite electrode as well as between the graphite electrode and the Cu-coated Kapton® window, different distinct lithium concentration levels are expected. Therefore, these transitions can be obtained from the inflection points of the NDP spectra,[10] which are traced in Fig. 6b by the differently colored segments with blue representing a part of the separator region, gray representing the graphite anode, and orange representing the Cu-coated Kapton® window. During lithium intercalation, the boundary of the graphite electrode towards the separator (blue/gray interface) is shifted towards lower energies, which implies that the electrode mass and therefore also the thickness of the electrode is increasing. This is

consistent with the literature, which shows a volume expansion of ≈10% during lithium intercalation.[23]

Quantification of the lithium concentration across the graphite electrode measured via NDP.—To quantify the lithium concentration in the SEI and the intercalated graphite, we first subtract from the NDP signals taken at different SOCs (shown in Fig. 6b) the signal contributions from the electrolyte contained within the pores of the separator and the graphite anode. This corresponds to the NDP signal from the pristine electrode (s. spectrum 1 in Fig. 6b), where lithium is only present in the electrolyte phase, based on the reasonable assumptions that (i) the void volume fraction is independent of the SOC at the applied slow cycling rate of C/16, and that (ii) the amount of formed SEI does not significantly alter the electrode void volume fraction over the only two charge/discharge cycles. In this way, NDP signals stemming from the lithium salt containing electrolyte within the electrode pores as well as undesired signals from *beta*- and *gamma*-induced background radiation are removed, so that the remaining NDP signals now only reflect the change of the lithium concentration (Δc_{Li}) that is due to the reversible intercalation in the graphite active material and due to the lithium-containing SEI. These NDP spectra corrected for the electrolyte contribution are shown in Fig. 7a.

Figure 7b shows the NDP spectra from Fig. 7a after transformation of the NDP count rate into lithium concentration in terms of Li atoms per $g_{electrode}$, plotted vs. the depth into the electrode (upper x-axis) or electrode mass loading in $mg_{electrode}$ per cm^2 (lower x-axis). The conversion of NDP signals to an absolute quantity was achieved via measuring a reference sample and by considering the fraction of the beam area that is occupied by the holes in the coin cell cap (s. Fig. 2c), as explained in detail in the Experimental section. Here, the systematic uncertainty bands of ±9.8%, arising mainly from the geometrical alignment uncertainty of the NDP measurement are shown. To convert the energy axis in Fig. 7a to the electrode mass loading or depth axis in Fig. 7b, the SRIM software was used,[15,20] considering the approximate composition of the graphite electrode vs. SOC, as outlined in the Experimental section. The energy resolutions near the electrode/current collector and near the anode/electrolyte interface are (24 ± 2) keV and (396 ± 15) keV, respectively (s. Fig. 7a). They correspond to mass loading resolutions of (0.09 ± 0.01) mg/cm^2 near the electrode/current collector and a lower resolution of (0.52 ± 0.02) mg/cm^2 at the electrode/separator interface, caused by the statistical nature of the charged-particle energy loss. Assuming a homogeneous material density of 1.7 $g/cm^3_{electrode}$, these limited mass loading resolutions translate to spatial resolutions of (0.53 ± 0.07) μm and (3.05 ± 0.12) μm, respectively (s. Fig. 7b).

As shown in Fig. 7b, rather constant lithium concentration profiles are observed for all SOCs, which indicates a homogeneous lithium accumulation across the electrode depth during battery operation. However, a small slope remains after translating the energy spectra to concentration profiles. It likely originates from the geometrical aspect ratio of the 500 μm holes in the 250 μm-thick coin cell cap, inducing an additional energy loss of the *triton* particles by scattering on the edges into the stainless-steel casing, which then could lead to a slight depletion of the *triton* signal near the graphite/current collector interface (i.e., in the region of ≈0–1.5 $mg_{electrode}/cm^2$ in Fig. 7b) and is currently being investigated in more detail. While across the graphite anode a rather constant lithium accumulation is measured, a distinct lithium enrichment at the anode surface near the current collector/electrode interface is observed over the course of cycling (i.e., an NDP signal peak near this interface), which remains even in the fully discharged state (spectrum 5 in Fig. 7b).

In the following, first the lithium concentrations measured across the graphite anode are quantitatively compared to the expected lithium concentrations based on the electrochemical data. Subsequently, the peak at the current collector/electrode interface will be quantitatively studied and verified using *ex situ* XPS.

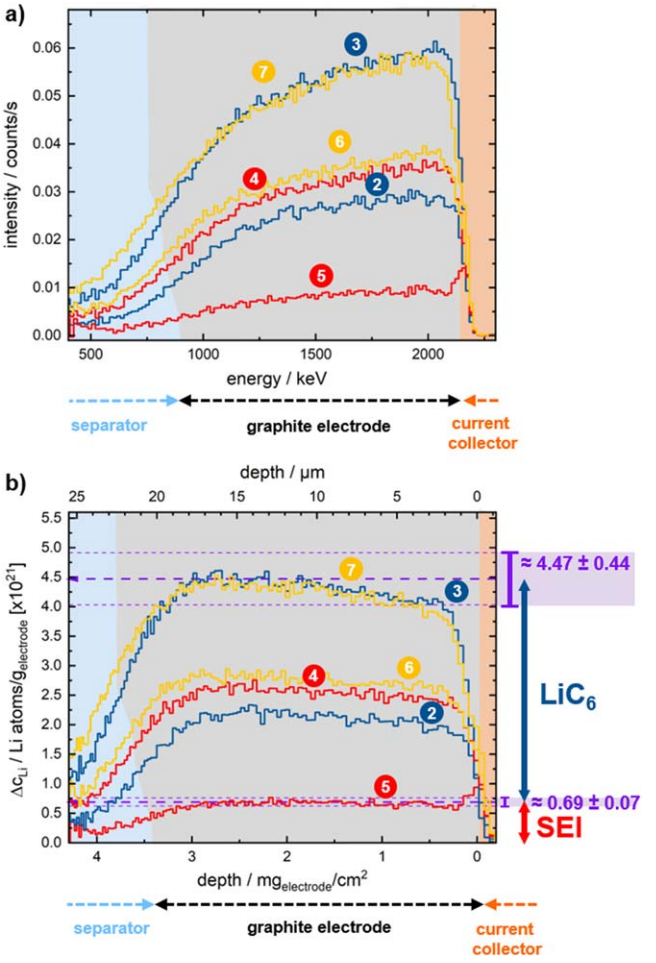

Figure 7. (a) Change of the NDP spectra with respect to the pristine state of the cell. Here, the spectra from Fig. 6b are shown after subtraction of the NDP spectrum of the pristine cell (i.e., before cycling, corresponding to spectrum 1 in Fig. 6b). (b) Transformation of the NDP signal count rate into Li concentration in terms of amount of Li atoms per $g_{electrode}$ as well as transformation of the *triton* energy into either depth into the electrode (upper x-axis) or electrode mass loading (lower x-axis). The differently numbered spectra were collected at the points marked in the charge/discharge profiles shown in Fig. 6a. Here, Δc_{Li} consists of the Li concentration levels in the electrode other than from the liquid electrolyte, which was subtracted beforehand. The Δc_{Li} concentration level at 100% SOC (spectra 3 and 7), which consists of lithium in the SEI and lithium intercalated in the graphite active material, is indicated by the upper dashed bold purple line. The concentration level measured for the fully discharged electrode (spectrum 5) after the first completed charge/discharge cycle consists only of lithium in the SEI and is marked by the lower dashed bold purple line. The concentration difference between these spectra (0% and 100% SOC) can be assigned to reversibly intercalated lithium and refers to LiC_6 formation. Systematic uncertainties of the NDP measurements are indicated as discussed in the Experimental section.

Comparison of lithium concentrations measured via NDP and estimated from the electrochemistry.—The lithium concentrations measured at 100% SOC after the first charging (spectrum 3 in Fig. 7b) and the second charging half-cycle (spectrum 7 in Fig. 7b) are both only composed of reversibly intercalated and irreversible bound lithium in the SEI, since signal from lithium in the electrolyte was eliminated by subtracting the signal obtained from the pristine anode (s. Fig. 7a). Since both spectra 3 and 7 show an almost identical lithium concentration, it can be concluded that the major part of the SEI formation was completed during the first charging, i.e., the first half-cycle. This is consistent with on-line electrochemical mass spectrometry (OEMS) analysis that shows that the gas evolution known to accompany SEI formation essentially vanishes at

the end of the first charge.[24,25] Even though the exact composition of the SEI is still under debate in the literature, the major constituents and the underlying formation mechanisms have been intensively investigated.[26–28] For example, it was found that a major pathway for reductive EC decomposition proceeds via formation of lithium ethylene dicarbonate (LEDC) and ethylene (C_2H_4),[24,29,30] which would imply the consumption of one lithium atom (i.e., its incorporation into the SEI) per one electron of irreversible charge, corresponding to a ratio of 1 Li/e^-.

Therefore, the major part of the SEI formation was assumed to take place during the first charging half-cycle, and thus the amount of lithium in the SEI is reflected by the lithium concentration of (0.69 ± 0.07) × 10^{21} Li atoms/$g_{electrode}$ in the fully discharged state after the first cycle (0% SOC, spectrum 5 in Fig. 7b). Furthermore, taking into account the lithium concentration of (4.47 ± 0.44) × 10^{21} Li atoms/$g_{electrode}$ obtained from the fully charged anode (spectra 3 and 7), the concentration of reversibly intercalated lithium was calculated to be (3.78 ± 0.37) × 10^{21} Li atoms/$g_{electrode}$ from the difference of both concentration levels (0% SOC and 100% SOC). In this way, the reversibly intercalated lithium (≈LiC_6, i.e., ≈350 mAh/$g_{graphite}$) and the irreversibly bound lithium in the SEI can be separated, as indicated by the arrows/labels at the right-hand-side of Fig. 7b.

In order to compare these values to the estimated lithium concentrations derived from the electrochemical measurements, the total mass of the graphite electrode, including PVDF binder, electrolyte, SEI, and intercalated lithium need to be considered, since NDP is sensitive to the lithium quantities per mass of matrix (i.e., per mass of the electrolyte-filled anode in this case). The mass of the electrode coating (graphite + PVDF binder) is well-known from weighing the electrode and the current collector and is (2.19 ± 0.03) mg (s. Table II). The mass of intercalated lithium can be calculated from the moles of lithium determined by the reversible capacity (25.84 μmol = 0.18 mg; s. second column of Table II). The mass of the electrolyte in the electrode pores of 1.08 mg (s. second column of Table II) was calculated from the electrode thickness of 17 μm (measured before cell assembly), the electrode porosity of 47% (calculated from electrode thickness and mass), and the electrolyte density of 1.19 g/cm^3. Finally, the mass of the SEI can be approximated from the moles of lithium that were deduced from the irreversible capacity (viz., 7.28 μmol), under the assumption that the total charge goes into the formation of LEDC with a molecular mass per lithium of 81 g_{LEDC}/mol_{Li}, resulting in 0.59 mg LEDC (from: 7.28 μmol × 81 g_{LEDC}/mol_{Li} = 0.59 mg of LEDC); note that this implicitly assumes a ratio of one lithium atom per electron irreversible charge (i.e., 1 Li/e^-) for SEI formation. Since other minor SEI components are formed, this somewhat overestimates the mass of the SEI (due to the lower mass of LiF and Li_2CO_3 per Li atom), but as the thus calculated SEI mass only constitutes ≈15% of the mass of the electrode (s. second column of Table II), this error is minor. Note that for the electrochemical calculation of the lithium concentrations, the following uncertainties based on the graphite electrode preparations were taken into account: a coating mass uncertainty of ± 0.034 mg was obtained from the standard deviation of 10 individual weight measurements. Furthermore, a thickness uncertainty of ±2 μm and an electrolyte concentration error of ±0.01 mol/L was assumed. The overall mass of the electrode would thus be estimated to be (4.04 ± 0.23) mg at the end of the first charge (≡$m_{electrolyte}$ + $m_{graphite+PVDF}$ + $m_{Li\text{-}int.}$ + $m_{Li\text{-}SEI}$, s. Table II) and (3.86 ± 0.23) mg at the end of the first discharge (≡$m_{electrolyte}$ + $m_{graphite+PVDF}$ + $m_{Li\text{-}SEI}$, s. Table II).

In a first step, we will now determine whether the amount of reversibly intercalated lithium that can be quantified precisely from the measured discharge capacity is indeed in quantitative agreement with the NDP data analysis. Taking into account that the electrochemically measured reversible capacity of ≈348 mAh/$g_{graphite}$ in the first discharge (s. Fig. 6a) must correspond to a ratio of 1 Li/e^-, this equates to 25.84 μmol lithium (≡1.56 × 10^{19} Li atoms). Then, the expected lithium concentration ($NDP_{Li\text{-}int.}$) would be the ratio of the calculated lithium atoms divided by the estimated electrode mass of (4.04 ± 0.23) mg in the fully charged state, which equates to $NDP_{Li\text{-}int.}$ = (3.86 ± 0.29) × 10^{21} Li atoms/$g_{electrode}$ (s. Table II), i.e., the concentration can be estimated with an accuracy of 7.5%. This value corroborates well with the reversible lithium concentration obtained from the NDP measurements which was found to be (3.78 ± 0.37) × 10^{21} Li atoms/$g_{electrode}$, thereby confirming that, within the stated errors, the here presented *operando* NDP cell design allows for a quantitative NDP measurement while at the same time providing good electrochemical performance.

In a second step, we will now determine whether the amount of lithium in the SEI measured by NDP, namely the determined (0.69 ± 0.07) × 10^{21} Li atoms/$g_{electrode}$ at the end of the first discharge (s. spectrum 5 in Fig. 7b), is consistent with what one would expect on the basis of one lithium atom per electron of irreversible charge (i.e., 1 Li/e^-) for SEI formation. Assuming the latter and considering the electrochemically observed irreversible capacity of ≈98 mAh/$g_{graphite}$ (i.e., the difference between the first charge and the first discharge capacity in Fig. 6a), the estimated amount of lithium irreversibly bound to the SEI would amount to 7.28 μmol (≡4.38 × 10^{18} Li atoms). Thus, the expected NDP signal from the SEI ($NDP_{Li\text{-}SEI}$) would correspond to the ratio of these estimated lithium atoms divided by the estimated electrode mass of (3.86 ± 0.23) mg in the fully discharged state (spectrum 5 in Fig. 7b), which equates to $NDP_{Li\text{-}SEI}$ = (1.14 ± 0.09) × 10^{21} Li atoms/$g_{electrode}$ (s. Table II). This value is within measurement uncertainties significantly larger than the concentration value of (0.69 ± 0.07) × 10^{21} Li atoms/$g_{electrode}$ measured at 0% SOC using *operando* NDP (spectrum 5 in Fig. 7b). Therefore, this finding suggests that the Li/e^- ratio for SEI formation determined in our experimental setup is much lower than our assumed ratio of 1 Li/e^-, and that the Li/e^- ratio determined by our *operando* NDP measurements would only be (0.61 ± 0.08). Possible explanations for this finding are that the intrinsic Li/e^- ratio during SEI formation is indeed significantly lower than 1 and/or that a notable fraction of the SEI products are soluble in the electrolyte and are thus not immobilized in the SEI, which is currently being investigated in a different study.

Analysis of the NDP lithium peak at the current collector/electrode interface.—Apart from the previously discussed lithium concentration signals within the graphite anode, also an apparent enrichment of lithium at the current collector/electrode interface is observed in the NDP spectrum at the end of the first discharge (spectrum 5 in Fig. 7). In the second charging cycle, this peak remains present and is superimposed with the NDP signal stemming from lithium intercalation, as can be seen upon closer inspection of spectra 6 and 7. The NDP signal peak at the interface between the graphite electrode and the Cu-coated Kapton® window indicates that there is a thin layer at this interface that is enriched in lithium. While this peak could be due to an increased SEI formation or an incomplete delithiation of graphite at this interface, a recent *operando* NDP study by Lv et al.[10] showed a lithium intercalation into the copper current collector. To verify that this is also the case in the herein investigated study, we mimicked the charging process in a second experiment in the *operando* cell by slowly sweeping the potential of a pure current collector, i.e., the Cu-coated Kapton® foil without graphite coating, to a potential region where intercalation of lithium in copper might occur. Here, the counter electrode was a lithium metal foil, and the interface was subsequently analyzed by *in situ* NDP and by *ex situ* XPS.

In order to confirm that the peak at the current collector interface really stems from lithium intercalation into copper, we recorded *in situ* NDP spectra of an *operando* NDP cell assembled with the bare Cu-coated Kapton® foil as WE and a metallic lithium CE. The potential of the WE was swept slowly from OCV (≈3 V vs. Li^+/Li) to 20 mV vs. Li^+/Li in a total time of ≈16 h, after which an *in situ* NDP spectrum was recorded (red line in Fig. 8). For comparison, a nominally identical cell was also measured by *in situ* NDP at its OCV, i.e., without polarizing the WE negatively (s. black line in

Table II. Calculations of the expected lithium concentrations within the *operando* cell, originating from lithium concentrations in the electrolyte, from reversibly intercalated lithium in the graphite active material, and from lithium bound irreversibly in the SEI. The mass contributions to the electrode (second column) and the lithium amount in the electrode (third column) were determined as follows: (i) electrolyte mass and lithium amount from the 17 μm thickness, the 47% porosity of the electrode, and the LP57 electrolyte density of 1.19 g/cm^3 ; (ii) graphite + PVDF from weight measurements; (iii) the intercalated lithium mass was calculated from the reversible capacity of the first cycle; (iv) the SEI mass and lithium amount were estimated assuming a ratio of 1 Li/e$^-$ and pure LEDC (81 g_{LEDC}/mol_{Li}). Based on these values, the expected NDP signals from the lithium in the electrolyte, intercalated in the graphite ($NDP_{Li\text{-}int.}$), and bound in the SEI ($NDP_{Li\text{-}SEI}$) are shown in the fourth column. Uncertainties are based on a coating mass error of ±0.034 mg, a thickness error of ±2 μm, and an assumed electrolyte concentration error of ±0.01 mol/L.

	mass contribution [mg]	Li amount [μmol]	expected lithium concentration [Li atoms/$g_{electrode} \times 10^{21}$]
1 M $LiPF_6$ electrolyte	1.08 ± 0.19	0.90 ± 0.16	0.17 ± 0.06
graphite + PVDF coating	2.19 ± 0.03	—	—
lithium intercalated in graphite based on ≈348 mAh/$g_{graphite}$ reversible capacity in the first *operando* NDP cycle; s. Fig. 2a	0.18 ± 0.003	25.84 ± 0.40	$NDP_{Li\text{-}int.}$= 3.86 ± 0.29
lithium bound to SEI based on ≈98 mAh/$g_{graphite}$ irrev. cap. during first *operando* NDP cycle and assuming that the SEI consists purely of LEDC	0.59 ± 0.01	7.28 ± 0.11	$NDP_{Li\text{-}SEI}$ = 1.14 ± 0.09

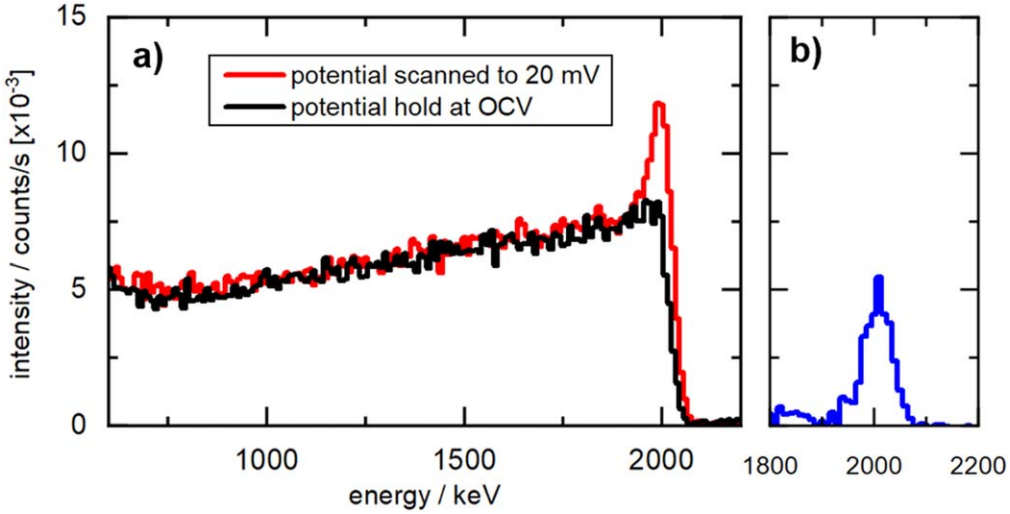

Figure 8. (a) *In situ* NDP spectra of two electrodes consisting of a 7.5 μm Kapton® foil covered with a 100 nm-thick Cu current collector and assembled against a metallic lithium counter electrode in the *operando* NDP cell. The potential of one electrode (red) was swept gradually from OCV (≈3 V vs. Li^+/Li) to 20 mV vs. Li^+/Li within 16 h; the second cell (black) was not cycled and measured at OCV. (b) Intensity difference between the two spectra from (a) showing the additional signal caused by alloy formation between the copper current collector and lithium.

Fig. 8). Only the cell scanned to 20 mV vs. Li^+/Li showed a pronounced peak at the energy corresponding to the copper interface (at ≈2000 keV in this case, due to a slightly higher He pressure in the NDP sample chamber), confirming that the peak measured during the *operando* measurement shown in Figs. 6b and 7 is due to lithium intercalation into the Cu current collector.[10] As shown in Fig. 8, the energy resolution of the NDP signal near the current collector is ≈25 keV, which corresponds to a depth resolution of ≈200 nm in Cu.[15] Within the Gaussian-shaped signal no internal structure is observed, which indicates a lithium distribution thinner than the NDP resolution. Although the lithium alloying depth profile can not be resolved using NDP, the integral of the isolated lithium alloying signal, as shown as spectra difference in Fig. 8b, allows to quantify the total lithium that was alloyed into the 100 nm-thick copper current collector layer to be $(1.77 \pm 0.17) \times 10^{16}$ atoms/cm^2 or (0.20 ± 0.02) μg_{Li}/cm^2. This value corroborates well with earlier findings of Lv et al.,[10] where they report the intercalation of lithium in a conventional 10 μm-thick Cu current collector. Comparing this finding to the total lithium amount of ≈160 μg_{Li}/cm^2 that was reversibly intercalated in the graphite electrode (≈25.84 μmol_{Li} = ≈181 μg_{Li} (s. Table II), taking into account the anode diameter of 12 mm) it shows that only ≈0.1% of the reversibly intercalated lithium amount, and is thus quasi non-detectable by electrochemical charge/discharge measurements. We therefore measured the lithium concentration using XPS as a complementary characterization technique on identical *ex situ* copper current collector anodes, which provides a depth resolution of a few nanometers. In the following, an XPS analysis on the lithiated copper film semi-quantitatively confirms the findings obtained *via* NDP.

***Analysis of lithium insertion into the copper current collector via* ex situ *XPS*.—**Figure 9a and b show the *ex situ* XPS spectra for Li 1 s and Cu 3p, respectively, recorded on a Cu-coated Kapton® foil electrode that was polarized to 20 mV vs. Li^+/Li in a conventional coin cell with a metallic lithium counter electrode. The cell underwent the same cycling procedure as that used for the *ex situ* NDP measurements described in the previous section. The Cu-coated Kapton® foil was harvested from the coin cell in a glovebox and inertly transferred under inert conditions into the XPS.

First, the surface of the Cu current collector was cleaned by sputtering to a depth of 0.6 nm with an Ar^+ ion gun, followed by recording an XPS spectrum. Afterwards, ≈1.8 nm per sputtering cycle were etched, recording Li 1s and Cu 3p spectra after each cycle. With increasing depth into the sample, the lithium

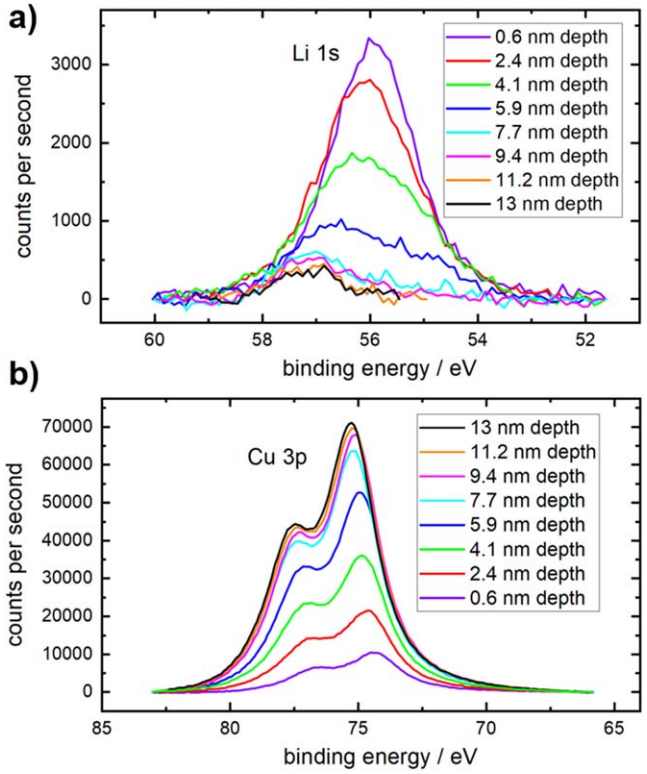

Figure 9. (a) Cu 3p and (b) Li 1s XPS spectra of an electrode consisting of a 7.5 μm Kapton® foil coated with a 100 nm-thick Cu layer. The potential of the electrode was swept from 3 V vs. Li^+/Li to 20 mV vs. Li^+/Li within 16 h; subsequently, the cell was opened in a glovebox and then transferred under inert conditions into the XPS. XPS spectra were taken after etching the surface to different depths, clearly showing that after removal of the Li-containing SEI (≈6 nm), the lithium signal is still visible. This suggests that Li electrochemically alloyed with the Cu from the current collector.

signal continuously decreases, whereas the copper signal increases (s. Fig. 9). At potentials below ≈0.8 V vs. Li^+/Li, it is expected that electrolyte is reductively decomposed[24,31] on the copper surface, forming an SEI similar to that on graphite particles in an LIB graphite anode.[32] The Cu 3p signal measured after the first two sputter cycles, corresponding to sputter depths of ≈0.6 and ≈2.4 nm,

Table III. Atomic ratio of lithium and copper within the copper current collector estimated from the XPS spectra (s. Fig. 9) recorded at different sputtering depths. Only sputtering depths beyond the ≈5.9 nm are considered, as there Cu and Li are the majority surface species.

at% Li	at% Cu	depth/nm
16	84	7.7
13	87	9.4
9	91	11.2
7	93	13.0

respectively, is still rather weak (s. black and red lines in Fig. 9), indicating the presence of an SEI layer. Since the Cu 3p signal is strongly increasing after the third sputtering cycle (at a depth of ≈4.1 nm, s. green line) and stays roughly constant after the fourth sputter cycle (≈5.9 nm, s. dark blue line), suggesting that the complete SEI is at latest removed after etching to a depth of ≈6 nm. SEI thicknesses on graphite are reported to range from 2 to several 10's of nanometers,[31,33] which is consistent with our observation. Sputtering into deeper layers, i.e., between ≈6 and ≈1 nm (represented by the blue, turquois, magenta and orange lines), the Li 1s signal is still clearly visible. These observations suggest that some lithium must have diffused into the copper phase forming a Cu-Li alloy. The Cu-Li phase diagram shows a maximum solubility of lithium in copper of up to ≈22 at%,[34] and Klemm and Volavsek[35] concluded that the lithium solubility extends up to ≈20 at% (or Cu_4Li), based on experiments reacting lithium with copper powder at temperatures from about 300 °C to 800 °C. Peñaloza et al.[36] reported on a Li-Cu alloy which they obtained by electroplating lithium from a LiCl/KCl salt melt onto an electrolytic copper cathode and Rehnlund et al.[37] could detect lithium traces in a copper current collector that they stored in contact with a lithium foil for several days at 50 °C.

Table III shows the atomic ratios of lithium and copper as a function of sputtering depth into the 100 nm-thick copper current collector layer, starting at a sputter depth of ≈7.7 nm, where only copper and lithium alloyed into copper are main species, i.e., where the SEI has been completely removed. At this point, the lithium concentration is ≈16 at%, which is reduced to ≈7 at% at a sputter depth of ≈13 nm. The concentration over this approximately 7.2 nm wide region is ≈11 at% lithium and ≈89 at% copper. Considering an atomic density of copper of $\approx 8.5 \times 10^{22}$ atoms/cm^3 and assuming that the atomic density does not change significantly upon lithiation, the total atoms of lithium in the copper foil in this 7.2 nm wide region can be estimated to be on the order of 0.6×10^{16} atoms/cm^2. While this clearly underestimates the total lithium concentration, since it only accounts for the lithium concentration between ≈7.7 and ≈13 nm, its magnitude is consistent with the lithium concentration determined by the *in situ* NDP analysis (1.77×10^{16} atoms/cm^2).

As copper foil current collectors are ubiquitously used in commercial LIBs, the rate and the extent of the electrochemical lithiation of a copper current collector during charging is expected to be very low, i.e., negligible compared to the intercalation capacity of a typical graphite electrode. Under the assumption that a 10 μm-thick copper foil used as current collector would be lithiated to form a Li-Cu alloy with ≈20 at% Li, the associated charge would result in an areal capacity of 0.95 mAh/cm^2. This would correspond to ≈38 % of the capacity of a typical graphite anode (assuming an areal capacity of 2.5 mAh/cm^2), which would be quite significant and there is no experimental data which would suggest that this occurs. Thus, the lithiation of copper must be a very slow process. While we have not sputtered deep enough to determine the maximum penetration of lithium into the copper current collector, Table III suggests that the diffusion of lithium into the Cu current collector does not extend much beyond ≈10 nm. Assuming this process to be driven by diffusion, the diffusion time, τ, should be proportional to the square of the diffusion distance x. Considering that the Cu current collector in these experiments was at a potential below 250 mV vs. Li^+/Li for 14 h, and assuming that this is low enough to drive lithium alloying into Cu, a lithium penetration of ≈1 μm into the copper foil would require ≈14^4 h or more than 4 years. This time scale is far beyond typical charging intervals of a LIB, which is why a parasitic lithiation of an anode current collector would generate too little charge to be measured electrochemically.

Conclusions

In this work, we introduce a newly developed cell setup suitable for *operando* Neutron Depth Profiling (NDP) measurements. We present *operando* NDP data recorded during formation of a conventional graphite electrode with a reasonable areal capacity of ≈0.62 mAh/cm^2 (corresponding to a thickness of ≈(17 ± 2) μm) at a rate of ≈C/16. To the best of our knowledge, this is the first study proving that the cycling performance in an *operando* NDP lithium-ion battery (LIB) cell is comparable to that of a standard laboratory coin cell. This was accomplished by using a thin Kapton® window permeable for *triton* particles together with a specially designed coin cell cap that is modified to contain a pattern of holes with a diameter of 500 μm in order to maximize the NDP signal while providing a good contact pressure on the electrodes. This design yielded good cell performance and, furthermore, it was shown to guarantee a homogenous lithiation across the entire electrode. A cell design with a more commonly used single window with a diameter of 4 mm was found to result in incomplete lithiation of the graphite active material in the center region of the window, even at a very slow charging rate of C/15, caused by the low and inhomogenous compression of the electrodes across the window area. However, since the fraction of the electrode outside the 4 mm window area is large compared to the window area, the cell voltage profile and the specific capacity gave no clear indication of the inhomogenous lithiation across the window area, so that NDP measurements in this configuration would obviously not yield data which could be correlated with the cell voltage profile and the measured state-of-charge. This underlines the importance of obtaining representative electrochemistry in *operando* cells, particularly in the window region.

By subtracting the NDP signal of a reference cell, it was possible to differentiate between lithium contained in the electrolyte, and additional lithium accumulating in the electrode upon cell cycling. Furthermore, we could distinguish between both irreversibly bound lithium within the SEI and reversibly intercalated lithium in the graphite active material, and also quantify the lithium concentrations in each case within a systematic uncertainty of ±9.8%. As outlined in our study, this rather large error results mostly from the uncertainty in alignment of the grid pattern of the holes with the neutron beam.

Within the here defined experimental errors, the concentration of reversibly intercalated lithium determined via NDP was found to be in excellent agreement with the electrochemically measured reversible capacity, for which a well defined ratio of 1 Li/e$^-$ is known. However, the lithium concentration observed at the end of the first charge/discharge cycle, corresponding to lithium bound in the SEI, was shown to be significantly lower than what one would calculate based on the expected 1 Li/e$^-$ ratio that is implied by the known electrolyte decomposition mechanisms. Instead, the NDP data suggest a ratio of (0.61 ± 0.08) Li/e$^-$, which either indicates electrochemical SEI formation reactions with an average ratio of $<$1 Li/e$^-$ or dissolution of lithium-containing SEI species after or during SEI formation. A detailed interpretation of this finding will be provided in a future study, which is currently in progress.

During slow charging of the cell, an increased lithium concentration at the interface between the graphite electrode and the copper current collector was identified which could be assigned to the electrochemical alloy formation between lithium and the surface-near region of the copper current collector; this was verified by *ex*

situ XPS sputter profiling. The quantitative amount of lithium detected via NDP was in agreement with the lithium amount estimated by XPS depth profiles, and corresponds to only ≈0.1% of the reversibly intercalated lithium, making it quasi non-detectable by electrochemical charge/discharge measurements.

The herein presented *operando* NDP cell design can be a useful tool to investigate dynamic lithium transport in battery electrodes during operation, at the same time allowing for a spatial resolution of concentration changes. Possible future applications could therefore be the determination of transport parameters for lithium (e.g., diffusion coefficients), which is usually a very challenging task, using specially designed model electrodes. Furthermore, an interesting study would be the investigation of lithium plating during fast-charging (e.g., on graphite), which is currently under progress in our group. For such an experiment, the cell has to deliver a good electrochemical performance also at high C-rates, and possible artefacts stemming from a lack of compression in a large hole, as we have proven to be the case in the course of this study, must be avoided. Especially, the spatial resolution is here of crucial importance, since the occurrence of lithium concentration gradients would presumably lead to an onset of lithium plating close to the separator/electrode interface. Another interesting application could be the exploration of the lithium plating and stripping processes on lithium metal anodes or in so called "anode-free" lithium-ion cells that are recently gaining increasing attention as an alternative to graphite anode-based LIBs.[38] Apart from battery applications, the presented design can be applied for many applications containing liquids or sensitive materials, which are hard to measure using NDP.

Acknowledgments

The authors want to thank SGL Carbon for providing the sieved graphite active material, and Daniel Pritzl for his assistance in recording the XPS sputter profiles. The Heinz Maier-Leibnitz Zentrum (MLZ) is kindly acknowledged for the possibility to use the high flux neutron beam at the PGAA facility. FL and MT gratefully acknowledge funding by the BMBF (Federal Ministry of Education and Research, Germany) for their financial support under the auspices of the "'ExZellTUM II" project (grant number 03XP0081) and the "N4DP" project (grant number 05K16WO1), respectively.

ORCID

Fabian Linsenmann https://orcid.org/0000-0001-8788-2584

References

1. R. G. Downing, R. F. Fleming, D. H. Vincent, and A. Arbor, *Nucl. Instruments Methods Phys. Res.*, **218**, 47 (1983).
2. S. C. Nagpure, R. G. Downing, B. Bhushan, S. S. Babu, and L. Cao, *Electrochim. Acta*, **56**, 4735 (2011).
3. ATIMA, Calculation based on ATIMA. ATIMA is a webtool for calculating energy loss in matter, developed by H. Weick at GSI, https://web-docs.gsi.de/~weick/atima/.
4. S. Whitney, S. R. Biegalski, Y. H. Huang, and J. B. Goodenough, *J. Electrochem. Soc.*, **156**, A886 (2009).
5. M. Wetjen, M. Trunk, L. Werner, R. Gernhäuser, B. Märkisch, Z. Révay, R. Gilles, and H. A. Gasteiger, *J. Electrochem. Soc.*, **165**, A2340 (2018).
6. J. Wang, D. X. Liu, M. Canova, R. G. Downing, L. R. Cao, and A. C. Co, *J. Radioanal. Nucl. Chem.*, **301**, 277 (2014).
7. X. Zhang, T. W. Verhallen, F. Labohm, and M. Wagemaker, *Adv. Energy Mater.*, **5**, 1500498 (2015).
8. D. X. Liu, L. R. Cao, and A. C. Co, *Chem. Mater.*, **28**, 556 (2016).
9. T. W. Verhallen, S. Lv, and M. Wagemaker, *Front. Energy Res.*, **6** (2018).
10. S. Lv, T. Verhallen, A. Vasileiadis, F. Ooms, Y. Xu, Z. Li, Z. Li, and M. Wagemaker, *Nat. Commun.*, **9**, 1 (2018).
11. D. X. Liu, J. Wang, K. Pan, J. Qiu, M. Canova, L. R. Cao, and A. C. Co, *Angew. Chemie - Int. Ed.*, **53**, 9498 (2014).
12. T. C. Bach, S. F. Schuster, E. Fleder, J. Müller, M. J. Brand, H. Lorrmann, A. Jossen, and G. Sextl, *J. Energy Storage*, **5**, 212 (2016).
13. Y. Hamon, T. Brousse, F. Jousse, P. Topart, P. Buvat, and D. M. Schleich, *J. Power Sources*, **97–98**, 185 (2001).
14. M. Trunk, M. Wetjen, L. Werner, R. Gernhäuser, B. Märkisch, Z. Révay, H. A. Gasteiger, and R. Gilles, *Mater. Charact.*, **146**, 127 (2018).
15. J. F. Ziegler, M. D. Ziegler, and J. P. Biersack, *Nucl. Instruments Methods Phys. Res.*, **268**, 1818 (2010).
16. D. Jantke, R. Bernhard, E. Hanelt, T. Buhrmester, J. Pfeiffer, and S. Haufe, *J. Electrochem. Soc.*, **166**, A3881 (2019).
17. L. Werner, M. Trunk, R. Gernhäuser, R. Gilles, B. Märkisch, and Z. Révay, *Nucl. Instruments Methods Phys. Res. Sect. A Accel. Spectrometers, Detect. Assoc. Equip.*, **911**, 30 (2018).
18. Z. Révay, P. Kudějová, K. Kleszcz, S. Söllradl, and C. Genreith, *Nucl. Instruments Methods Phys. Res. Sect. A Accel. Spectrometers, Detect. Assoc. Equip.*, **799**, 114 (2015).
19. NIST, Official NIST Certificate of Analysis, https://www-s.nist.gov/srmors/certificates/2137.pdf.
20. J. F. Ziegler, *Handbook of Helium Stopping Powers and Ranges in All Elements* (Pergamon Press, New York) 4 (1977).
21. S. J. Harris, A. Timmons, D. R. Baker, and C. Monroe, *Chem. Phys. Lett.*, **485**, 265 (2010).
22. K. U. Schwenke, S. Solchenbach, J. Demeaux, B. L. Lucht, and H. A. Gasteiger, *J. Electrochem. Soc.*, **166**, A2035 (2019).
23. M. Winter, G. H. Wrodnigg, J. O. Besenhard, W. Biberacher, and P. Novák, *J. Electrochem. Soc.*, **147**, 2427 (2002).
24. B. Zhang, M. Metzger, S. Solchenbach, M. Payne, S. Meini, H. A. Gasteiger, A. Garsuch, and B. L. Lucht, *J. Phys. Chem. C*, **119**, 11337 (2015).
25. M. Metzger, B. Strehle, S. Solchenbach, and H. A. Gasteiger, *J. Electrochem. Soc.*, **163**, A798 (2016).
26. D. Aurbach, Y. Ein-Ely, O. Chusid, Y. Carmeli, M. Babai, and H. Yamin, *J. Electrochem. Soc.*, **141**, 603 (1994).
27. P. Verma, P. Maire, and P. Novák, *Electrochim. Acta*, **55**, 6332 (2010).
28. M. Nie, D. Chalasani, D. P. Abraham, Y. Chen, A. Bose, and B. L. Lucht, *J. Phys. Chem. C*, **117**, 1257 (2015).
29. D. Aurbach, M. L. Daroux, P. W. Faguy, and E. Yeager, *J. Electrochem. Soc. Soc.*, **134**, 1611 (1997).
30. R. Bernhard, M. Metzger, and H. A. Gasteiger, *J. Electrochem. Soc.*, **162**, 1984 (2015).
31. K. Edström, M. Herstedt, and D. P. Abraham, *J. Power Sources*, **153**, 380 (2006).
32. J. Shu, M. Shui, F. Huang, D. Xu, Y. Ren, L. Hou, J. Cui, and J. Xu, *Electrochim. Acta*, **56**, 3006 (2011).
33. J. E. Owejan, J. P. Owejan, S. C. Decaluwe, and J. A. Dura, *Chem. Mater.*, **24**, 2133 (2012).
34. A. D. Pelton, *Bull. Alloy Phase Diagrams*, **7**, 142 (1986).
35. W. Klemm, B. Volavsek, and Z Anorg, *Allg. Chem.*, **296**, 184 (1958).
36. A. Peñaloza, M. Ortíz, and C. H. Wörner, *J. Mater. Sci. Lett.*, **14**, 511 (1995).
37. D. Rehnlund, F. Lindgren, S. Böhme, T. Nordh, Y. Zou, J. Pettersson, U. Bexell, M. Boman, K. Edström, and L. Nyholm, *Energy Environ. Sci.*, **10**, 1350 (2017).
38. R. Weber, M. Genovese, A. J. Louli, S. Hames, C. Martin, I. G. Hill, and J. R. Dahn, *Nat. Energy*, **4**, 683 (2019).

3.2.2 Spatially- and Time-Resolved Detection of Lithium Plating Using *Operando* NDP

This section presents the manuscript *"Spatially- and Time-Resolved Detection of Lithium Plating During Fast-Charging of a Graphite-Based Lithium-Ion Battery"*.

Reducing the charging time for electric vehicles (EVs) is one crucial requirement to increase customers acceptance and to enable mass market penetration.[227, 228] The main reason that prevents fast-charging of LIB cells is the hazard of metallic lithium being deposited on the graphite anode, so-called lithium plating, which leads to accelerated battery ageing and also presents a safety risk.[229] Lithium plating becomes thermodynamically possible during charging (lithiation of the anode) of a LIB cell, if the local electrode potential falls below 0 V *vs.* Li^+/Li, which can be caused by ohmic, mass transport (liquid or solid), and/or kinetic overpotentials at the graphite anode.[230, 231] Possible reasons for overpotentials due to mass transport resistances in the liquid phase are lithium-ion concentration gradients that develop across the thickness of the electrode during lithium intercalation which is favored by fast charging rates, high electrode loadings, low electrode porosities, and high electrode tortuosities.

Operando detection of lithium plating in combination with spatial information about the location within the electrode is extremely challenging. Employing the novel cell design described in section 3.2.1, we managed to visualize the lithium concentration change across a graphite electrode during fast-charging using *operando* Neutron Depth Profiling (NDP). This was made possible by two critical factors: 1) the excellent high rate performance of the newly designed operando NDP cell due to the homogeneous cell stack compression afforded by the 500 µm (and later 300 µm) diameter hole pattern; 2) the isotopic enrichment of ^6Li in the electrolyte and the $LiFePO_4$ counter electrode, which allowed to reduce the NDP spectrum acquisition time from ≈1 h to ≈2 min. Furthermore, since the viewing depth of *operando* NDP is limited to ≈25-30 µm, thin graphite electrodes had to be used, in which case, however, high current densities and high charging rates are required to generate large concentration gradients in the electrolyte within the pores of the graphite electrode. Therefore, in order to provoke severe lithium

plating already at lower C-rates (2 C in this study), the conductive lithium salt concentration in the electrolyte was reduced from the commonly employed 1 M to 0.31 M $LiPF_6$.

Based on the above considerations, *operando* NDP could be used to follow the lithium concentration evolution across a graphite electrode during cycling, gradually increasing the charging (graphite lithiation) rate from C/4, C/2, 1 C to 2 C, keeping the discharging rate at C/4 to assure a complete delithiation of the graphite electrode. While charging rates of up to 1 C result in approximately homogeneous lithium concentration profiles across the graphite electrode, the lithium concentration across the thickness of the electrode becomes very inhomogeneous during a 2 C charge with high lithium concentration towards the separator/electrode and low concentration at the electrode/current collector interface. The lithiation degree of particles close to the electrode/current collector interface reaches a maximum of ≈30 % (100 % ≙ LiC_6). Since these parts of the electrode are only partially lithiated, but the lithium amount corresponding to close to 100 % of the theoretical graphite electrode capacity was exchanged, we conclude that lithium plating must have occurred during the 2 C charging process. This hypothesis is supported by the fact that in an open-circuit voltage rest after the 2 C charge, the lithium concentration equilibrates across the electrode thickness within only ≈20 min, indicating dissolution and redistribution of plated lithium.

Author contributions

F.L. and P.R. developed the cell setup, ^{6}Li-enrichment process, and performed all electrochemical tests. F.L., P.R., M.T., and R.G. developed the *operando* cell holder. F.L., P.R., and M.T. conducted the *operando* NDP measurements at the NIST Center for Neutron Research (NCNR), Gaithersburg (MD, USA). J.W. assisted in operating the NDP beamline at the NCNR. The manuscript was written by F.L., M.T., and P.R. All authors discussed the data and commented on the results.

Spatially- and Time-Resolved Detection of Lithium Plating During Fast-Charging of a Graphite-Based Lithium-Ion Battery

Fabian Linsenmann,[1,#] Philip Rapp,[1] Markus Trunk,[2, 3] Jamie Weaver,[4] Roman Gernhäuser,[2] Bastian Märkisch,[2] and Hubert A. Gasteiger[1]

[1] Chair of Technical Electrochemistry, Department of Chemistry and Catalysis Research Center, Technische Universität München, Lichtenbergstr. 4, 85748 Garching

[2] Particle Physics at Low Energies, *Physics Department*, Technische Universität München, James-Franck-Str. 1, 85748 Garching

[3] Heinz Maier-Leibnitz-Zentrum, Technische Universität München, Lichtenbergstr. 1, 85748 Garching

[4] Material Measurement Laboratory, National Institute of Standards and Technology, Gaithersburg, Maryland, 20899

[#]corresponding author

The fast-charging capability of lithium-ion batteries (LIBs) is considered a key enabler for a widespread adoption of electric mobility. State-of-the-art liquid electrolyte-based LIBs can only be fast-charged to ≈ 80 % state-of-charge (SOC), after which the charging power must be strongly decreased in order to avoid degradation of the cell performance. Therefore, charging times of several minutes, which would be comparable to refuelling a combustion engine vehicle, remain unfeasible. The rate limiting factor is the negative graphite electrode, where lithium is being intercalated during battery charging. Fast-charging at a high SOC carries the risk for the deposition of metallic lithium on the surface of the graphite particles instead of intercalating lithium-ions, which reduces battery lifetime and poses severe safety hazards due to potential cell short-circuiting by lithium dendrites. In this study, we for the first time directly visualize lithium plating during fast-charging in an operating cell by monitoring the spatially-resolved lithium concentration change across a graphite electrode using time-resolved *operando* Neutron Depth Profiling (NDP).

Besides expanding the battery size, an alternative approach to reduce customers range anxiety and to achieve mass market penetration of electric vehicles (EVs) is to increase the charging power, and thus, to significantly lower charging times.[1, 2] *E.g.*, the US Advanced Battery Consortium targets fast-charging of EV batteries in 15 minutes to 80 % state-of-charge (SOC) by 2023,[3] which would correspond to a required constant charging power of 272 kW for a 85 kWh EV. In April 2019, Tesla announced that a charging time reduction of 25 % could be achieved for current Tesla models after issuing a software update that pre-conditions the battery by warming-up the cells allowing them to accept a higher charging rate.[4]

To date, commercial lithium-ion battery (LIB) cells are still almost exclusively based on graphite as an anode active material.[5, 6] Apart from its relatively high practical capacity of ≈ 355 mAh $g^{-1}_{graphite}$, the low average discharge potential is what enables the high energy density of the electrode.[7] However, the low anodic potential also limits the charging currents to prevent metallic lithium deposition on the surface of the graphite active material particles, so-called lithium plating.[8] Lithium plating can thermodynamically occur in regions of the electrode where the potential drops below 0 V *vs.* Li^+/Li during intercalation.[9] Driving forces for lithium plating are polarizations caused by impeded charge transfer (kinetic overpotentials[10]), limited lithium-ion transport through the electrolyte or the solid active material phase (mass transport overpotentials[11]), and/or increased ohmic resistances at high current rates (ohmic overpotentials), which are essential for fast-charging.[12] Thus, the most straightforward way to improve the fast-charging capability of an electrode is to reduce the active material loading,[13] decrease the MacMullin number of the electrode, *i.e.*, the ratio of tortuosity and porosity,[14] and to avoid low temperatures during charging, which lower electrolyte conductivity and slow down mass transport and charge transfer kinetics.[15, 16] Furthermore, the urge to maximize the energy density on cell level by narrowing the capacity balancing between cathode and anode increases the probability for lithium plating, especially in combination with uneven current distributions, *e.g.*, due to coating defects or uneven pressure distribution.[17]

Plated lithium is highly reactive, and therefore provokes irreversible reactions with the electrolyte which leads to lithium inventory loss and SEI growth, resulting in impedance build-up.[16] These ageing processes can

strongly reduce the lifetime of a cell. Severe lithium plating also incorporates a serious safety hazard because lithium dendrites can short-circuit a battery cell, which might trigger a thermal runaway of a whole battery pack.[18]

Detecting lithium plating

Studying lithium plating in a battery cell is very challenging as *post-mortem* diagnostics usually do not reflect the electrode state during operation since the chemical system is altering over time. Plated lithium can react with electrolyte and is thermodynamically favoured to chemically intercalate into partially lithiated graphite particles, and to dissolve and redistribute across the graphite electrode, which occurs on a timescale of minutes at room temperature after deposition on the particle surface.[19, 20] Hence, *in situ* or ideally *operando* techniques are necessary to elucidate and follow lithium plating mechanisms in a LIB without harming the cell chemistry. There are diagnostic approaches that allow probing electrochemical processes without opening the cell, and live during cell operation, respectively. Electrochemically-based methods can be used to indirectly trace back the occurrence of lithium plating *via* precisely measuring coulombic efficiency,[18] analysing the shape of the full-cell voltage profile,[19, 21, 22, 23] or probing the graphite electrode potential by means of a reference electrode.[24, 25] While these methods offer the advantage of being quick and comparatively easy to implement, no direct information on the exact plating onset potential, the amount of plated lithium, and the location within an electrode can be obtained. In the literature, there are few reports employing advanced analytical techniques, which are suitable to detect plated lithium, such as electron paramagnetic resonance spectroscopy (EPR),[26, 27] nuclear magnetic resonance spectroscopy (NMR),[28] microcalorimetry,[29] or thickness measurements *via* laser triangulation.[30]

However, and to the best of our knowledge, only one study presents a time-resolved and also quantitative detection of lithium plating.[27] The main reason for the occurrence of lithium plating during fast-charging of a graphite anode at room temperature are lithium-ion concentration gradients forming across the depth of the electrode. This is the result of lithium-ions being depleted in the vicinity of the current collector due to limited mass transport,[13] which can be modeled[31] using fundamental energy and transport equations according to Newman *et al*.[32, 33] Since during fast-charging the lithium-ion concentration is at its highest at the interface to the separator, where lithium transport from the separator pores can proceed most rapidly, lithium plating is expected to commence and predominantly occur on the surface of graphite particles located in the proximity of the electrode/separator interface.[34, 35] It is well known that opening a cell, which suffered from severe lithium plating on the graphite electrode, often reveals visually observable metallic lithium deposits on the graphite electrode surface.[13, 18, 21] These metallic deposits cannot dissolve and redistribute in empty or partially lithiated graphite particles within the electrode because they are electrically isolated, so called dead lithium,[36] and therefore, are also found in cells disassembled in a completely discharged state.[13] To the best of our knowledge, a spatially-resolved detection of lithium plating induced by lithium-ion concentration gradients in an operating cell has not yet been demonstrated.

Spatially- and time-resolved measurement of the lithium concentration in a battery cell

As a non-destructive and lithium-sensitive technique, we here use Neutron Depth Profiling (NDP)[37, 38] as an analytical method to determine the lithium concentration as a function of depth within a graphite anode during cell operation. The neutron capture reaction of ^{6}Li produces *triton* ($^{3}H^{+}$) and *alpha* ($^{4}He^{2+}$) particles at well-defined energies (s. Figure 1a). A lithium concentration depth profile within a sample can be determined by measuring the energy loss of the charged particles due to their interaction with the sample matrix.[39, 40, 41] The set-up of the employed *operando* NDP cell is depicted in Figure 1b and described in detail in a recent publication by Linsenmann and Trunk *et al.*[42] The graphite electrode was doctor blade-coated onto a 7.5 µm Kapton® foil with a previously sputtered 100 nm-thick copper layer serving as current collector. At the same time, the Kapton® window seals the cap of a standard CR2032 coin cell, which was perforated by laser-cutting a hexagonal pattern consisting of 139 holes with a diameter of 300 µm (s. Figure 1d).[42]

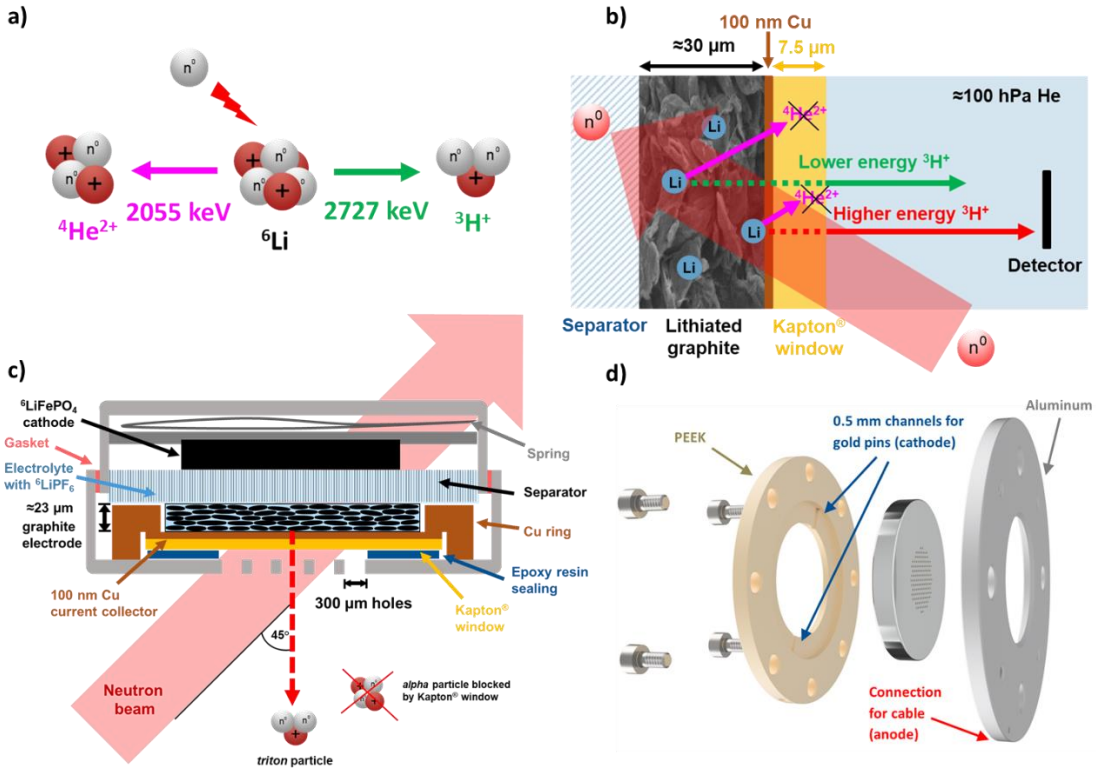

Fig 1. NDP working principle and *operando* NDP cell design. a) Neutron capture reaction of ^{6}Li which decays into a *triton* ($^{3}H^{+}$) and an *alpha* particle ($^{4}He^{2+}$) with fixed energies of 2727 keV and 2055 keV, respectively. **b)** Charged particles lose energy when passing through the electrode, the Kapton® window and the helium atmosphere. The remaining energy measured by the detector is a function of depth within the graphite electrode. *Alpha* particles are blocked by the nominally 7.5 µm-thick Kapton® window. **c)** Cross-sectional sketch of the cell designed for *operando* NDP measurements. The neutron beam illuminates the cell at an angle of 45 °. Since the beam area is larger than the coin cell window area, *triton* particles exit the cell through all 300 µm diameter holes laser-cut into the coin cell cap. **d)** Exploded view of the *operando* NDP cell mounted on a specially designed unit, which is then placed on the sample holder. The 300 µm-wide exit holes are arranged in a hexagonal order.

The Kapton® window is permeable for *tritons* but blocks *alpha* particles due to the higher stopping power of these double positively charged particles by the capping material.[38] The special design of the LIB cell optimized for *operando* NDP measurements does not alter the cycling performance compared to a standard

laboratory test cell (s. Figure 8), and thus, it also mimics the electrochemical processes that would occur in a commercial cell. The NDP measurements were performed at the NIST Center for Neutron Research at the neutron guide NG5 where the Cold Neutron Depth Profiling (CNDP) instrument is situated.[43] The vacuum chamber was filled with helium gas at a nominal pressure of ≈ 150 hPa in order to prevent the liquid electrolyte in the cell from evaporating and at the same time to minimize the energy loss of the *triton* particles between the *operando* cell and the detector (s. Figure 1b).

Considering the energy losses originating from the electrolyte, the copper current collector, the Kapton® foil, and the helium atmosphere, the viewing depth into the graphite electrode is limited to ≈ 30 µm.[44] A typical commercial artificial graphite exhibits a particle size distribution (PSD) around ≈ 20 µm (d_{50} = 17 µm), which means that the particle diameters are relatively large compared to the maximum viewing depth of NDP. In order to improve the homogeneity and to avoid particle cracking during compression of the electrode, the graphite active material used in this study was sieved to obtain a narrow particle size distribution around a d_{50}-value of ≈6 µm.[42] SEM images reveal that the shape of the graphite particles is plate-like resulting in a length of ≈6 µm and a height of ≈0.5-1 µm (s. SEM cross-section in Figure 7). To yield a sufficient resolution of the relaxation processes within the graphite electrode after lithium plating, a time resolution within the order of a few minutes is required. Since NDP is sensitive to the ^{6}Li isotope only (natural abundance of ≈ 7.59 %), we used in-house ^{6}Li-enriched $LiFePO_4$ (^{6}LFP) as cathode active material and commercial $^6LiPF_6$ as conductive salt of the electrolyte. All lithium sources within the cell set-up were enriched to ≈ 95 at% ^{6}Li, allowing for a reasonable statistical significance in a 2 min data collection time interval.

Due to their low loading of only ≈ 0.82 mAh cm^{-2} and moderate porosity of ≈ (52 ± 4) %, the graphite electrodes used in this study intrinsically possess a very high power capability. At room temperature, the formation of lithium-ion concentration gradients large enough to induce significant overpotentials during lithium intercalation, which would lead to a drop of the anode potential below 0 V *vs.* Li^+/Li, and thus thermodynamically favour lithium plating, occurs only at very high charging rates. In order to achieve severe lithium plating already at a charging rate of ≈ 2 C and resolve the concentration gradient build-up during fast-charging, we employed an electrolyte with a reduced lithium-ion concentration (≈ 0.31 mol L^{-1} compared to the commonly used concentration of ≈ 1 mol L^{-1}). Figure 2a and 2b show the NDP energy spectra measured at 0 % SOC (blue), *i.e.*, immediately before starting the *operando* NDP experiment, and 100 % SOC (orange), recorded after one complete charge of the cell at a rate of C/4. Prior to the *operando* NDP experiment, the cell was cycled at a slow rate of C/10 for three cycles to assure a complete and homogeneous formation of the solid electrolyte interphase (SEI).

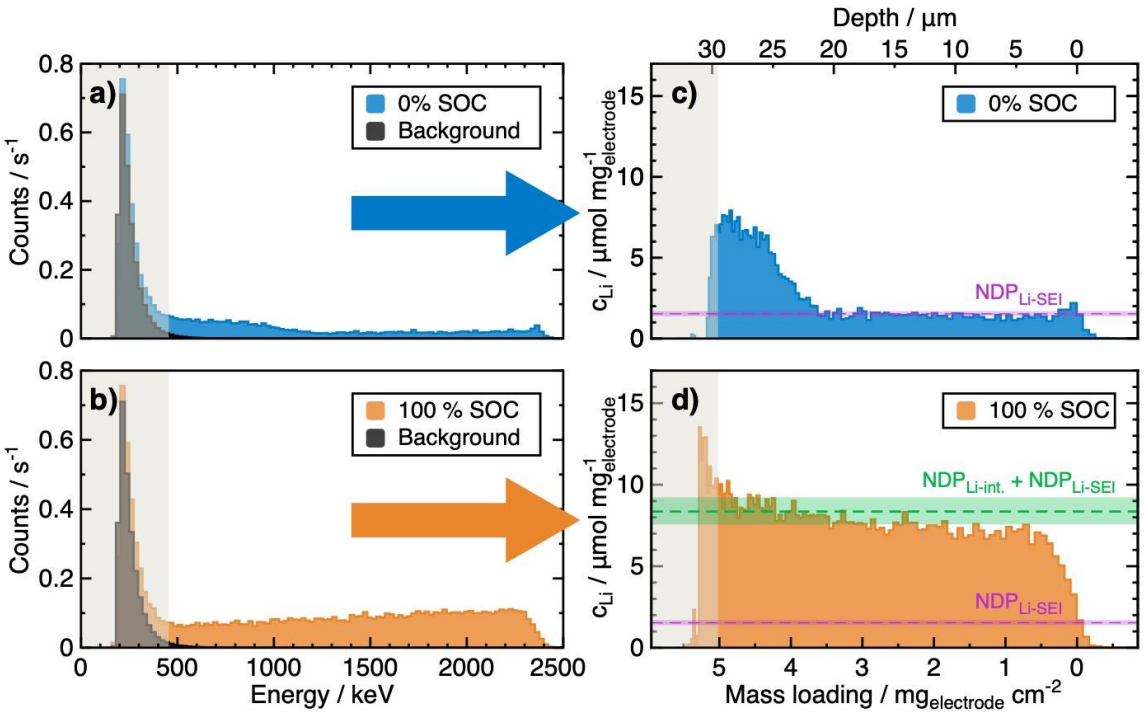

Fig 2. NDP energy spectra and transformation into lithium depth profiles. *Operando* NDP spectra normalized to counting rates recorded at, **a)** 0 % SOC (blue) and, **b)** 100 % SOC (orange) after charging at a rate of C/4. As a comparison, the background signal measured in a cell containing a pristine graphite electrode without electrolyte is shown (black, averaged over 60 min). The grey boxes mark NDP data where the background corresponds to ≥20 % of the sample signal and is therefore excluded from the following analysis. **c)** +**d)** Depth profiles obtained from the spectra in **a)** and **b)** by transforming the energy scale into a depth scale and the count rate into lithium concentration. The depth is expressed in terms of both mass loading (lower x-axis) and depth in µm (upper x-axis). The expected NDP signals (calculated based on the electrochemical data) for 0 % SOC ($NDP_{Li\text{-}SEI}$) and 100 % SOC ($NDP_{Li\text{-}int.} + NDP_{Li\text{-}SEI}$) are indicated as purple and green bands, respectively. The width of the bands was obtained by taking into account a systematic uncertainty of ± 6.4 % for the measured NDP data (s. Methods) and an error of ± 4 % for the calculated NDP signals (s. Table 1), resulting in a maximum total uncertainty of ± 10.4 %.

The signal measured at 0 % SOC can be attributed to lithium conductive salt in the electrolyte-filled pores and lithium-containing electrolyte decomposition products in the SEI, which is a lithium-conducting nm-thick layer on the surface of the graphite active material particles. In a fully charged state (100 % SOC), the NDP signal is increased by reversibly intercalated lithium in the graphite particles up to a stoichiometry of ≈LiC_6. Figure 2c and 2d depict the NDP spectra from 2a and 2b after transforming count rate and particle energies into a lithium concentration depth profile across the graphite electrode by using the stopping range tables according to *Stopping and Range of Ions in Matter* (SRIM)[45, 44] for *triton* particles ($^3H^+$) according to Ziegler *et al*. For the stopping power calculations, a matrix consisting of a homogeneous mixture of graphite (91 m%) and PVDF binder (9 m%) with a porosity of ≈ (52 ± 4) %, whose pores are filled with electrolyte (≈ 0.31 M $^6LiPF_6$ in EC/EMC = 30 m%/70 m%), was considered. The background signal shown in Figure 2a and 2b in black colour was obtained from a reference anode assembled in an empty *operando* NDP cell, *i.e.*, without electrolyte or LFP counter electrode. Apart from neutron scattering in the NDP setup, the background signal originates from *beta*- and *gamma*-radiation due to neutrons interacting with the stainless-steel casing and the aluminium cell holder. The grey areas in all panels mark the low energy region in the spectra where the background signal reaches ≥20 % of the *operando* cell signal. These areas were therefore excluded from all further data analysis. The NDP measurement in Figure 2c (0 % SOC) shows a flat lithium concentration profile

between ≈ 0 $mg_{electrode}$ cm^{-2} and ≈ 3.8 $mg_{electrode}$ cm^{-2} indicating a homogeneous lithium accumulation, *i.e.*, SEI formation, across this region of the graphite electrode. In a depth between ≈ 3.8 $mg_{electrode}$ cm^{-2} and ≈ 5 $mg_{electrode}$ cm^{-2}, a lithium concentration increase is observed (0 % SOC, s. also Figure 3b, spectra 1, 3, 5, and 7). This NDP signal was not visible in the background measurement (s. Figure 2a, black area), *i.e.*, an identically constructed cell without any lithium, and thus it is unlikely to originate from the measurement setup, but must stem from a true lithium enrichment. A possible reason for the increased lithium signal in the vicinity to the separator could be additional SEI formation in this region. Locally enhanced SEI formation in this region might be related to transition metal ion reduction and subsequent SEI degradation originating from HF impurities in the electrolyte and/or transition metal ion leaching from either the LFP counter electrode (Fe) or the metal casing/aluminum spacer (*e.g.*, Mn, Al, Mg). The reduction of transition metals would predominantly occur at the interphase to the separator due to the shorter diffusion pathway. In the same NDP spectrum, a lithium peak at the interphase between electrode coating and the copper-sputtered Kapton® window is observed (depth = 0 µm) which is superimposed with the lithium signal within the electrode for the 100 % SOC measurement (s. Figure 2d). It originates from an electrochemical alloy formation of lithium and copper during cycling as demonstrated in a recent study by Linsenmann and Trunk *et al.*[42] The NDP spectrum recorded after one complete constant current charge (C/4, s. Figure 2d), ending the charging phase by a potential cutoff at 3.42 V_{cell} and a subsequent constant voltage phase until a current cutoff of C/40, also shows a rather homogeneous lithium concentration profile, with a slightly increased concentration between ≈ 3 $mg_{electrode}$ cm^{-2} and ≈ 5 $mg_{electrode}$ cm^{-2}. In the following, the lithium concentrations quantified in the graphite anode using NDP are compared to the values expected from the cell setup and electrochemical performance of the LIB. The second column in Table 1 sums up the expected mass contributions within the electrode, *i.e.*, the graphite/binder coating, liquid electrolyte within the pores of the coating, reversibly intercalated lithium, and the (estimated) amount of SEI built up during cell formation, and the third column presents calculated absolute lithium amounts (in µmol) in the respective phases as deduced from the electrochemical cycling data. These calculations are based on: i) electrolyte mass and lithium amount from the ≈25 µm thickness, the 52 % porosity of the electrode, and the ≈ 0.31 M $^{6}LiPF_6$ in EC/EMC = 30 m%/70 m% electrolyte with an approximated density of ≈1.19 g cm^{-3}; ii) graphite / PVDF from weight measurements; iii) the intercalated lithium mass was calculated from the reversible capacity of the first discharge during *operando* cycling at C/4 (≈ 369 mAh $g^{-1}_{graphite}$); iv) the SEI mass and lithium amount are estimated using 62 % of the cumulative irreversible capacity measured during the three formation cycles (≈ 122 mAh $g^{-1}_{graphite}$, *i.e.*, ≈ 76 mAh $g^{-1}_{graphite}$) assuming a Li/e^- ratio of 0.62/1 and pure LEDC (80 g_{LEDC} mol^{-1}_{Li}). The share of 62 % originates from *post-mortem* elemental analysis (ICP-OES) of a pre-formed completely discharged graphite electrode after cell disassembly where we found significantly less lithium than expected based on the irreversible capacity (*i.e.*, (62 ± 4) %, assuming one lithium per electron of charge).[42] This finding was confirmed in a recent NDP study where we measured only ≈61% of the lithium inventory expected from the irreversible capacity in the SEI.[42] The exact composition of the SEI has little impact on the matrix composition, and thus on the stopping power for *triton* particles, making the assumption that the SEI consists purely of LEDC a reasonable approximation.

The forth column shows the calculated expected NDP signals (in the units of µmol $mg^{-1}_{electrode}$) in the electrolyte, intercalated in the graphite active material ($NDP_{Li\text{-}int.}$), and bound in the SEI ($NDP_{Li\text{-}SEI}$).

Table 1. Calculated NDP signals. Estimated NDP signals of the *operando* cell stemming from lithium conductive salt in the electrolyte, reversibly intercalated lithium in the graphite active material, and irreversibly bound lithium in the SEI. The mass contributions to the electrode (second column) and the absolute amounts of lithium in the electrode (third column) were calculated based on: i) electrolyte mass and lithium amount from the 25 µm thickness, the 52 % porosity of the electrode, and the ≈ 0.31 M $^6LiPF_6$ in EC/EMC = 30 m%/70 m% electrolyte with an approximated density of ≈1.19 g cm^{-3}; ii) graphite / PVDF from weight measurements; iii) the intercalated lithium mass was calculated from the reversible capacity of the first discharge during *operando* cycling; iv) the SEI mass and lithium amount were estimated assuming a Li/e^- ratio of 0.62/1[42] and pure LEDC (80 g_{LEDC} mol^{-1}_{Li}). The expected NDP signals from the lithium in the electrolyte, intercalated in the graphite ($NDP_{Li\text{-}int.}$), and bound in the SEI ($NDP_{Li\text{-}SEI}$) are shown in the fourth column. Uncertainties are based on a coating mass error of ± 0.034 mg, a thickness error of ± 2 µm, a porosity error of ± 4 %, and an electrolyte concentration error of ± 0.003 mol L^{-1}. Other errors were calculated by Gaussian error propagation. This yields errors for $NDP_{Li\text{-}int.}$ and $NDP_{Li\text{-}int.}$ + $NDP_{Li\text{-}SEI}$ of 4 %.

	Mass contribution mg	Li amount µmol	Expected NDP signal µmol $mg^{-1}_{electrode}$	
electrolyte in pores based on 52 % porosity and ≈ 0.31 M $LiPF_6$)	1.46 ± 0.2	0.38 ± 0.05	0.087 ± 0.011	
graphite + binder coating	2.88 ±0.03	-	-	
lithium intercalated in graphite based on ≈368.9 mAh $g^{-1}_{graphite}$ reversible capacity in the first *operando* NDP cycle	0.22 ± 0.003	36.05 ± 0.43	$NDP_{Li\text{-}int.}$ = 7.01 ± 0.28	$NDP_{Li\text{-}int.}$ + $NDP_{Li\text{-}SEI}$ = 8.51 ± 0.29
SEI based on 76 mAh $g^{-1}_{graphite}$ = 62 %[42] of the total irrev. cap. during the three formation cycles and assuming that the SEI consists only of LEDC	0.59 ± 0.01	7.39 ± 0.09	$NDP_{Li\text{-}SEI}$ = 1.50 ± 0.06	

The calculated lithium concentrations for SEI ($NDP_{Li\text{-}SEI}$ = 1.50 µmol $mg^{-1}_{electrode}$) and the sum of SEI and reversibly intercalated lithium ($NDP_{Li\text{-}int.}$ + $NDP_{Li\text{-}SEI}$ = 8.51 µmol $mg^{-1}_{electrode}$) are indicated as purple and green horizontal dashed lines, respectively, in Figure 2c and 2d. The error band around those lines represents the systematic uncertainty of the measured NDP data of 6.4 % (s. Methods) and an error of ± 4 % for the calculated NDP signals (s. Table 1), resulting in a maximum total uncertainty of ± 10.4 %. The fraction of the signal attributable to lithium in the electrolyte is only ≈ 6 % of the SEI signal, and therefore negligible. The lithium concentration measured using NDP at 0 % and 100 % SOC corroborates well with the expected concentration for lithium in the SEI and the sum of SEI and intercalated lithium from Table 1.

Lithium plating on a graphite anode induced by fast-charging

In the following section, the lithium concentration distribution across the thickness of a graphite electrode was investigated during a rate test which is depicted in Figure 3a. Three formation cycles at a slow cycling rate of C/10 prior to the *operando* NDP experiment were performed. During cycling, the end-of-charge was controlled *via* a cell potential cutoff only during the first charge (C/4 charge until 3.42 V_{cell} and a subsequent

constant voltage phase until a current cutoff of C/20). For higher charging rates (C/2, 1 C, 2 C), cycling was terminated by a capacity limit corresponding to 100 % of the maximum practical capacity for the graphite active material, which was defined here as 355 mAh $g^{-1}_{graphite}$. Thus, the potential of the graphite anode may drop below 0 V *vs.* Li^+/Li to provide large enough currents during accelerated charging. This will occur if the charging rate exceeds a certain threshold, such that overpotentials, *inter alia* caused by concentration gradients, become sufficiently large. The charging rate was therefore increased from C/4, C/2, and 1 C to 2 C for each cycle. The discharge was constantly performed at a slow C-rate (C/4) in order to assure complete delithiation of the electrode. Both charge and discharge were followed by a 30 min open-circuit voltage (OCV) relaxation phase indicated as grey areas in Figure 3a. SOCs where NDP energy spectra were recorded are labelled from 1-8 by Arabic numbers, 0 % SOC (blue), 100 % SOC (orange). The corresponding NDP spectra are shown in Figure 3b.

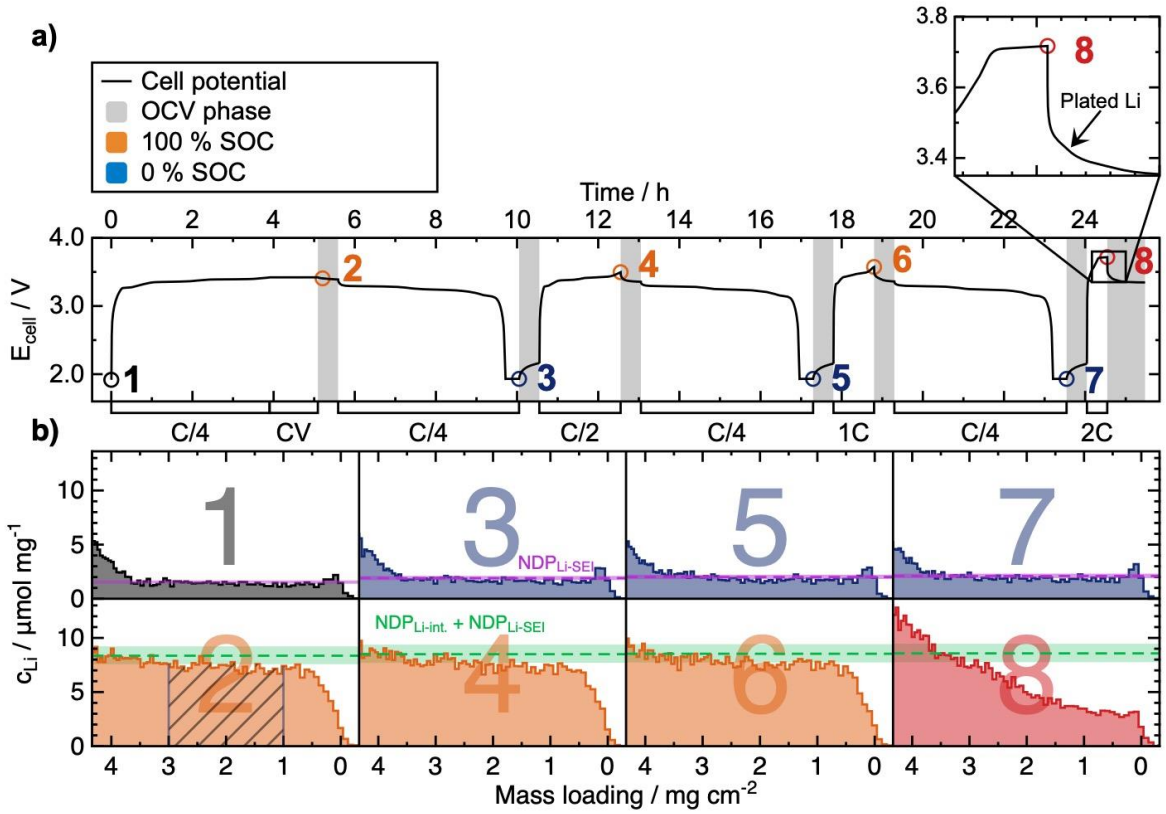

Fig 3. Lithium plating on graphite induced by fast-charging. a) The graphite anode (≈ 0.82 mAh cm^{-2}) was cycled *vs.* a capacitively oversized ^{6}LFP cathode in the *operando* NDP cell using a ≈ 0.31 M $^6LiPF_6$ in EC/EMC = 30 m%/70 m% electrolyte at charging rates of C/4, C/2, 1 C to 2 C. The discharge was always performed at C/4 to assure complete delithiation of the graphite anode. After each half-cycle the cell was rested at OCV for 30 min and 60 min after the final 2 C charge (grey areas). The voltage profile recorded during the last relaxation phase is magnified to visualize the non-exponential potential decay after switching off the current which is an indication that lithium plating occurred during charging. **b)** *In situ* NDP spectra averaged over the first 2 min of the relaxation phase showing lithium concentration *vs.* mass loading for selected points at 0 (blue) and 100 % SOC (orange) marked on the voltage profile in a). The lithium-ion concentration gradient forming across the electrode during fast-charging at 2 C causes lithium plating to occur on graphite particles located in the vicinity of the separator. The region used for calculating the coulombic efficiency based on the lithium concentration within the cell is marked in spectrum 2 (1 mg cm^{-2} - 3 mg cm^{-2}). The expected NDP signals (calculated based on the electrochemical data) for 0 % SOC ($NDP_{Li\text{-}SEI}$) and 100 % SOC ($NDP_{Li\text{-}int.}$ + $NDP_{Li\text{-}SEI}$) are indicated as purple and green bands, respectively. The width of the bands was obtained by taking into account a systematic uncertainty of ± 6.4 % for the measured NDP data (s. Methods) and an error of ± 4 % for the calculated NDP signals (s. Table 1), resulting in a maximum total uncertainty of ± 10.4 %.

The two NDP spectra labelled with 1 and 2 show the same data as plotted in Figure 2c and 2d, cut at a depth of 4.25 $mg_{electrode}$ cm^{-2}. As explained above, the spectra shown in Figure 3b were obtained by converting NDP data from an energy into depth scale and from intensity into lithium concentration. All spectra were recorded during the first 2 min of an OCV phase directly after the end-of-charge and end-of-discharge, respectively. Spectrum 1 shows the lithium distribution within the electrode before starting *operando* cycling. As stated above, the NDP signal originates mainly from lithium in the SEI since the cell was pre-formed. Spectra 1-7 show a horizontal profile, *i.e.*, a homogeneous SEI formation (spectra 1, 3, 5, and 7) and a homogeneous graphite particle lithiation (2, 4, and 6) across the electrode, which is reproducible for all cycles. Table 2 compares the coulombic efficiencies (CE) measured electrochemically during charging and discharging the cell with the CE calculated from the lithium inventory determined by NDP. The lithium amount (in µmol cm^{-2}) used for calculating the CE was obtained by integrating the NDP spectra in Figure 3b between 1 mg cm^{-2} and 3 mg cm^{-2}, such as to exclude regions in the spectrum > ≈ 3.5 $mg_{electrode}$ cm^{-2} , comprising a lithium enrichment with unknown origin, and < ≈ 0.5 $mg_{electrode}$ cm^{-2} where lithium alloying with the copper current collector is superimposed. The CE values measured electrochemically and the corresponding ones calculated from NDP are in good agreement which supports that the irreversible capacity predominantly results in electrolyte decomposition and SEI formation increasing the amount of lithium in the SEI.

Table 2. Comparison of the coulombic efficiencies (CEs) from electrochemistry and NDP. The CEs were determined from the charge/discharge capacities during cycling and calculated based on the NDP signals at 0 % and 100 % SOC, respectively. For that, NDP signals were integrated between 1-3 $mg_{electrode}$ cm^{-2} to exclude regions >≈3.5 $mg_{electrode}$ cm^{-2} that might be superimposed by an additional lithium signal with unknown origin and <≈0.5 $mg_{electrode}$ cm^{-2} superimposed by lithium alloying with the copper current collector. The reversible capacity during the last formation cycle was 366.5 mAh $g^{-1}_{graphite}$.

Cycle	SOC %	(Dis)charge capacity $mAhg^{-1}$	Integral (1-3 $mg_{electrode}$ cm^{-2}) µmol cm^{-2}	CE (cycling) %	CE (NDP) %
0	0	0	2.67	-	-
1	100	390.5	13.68	94.5	95.0
	0	368.9	3.22		
2	100	355.1 (fixed)	14.01	98.2	99.0
	0	348.8	3.33		
3	100	355.1(fixed)	14.36	98.4	98.8
	0	349.5	3.46		
4	100	355.1(fixed)	9.91	-	-

The significantly lower CE in the first cycle (C/2, ≈ 95 %) could be related to the two-week storage/transport of the cell between formation (Germany) and NDP measurement (USA) during which the integrity of the SEI might have been affected. During 2 C charging the cell potential increases to > 3.7 V_{cell} (s. magnification in Figure 3a) and only ≈ 3.5 V_{cell} at 1 C which means that the graphite electrode potential must have dropped significantly below 0 V *vs*. Li^+/Li. NDP spectrum 8 displays the lithium concentration distribution across the electrode during the first 2 min after fast-charging at 2 C, *i.e.*, after severe lithium plating occurring on the graphite electrode. The lithium profile is here strongly inhomogeneous, showing an

approximately linear concentration gradient across the electrode with lower lithium concentrations within the electrode region adjacent to the current collector where the lithium-ion concentration in the electrolyte is depleted due to limited mass transport through the tortuous pore structure of the graphite electrode. The concentration overpotential results in a potential drop on the graphite electrode below 0 V *vs.* Li^+/Li, thereby favouring the onset of metallic lithium deposition on the particle surface. Lithium plating will predominantly occur within parts of the electrode in the vicinity of the porous separator due to the higher lithium-ion concentration in the electrolyte surrounding graphite particles located there. At mass loadings $> 3.5\ mg_{electrode}\ cm^{-2}$, the lithium concentration exceeds the lithium level of fully intercalated graphite, as clearly visible in spectra 2, 4, and 6 (each 100 % SOC). However, we also see a lithium signal enrichment in this region in the discharged state of the electrode (spectra 1, 3, and 5). As speculated above, this might be related to additional SEI formed presumably by impurities in the electrolyte. Since we do not see the lithium enrichment in this region in spectra 2, 4, and 6, *i.e.*, 100 % SOC, we believe that the NDP spectrum 8 is not superimposed by this additional lithium signal. The coulombic efficiency in this last cycle is only ≈ 92.9 % (discharge not shown) which means that ≈ 7 % of the charge went into irreversible reactions, such as the reaction of reactive plated lithium with electrolyte or the formation of electrically isolated lithium, so called dead lithium.[27]

Discussion

Relaxation of the lithium distribution after plating

Figure 4a shows a magnification of the cell potential profile recorded during the 2 C charging phase, *i.e.*, 30 min charge (s. Figure 3b, spectrum 8), and the subsequent potential relaxation at OCV over the course of 30 min. The spatially resolved lithium concentration across the graphite electrode is visualized by a time-dependent 2-dimensional colour map in Figure 4b, with the time in x-direction and mass loading in the y-direction, where $0\ mg_{electrode}\ cm^{-2}$ corresponds to the current collector/graphite electrode interface. The lithium concentration pixels are averaged over 2 min along the time scale with yellow representing high and blue low lithium concentration.

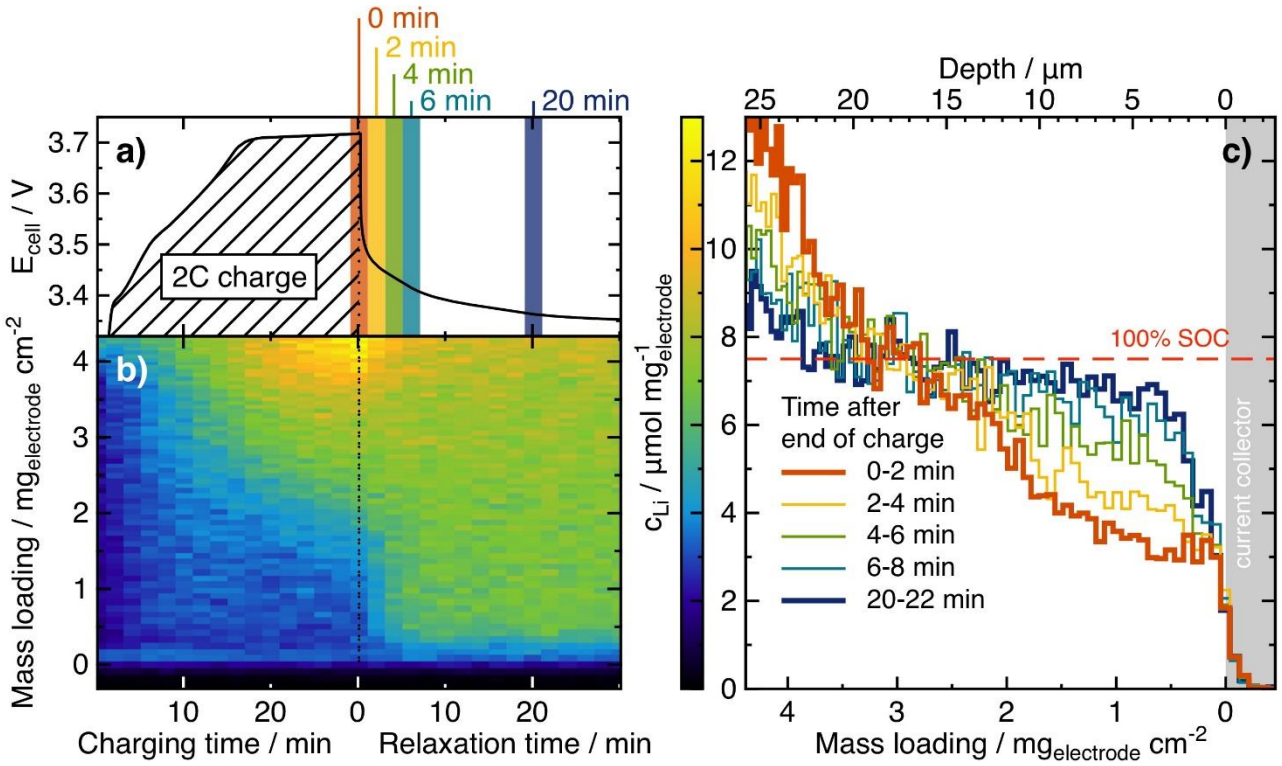

Fig 4. Fast-charging and lithium redistribution across the graphite electrode during OCV relaxation. a) Full-cell potential profile of a ^{6}LFP/graphite cell during a 2 C charge and subsequent OCV relaxation phase over 30 min. **b)** 2D representation of the time-dependent lithium concentration profiles in the graphite electrode, with depth into the graphite electrode on the y-axis (0 corresponds to the current collector/graphite electrode interface); the colour describes the lithium concentration (colour code is shown next to panel c). **c)** Selected lithium concentration profiles following the 2 C charge between 0 min and 20 min after end-of-charge (averaged over 2 min). The depth into the graphite electrode is shown as mass loading (lower scale) and depth in µm (upper scale). The dashed red line indicates the lithium level expected for the fully intercalated graphite electrode (100 % SOC, 7.5 µmol cm^{-2}), taken from Figure 3, spectrum 2.

At the beginning of the charging phase, the colour is dark blue across almost the complete depth (0 $mg_{electrode}$ cm^{-2} - 4 $mg_{electrode}$ cm^{-2}) with the lithium signal predominantly stemming from lithium compounds in the SEI which is approximately homogeneously distributed over the total depth probed by NDP (s. Figure 3b, spectrum 1). After ≈ 10 min, the lithium concentration starts to increase inhomogeneously, with a more rapid growth in the separator facing region of the electrode, and building-up a concentration gradient across the electrode. The evolution of a concentration gradient originates from the non-unity transference number for lithium-ions in a liquid LIB electrolyte,[32, 13] which is ≈ 0.3 - 0.4 (unitless) for the electrolyte used in this study (≈ 0.31 M $LiPF_6$ in EC/EMC = 30 m%/70 m%).[46] The lithium concentration gradient gradually becomes steeper during charging indicating that lithium intercalation occurs primarily in graphite particles located in proximity to the separator and the lithium concentration culminates at 100 % SOC (≈ 12.5 µmol $mg^{-1}_{electrode}$), reflected by the bright yellow colour. At the end-of-charge, a steep concentration gradient has formed across the electrode (bold red line in panel c) of Figure 4). It is clearly visible that the lithium concentration exceeds the level measured at 100 % SOC at the end of the C/4 charging half-cycle (indicated by the dashed red horizontal line in Figure 4c) where the graphite electrode must have been fully lithiated since a reversible capacity of 368.9 mAh $g^{-1}_{graphite}$ was obtained. We believe that this high lithium concentration can be explained by plating of metallic lithium on the graphite particle surface. A lithium concentration gradient across an aged graphite electrode, which was cycled in a way to provoke lithium plating during charging (3 C charge at 5 °C),

with higher concentration at the surface (*i.e.*, the electrode/separator interface) was also found by Ghanbari *et al.* by *post-mortem* analysis using glow discharge optical emission spectroscopy (GD-OES) depth profiling.[47] Furthermore, the lithium concentration in the vicinity of the current collector/graphite electrode interface is only little higher than the calculated signal for the SEI, underlining that the graphite particles in the vicinity of the current collector are only partly lithiated due to lithium-ion depletion. Figure 4c also shows the time-dependent evolution of the lithium concentration distribution across the electrode for selected times (always averaged over 2 min) after the end-of-charge, which is reflecting the lithium concentration changes during potential relaxation. The potential and concentration gradient across the graphite electrode formed during fast-charging results in a lithium flux from within the electrode in the direction of the current collector. Immediately after stopping the charging current (dashed line in Figure 4a and 4b), the gradient in lithium concentration that has developed across the electrode is levelling, which can be driven by two mechanisms: 1) lithium-ion diffusion along the lithium-ion concentration gradient in the electrolyte phase, 2) dissolution of plated lithium, migration/diffusion through the liquid electrolyte phase and subsequent intercalation in graphite particles with lower SOC to balance the potential gradient across the electrode. Comparing the evolution of the lithium concentration profiles during OCV relaxation over the course of ≈ 20 min, from the bold red to the bold blue curve in Figure 4c, it can be clearly seen that the concentration decreases between ≈ 2.5 $mg_{electrode}$ cm^{-2} - 4.2 $mg_{electrode}$ cm^{-2}, whereas it increases between ≈ 0 $mg_{electrode}$ cm^{-2} - 2.5 $mg_{electrode}$ cm^{-2} approaching an approximately homogeneous level of ≈ 7.5 µmol $mg^{-1}_{electrode}$ across the electrode.

The change of the lithium concentration in various depths within the electrode, and thus the varying lithium degree of the graphite particles can be more easily followed by plotting the lithium concentration *vs.* charging and relaxation time, respectively, which is depicted in Figure 5. At begin-of-charge, the lithium concentration starts from approximately the same level for mass loadings between ≈ 2.1 $mg_{electrode}$ cm^{-2} - 3.8 $mg_{electrode}$ cm^{-2}. The initial level is only higher for ≈ 4.2 $mg_{electrode}$ cm^{-2}, *i.e.*, the maximum depth that can still be probed in this experiment before the signal is superimposed by an additional lithium signal discussed above leading to the slight deviation from the homogeneous lithium concentration. The graphite particles close to the current collector (turquoise curve, 1.0 $mg_{electrode}$ cm^{-2} - 1.4 $mg_{electrode}$ cm^{-2}) are only lithiated during the first 10 min to a maximum SOC of ≈ 20 %. The lithiation degree then stays constant until the current is stopped and the relaxation process starts leading to a sharp increase in SOC reaching saturation after ≈ 20 min. For the green curve (≈ 2.1 $mg_{electrode}$ cm^{-2} - 2.4 $mg_{electrode}$ cm^{-2}), we observe an approximately linear increase throughout the charging phase and the first ≈10 min of the relaxation phase after which the maximum concentration is reached that stays constant afterwards. For the depth of ≈ 3.1 $mg_{electrode}$ cm^{-2} - 3.4 $mg_{electrode}$ cm^{-2} (yellow curve), the concentration increase during charging is much more rapid and the maximum SOC coincides with the end-of-charge, staying constant afterwards.

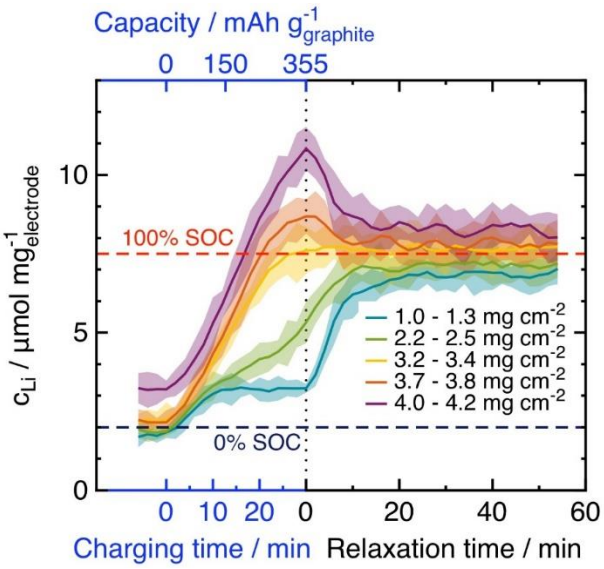

Fig 5. Lithium concentration evolution during fast-charging and OCV relaxation at various depths across a graphite electrode. The lithium concentration change during the 2 C charge and subsequent potential relaxation over the course of 60 min was determined *via* NDP and is shown for five depth intervals averaged over ≈ 0.1 $mg_{electrode}$ cm^{-2} - 0.4 $mg_{electrode}$ cm^{-2}, the varying averaging ranges are due to data transformation from energy to real space. The coloured bands display the standard deviation obtained by summarizing eight depths for each of the five depth intervals. The dashed red line indicates the lithium level expected for the fully intercalated graphite electrode (100 % SOC, 7.5 µmol $mg^{-1}_{electrode}$) and the dark blue dashed line for the completely delithiated graphite electrode (0 % SOC, 2 µmol $mg^{-1}_{electrode}$), taken from Figure 3, spectrum 2 and 7.

The lithium concentration in greater depths, *i.e.*, ≈ 3.6 $mg_{electrode}$ cm^{-2} - 3.8 $mg_{electrode}$ cm^{-2} (orange curve) and ≈ 4.1 $mg_{electrode}$ cm^{-2} - 4.2 $mg_{electrode}$ cm^{-2} (purple curve), exceeds the level where the graphite electrode is fully intercalated after charging for ≈ 15 min - 20 min by ≈ 20 % and 50 %, respectively, indicating that severe lithium plating must have occurred. After reaching maximum concentration at the end-of-charge, the concentration quickly decreases within ≈ 10 min and further remains on a constant level. As in Figure 4, the lithium level expected for a fully lithiated graphite electrode (100 % SOC) is indicated as a red dashed horizontal line.

During the relaxation process, the lithium concentration in the electrode region close to the current collector increases from ≈ 55 % SOC to ≈ 90 % (referencing to 7.5 µmol cm^{-2} as 100 % SOC and 2 µmol cm^{-2} as 0 % SOC) within ≈ 20 min. To enable a lithium redistribution from the high concentration region closer to the separator towards particles near the current collector, lithium-ions must be transported through the electrolyte, and subsequently intercalated into graphite particles with lower SOC, which is the thermodynamically favoured process. Figure 6 shows a schematic cross-sectional representation of the *operando* NDP cell directly after the end-of-charge of the 2 C charging half-cycle.

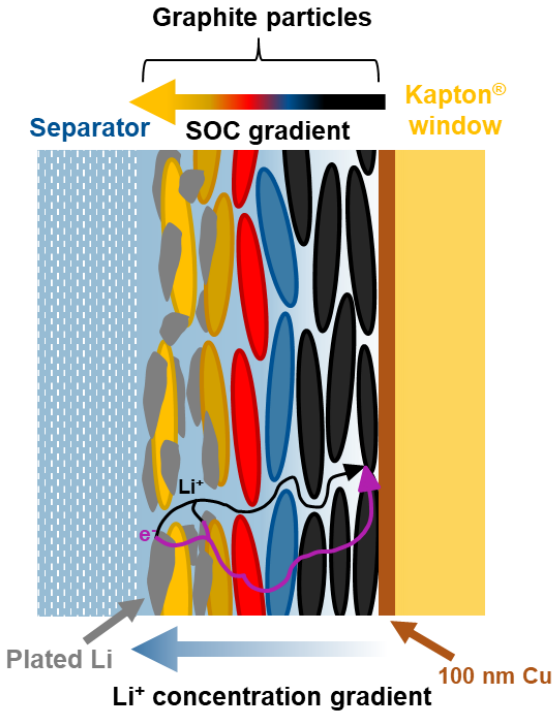

Fig 6. Cross-section across the graphite electrode after plating. The scheme qualitatively depicts the SOC gradient across the through-plane direction of the graphite electrode formed during fast-charging at 2 C directly after the end-of-charge. The SOC increases from black *via* blue and red to yellow. On the surface of particles in the vicinity of the electrode/separator interface metallic lithium is deposited. Plated lithium dissolves and is transported *via* the electrolyte phase to graphite particles with lower SOC where it intercalates and recombines with electrons conducting through the graphite particle network.

Graphite particles located close to the electrode/separator interface show deposits of metallic lithium on their surface. During the OCV relaxation phase, the SOC gradient across the electrode leads to dissolution of plated lithium, lithium-ion transport through the electrolyte governed by diffusion and migration, followed by intercalation into electrode regions with lower SOC, thereby reducing the SOC and lithium concentration gradient across the electrode. Since lithium transport through the electrode comprises several consecutive steps, *i.e.*, lithium dissolution, transport through the electrolyte, charge transfer into the graphite particle, and diffusion through the particle, the rate at which the lithium concentration equalization proceeds is limited by the slowest process step. Diffusion times of lithium-ions in the liquid electrolyte and in the solid phase of the graphite particle can be roughly estimated using $t_{diff} = x^2/(4D)$, where t_{diff} is the diffusion time, x the effective diffusion length through a porous medium with length L and a given tortuosity, τ ($x \approx L \times \tau$), and D the diffusion coefficient in the liquid or solid phase, respectively. The liquid phase diffusion coefficient D_{liquid} for the here employed electrolyte (≈ 0.31 M $LiPF_6$ in EC/EMC = 30 m%/70 m%) was determined by Nyman *et al.*[48] and Landesfeind *et al.*[46] to be $\approx 4 \cdot 10^{-6}$ cm^2 s^{-1} - $5 \cdot 10^{-6}$ cm^2 s^{-1} at 25 °C. In case of the solid state diffusion coefficient D_{solid} for lithium in graphite, the values reported in the literature range over several orders of magnitude, however, most of the numbers found are between $\approx 1 \cdot 10^{-9}$ cm^2 s^{-1} - $1 \cdot 10^{-10}$ cm^2 s^{-1}.[49, 50, 51, 52] Based on an effective diffusion length of 125 µm, resulting from the ≈ 25 µm thickness of the electrode and a tortuosity of 5 and $D_{liquid} = 4.5 \cdot 10^{-6}$ cm^2 s^{-1}, we obtain an order of magnitude estimation for the diffusion time through the electrolyte phase of the electrode of ≈ 8 s. In comparison, considering a solid state diffusion length

through the graphite particle of ≈ 0.5 µm, which is estimated based on SEM images (s. Figure 7), yields an estimated diffusion time of ≈ 1 s (for $D_{solid} = 5 \cdot 10^{-10}$ cm^2 s^{-1}, neglecting a possible SOC-dependency[53]), *i.e.*, the same order of magnitude as for the liquid phase. These estimations underline that the geometry of the electrode (thickness, particle size etc.) used in this plating experiment does not allow to definitively identify one of the two diffusion processes to be rate-limiting. In order to probe the achievable lithium intercalation rate into the high surface-area graphite used in this study, we conducted rate tests with uncompressed graphite electrodes with very low loading (≈ 126 µAh cm^{-2}, thickness ≈ 10 µm) and an electrolyte with the same solvent composition as in the NDP experiment but a 1 M $LiPF_6$ concentration, with the goal to reduce the influence of liquid phase concentration gradients on the lithiation capacity. The rate tests were performed in a three-electrode setup controlling the graphite electrode potential *vs.* a lithium reference electrode using a constant current and a potential cutoff of 10 mV *vs.* Li$^+$/Li. The rate dependency is depicted in Figure 7.

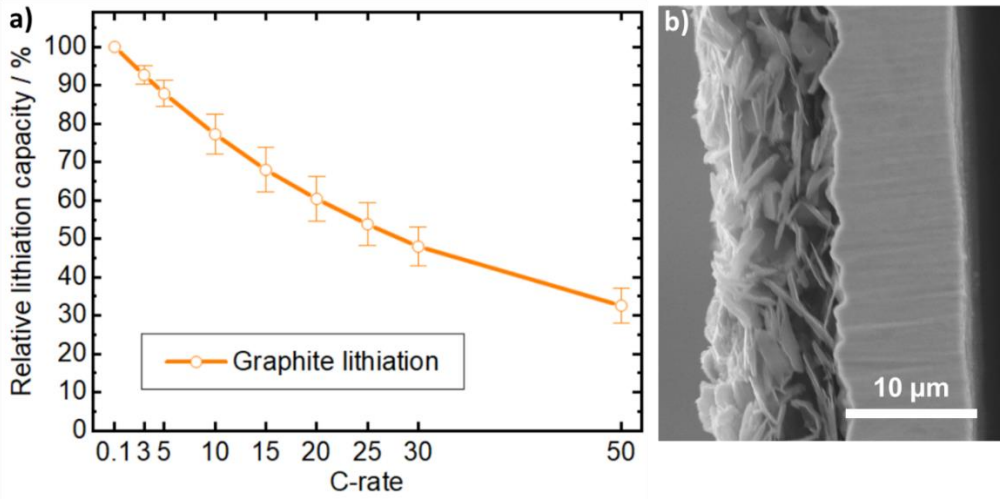

Fig 7. Lithiation rate test for a thin graphite electrode. a) Relative lithiation capacity (normalized to the lithiation capacity in the third formation cycle at C/10) of a graphite electrode with a loading of ≈ 126 µAh cm^{-2} determined in a graphite/Li cell controlling the graphite electrode potential *vs.* a lithium reference electrode (1.5 V-10 mV vs. Li$^+$/Li). Circles show mean capacity of two nominally identical cells, error bars indicate the maximum and minimum values. At a lithiation rate of 10 C ≈ 75 % of the maximum capacity can still be obtained suggesting that solid state diffusion of lithium-ions through the graphite particles is not rate-limiting for lithium redistribution in the relaxation phase after plating. **b)** Cross-sectional SEM image of the high-surface area artificial graphite (≈ 15 m^2 g^{-1}) used in this study coated on a 10 µm thick copper current collector. The plate-like particles have a height of ≈ 1 µm and a length of ≈ 6 µm.

It is evident that the very low graphite loading reduces mass transport limitations of lithium-ions in the electrolyte phase, and thus concentration overpotentials, largely, such that at a rate of 10 C still ≈ 75 % of the maximum capacity can be obtained (≈ 30 % at 50 C). During the potential relaxation after the plating experiment at a 2 C charging rate, we found that the lithiation of the particles in the vicinity of the current collector increases from ≈ 55 % to ≈ 80 % SOC within ≈ 10 min, based on the first steep increase of the concentration in Figure 5 (turquoise curve). This would correspond to a lithiation rate of ≈ 1.5 C where full capacity is still achieved, taking into account the graphite rate behaviour shown in Figure 7.

Methods

Preparation of the graphite electrodes. The short range of the charged particles formed during NDP limits the coating thickness of the electrode to ≈ 30 µm. A typical commercial graphite has a d_{50}-value of ≈ 20 µm. Thus, larger particles would likely be cracked during electrode compression. This is why, for this study, an artificial graphite (Sigracell® SG3, SGL Carbon, Germany) with a BET area of 4 $m^2\ g^{-1}$ (d_{50} = 17 µm, d_{90} = 35 µm) was sieved to obtain graphite with smaller particles and a more narrow particle size distribution around ≈ 6 µm and a BET surface area of ≈ 15 $m^2\ g^{-1}$ (d_{50} = 5.8 µm, d_{90} = 8.5 µm). Graphite electrodes were prepared by mixing the sieved graphite with polyvinylidene difluoride (PVDF, Kynar HSV 900, Arkema, France) at a mass ratio of 91:9 and using N-methyl-pyrrolidone (NMP, anhydrous, 99.5 %, Sigma-Aldrich, Germany) as solvent. For mixing of the slurry, a planetary mixer (Thinky, USA) was used. First, the dry powders were mixed at a speed of 1500 rpm for 5 min. Then, NMP was added in three steps at 2000 rpm until a solid content of 28 wt% was obtained. The active material ink was doctor blade-coated onto a 7.5 µm-thick Kapton® substrate (DuPont, USA), which was sputtered with a 100 nm-thick copper layer (Movatec, Germany) serving as current collector. The graphite coating had a loading of ≈ (2.30 ± 0.027) $mg_{graphite}\ cm^{-2}$ (= 0.82 mAh cm^{-2}, assuming a reversible capacity of 355 mAh $g^{-1}{}_{graphite}$) and a thickness of ≈ (25 ± 2) µm (Mitutoyo, Japan). The electrodes for the *operando* cells were produced by a template coating process through an 80 µm-thick mask made from a PTFE coated fiberglass gasket (Fiberflon, Fiberflon GmbH & Co. KG, Germany), in which holes with a diameter of 12 mm were punched. The coating together with the mask was dried at 50 °C in a convection oven for 10 min, after which the mask was removed and drying was continued for another 3 h. Electrodes were then punched out with a diameter of 15 mm, to allow for contacting the electrode electrically with the coin cell cap using a 10 µm-thick copper foil annulus. Eventually, the electrodes were compressed to a porosity of ≈ (52 ± 4) % (error determined *via* Gaussian error propagation from errors in coating mass ± 0.034 mg and thickness ±2 µm) using a Static Materials Testing Machine (ZwickRoell GmbH & Co. KG, Germany). The uncertainty in porosity was calculated based on an assumed error in the electrode thickness of ±2 µm.

Preparation of the $^6LiFePO_4$ electrodes. The cathodes used as counter electrode in the *operando* cells were made from electrode tapes of commercial $LiFePO_4$ (LFP, 3.5 mAh cm^{-2}, Custom Cells Itzehoe GmbH, Germany). A 30 mm x 30 mm electrode was assembled in a pouch cell *vs.* a lithium foil electrode (450 µm, 99.9 %, Rockwood Lithium) using a glass fibre separator (38 mm x 38 mm, glass microfiber filter 691, VWR, Germany) and 1 mL LP57 electrolyte (1 M $LiPF_6$ in EC:EMC = 30m%:70m%, BASF SE). The LFP was delithiated with a C-rate of C/10 at constant current to a cell potential cut-off of 4 V. The cell was held at 4 V until the current fell below C/100 to assure complete delithiation. The cell was then opened inside a glovebox (<0.1 ppm O_2 and H_2O, MBraun, Germany), the lithium counter electrode and the separator were removed and replaced by ^6Li foil obtained from ^6Li chunks (99.8 %, enrichment 95 at%, Sigma Aldrich) and a polyolefin separator (C2500, Celgard, USA). As electrolyte, 100 µL of 1 M $^6LiPF_6$ (99.8 %, enrichment 95 at%, Sigma Aldrich) in ethylene carbonate (EC, ≥99 %, Sigma Aldrich) and ethyl methyl carbonate (BASF SE, Germany) in a ratio of 30m%/70m% were used. The $^6LiPF_6$ salt was dried at 80 °C under dynamic vacuum in a glass oven (drying oven 585, Büchi, Switzerland). The delithiated $FePO_4$ electrode was relithiated with constant current at a C-rate of C/10 to a cell cut-off potential of 2 V, the cell then opened inside a glovebox and $^6LiFePO_4$ (^6LFP) electrodes with a diameter of 10 mm were harvested.

Cell assembly and cell cycling. The graphite electrodes were glued into a commercial CR2032 coin cell cap (Hohsen Corp., Japan) using epoxy resin (UHU Plus Endfest, Bolton Group S.r.l., Italy). The coin cell cap contained a laser-cut grid of 139 holes with a diameter of 300 µm arranged in a hexagonal pattern with a centre-to-centre distance of 650 µm (s. Fig. 2b). The electrode was dried overnight at 80 °C under dynamic vacuum in a glass oven (drying oven 585, Büchi,

Switzerland) and transferred into an argon-filled glovebox without exposure to air. To assure electrical contact between the copper current collector and the stainless-steel coin cell cap, a 10 µm-thick copper foil annulus with an inner diameter of 13 mm and an outer diameter of 19 mm was positioned around the graphite electrode. The coin cell was built using six glass fibre separators with a diameter of 17 mm and an uncompressed thickness of 250 µm (glass microfiber filter 691, VWR, Germany), soaked with 270 µL of ≈ (0.31 ± 0.01) M $^{6}LiPF_6$ (concentration determined by ICP-OES) in a mixture of ethylene carbonate (EC, ≥ 99 %, Sigma Aldrich) and ethyl methyl carbonate (BASF SE, Germany) in a ratio of 30m%/70m%. The ^{6}LFP cathodes with a diameter of 10 mm described above were used as ≈ 3.5-fold capacitively oversized counter electrode (CE) serving as lithium reservoir. Thus, the graphite anodes were geometrically by a factor of 1.44 oversized. The cell pressure was adjusted to ≈3 bar with a 0.5 mm-thick aluminium spacer containing a 100 µm x 10.1 mm circular milled slot, which at the same time precisely centred the LFP CE during cell assembly.

To benchmark the performance of the ^{6}Li-enriched *operando* NDP cell with a laboratory cell, Figure 8 shows the formation of an *operando* NDP cell (1 M $^{6}LiPF_6$ in EC/EMC = 30m%/70m%, ^{6}LFP CE) and of a Swagelok®-type T-cell (1 M $^{7}LiPF_6$ in EC/EMC = 30m%/70m%, ^{7}LFP CE, graphite coated on 10 µm copper foil) using the same graphite active material and amount of separators. Note that in the case of the Swagelok®-type T-cell, both electrodes had a diameter of 11 mm, and therefore the graphite anode was geometrically not oversized explaining the slightly longer constant voltage (CV) phase in case of the *operando* NDP setup.

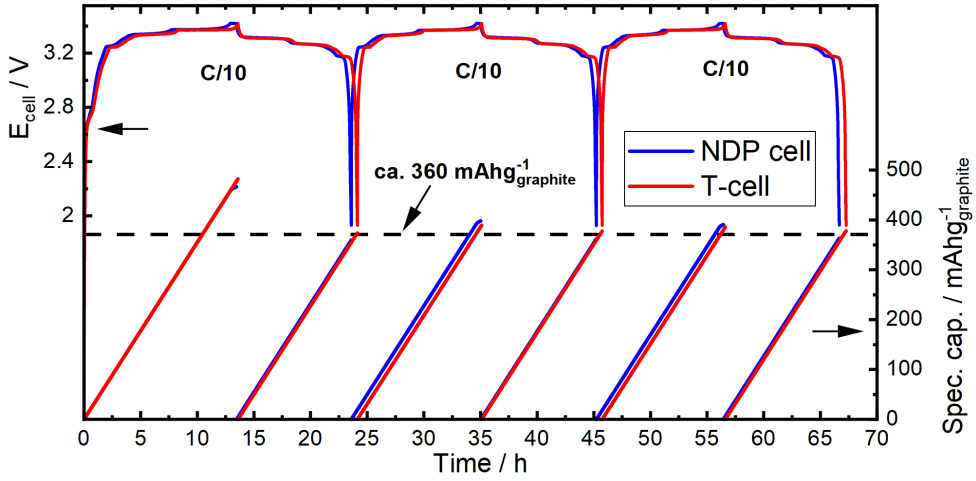

Fig 8. Benchmark of the ^{6}Li-enriched *operando* NDP cell. Cell potential profile and capacities for a ^{6}LFP/graphite *operando* NDP cell (1 M $^{6}LiPF_6$ in EC/EMC = 30 m%/70 m%) and a ^{6}LFP/graphite Swagelok®-type T-cell (1 M $^{6}LiPF_6$ in EC/EMC = 30 m%/70 m%) during three formation cycles at C/10.

All cells were formed with constant current for three cycles between 3.42 V_{cell} and 1.93 V_{cell} at a C-rate of C/10 (with respect to the first delithiation capacity) with a constant voltage step until a cutoff current of C/40 to end the charging phase. The plating experiment in the *operando* NDP cell was performed by increasing the charging rate from 0.25 C, 0.5 C, 1 C to 2 C, keeping the discharging rate always constant at 0.25 C to assure complete delithiation of the graphite electrode. The end-of-charge is defined *via* a time cutoff corresponding to a charging capacity of 355 mAh $g^{-1}_{graphite}$, such that the transferred charging capacity is identical for all C-rates. Formation of all *operando* coin cells was done at the Technical University of Munich. The coin cells were cycled in an argon-filled glovebox using a VMP3 potentiostat (Biologic, France) and the Swagelok®-type T-cells on a battery cycler (Maccor, series 4000, USA). For the *operando* cycling at NIST, an SP300 potentiostat (Biologic, France) was used. The pre-formed cells were sealed in air-tight pouch foil inside a glovebox and then inertly transferred to the beamline at NIST. For sample transfer into the NDP chamber at

NIST, the cells were exposed to air for ≈ 5 min. For this timeframe the copper-sputtered Kapton® window is tight against oxygen and moisture.

The rate capability of the graphite electrodes with low loading was tested in a three-electrode Swagelok®-type T-cells cycling *vs.* a lithium metal counter electrode using four glass fiber separators (glass microfiber filter 691, VWR, Germany) to avoid cell short-circuiting at high cycling rates and 240 µL of electrolyte. Cycling was performed using a battery cycler (Series 4000, Maccor, USA) within a potential window between 1.5 V_{cell} – 0.01 V_{cell} controlling the graphite electrode potential *vs.* a lithium metal reference electrode. The loading was (126 ± 19) µAh cm^{-2}, the error mainly originating from the mass uncertainty of the copper current collector foil, which is (8.10 ± 0.05) mg. The cells first underwent three formation cycles at C/10 (based on a graphite capacity of 355 mAh $g^{-1}_{graphite}$) In the subsequent rate test, the lithiation rates were 3 C, 5 C, 10 C, 15 C, 20 C, 25 C, 30 C, and 50 C, three cycles each, with galvanostatic cycling. The delithiation rate was always kept constant at 0.2 C for higher rates in order to assure complete delithiation of the electrode at the end of each cycle. For the evaluation of the rate-performance the third cycle of each C-rate was used.

Scanning electron microscopy (SEM). Electrode cross-sections were prepared by argon ion beam polishing using a JEOL Cross Section Polisher IB-19520CCP (JEOL, Japan). Afterwards, SEM images were taken on a JEOL JCM-6000 NeoScope (JEOL, Japan).

Neutron depth profiling (NDP).

Setup

NDP measurements were recorded at the Cold Neutron Depth Profiling (CNDP) instrument at the National Institute for Standards and Technology (NIST) in Gaithersburg, MD, USA.[43] The cold neutron beam exhibits a flux of 1.22×10^9 cm^{-2} s^{-1} determined by a gold foil activation analysis experiment. In order to perform cycling at a gas pressure above the vapour pressure of the liquid electrolyte in the cell, the NDP chamber was filled with high purity helium gas at a nominal pressure of ≈ 150 hPa. Thus, additional energy loss of the charged particles while travelling through the chamber atmosphere before reaching the detector was minimized, which maximized the viewing depth into the sample to about 30 µm. The coin cell was mounted in a specially designed *operando* sample holder shown in Figure 1d. The sample holder was positioned at an angle of 45 ° with respect to the incoming neutron beam with the holes in the coin cells facing the charged particle detector (AB-018-150-150, ORTEC) placed at a distance of ≈ 22 cm from the sample. The samples could be placed behind hand-made holes with a diameter of ≈ 8 mm on a Teflon® target stage to define the area from where charged particles could emanate.

Energy calibration

The digitized measurement channels were calibrated to an absolute energy scale using six calibration points induced by neutron capture on a 10 nm-thick B_4C film on the surface of a silicon wafer and a nominally 1.1 µg cm^{-2}-thick LiF layer on the surface of a Mylar foil[40] using a quadratic fit.

Concentration calibration

Two different hole areas of the hand-made Teflon® sample holder were determined using a lithium-containing reference sample. The measurement uncertainties of these independent position measurements, for each hole determined by the ratio of the count rate and the square root of the total number of counts, results in a total systematic error of 2.2 % when normalizing the energy spectra to an absolute quantity. Additionally, the lowered signal intensity caused by the reduced NDP active area of the coin cell cap (139 holes with a diameter of 300 µm) compared to a reference position was analogously determined with a precision of 1.2 % using a nominally 6.3 µm-thick LiF film behind both positions. For conversion of NDP signals to an absolute quantity, a NIST in-house ^{10}B reference material (RR8B16) was used as a calibration sample, and all count rates were normalized to it. It has a well-known ^{10}B implantation in silicon with a

systematic uncertainty of 1.4 % and the boron amount was determined with a precision of 0.4 % using NDP. Considering the capture cross-sections of ^{10}B and ^{6}Li, respectively, NDP signals were converted to an absolute lithium amount. During all measurements, the neutron beam was monitored measuring a boron-containing reference sample. A variation in the neutron flux of 2.5 % was observed during the measurement time by integrating the measurement signal of the beam monitor in 2 h intervals and is the result of a rotating monochromator upstream of the NDP neutron guide. As an estimation of the maximum systematic error of the NDP measurement, the three systematic uncertainties, namely given by the uncertainty of the reference standard (1.4 %), the calibration uncertainties (independently consisting of the area measurements (2.2 % and 1.2 %) and the statistical uncertainty of the RR8B16 (0.4 %) which result in a total calibration error of 2.5 %) and the variation of the neutron flux (2.5 %) add up together to 6.4 %.

Depth Profile Conversion

To convert the energy spectra to depth profiles, the stopping power of *triton* particles provided by the *Stopping and Range of Ions in Matter* (SRIM) software was used.[45, 44] Here, the energy losses from the initial *triton* production energy of 2727 keV caused by the successive materials between anode and detector surface were estimated to be ≈ 11 keV from the 100 nm-thick copper current collector, ≈ 301 keV from the nominal 7.5 µm-thick Kapton® foil, and ≈ 51 keV from the helium gas atmosphere between sample and detector.[54] The graphite electrode, *i.e.*, coated material and electrolyte-filled pores, composition was assumed to be constant with depth. It was modelled using the elemental composition of the pristine anode, consisting of 91 m%/9 m% graphite/PVDF binder. After compression, the anode porosity was determined to ≈ (52 ± 4) %. When mounted in the *operando* cell, the pores of the anode are filled with liquid electrolyte, and thus its composition was corrected for the liquid electrolyte (composition: ≈ (0.31 ± 0.01) M $^{6}LiPF_6$ in EC/EMC = 30 m%/70 m%), assuming a complete pore filling of the graphite anode. From the electrode composition an average density of 1.7 g cm^{-3} was determined. The concentration profile within the electrode was then determined using the combined material stopping powers.[38, 55] Before measuring *operando* NDP, an SEI layer was formed on the pristine anode during the three formation cycles at C/10 which additionally changed the composition of the electrolyte-filled anode. All elements contained in the SEI other than lithium originate from electrochemical reduction of the liquid electrolyte, and were thus already present within the pristine graphite electrode filled with electrolyte. Within this model, minor composition changes caused by a possible material density change of the electrolyte upon electrochemical reduction (SEI formation) are neglected. Therefore, the elemental composition change was assumed to be mainly affected by lithium-ions electrochemically transferred from the LFP cathode to the graphite anode. The electrode composition was corrected for the lithium in the SEI (s. row 3 in Table 3) based on a previous NDP study:[42] Taking into account that ≈ 62 % of the lithium expected from the irreversible capacity (assuming 1 Li/e^-) can be detected in the SEI in form of Li-containing decomposition products, the ratio of the lithium content in the graphite electrode after SEI formation is expected to be 20.5 times higher than the lithium content in the pristine electrode stemming from the liquid electrolyte containing ≈ 0.31 M $^{6}LiPF_6$.[42] The further composition changes upon cell operation were taken into account by quantifying the total lithium content accumulated in the graphite electrode by integrating the NDP spectra and adjusting the anode composition for each SOC (s. row 4-10 in Table 3).[38, 42, 55] It is to state that the NDP calculations based on this density and composition model are only valid within the measured electrolyte-filled graphite electrode and are no longer correct outside of the anode, *i.e.*, within the electrolyte. Therefore, we focus in this work only on the lithium formation within the electrolyte-filled graphite anode.

Table 3. Modelled graphite electrode compositions. Elemental composition of the graphite anode estimated for different SOCs. For the pristine graphite anode coating the composition (graphite + PVDF) is well known and it is assumed that the pores (52 % porosity) in the graphite coating are completely filled with electrolyte. After cell formation, an SEI layer has formed on the graphite particles. Only the additional lithium amount in the SEI was taken into account

to estimate the new electrode composition after formation. The accumulation of lithium was calculated based on 62 % of the irreversible capacity loss (*i.e.*, a 0.62 Li/e^- instead of a commonly assumed 1 Li/e^- decomposition mechanism, as demonstrated in a recent NDP study[42]). During operation, lithium-ions are (de-)intercalated in the graphite anode, which additionally changes the electrode composition. The reversibly intercalated lithium was determined *via* integration of the NDP energy spectra and was taken into account to model the electrode composition as a function of SOC.

Anode SOC (spectrum #)	H (mol%)	Li (mol%)	C (mol%)	O (mol%)	F (mol%)	P (mol%)
Pristine	22.3	0.1	65.8	9.2	2.5	0.1
0 % SOC (1)	22.0	1.7	64.7	9.0	2.4	0.1
100 % SOC (2)	20.5	8.5	60.3	8.4	2.3	0.1
0 % SOC (3)	21.9	2.1	64.5	9.0	2.4	0.1
100 % SOC (4)	20.4	8.7	60.1	8.4	2.3	0.1
0 % SOC (5)	21.9	2.2	64.4	9.0	2.4	0.1
100 % SOC (6)	20.4	8.9	60.0	8.4	2.3	0.1
0 % SOC (7)	21.9	2.2	64.4	9.0	2.4	0.1
100 % SOC (8)	20.6	7.7	60.8	8.5	2.3	0.1

Acknowledgment

SGL Carbon is kindly acknowledged for providing the sieved graphite active material. The authors gratefully acknowledge funding by the BMBF (Federal Ministry of Education and Research, Germany) under the auspices of the “N4DP”, grant numbers 05K16WO1 and 05K19WO8, and the ”ExZellTUM II” project, grant number 03XP0081.

Trade names and commercial products are identified in this paper to specify the experimental procedures in adequate detail. This identification does not imply recommendation or endorsement by the authors or by the National Institute of Standards and Technology, nor does it imply that the products identified are necessarily the best available for the purpose. Contributions of the National Institute of Standards and Technology are not subject to copyright.

References

1. Liu, Y., Zhu, Y. & Cui, Y. Challenges and opportunities towards fast-charging battery materials. *Nat. Energy* **4**, 540–550 (2019).

2. Andre, D. *et al.* Future generations of cathode materials: An automotive industry perspective. *J. Mater. Chem. A* **3**, 6709–6732 (2015).

3. Howell, D., Duong, T., Faguy, P. & Cunningham, B. U.S. DOE vehicle battery R&D: Progress update. (2011).

4. Field, K. 'Breaking! Tesla Increases Supercharging V2 Speeds As S & X Get On-Route Battery Warmup'. Available at: https://cleantechnica.com/2019/04/26/breaking-tesla-increases-supercharging-v2-speeds-as-s-x-get-on-route-battery-warmup/. (Accessed: 30th November 2019)

5. Schmuch, R., Wagner, R., Hörpel, G., Placke, T. & Winter, M. Performance and cost of materials for lithium-based rechargeable automotive batteries. *Nat. Energy* **3**, 267–278 (2018).

6. Kwade, A. *et al.* Current status and challenges for automotive battery production technologies. *Nat. Energy* **3**, 290–300 (2018).

7. Dahn, J. R. Phase diagram of LixC6. *Phys. Rev. B* **44**, (1991).

8. Ahmed, S. *et al.* Enabling fast charging – A battery technology gap assessment. *J. Power Sources* **367**, 250–262 (2017).

9. Goodenough, J. B. & Kim, Y. Challenges for Rechargeable Li Batteries. *Chem. Mater.* **22**, 587–603 (2010).

10. Hasan, M. F., Chen, C. F., Shaffer, C. E. & Mukherjee, P. P. Analysis of the implications of rapid charging on lithium-ion battery performance. *J. Electrochem. Soc.* **162**, A1382–A1395 (2015).

11. Li, J. *et al.* Limiting factors for low-temperature performance of electrolytes in LiFePO 4/Li and graphite/Li half cells. *Electrochim. Acta* (2012). doi:10.1016/j.electacta.2011.10.041

12. Nyman, A., Zavalis, T. G., Elger, R., Behm, M. & Lindbergh, G. Analysis of the polarization in a Li-ion battery cell by numerical simulations. *J. Electrochem. Soc.* **157**, 1236–1246 (2010).

13. Gallagher, K. G. *et al.* Optimizing areal capacities through understanding the limitations of lithium-ion electrodes. *J. Electrochem. Soc.* **163**, A138–A149 (2016).

14. Landesfeind, J., Hattendorff, J., Ehrl, A., Wall, W. A. & Gasteiger, H. A. Tortuosity Determination of Battery Electrodes and Separators by Impedance Spectroscopy. *J. Electrochem. Soc.* **163**, A1373–A1387 (2016).

15. Yang, X. G., Zhang, G., Ge, S. & Wang, C. Y. Fast charging of lithium-ion batteries at all temperatures. *Proc. Natl. Acad. Sci. U. S. A.* **115**, 7266–7271 (2018).

16. Li, Z., Huang, J., Yann Liaw, B., Metzler, V. & Zhang, J. A review of lithium deposition in lithium-ion and lithium metal secondary batteries. *J. Power Sources* **254**, 168–182 (2014).

17. Bach, T. C. *et al.* Nonlinear aging of cylindrical lithium-ion cells linked to heterogeneous compression. *J. Energy Storage* **5**, 212–223 (2016).

18. Burns, J. C., Stevens, D. A. & Dahn, J. R. In Situ Detection of Lithium Plating Using High Precision Coulometry. *J. Electrochem. Soc.* **162**, A959–A964 (2015).

19. Uhlmann, C., Illig, J., Ender, M., Schuster, R. & Ivers-Tiffée, E. In situ detection of lithium metal plating on graphite in experimental cells. *J. Power Sources* (2015).

20. Zinth, V. *et al.* Lithium plating in lithium-ion batteries at sub-ambient temperatures investigated by in situ neutron diffraction. *J. Power Sources* **271**, 152–159 (2014).

21. Petzl, M. & Danzer, M. A. Nondestructive detection, characterization, and quantification of lithium plating in commercial lithium-ion batteries. *J. Power Sources* **254**, 80–87 (2014).

22. Anseán, D. *et al.* Operando lithium plating quantification and early detection of a commercial LiFePO4 cell cycled under dynamic driving schedule. *J. Power Sources* **356**, 36–46 (2017).

23. Von Lüders, C. *et al.* Lithium plating in lithium-ion batteries investigated by voltage relaxation and in situ neutron diffraction. *J. Power Sources* **342**, 17–23 (2017).

24. Zhang, S. S. The effect of the charging protocol on the cycle life of a Li-ion battery. *J. Power Sources* **161**, 1385–1391 (2006).

25. Waldmann, T. *et al.* Interplay of Operational Parameters on Lithium Deposition in Lithium-Ion Cells: Systematic Measurements with Reconstructed 3-Electrode Pouch Full Cells. *J. Electrochem. Soc.* **163**, A1232–A1238 (2016).

26. Zhuang, L., Lu, J., Ai, X. & Yang, H. In-situ ESR study on electrochemical lithium intercalation into petroleum coke. *J. Electroanal. Chem.* **397**, 1–5 (1995).

27. Wandt, J., Jakes, P., Granwehr, J., Eichel, R. A. & Gasteiger, H. A. Quantitative and time-resolved detection of lithium plating on graphite anodes in lithium ion batteries. *Mater. Today* **21**, 231–240 (2018).

28. Gotoh, K. *et al.* In situ 7Li nuclear magnetic resonance study of the relaxation effect in practical lithium ion batteries. *Carbon N. Y.* **79**, 380–387 (2014).

29. Downie, L. E. *et al.* In Situ Detection of Lithium Plating on Graphite Electrodes by Electrochemical Calorimetry. *J. Electrochem. Soc.* **160**, A588–A594 (2013).

30. Birkenmaier, C., Bitzer, B., Harzheim, M., Hintennach, A. & Schleid, T. Lithium Plating on Graphite Negative Electrodes: Innovative Qualitative and Quantitative Investigation Methods. *J. Electrochem. Soc.* **162**, A2646–A2650 (2015).

31. Yang, X. G., Leng, Y., Zhang, G., Ge, S. & Wang, C. Y. Modeling of lithium plating induced aging of lithium-ion batteries: Transition from linear to nonlinear aging. *J. Power Sources* **360**, 28–40 (2017).

32. Doyle, M., Fuller, T. F. & Newman, J. The Importance of the Lithium Ion Transference Number in Lithium/Polymer Cells. *Electrochim. Acta* **29**, 2073–2081 (1994).

33. Newman. *Electrochemical Systems*. (2004).

34. Waldmann, T., Hogg, B. I. & Wohlfahrt-Mehrens, M. Li plating as unwanted side reaction in commercial Li-ion cells – A review. *J. Power Sources* **384**, 107–124 (2018).

35. Waldmann, T. & Wohlfahrt-Mehrens, M. Effects of rest time after Li plating on safety behavior—ARC tests with commercial high-energy 18650 Li-ion cells. *Electrochim. Acta* **230**, 454–460 (2017).

36. Kushima, A. *et al.* Liquid cell transmission electron microscopy observation of lithium metal growth and dissolution: Root growth, dead lithium and lithium flotsams. *Nano Energy* **32**, 271–279 (2017).

37. Ziegler, J. F., Cole, G. W. & Baglin, J. E. E. Technique for determining concentration profiles of boron impurities in substrates. *J. Appl. Phys.* **43**, 3809–3815 (1972).

38. Trunk, M. *et al.* Materials science applications of Neutron Depth Profiling at the PGAA facility of Heinz Maier-Leibnitz Zentrum. *Mater. Charact.* **146**, 127–134 (2018).

39. Wetjen, M. *et al.* Quantifying the Distribution of Electrolyte Decomposition Products in Silicon-Graphite Electrodes by Neutron Depth Profiling. *J. Electrochem. Soc.* **165**, A2340–A2348 (2018).

40. Werner, L. *et al.* The new neutron depth profiling instrument N4DP at the Heinz Maier-Leibnitz Zentrum. *Nucl. Instruments Methods Phys. Res.* **911**, 30–36 (2018).

41. Weaver, J. L. & Turkoglu, D. Natural alteration of 6Li alumino-silicate glass. *J. Nucl. Mater.* **512**, 56–64 (2018).

42. Linsenmann, F. *et al.* Formation of the Solid Electrolyte Interphase on a Graphite Anode Studied by Operando Neutron Depth Profiling. *submitted*

43. Downing, R. G., Fleming, R. F., Vincent, D. H. & Arbor, A. Neutron Depth Profiling at the National Bureau of Standards. *Nucl. Instruments Methods Phys. Res.* **218**, 47–51 (1983).

44. Ziegler, J. F., Ziegler, M. D. & Biersack, J. P. SRIM - The stopping and range of ions in matter (2010). *Nucl. Instruments Methods Phys. Res.* **268**, 1818–1823 (2010).

45. Ziegler, J. F. *Handbook of Helium Stopping Powers and Ranges in All Elements, Vol. 4*. (Pergamon Press, New York, 1977).

46. Landesfeind, J. & Gasteiger, H. A. Temperature and concentration dependence of the ionic transport properties of lithium-ion battery electrolytes. *J. Electrochem. Soc.* **166**, A3079–A3097 (2019).

47. Ghanbari, N., Waldmann, T., Kasper, M., Axmann, P. & Wohlfahrt-Mehrens, M. Detection of Li deposition by Glow discharge optical emission spectroscopy in post-mortem analysis. *ECS Electrochem. Lett.* **4**, A100–A102 (2015).

48. Nyman, A., Behm, M. & Lindbergh, G. Electrochemical characterisation and modelling of the mass transport phenomena in LiPF6-EC-EMC electrolyte. *Electrochim. Acta* **53**, 6356–6365 (2008).

49. Verbrugge, M. W. Electrochemistry of Intercalation Materials Charge-Transfer Reaction and Intercalate Diffusion in Porous Electrodes. *J. Electrochem. Soc.* **146**, 833 (1999).

50. Doyle, M. Comparison of Modeling Predictions with Experimental Data from Plastic Lithium Ion Cells. *J. Electrochem. Soc.* **143**, 1890 (1996).

51. Doyle, M. & Fuentes, Y. Computer Simulations of a Lithium-Ion Polymer Battery and Implications for Higher Capacity Next-Generation Battery Designs. *J. Electrochem. Soc.* **150**, A706 (2003).

52. Rheinfeld, A. *et al.* Quasi-Isothermal External Short Circuit Tests Applied to Lithium-Ion Cells: Part II. Modeling and Simulation. *J. Electrochem. Soc.* **166**, A151–A177 (2019).

53. Levi, M. D. & Aurbach, D. Diffusion coefficients of lithium ions during intercalation into graphite derived from the simultaneous measurements and modeling of electrochemical impedance and potentiostatic intermittent titration characteristics of thin graphite electrodes. *J. Phys. Chem. B* **101**, 4641–4647 (1997).

54. Geissel, H., Weick, C. & Scheidenberger, H. G. H. für Schwerionenforschung GmbH. (2019). Available at: https://www.isotopea.com/webatima/.

55. Verhallen, T. W., Lv, S. & Wagemaker, M. Operando Neutron Depth Profiling to Determine the Spatial Distribution of Li in Li-ion Batteries. *Front. Energy Res.* **6**, (2018).

4 Conclusions and Outlook

Gaining insights into fundamental (electro)chemical processes and degradation mechanisms occurring in rechargeable batteries requires in many cases to probe materials in an actually operating cell in order to exclude altering the system properties by post-operational treatment, such as cell disassembly, material extraction, or the analytical technique itself, which necessarily changes the sample environment.[232, 233] Therefore, the primary scope of this PhD thesis was the development of two novel analytical tools for *in situ* and *operando* investigations of electrochemical processes in sodium-ion batteries (SIBs) and lithium-ion batteries (LIBs), respectively. The diagnostic techniques employed are based on, a) Electrochemical Impedance Spectroscopy (EIS) using a μ-reference electrode (section 3.1), and b) Neutron Depth Profiling (NDP) (section 3.2).

The key developments and major studies conducted in this work are summarized in Figure 21.

4.1 Summary of the Key Developments of This Work

The already established impedance technique using a gold wire μ-reference electrode (µ-GWRE) to measure the individual impedances of both cathode and anode in a LIB full-cell, without having to harvest the electrodes for *ex situ* analysis in symmetrical cells, was expanded to the field of SIBs. Since sodium, in contrast to lithium, does not readily alloy with gold, a μ-reference electrode based on a sodiated tin-coated copper wire was developed, taking advantage of the facile alloy formation between sodium and tin. The accuracy of the measured EIS responses was validated *via* comparison with EIS data obtained with the symmetrical cell approach. The publication introducing this new method to the field of sodium-ion

battery research is presented in section 3.1.1. A follow-up study applies these μ-REs to compare the electrode impedances associated with sodium and lithium intercalation in a hard carbon anode. This study underlines that the overall cell impedance changes measured in half-cells with sodium or lithium CEs do generally not allow inferences on the impedance changes of the WE, due to the large contribution of the CE to the overall cell impedance during cycling, which also changes over time. An important finding in this study is the fact that the electrode impedance of a sodiated hard carbon electrode is by a factor of ≈10 larger compared to a lithiated hard carbon electrode (at 100 % SOC), and that it is dominated by a large charge transfer resistance. The very larger hard carbon electrode impedance for (de)sodiation was found to substantially decrease its sodiation rate capability, suggesting that the commonly used hard carbon anode in SIBs would also likely limit its fast-charging capability. The article described above is presented in section 3.1.2.

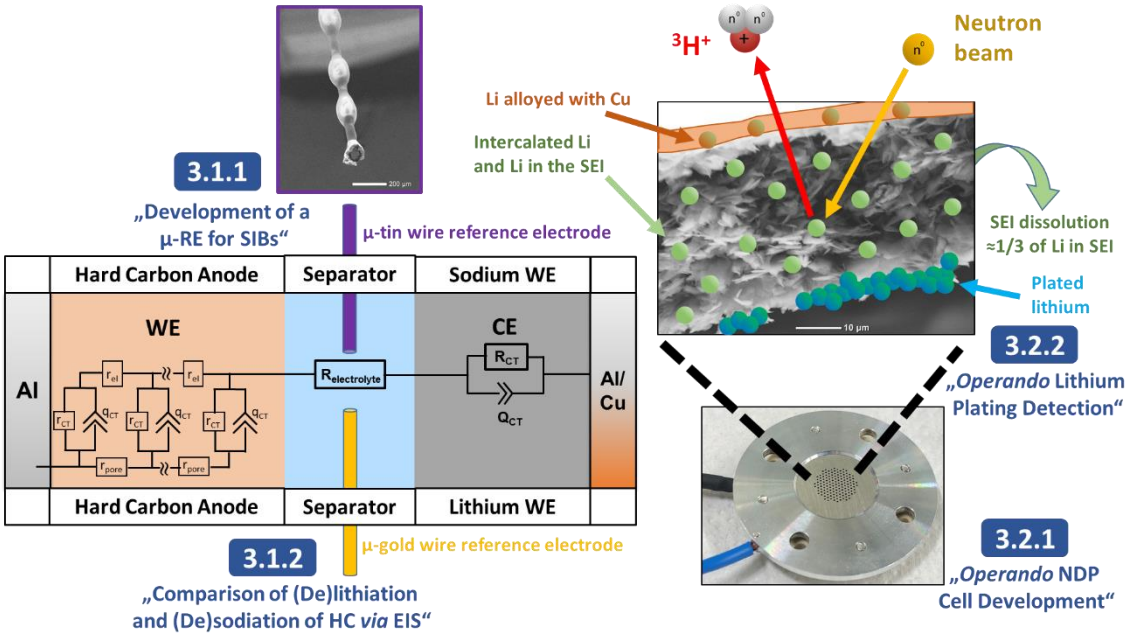

Figure 19. Graphical summary of the key results of this PhD thesis: the development of a μ-RE for impedance measurements in SIBs (section 3.1.1), a direct comparison between electrode impedances of a HC material during sodiation and lithiation using μ-REs (section 3.1.2), the development of a cell design for *operando* NDP measurements (section 3.2.1), and the detection of lithium plating during fast-charging using *operando* NDP (section 3.2.2).

Apart from Electrochemical Impedance Spectroscopy, the second analytical technique that was in focus of this PhD thesis is Neutron Depth Profiling (NDP). Unique to this technique is its capability to quantify lithium concentrations within

a sample as a function of depth and the fact that it is non-destructive, which makes it suitable for *operando* observations of lithium concentrations across the thickness of an electrode in a LIB. To fully exploit the capabilities of NDP, an *operando* LIB cell design is required which possesses comparable performance to standard laboratory cells, thereby guaranteeing that the studied electrochemical processes are actually representative of reactions that would also occur in commercial cells, so that the mechanistic findings are of practical relevance. Section 3.2.1 introduces a novel LIB *operando* NDP cell design which on the one hand accomplishes an electrochemical performance as in a laboratory cell even at elevated cycling rates, and on the other hand is optimized in a way such that NDP spectra can be recorded with high quality during cell operation. The key property of this new cell design is the use of a pattern of very small holes (300 or 500 µm) in the cell casing, sealed by a thin copper-sputtered 7.5 µm thick Kapton® foil as exit window for the charged particles formed by a nuclear reaction between ^{6}Li and neutrons inside the electrode of an operating cell. The new cell setup is then used to study the lithium concentration changes in a graphite anode during formation, allowing for an identification and quantification of lithium in the electrolyte, of reversibly intercalated lithium, and of lithium that is part of the solid electrolyte interphase formed by irreversible reactions between electrolyte and lithiated active material. It was found that lithium alloys with the copper in the near-surface region (≈10 nm) of the copper current collector. Moreover, to the best of our knowledge, it was for the first time possible to *in situ* quantify the total amount of lithium captured in the SEI, and thus to correlate the expected lithium amount from the irreversible capacity (based on the commonly assumed ratio of one lithium per electron of irreversible charge) with the actual lithium amount in the SEI after cell formation. Here, we could show that only ≈61 % of the lithium expected from the irreversible capacity is captured in the SEI, from which we conclude that ≈39 % of the lithium-containing SEI components dissolve in the battery electrolyte.

4.2 Potential Future Applications of the Here Developed Diagnostics

In a second study presented in section 3.2.2, we employ the newly developed *operando* NDP cell to investigate lithium plating during fast-charging of a graphite anode in a lithium-ion battery cell. Here, we managed to directly monitor lithium plating both spatially and time-resolved on a graphite anode. The two key enablers for this accomplishment were: 1) a homogeneous compression of the cell stack by the hole patterned coin cell cap, enabling fast-charging; 2) enrichment of electrolyte and CE with ^{6}Li in order to reduce the NDP spectrum acquisition time from ≈1 h to 2 min. We could thereby prove that lithium plating induced by a lithium-ion concentration gradient, as it would also be the case in a commercial cell if the battery is charged too rapidly, initiates at the separator/graphite anode interface, and that this plated lithium redistributes homogeneously across the electrode, within ≈2 min once the charging process is stopped.

The μ-TWRE can serve as a useful tool for all researchers working in the field of materials development for SIBs to study the effect of additives on electrode impedance,[41] to study phase transformations upon desodiation of cathode active materials, which are often associated with large impedance changes,[94] or to enable the deconvolution of different contributions to the total impedance of anindividual electrode, such as $R_{contact}$, R_{pore}, and R_{CT}, similar to studies performed for LIB cells.[186, 184]

The *operando* NDP cell developed in this PhD thesis also presents a versatile tool for many other applications where lithium distributions across the thickness of an electrode need to be probed during cell operation. Analogous to the lithium plating study on graphite, an interesting future experiment would be to examine the onset of lithium plating and the rate of its subsequent redistribution in a silicon electrode. Due to its higher specific capacity, lower mass loadings and thus lower electrode thicknesses are sufficient to obtain areal capacities representative of commercial applications (≈2 mAh/cm^2). Since the probing depth of NDP is limited, thinner electrodes are beneficial in order to obtain a lithium concentration profile across the entire electrode. The density of silicon is similar compared to graphite (ρ_{Si} = 2.32 g/cm^3, $\rho_{graphite}$ = 2.26 g/cm^3), resulting in viewing depths comparable to

those of the studies presented in this thesis. The average lithiation potential of silicon anodes is significantly higher compared to graphite ($\bar{V}_{Si}$≈217 mV, $\bar{V}_{graphite}$≈117 mV at C/10, s. Fig. 22), which in principle should be advantageous with respect to avoiding lithium plating during fast-charging.

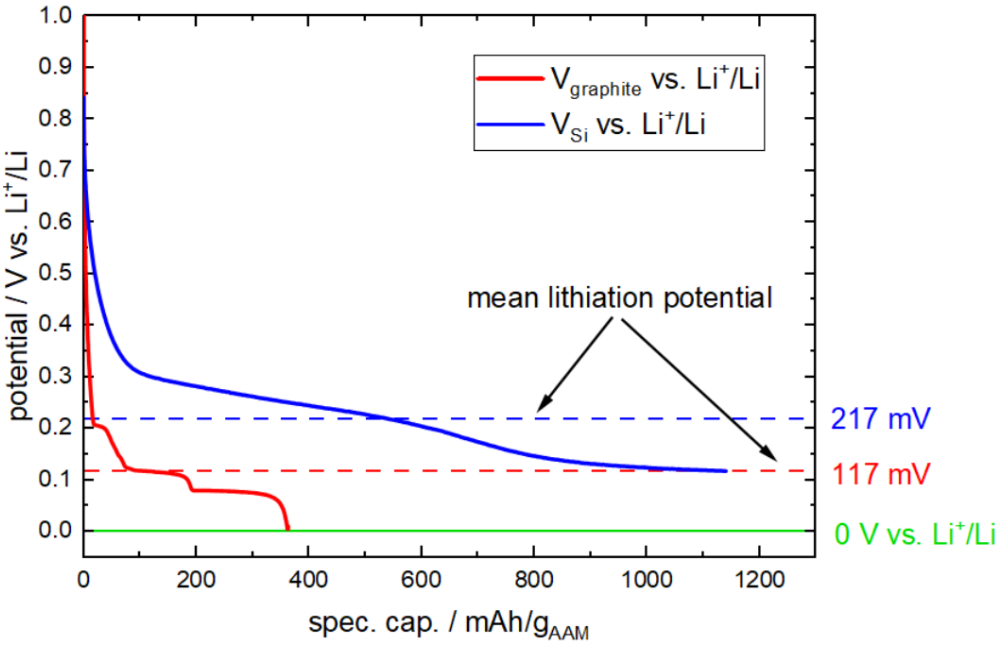

Figure 20. Comparison of the lithiation profiles of a graphite (red) (95wt% graphite, 5wt% PVDF; 2 mAh/cm²) and a silicon (blue) electrode (70 wt% Si, 25 wt% conductive graphite; 2 mAh/cm²) at a C-rate of C/10. Additionally, the mean lithiation potential is indicated by a dashed line, which is ≈117 mV for graphite and ≈217 mV in the case of silicon.

Furthermore, the electrode architecture has to be designed with a higher porosity compared to graphite to allow for a volume expansion of the silicon particles during lithiation, *e.g.*, ≈60 % (*i.e.*, uncalendered), as shown in a recent study by Jantke *et al.*[120] using µm-sized silicon and a partial lithiation approach. In comparison, state-of-the-art graphite electrodes have porosities of ≈20-25 % (corresponding to a coating density of ≈1.6-1.8 g/cm³) in order to maximize the electrode's energy density.[120, 44] The higher porosity in these silicon electrodes should additionally be favorable to delay the onset of lithium plating, since it reduces the formation of lithium-ion concentration gradients.

Apart from that, the NDP cell holder designed in this thesis can be equipped with a cooling feature (s. technical drawings in the Appendix), allowing for cooling the cell holder and the *operando* cells to a defined temperature down to -20 °C. This setup can be, *inter alia*, used to study lithium plating at low temperatures,[234, 235] a

scenario that for example might occur during fast-charging of a cold EV battery parked outdoors in winter.

A different approach to increase the energy density of a LIB cell, other than increasing the specific capacity of the anode material, *e.g.*, by using silicon, are so called "anode-free" cell designs, where the lithium anode is formed by *in situ* plating lithium from the cathode's lithium inventory. [126, 127, 128, 129] In these cells, the anode active material would be completely eliminated, constituting a Cu/separator/cathode/Al configuration, thereby increasing the energy density of the cell significantly; at the same time, such cells would operate at a can operate at ≈0.1 V higher potential compared to a graphite-based LIB.[128] The greatest challenge of this upcoming cell chemistry is the relatively low lithium plating/stripping efficiency of the *in situ* formed lithium anode, limiting the cycle life. However, in a recent study by Weber *et al*. 90 cycles until a remaining capacity of 80 % could be achieved using an optimized electrolyte system (LiDFOB + $LiBF_4$ in FEC/DEC).[129] The lithium plating/stripping processes on the copper current collector during operation could be monitored with high resolution using *operando* NDP and provide many fundamental insights on the effect of the electrolyte (additives) on the morphology of the plated lithium over the course of cycling.

5 Appendix

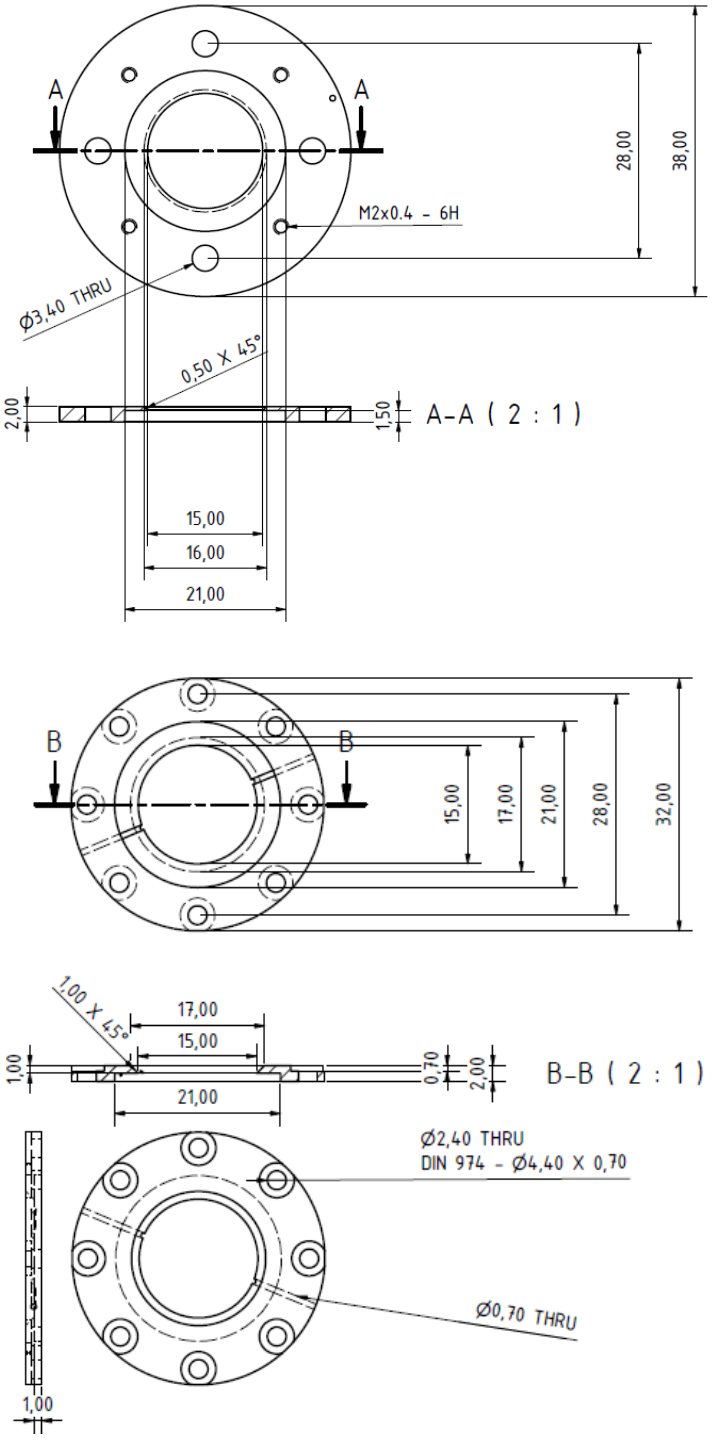

Figure 21. Technical drawings of the coin cell holder used for *operando* NDP measurements at neutron reactor at NIST in Gaithersburg, USA. Here, one coin cell can be mounted and cycled at a time.

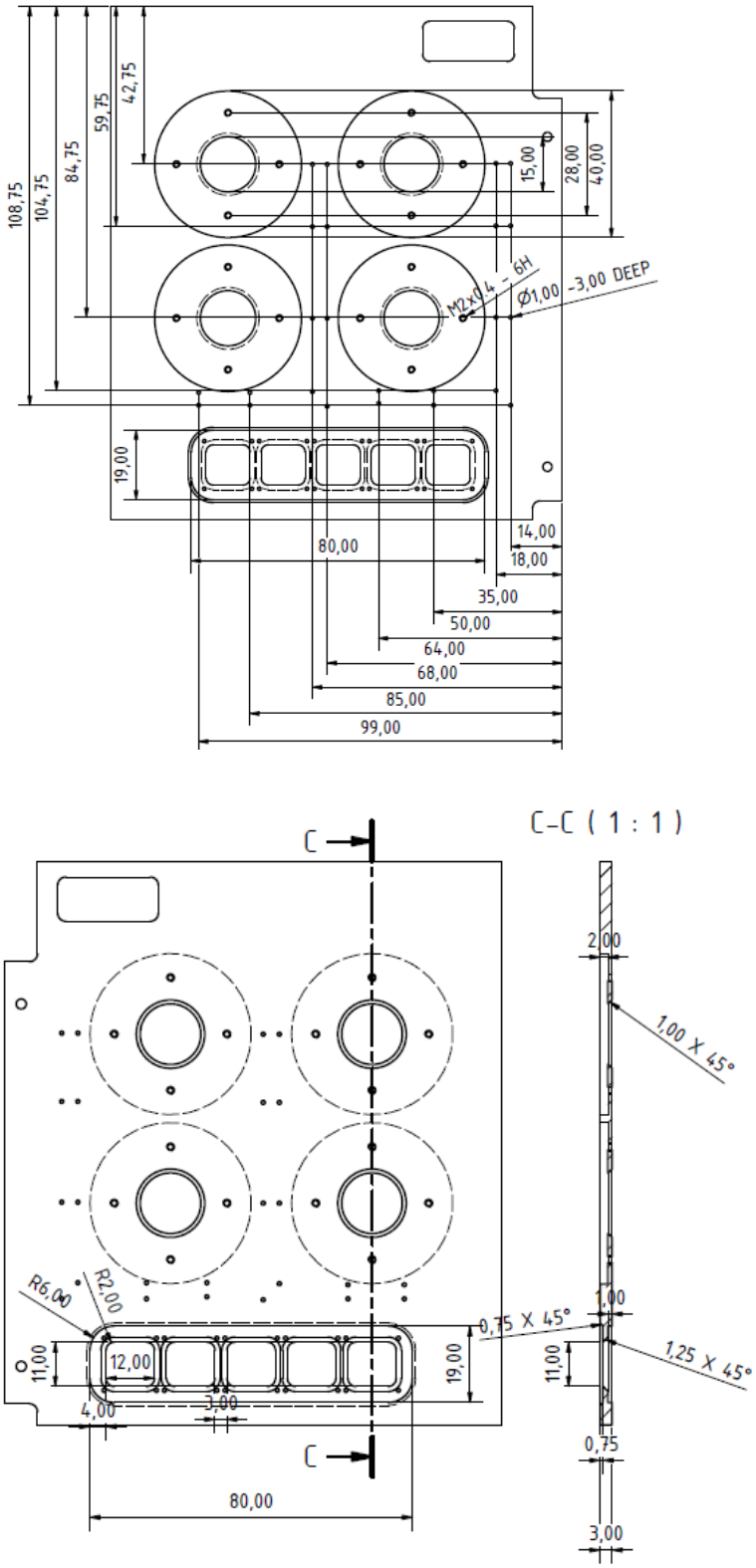

Figure 22. Technical drawings of the coin cell holder used for *operando* NDP measurements at the neutron reactor FRM2 in Garching. Here, four coin cells and six reference samples can be mounted at a time.

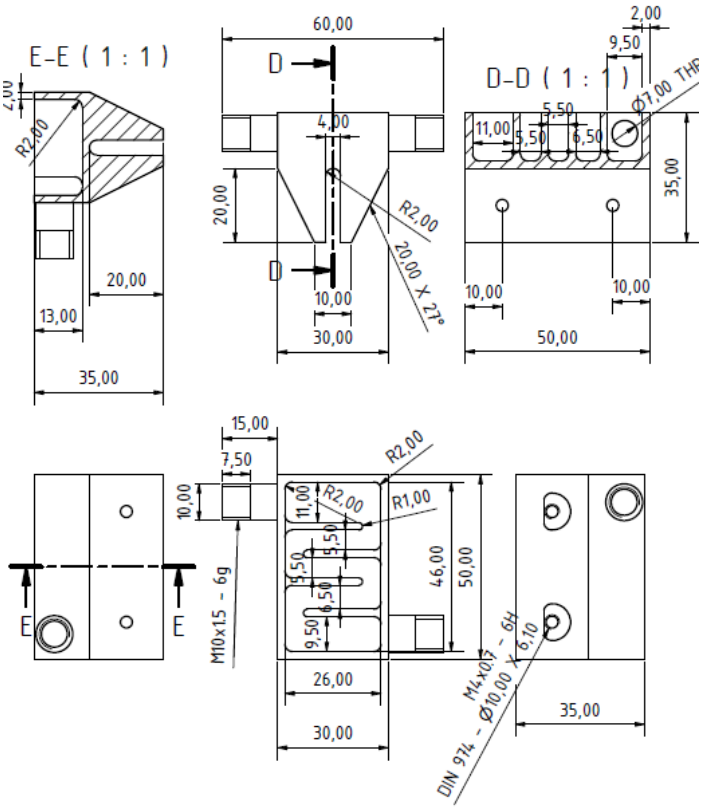

Figure 23. Technical drawings of a adapter that can be used to cool or heat the sample holder depicted in Figure 24 in order to perform cycling experiments between ca. -20 and +45 °C.

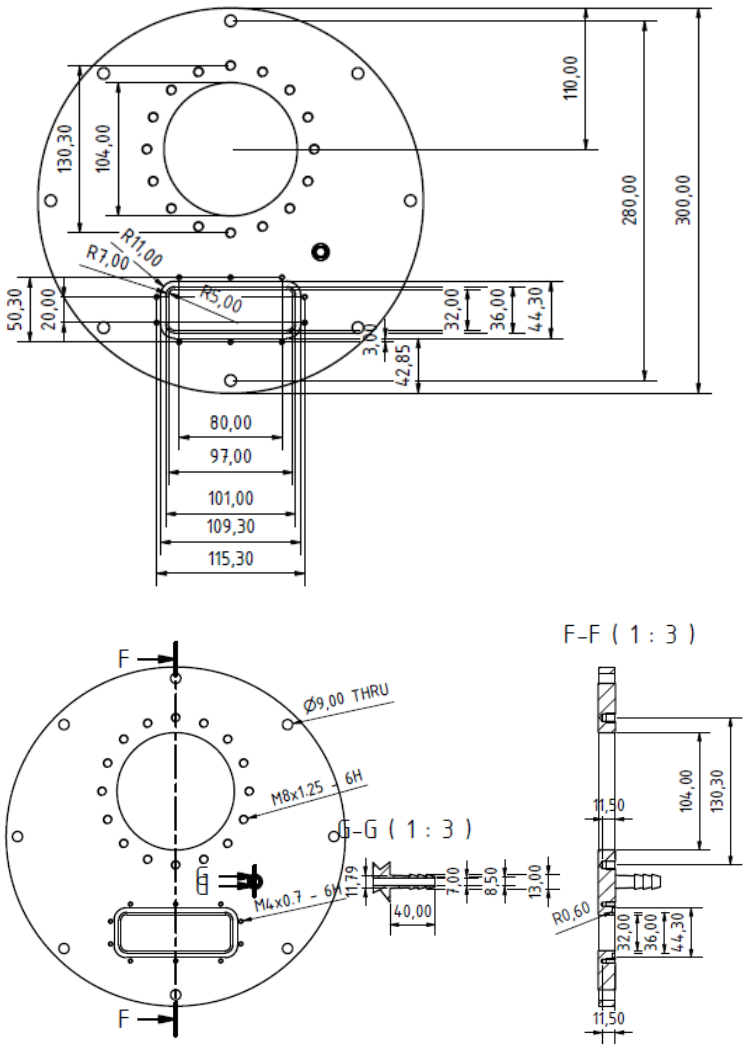

Figure 24. Technical drawings of the lid for a vacuum chamber that can be used to test the cell cycling performance of *operando* NDP cells under reduced pressure.

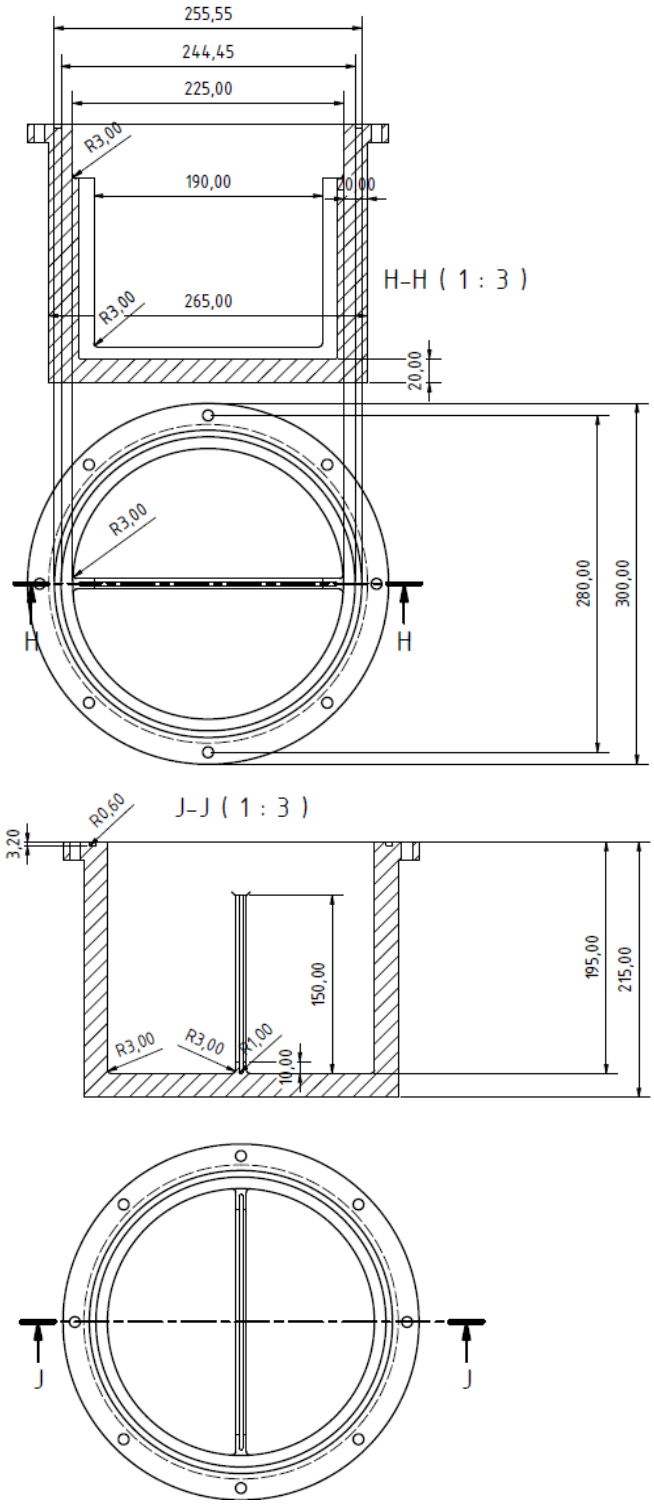

Figure 25. Technical drawings of a vacuum chamber that can be used to test the cell cycling performance of *operando* NDP cells under reduced pressure.

6 References

1. The Royal Swedish Academy of Science. The Nobel Prize in Chemistry 2019 -Press Release. **https://www.nobelprize.org/uploads/2019/10/press-chemistry-2019-2.pdf, accessed 11/24/2020.**

2. Nishi, Y. The Dawn of Lithium-Ion Batteries. *ECS Interface.* **25**, 71–74 **(2016)**.

3. UNFCCC. The Paris Agreement on Climate Change. **https://unfccc.int/sites/default/files/english_paris_agreement.pdf accessed 11/24/2020.**

4. UN Environment Programme. Emissions Gap Report 2019 - Executive Summary. **https://unepdtu.org/publications/emissions-gap-report-2019-executive-summary/, accessed 11/24/2020.**

5. 'Tracking Transport', International Energy Agency. **https://www.iea.org/reports/tracking-transport-2019, accessed 11/24/2020.**

6. VW erhöht Produktionsziel für E-Autos. **https://www.spiegel.de/wirtschaft/unternehmen/volkswagen-vw-will-produktionsziel-fuer-e-autos-frueher-erreichen-a-1302860.html, accessed 11/24/2020.**

7. European Union. Reducing CO2 emissions from passenger cars. **https://ec.europa.eu/clima/policies/transport/vehicles/cars_en#tab-0-0**, **accessed 11/24/2020.**

8. Schaal, S. China erhöht die NEV-Quote ab 2021 moderat. **https://www.electrive.net/2019/07/11/china-erhoeht-die-nev-quote-ab-2021-moderat/, accessed 11/24/2020.**

9. Harris, W. S. Electrochemical studies in cyclic esters. *PhD Thesis, University of California, Berkeley* **(1958)**.

10. Brandt, K. Historical development of secondary lithium batteries. *Solid State Ionics* **69**, 173–183 **(1994)**.

11. Whittingham, M. S. History, Evolution, and Future Status of Energy Storage. *Proc. IEEE* **100**, 1518–1534 **(2012)**.

12. Mauger, A., Julien, C. M., Goodenough, J. B. & Zaghib, K. Tribute to Michel Armand : from Rocking Chair – Li-ion to Solid-State Lithium Batteries. **(2020)**.

13. Arora, P. & Zhang, Z. Battery separators. *Chem. Rev.* **104**, 4419–4462 **(2004)**.

14. Xu, K. Electrolytes and Interphases in Li-Ion Batteries and Beyond. *Chem. Rev.* **114**, 11503–11618 **(2014)**.

15. Rüdorff, W. Über die Einlagerung von unedlen Metallen in Graphit sowie in Metallchalkogenide vom Typ MeX_2. *Chimia (Aarau).* **19**, 489–499 **(1965)**.

16. Whittingham, M. S. The Role of Ternary Phases in Cathode Reactions. *J. Electrochem. Soc.* **123**, 315–320 **(1976)**.

17. Whittingham, M. S. Chemistry of intercalation compounds: Metal guests in chalcogenide hosts. *Prog. Solid State Chem.* **12**, 41–99 **(1978)**.

18. Whittingham, M. S. Lithium batteries and cathode materials. *Chem. Rev.* **104**, 4271–4301 **(2004)**.

19. Mizushima, K., Jones, P. C., Wiseman, P. J. & Goodenough, J. B. Li_xCoO_2 - A New Cathode Material for Batteries of High Energy Denisty. *Solid State Ionics* **4**, 171–174 **(1981)**.

20. Goodenough, J. B. & Mizushima, K. US Patent 4,357,215. **(1982)**.

21. Flandrois, S. & Simon, B. Carbon materials for lithium-ion rechargeable batteries. *Carbon N. Y.* **37**, 165–180 **(1999)**.

22. Hérold, A. Research on the graphite intercalation compounds. *Bull. Soc. Chim. Fr* **187**, 999 **(1955)**.

23. Guerard, D. & Hérold, A. Intercalation of lithium into graphite and other carbons. *Carbon N. Y.* **13**, 337–345 **(1975)**.

24. Besenhard, J. O. & Eichinger, G. High Energy Density Lithium Cells - Part I Electrolytes and Anodes. *J. Electroanal. Chem.* **68**, 1–18 **(1976)**.

25. Arakawa, M. & Yamaki, J. The Cathodic Decomposition of Propylene Carbonate in Lithium Batteries. *J. Electroanal. Chem.* **219**, 273–280 **(1987)**.

26. Dey, A. N. & Sullivan, B. P. The Electrochemical Decomposition of Propylene Carbonate on Graphite. *J. Electrochem. Soc.* **117**, 222–224 **(1970)**.

27. Yazami, R. & Touzain, P. A reversible graphite-lithium negative electrode for electrochemical generators. *J. Power Sources* **9**, 365–371 **(1983)**.

28. Franklin, R. E. The structure of graphitic carbons. *Acta Crystallogr.* **4**, 253–261 **(1951)**.

29. Mohri, M., Yanagisawa, N., Tajima, Y., Tanaka, H., Mitate, T., Nakajima, S., Yoshida, M., Yoshimoto, Y., Suzuki, T. & Wada, H. Rechargeable lithium battery based on pyrolytic carbon as a negative electrode. *J. Power Sources* **26**, 545–551 **(1989)**.

30. Yoshino, A., Sanechika, K. & Nakajima, T. US Patent 4,668,595. **(1987)**.

31. Blomgren, G. E. The Development and Future of Lithium Ion Batteries. *J. Electrochem. Soc.* **164**, A5019–A5025 **(2017)**.

32. Nishi, Y. Lithium ion secondary batteries; past 10 years and the future. *J. Power Sources* **100**, 101–106 **(2001)**.

33. Ovshinsky, S. R., Fetcenko, M. A. & Ross, J. A Nickel Metal Hydride battery for electric vehicles. *Science (80-.).* **260**, 176–181 **(1992)**.

34. Fong, R., von Sacken, U. & Dahn, J. R. Studies of Lithium Intercalation into Carbons Using Nonaqueous Electrochemical Cells. *J. Electrochem. Soc.* **137**, 2009–2013 **(1990)**.

35. Peled, E. The Electrochemical Behavior of Alkali and Alkaline Earth Metals in Nonaqueous Battery Systems—The Solid Electrolyte Interphase Model. *J. Electrochem. Soc.* **126**, 2047–2051 **(1979)**.

36. Peled, E., Golodnitsky, D. & Ardel, G. Advanced model for solid electrolyte interphase electrodes in liquid and polymer electrolytes. *J. Electrochem. Soc.* **144**, 208–210 **(1997)**.

37. Peled, E. & Menkin, S. Review—SEI: Past, Present and Future. *J. Electrochem. Soc.* **164**, A1703–A1719 **(2017)**.

38. Aurbach, D., Daroux, M. L., Faguy, P. W. & Yeager, E. Identification of Surface Films Formed on Lithium in Propylene Carbonate Electrolyte. *J. Electrochem. Soc. Soc.* **134**, 1611–1620 **(1997)**.

39. Aurbach, D., Ein-Ely, Y. & Zaban, A. The Surface Chemistry of Lithium Electrodes in Alkyl Carbonate Solutions. *J. Electrochem. Soc.* **141**, L1–L3 **(1994)**.

40. Nie, M., Demeaux, J., Young, B. T., Heskett, D. R., Chen, Y., Bose, A., Woicik, J. C. & Lucht, B. L. Effect of vinylene carbonate and fluoroethylene carbonate on SEI formation on graphitic anodes in Li-ion batteries. *J. Electrochem. Soc.* **162**, A7008–A7014 **(2015)**.

41. Pritzl, D., Solchenbach, S., Wetjen, M. & Gasteiger, H. A. Analysis of Vinylene Carbonate (VC) as Additive in Graphite/$LiNi_{0.5}Mn_{1.5}O_4$ Cells. *J. Electrochem. Soc.* **164**, A2625–A2635 **(2017)**.

42. Dahn, J. R. Phase diagram of Li_xC_6. *Phys. Rev. B* **44**, 9170–9177 **(1991)**.

43. Nishi, Y. The Development of Lithium Ion Secondary Batteries. *Chem. Rec.* **1**, 406–413 **(2001)**.

44. Glazier, S. L., Li, J., Louli, A. J., Allen, J. P. & Dahn, J. R. An Analysis of Artificial and Natural Graphite in Lithium Ion Pouch Cells Using Ultra-High Precision Coulometry, Isothermal Microcalorimetry, Gas Evolution, Long Term Cycling and Pressure Measurements. *J. Electrochem. Soc.* **164**, A3545–A3555 **(2017)**.

45. Pillot, C. The Rechargeable Battery Market and Main Trends 2017-2025. *The Battery Show Hannover* **https://www.rechargebatteries.org/wp-content/uploads/2019/05/Avicenne_The-Rechargeable-Battery-Market-2017-2025.pdf (2018)**.

46. Thackeray, M. M., David, W. I. F., Bruce, P. G. & Goodenough, J. B. Lithium Insertion Into Manganese Spinels. *Mater. Res. Bull.* **18**, 461–472 **(1983)**.

47. Metal Prices. **https://www.metalary.com/manganese-price/**.

48. Yang, L., Takahashi, M. & Wang, B. A study on capacity fading of lithium-ion battery with manganese spinel positive electrode during cycling. *Electrochim. Acta* **51**, 3228–3234 **(2006)**.

49. Jung, R., Linsenmann, F., Thomas, R., Wandt, J., Solchenbach, S., Maglia, F., Stinner, C., Tromp, M. & Gasteiger, H. A. Nickel, manganese, and cobalt dissolution from Ni-Rich NMC and their effects on NMC622-graphite cells. *J. Electrochem. Soc.* **166**, A378–A389 **(2019)**.

50. Solchenbach, S., Hong, G., Freiberg, A. T. S., Jung, R. & Gasteiger, H. A. Electrolyte and SEI Decomposition Reactions of Transition Metal Ions Investigated by On-Line Electrochemical Mass Spectrometry. *J. Electrochem. Soc.* **165**, A3304–A3312 **(2018)**.

51. Ding, Y., Cano, Z. P., Yu, A., Lu, J. & Chen, Z. Automotive Li-Ion Batteries: Current Status and Future Perspectives. *Electrochem. Energy Rev.* **2**, 1–28 **(2019)**.

52. Zhong, Q., Bonakdarpour, A., Zhang, M., Gao, Y. & Dahn, J. R. Synthesis and electrochemistry of $LiNi_xMn_{2-x}O_4$. *J. Electrochem. Soc.* **144**, 205–213 **(1997)**.

53. Amine, K., Tukamoto, H., Yasuda, H. & Fujita, Y. Preparation and electrochemical investigation of $LiMn_{2-x}Me_xO_4$ (Me: Ni, Fe, and x = 0.5, 1)

cathode materials for secondary lithium batteries. *J. Power Sources* **68**, 604–608 **(1997)**.

54. Choi, W. & Manthiram, A. Comparison of metal ion dissolutions from lithium ion battery cathodes. *J. Electrochem. Soc.* **153**, 1760–1764 **(2006)**.

55. Padhi, A. K., Nanjundaswamy, K. S. & Goodenough, J. B. Phospho-olivines as Positive-Electrode Materials for Rechargeable Lithium Batteries. *J. Electrochem. Soc.* **144**, 1188–1194 **(1997)**.

56. Ravet, N., Besner, S., Simoneau, M., Vallée, A. & Armand, M. CA Patent 2270771. **(1999)**.

57. Huang, H., Yin, S. C. & Nazar, L. F. Approaching theoretical capacity of $LiFePO_4$ at room temperature at high rates. *Electrochem. Solid-State Lett.* **4**, 170–172 **(2001)**.

58. Pelegov, D. V. & Pontes, J. Main drivers of battery industry changes: Electric vehicles—A market overview. *Batteries* **4**, 1–13 **(2018)**.

59. Venkatraman, S. & Manthiram, A. Synthesis and Characterization of P3-Type $CoO_{2-\delta}$. *Chem. Mater.* 3907–3912 **(2002)**.

60. Venkatraman, S., Shin, Y. & Manthiram, A. Phase relationships and structural and chemical stabilities of charged $Li_{1-x}CoO_{2-\delta}$ and $Li_{1-x}Ni_{0.85}Co_{0.15}O_{2-\delta}$. *Electrochem. Solid-State Lett.* **6**, 13–16 **(2003)**.

61. Delmas, C., Fouassier, C. & Hagenmuller, P. Structural classification and properties of the layered oxides. *Physica* **99B**, 81–85 **(1980)**.

62. Dahn, J. R., von Sacken, U. & Michal, C. A. Structure and electrochemistry of $Li_{1\pm y}NiO_2$ and a new Li_2NiO_2 phase with the $Ni(OH)_2$ structure. *Solid State Ionics* **44**, 87–97 **(1990)**.

63. Dahn, J. R., von Sacken, U., Juzkow, M. W. & Al-Janaby, H. Rechargeable $LiNiO_2$/Carbon Cells. *J. Electrochem. Soc.* **138**, 2207–2211 **(1991)**.

64. Ohzuku, T., Ueda, A., Nagayama, M., Iwahoshi, Y. & Komori, H. Comparative study of $LiCoO_2$, $LiNi_{0.5}Co_{0.5}O_2$ and $LiNiO_2$ for 4 volt secondary lithium cells. *Electrochim. Acta* **38**, 1159–1167 **(1993)**.

65. Dahn, J. R., Fuller, E. W., Obrovac, M. & von Sacken, U. Thermal stability of Li_xCoO_2, Li_xNiO_2 and λ-MnO_2 and consequences for the safety of Li-ion cells. *Solid State Ionics* **69**, 265–270 **(1994)**.

66. Jung, R., Morasch, R., Karayaylali, P., Phillips, K., Maglia, F., Stinner, C., Shao-Horn, Y. & Gasteiger, H. A. Effect of ambient storage on the degradation of ni-rich positive electrode materials (NMC811) for Li-ion batteries. *J. Electrochem. Soc.* **165**, A132–A141 **(2018)**.

67. Sicklinger, J., Metzger, M., Beyer, H., Pritzl, D. & Gasteiger, H. A. Ambient storage derived surface contamination of NCM811 and NCM111: Performance implications and mitigation strategies. *J. Electrochem. Soc.* **166**, A2322–A2335 **(2019)**.

68. Delmas, C. & Saadoune, I. Electrochemical and physical properties of the $Li_xNi_{1-y}Co_yO_2$ phases. *Solid State Ionics* **53**, 370–375 **(1992)**.

69. Liu, Z., Yu, A. & Lee, J. Y. Synthesis and characterization of $LiNi_{1-x-y}Co_xMn_yO_2$ as the cathode materials of secondary lithium batteries. *J. Power Sources* **81-82**, 416–419 **(1999)**.

70. Lu, Z., MacNeil, D. D. & Dahn, J. R. Layered cathode materials $Li[Ni_xLi_{(1/3-2x/3)}Mn_{(2/3-x/3)}]O_2$ for lithium-ion batteries. *Electrochem. Solid-State Lett.* **4**, 191–194 **(2001)**.

71. Ohzuku, T. & Makimura, Y. Layered lithium insertion material of $LiCo_{1/3}Ni_{1/3}Mn_{1/3}O_2$ for lithium-ion batteries. *Chem. Lett.* 642–643 **(2001)**.

72. Blomgren, G. E. The Development and Future of Lithium Ion Batteries. **164**, 5019–5025 **(2017)**.

73. Harlow, J. E., Ma, X., Li, J., Logan, E., Liu, Y., Zhang, N., Ma, L., Glazier, S. L., Cormier, M. M. E., Genovese, M., Buteau, S., Cameron, A., Stark, J. E. & Dahn, J. R. A Wide Range of Testing Results on an Excellent Lithium-Ion Cell Chemistry to be used as Benchmarks for New Battery Technologies. *J. Electrochem. Soc.* **166**, A3031–A3044 **(2019)**.

74. Li, J., Li, H., Stone, W., Weber, R., Hy, S. & Dahn, J. R. Synthesis of Single Crystal LiNi 0.5 Mn 0.3 Co 0.2 O 2 for Lithium Ion Batteries . *J. Electrochem. Soc.* **164**, A3529–A3537 **(2017)**.

75. Li, J., Cameron, A. R., Li, H., Glazier, S., Xiong, D., Chatzidakis, M., Allen, J., Botton, G. a. & Dahn, J. R. Comparison of Single Crystal and Polycrystalline LiNi 0.5 Mn 0.3 Co 0.2 O 2 Positive Electrode Materials for High Voltage Li-Ion Cells . *J. Electrochem. Soc.* **164**, A1534–A1544 **(2017)**.

76. Kim, Y. Lithium nickel cobalt manganese oxide synthesized using alkali chloride flux: Morphology and performance as a cathode material for lithium ion batteries. *ACS Appl. Mater. Interfaces* **4**, 2329–2333 **(2012)**.

77. Qian, G., Zhang, Y., Li, L., Zhang, R., Xu, J., Cheng, Z., Xie, S., Wang, H., Rao, Q., He, Y., Shen, Y., Chen, L., Tang, M. & Ma, Z. F. Single-crystal nickel-rich layered-oxide battery cathode materials: synthesis, electrochemistry, and intra-granular fracture. *Energy Storage Mater.* **27**, 140–149 **(2020)**.

78. BMW Press Release. **https://www.press.bmwgroup.com/deutschland/article/detail/T030**

3913DE/sechs-jahre-bmw-i3:-elektro-pioniere-der-ersten-stunde-ziehen-bilanz-nach-jeweils-mehr-als-200-000-kilometern (2020).

79. Nitta, N., Wu, F., Lee, J. T. & Yushin, G. Li-ion battery materials: Present and future. *Mater. Today* **18**, 252–264 **(2015)**.

80. Myung, S.-T., Maglia, F., Park, K.-J., Yoon, C. S., Lamp, P., Kim, S.-J. & Sun, Y.-K. Nickel-Rich Layered Cathode Materials for Automotive Lithium-Ion Batteries: Achievements and Perspectives. *ACS Energy Lett.* **2**, 196–223 **(2017)**.

81. Ohzuku, T., Ueda, A. & Kouguchi, M. Synthesis and Characterization of $LiAl_{1/4}Ni_{3/4}O_2$ (R3m) for Lithium-Ion (Shuttlecock) Batteries. **142**, 4033–4039 **(1995)**.

82. Guilmard, M., Rougier, A., Grüne, M., Croguennec, L. & Delmas, C. Effects of aluminum on the structural and electrochemical properties of $LiNiO_2$. *J. Power Sources* **115**, 305–314 **(2003)**.

83. Li, H., Cormier, M., Zhang, N., Inglis, J., Li, J. & Dahn, J. R. Is cobalt needed in Ni-rich positive electrode materials for lithium ion batteries? *J. Electrochem. Soc.* **166**, A429–A439 **(2019)**.

84. Hajek, S. Zerlegung eines Rivalen. **https://www.wiwo.de/my/technologie/mobilitaet/tesla-model-3-zerlegung-eines-rivalen/22625200.html?ticket=ST-41058627-MKmBjVrJlaMg3ZVx9PFh-ap3 (2018)**.

85. Quinn, J. B., Waldmann, T., Richter, K., Kasper, M. & Wohlfahrt-Mehrens, M. Energy density of cylindrical Li-ion cells: A comparison of commercial 18650 to the 21700 cells. *J. Electrochem. Soc.* **165**, A3284–A3291 **(2018)**.

86. Cho, J., Kim, Y. J. & Park, B. Novel $LiCoO_2$ cathode material with Al_2O_3 coating for a Li ion cell. *Chem. Mater.* **12**, 3788–3791 **(2000)**.

87. Kannan, A. M., Rabenberg, L. & Manthiram, A. High capacity surface-modified $LiCoO_2$ cathodes for lithium-ion batteries. *Electrochem. Solid-State Lett.* **6**, A16–A18 **(2003)**.

88. Noh, H.-J. & Sun, Y.-K. A Novel Concentration-Gradient $Li[Ni_{0.83}Co_{0.07}Mn_{0.10}]O_2$ Cathode Material for High-Energy Rechargeable Li-Ion Batteries. in *Meeting Abstracts* 265 **(The Electrochemical Society, 2012).**

89. Sun, Y.-K., Chen, Z., Noh, H.-J., Lee, D.-J., Jung, H.-G., Ren, Y., Wang, S., Yoon, C. S., Myung, S.-T. & Amine, K. Nanostructured high-energy cathode materials for advanced lithium batteries. *Nat. Mater.* **11**, 942 **(2012)**.

90. Jung, R., Metzger, M., Maglia, F., Stinner, C. & Gasteiger, H. A. Oxygen release and its effect on the cycling stability of $LiNi_xMn_yCo_zO_2$(NMC) cathode materials for li-ion batteries. *J. Electrochem. Soc.* **164**, A1361–A1377 **(2017)**.

91. Jung, R., Metzger, M., Maglia, F., Stinner, C. & Gasteiger, H. A. Chemical versus electrochemical electrolyte oxidation on NMC111, NMC622, NMC811, LNMO, and conductive carbon. *J. Phys. Chem. Lett.* **8**, 4820–4825 **(2017)**.

92. Freiberg, A. T. S., Roos, M. K., Wandt, J., De Vivie-Riedle, R. & Gasteiger, H. A. Singlet Oxygen Reactivity with Carbonate Solvents Used for Li-Ion Battery Electrolytes. *J. Phys. Chem. A* **122**, 8828–8839 **(2018)**.

93. Wandt, J., Freiberg, A. T. S., Ogrodnik, A. & Gasteiger, H. A. Singlet oxygen evolution from layered transition metal oxide cathode materials and its implications for lithium-ion batteries. *Mater. Today* **21**, 825–833 **(2018)**.

94. Pritzl, D., Teufl, T., Strehle, B., Sicklinger, J., Sommer, H., Hartmann, P. & Gasteiger, H. A. Washing of nickel-rich cathode materials for lithium-ion batteries – Towards a mechanistic understanding. *J. Electrochem. Soc.* **166**, 4056–4066 **(2019)**.

95. Tsurukawa, N., Prakash, S. & Manhart, A. Social impacts of artisanal cobalt mining in Katanga, Democratic Republic of Congo. *Öko-Institut eV - Institute for Applied Ecology, Freiburg* **http://resourcefever.com/publications/reports/OEKO_2011_cobalt_mining_congo.pdf (2011)**.

96. Thackeray, M. M., Johnson, C. S., Amine, K. & Kim, J. US 6,677,082 B2. **(2001)**.

97. Strehle, B., Kleiner, K., Jung, R., Chesneau, F., Mendez, M., Gasteiger, H. A. & Piana, M. The role of oxygen release from Li- and Mn-Rich layered oxides during the first cycles investigated by on-line electrochemical mass spectrometry. *J. Electrochem. Soc.* **164**, A400–A406 **(2017)**.

98. Teufl, T., Strehle, B., Müller, P., Gasteiger, H. A. & Mendez, M. A. Oxygen release and surface degradation of Li- and Mn-rich layered oxides in variation of the Li_2MnO_3 content. *J. Electrochem. Soc.* **165**, A2718–A2731 **(2018)**.

99. Teufl, T., Pritzl, D., Solchenbach, S., Gasteiger, H. A. & Mendez, M. A. State of charge dependent resistance build-up in Li- And Mn-rich layered oxides during lithium extraction and insertion. *J. Electrochem. Soc.* **166**, A1275–A1284 **(2019)**.

100. Croy, J. R., Gutierrez, A., He, M., Yonemoto, B. T., Lee, E. & Thackeray, M. M. Development of manganese-rich cathodes as alternatives to nickel-rich chemistries. *J. Power Sources* **434**, 226706 **(2019)**.

101. Schmuch, R., Wagner, R., Hörpel, G., Placke, T. & Winter, M. Performance and cost of materials for lithium-based rechargeable automotive batteries. *Nat. Energy* **3**, 267–278 **(2018)**.

102. Asenbauer, J., Eisenmann, T., Kuenzel, M., Kazzazi, A., Chen, Z. & Bresser, D. The success story of graphite as a lithium-ion anode material – fundamentals, remaining challenges, and recent developments including silicon (oxide) composites. *Sustain. Energy Fuels* **00**, 1–30 **(2020)**.

103. Magampa, P. P., Manyala, N. & Focke, W. W. Properties of graphite composites based on natural and synthetic graphite powders and a phenolic novolac binder. *J. Nucl. Mater.* **436**, 76–83 **(2013)**.

104. Aurbach, D., Gamolsky, K., Markovsky, B., Gofer, Y., Schmidt, M. & Heider, U. On the use of vinylene carbonate (VC) as an additive to electrolyte solutions for Li-ion batteries. *Electrochim. Acta* **47**, 1423–1439 **(2002)**.

105. Zhang, S. S. A review on electrolyte additives for lithium-ion batteries. *J. Power Sources* **162**, 1379–1394 **(2006)**.

106. Obrovac, M. N. & Chevrier, V. L. Alloy negative electrodes for li-ion batteries. *Chem. Rev.* **114**, 11444–11502 **(2014)**.

107. Wetjen, M. Studies on the Differentiation and Quantification of Degradation Phenomena in Silicon-Graphite Anodes for Lithium-Ion Batteries. *PhD Thesis, Technical University of Munich* **(2018)**.

108. Besenhard, J. O., Yang, J. & Winter, M. Will advanced lithium-alloy anodes have a chance in lithium-ion batteries? *J. Power Sources* **68**, 87–90 **(1997)**.

109. Liu, X. H., Zhong, L., Huang, S., Mao, S. X., Zhu, T. & Huang, J. Y. Size-Dependent Fracture of Silicon. *ACS Nano* **6**, 1522–1531 **(2012)**.

110. Liu, X. H. & Huang, J. Y. In situ TEM electrochemistry of anode materials in lithium ion batteries. *Energy Environ. Sci.* **4**, 3844–3860 **(2011)**.

111. Ashuri, M., He, Q. & Shaw, L. L. Silicon as a potential anode material for Li-ion batteries: Where size, geometry and structure matter. *Nanoscale* **8**, 74–103 **(2016)**.

112. Shao, D., Tang, D., Mai, Y. & Zhang, L. Nanostructured silicon/porous carbon spherical composite as a high capacity anode for Li-ion batteries. *J. Mater. Chem. A* **1**, 15068–15075 **(2013)**.

113. Yang, X. Q., McBreen, J., Yoon, W. S., Yoshio, M., Wang, H., Fukuda, K. & Umeno, T. Structural studies of the new carbon-coated silicon anode materials using synchrotron-based in situ XRD. *Electrochem. commun.* **4**, 893–897 **(2002)**.

114. Liu, N., Wu, H., McDowell, M. T., Yao, Y., Wang, C. & Cui, Y. A yolk-shell design for stabilized and scalable Li-ion battery alloy anodes. *Nano Lett.* **12**, 3315–3321 **(2012)**.

115. Liu, N., Lu, Z., Zhao, J., Mcdowell, M. T., Lee, H. W., Zhao, W. & Cui, Y. A pomegranate-inspired nanoscale design for large-volume-change lithium battery anodes. *Nat. Nanotechnol.* **9**, 187–192 **(2014)**.

116. Choi, N. S., Yew, K. H., Lee, K. Y., Sung, M., Kim, H. & Kim, S. S. Effect of fluoroethylene carbonate additive on interfacial properties of silicon thin-film electrode. *J. Power Sources* **161**, 1254–1259 **(2006)**.

117. Jung, R., Metzger, M., Haering, D., Solchenbach, S., Marino, C., Tsiouvaras, N., Stinner, C. & Gasteiger, H. A. Consumption of fluoroethylene carbonate (FEC) on Si-C composite electrodes for Li-ion batteries. *J. Electrochem. Soc.* **163**, A1705–A1716 **(2016)**.

118. Ma, D., Cao, Z. & Hu, A. Si-based anode materials for Li-ion batteries: A mini review. *Nano-Micro Lett.* **6**, 347–358 **(2014)**.

119. Haufe, S. EP 3335262B1. **(2019)**.

120. Jantke, D., Bernhard, R., Hanelt, E., Buhrmester, T., Pfeiffer, J. & Haufe, S. Silicon-Dominant Anodes Based on Microscale Silicon Particles under Partial Lithiation with High Capacity and Cycle Stability. *J. Electrochem. Soc.* **166**, A3881–A3885 **(2019)**.

121. Lin, D., Liu, Y. & Cui, Y. Reviving the lithium metal anode for high-energy batteries. *Nat. Nanotechnol.* **12**, 194–206 **(2017)**.

122. Liu, J., Bao, Z., Cui, Y., Dufek, E. J., Goodenough, J. B., Khalifah, P., Li, Q., Liaw, B. Y., Liu, P., Manthiram, A., *et al.* Pathways for practical high-energy long-cycling lithium metal batteries. *Nat. Energy* **4**, 180–186 **(2019)**.

123. Wu, B., Yang, Y., Liu, D., Niu, C., Gross, M., Seymour, L., Lee, H., Le, P. M. L., Vo, T. D., Deng, Z. D., Dufek, E. J., Whittingham, M. S., Liu, J., Xiao, J., Physical, A., Hcm, V. N. U., Chi, H. & City, M. Good Practices for Rechargeable Lithium Metal Batteries. *J. Electrochem. Soc.* **166**, A4141–A4149 **(2019)**.

124. Albertus, P., Babinec, S., Litzelman, S. & Newman, A. Status and challenges in enabling the lithium metal electrode for high-energy and low-cost rechargeable batteries. *Nat. Energy* **3**, 16–21 **(2018)**.

125. Betz, J., Bieker, G., Meister, P., Placke, T., Winter, M. & Schmuch, R. Theoretical versus Practical Energy: A Plea for More Transparency in the Energy Calculation of Different Rechargeable Battery Systems. *Adv. Energy Mater.* **9**, 1–18 **(2019)**.

126. Genovese, M., Louli, A. J., Weber, R., Hames, S. & Dahn, J. R. Measuring the Coulombic efficiency of lithium metal cycling in anode-free lithium metal batteries. *J. Electrochem. Soc.* **165**, A3321–A3325 **(2018)**.

127. Neudecker, B. J., Dudney, N. J. & Bates, J. B. 'Lithium-free' thin-film battery with in situ plated Li anode. *J. Electrochem. Soc.* **147**, 517–523 **(2000)**.

128. Qian, J., Adams, B. D., Zheng, J., Xu, W., Henderson, W. a., Wang, J., Bowden, M. E., Xu, S., Hu, J. & Zhang, J. G. Anode-Free Rechargeable Lithium Metal Batteries. *Adv. Funct. Mater.* **26**, 7094–7102 **(2016)**.

129. Weber, R., Genovese, M., Louli, A. J., Hames, S., Martin, C., Hill, I. G. & Dahn, J. R. Long cycle life and dendrite-free lithium morphology in anode-free lithium pouch cells enabled by a dual-salt liquid electrolyte. *Nat. Energy* **4**, 683–689 **(2019)**.

130. Ahlswede, A. Weltweite Preisentwicklung für Lithium-Ionen-Batterien von 2013 bis 2022 - Statista. **https://de.statista.com/statistik/daten/studie/534429/umfrage/weltweite-preise-fuer-lithium-ionen-akkus/, accessed 11/24/2020.**

131. Lambert, F. How Automakers Can Drive Electrified Vehicle Sales and Profitability. *McKinsey&Company* **https://www.mckinsey.com/industries/automotive-and-assembly/our-insights/electrifying-insights-how-automakers-can-drive-electrified-vehicle-sales-and-profitability, accessed 11/24/2020.**

132. Schaal, S. VW ID.3: Weniger als 100 Dollar pro kWh Batteriekosten? **https://www.electrive.net/2019/09/09/vw-weniger-als-100-dollar-pro-kwh-batteriekosten-beim-id-3/, accessed 11/24/2020.**

133. Faradion. The world leader in non-aqueous sodium-ion cell technology. **https://www.faradion.co.uk/, accessed 11/24/2020.**

134. HiNa Battery, Company profile. **http://www.hinabattery.com/en/index.php?catid=7, accessed 11/24/2020.**

135. Vaalma, C., Buchholz, D., Weil, M. & Passerini, S. A cost and resource analysis of sodium-ion batteries - Supplementary Information. *Nat. Rev. Mater.* **3**, 18013 **(2018)**.

136. Anderson, D. L. *Theory of the Earth*. Blackwell Scientific Publications, **(1989).**

137. Stevens, D. A. & Dahn, J. R. The Mechanisms of Lithium and Sodium Insertion in Carbon Materials. *J. Electrochem. Soc.* **148**, A803 **(2001)**.

138. Ge, P. & Fouletier, M. Electrochemical intercalation of sodium in graphite. *Solid State Ionics* **28-30**, 1172–1175 **(1988)**.

139. Stevens, D. A. & Dahn, J. R. High Capacity Anode Materials for Rechargeable Sodium-Ion Batteries. *J. Electrochem. Soc.* **147**, 1271 **(2002)**.

140. Chayambuka, K., Mulder, G., Danilov, D. L. & Notten, P. H. L. Sodium-Ion Battery Materials and Electrochemical Properties Reviewed. *Adv. Energy Mater.* **8**, 1–49 **(2018)**.

141. Chiba, K., Kijima, N., Takahashi, Y., Idemoto, Y. & Akimoto, J. Synthesis, structure, and electrochemical Li-ion intercalation properties of Li2Ti3O7 with Na2Ti3O7-type layered structure. *Solid State Ionics* **178**, 1725–1730 **(2008)**.

142. Kim, S. W., Seo, D. H., Ma, X., Ceder, G. & Kang, K. Electrode materials for rechargeable sodium-ion batteries: Potential alternatives to current lithium-ion batteries. *Adv. Energy Mater.* **2**, 710–721 **(2012)**.

143. Palomares, V., Serras, P., Villaluenga, I., Hueso, K. B., Carretero-González, J. & Rojo, T. Na-ion batteries, recent advances and present challenges to become low cost energy storage systems. *Energy Environ. Sci.* **5**, 5884–5901 **(2012)**.

144. Palomares, V., Casas-Cabanas, M., Castillo-Martínez, E., Han, M. H. & Rojo, T. Update on Na-based battery materials. A growing research path. *Energy Environ. Sci.* **6**, 2312–2337 **(2013)**.

145. Kundu, D., Talaie, E., Duffort, V. & Nazar, L. F. The emerging chemistry of sodium ion batteries for electrochemical energy storage. *Angew. Chemie - Int. Ed.* **54**, 3432–3448 **(2015)**.

146. Yabuuchi, N., Kubota, K., Dahbi, M. & Komaba, S. Research development on sodium-ion batteries. *Chem. Rev.* **114**, 11636–11682 **(2014)**.

147. Kummer, J. T. & Weber, N. US 3413150A. **(1966)**.

148. Bones, R. J., Teagle, D. A., Brooker, S. D. & Cullen, F. L. Development of a Ni, $NiCl_2$ Positive Electrode for a Liquid Sodium (ZEBRA) Battery Cell. *J. Electrochem. Soc.* **136**, 1274–1277 **(1989)**.

149. Sudworth, J. L. The sodium/nickel chloride (ZEBRA) battery. *J. Power Sources* **100**, 149–163 **(2001)**.

150. Nagelberg, A. S. & Worrel, W. L. A thermodynamic study of sodium-intercalated TaS_2 and TiS_2. *J. Solid State Chem.* **29**, 345–354 **(1979)**.

151. Delmas, C., Braconnier, J.-J., Fouassier, C. & Hagenmuller, P. Electrochemical Intercalation of Sodium in Na_xCoO_2 Bronzes. *Solid State Ionics* **4**, 165–169 **(1981)**.

152. Molenda, J., Delmas, C. & Hagenmuller, P. Electronic and electrochemical properties of Na_xCoO_{2-y} cathode. *Solid State Ionics* **9**, 431–436 **(1983)**.

153. Shacklette, L. W., Jow, T. R. & Townsend, L. Rechargeable Electrodes from Sodium Cobalt Bronzes. *J. Electrochem. Soc.* **135**, 2669–2674 **(1988)**.

154. Tarascon, J.-M. & Hull, G. W. Sodium intercalation into the layer oxides $Na_xMo_2O_4$. *Solid State Ionics* **22**, 85–96 **(1986)**.

155. Jow, T. R., Shacklette, L. W., Maxfield, M. & Vernick, D. Role of Conductive Polymers in Alkali-Metal Secondary Electrodes. *Proc. - Electrochem. Soc.* **134**, 1730–1733 **(1987)**.

156. West, K., Zachau-Christiansen, B., Jacobsen, T. & Skaarup, S. Sodium insertion in vanadium oxides. *Solid State Ionics* **28-30**, 1128–1131 **(1988)**.

157. Sauvage, F., Laffont, L., Tarascon, J. M. & Baudrin, E. Study of the insertion/deinsertion mechanism of sodium into $Na_{0.44}MnO_2$. *Inorg. Chem.* **46**, 3289–3294 **(2007)**.

158. Braconnier, J.-J., Delmas, C. & Hagenmuller, P. Etude par desintercalation electrochimique des systemes Na_xCrO_2 et Na_xNiO_2. *Mater. Res. Bull.* **17**, 993–1000 **(1982)**.

159. Mendiboure, A., Delmas, C. & Hagenmuller, P. Electrochemical Intercalation and Deintercalation of Na_xMnO_2 Bronzes. *J. Solid State Chem.* **57**, 323–331 **(1985)**.

160. Takeda, Y., Nakahara, K., Nishijima, M., Imanishi, N. & Yamamoto, O. Sodium deintercalation from sodium iron oxide. *Mater. Res. Bull.* **29**, 659–666 **(1994)**.

161. Yuan, D., He, W., Pei, F., Wu, F., Wu, Y., Qian, J., Cao, Y., Ai, X. & Yang, H. Synthesis and electrochemical behaviors of layered $Na_{0.67}[Mn_{0.65}Co_{0.2}Ni_{0.15}]O_2$ microflakes as a stable cathode material for sodium-ion batteries. *J. Mater. Chem. A* **1**, 3895–3899 **(2013)**.

162. Berthelot, R., Carlier, D. & Delmas, C. Electrochemical investigation of the P2-Na_xCoO_2 phase diagram. *Nat. Mater.* **10**, 74–80 **(2011)**.

163. Yoshida, H., Yabuuchi, N. & Komaba, S. $NaFe_{0.5}Co_{0.5}O_2$ as high energy and power positive electrode for Na-ion batteries. *Electrochem. commun.* **34**, 60–63 **(2013)**.

164. Vassilaras, P., Toumar, A. J. & Ceder, G. Electrochemical properties of $NaNi_{1/3}Co_{1/3}Fe_{1/3}O_2$ as a cathode material for Na-ion batteries. *Electrochem. commun.* **38**, 79–81 **(2014)**.

165. Yabuuchi, N., Yoshida, H. & Komaba, S. Crystal structures and electrode performance of alpha-$NaFeO_2$ for rechargeable sodium batteries. *Electrochemistry* **80**, 716–719 **(2012)**.

166. Hasa, I., Buchholz, D., Passerini, S., Scrosati, B. & Hassoun, J. High Performance $Na_{0.5}[Ni_{0.23}Fe_{0.13}Mn_{0.63}]O_2$ Cathode for Sodium-Ion Batteries. *Adv. Energy Mater.* **4**, 0–6 **(2014)**.

167. Manthiram, A. & Goodenough, J. B. Lithium Insertion into $Fe_2(MO_4)_3$ Frameworks: Comparison of M = W with M = Mo. *J. Solid State C* **71**, 349–360 **(1987)**.

168. Masquelier, C. & Croguennec, L. Polyanionic (phosphates, silicates, sulfates) frameworks as electrode materials for rechargeable Li (or Na) batteries. *Chem. Rev.* **113**, 6552–6591 **(2013)**.

169. Scrosati, B., Abraham, K. M., van Schalkwijk, W. A. & Hassoun, J. *Lithium batteries: advanced technologies and applications*. vol. 58, John Wiley & Sons **(2013).**

170. Ellis, B. L., Makahnouk, W. R. M., Makimura, Y., Toghill, K. & Nazar, L. F. A multifunctional 3.5V iron-based phosphate cathode for rechargeable batteries. *Nat. Mater.* **6**, 749–753 **(2007)**.

171. Ong, S. P., Chevrier, V. L., Hautier, G., Jain, A., Moore, C., Kim, S., Ma, X. & Ceder, G. Voltage, stability and diffusion barrier differences between sodium-ion and lithium-ion intercalation materials. *Energy Environ. Sci.* **4**, 3680–3688 **(2011)**.

172. Zhu, Y., Xu, Y., Liu, Y., Luo, C. & Wang, C. Comparison of electrochemical performances of olivine $NaFePO_4$ in sodium-ion batteries and olivine $LiFePO_4$ in lithium-ion batteries. *Nanoscale* **5**, 780–787 **(2013)**.

173. Li, C., Miao, X., Chu, W., Wu, P. & Tong, D. G. Hollow amorphous $NaFePO_4$ nanospheres as a high-capacity and high-rate cathode for sodium-ion batteries. *J. Mater. Chem. A* **3**, 8265–8271 **(2015)**.

174. Jiang, Y., Yang, Z., Li, W., Zeng, L., Pan, F., Wang, M., Wei, X., Hu, G., Gu, L. & Yu, Y. Nanoconfined carbon-coated $Na_3V_2(PO_4)_3$ particles in mesoporous carbon enabling ultralong cycle life for sodium-ion batteries. *Adv. Energy Mater.* **5**, 1–8 **(2015)**.

175. Rui, X., Sun, W., Wu, C., Yu, Y. & Yan, Q. An Advanced Sodium-Ion Battery Composed of Carbon Coated $Na_3V_2(PO_4)_3$ in a Porous Graphene Network. *Adv. Mater.* **27**, 6670–6676 **(2015)**.

176. Lim, S. Y., Kim, H., Chung, J., Lee, J. H., Kim, B. G., Choi, J. J., Chung, K. Y., Cho, W., Kim, S. J., Goddard, W. a., Jung, Y. & Choi, J. W. Role of intermediate phase

for stable cycling of $Na_7V_4(P_2O_7)_4PO_4$ in sodium ion battery. *Proc. Natl. Acad. Sci. USA* **111**, 599–604 **(2014)**.

177. Yamada, A., Chung, S. C. & Hinokuma, K. Optimized $LiFePO_4$ for lithium battery cathodes. *J. Electrochem. Soc.* **148**, 224–229 **(2001)**.

178. Bianchini, M., Fauth, F., Brisset, N., Weill, F., Suard, E., Masquelier, C. & Croguennec, L. Comprehensive investigation of the $Na_3V_2(PO_4)_2F_3$-$NaV_2(PO_4)_2F_3$ system by operando high resolution synchrotron X-ray diffraction. *Chem. Mater.* **27**, 3009–3020 **(2015)**.

179. Liu, Q., Wang, D., Yang, X., Chen, N., Wang, C., Bie, X., Wei, Y., Chen, G. & Du, F. Carbon-coated $Na_3V_2(PO_4)_2F_3$ nanoparticles embedded in a mesoporous carbon matrix as a potential cathode material for sodium-ion batteries with superior rate capability and long-term cycle life. *J. Mater. Chem. A* **3**, 21478–21485 **(2015)**.

180. Wang, L., Song, J., Qiao, R., Wray, L. A., Hossain, M. a., Chuang, Y. De, Yang, W., Lu, Y., Evans, D., Lee, J. J., Vail, S., Zhao, X., Nishijima, M., Kakimoto, S. & Goodenough, J. B. Rhombohedral Prussian white as cathode for rechargeable sodium-ion batteries. *J. Am. Chem. Soc.* **137**, 2548–2554 **(2015)**.

181. Lazia, A. *Electrochemical impedance spectroscopy and it applications*. Springer, New York **(2014).**

182. Lvovich, V. F. *Impedance spectroscopy: applications to electrochemical and dielectric phenomena*. John Wiley & Sons **(2012).**

183. Orazem, M. E. & Tribollet, B. *Electrochemical impedance spectroscopy*. John Wiley & Sons **(2017).**

184. Pritzl, D., Landesfeind, J., Solchenbach, S. & Gasteiger, H. A. An Analysis Protocol for Three-Electrode Li-Ion Battery Impedance Spectra: Part II. Analysis of a Graphite Anode Cycled vs. LNMO. *J. Electrochem. Soc.* **165**, A2145–A2153 **(2018)**.

185. Solchenbach, S., Pritzl, D., Kong, E. J. Y., Landesfeind, J. & Gasteiger, H. A. A Gold Micro-Reference Electrode for Impedance and Potential Measurements in Lithium Ion Batteries. *J. Electrochem. Soc.* **163**, A2265–A2272 **(2016)**.

186. Landesfeind, J., Pritzl, D. & Gasteiger, H. A. An Analysis Protocol for Three-Electrode Li-Ion Battery Impedance Spectra: Part I. Analysis of a High-Voltage Positive Electrode. *J. Electrochem. Soc.* **164**, A1773–A1783 **(2017)**.

187. Pritzl, D., Bumberger, A. E., Wetjen, M., Landesfeind, J., Solchenbach, S. & Gasteiger, H. A. Identifying contact resistances in high-voltage cathodes by impedance spectroscopy. *J. Electrochem. Soc.* **166**, A582–A590 **(2019)**.

188. Linsenmann, F., Pritzl, D. & Gasteiger, H. A. A Reference Electrode for In Situ Impedance Measurements in Sodium-Ion Batteries. *J. Electrochem. Soc.* **166**, A3668–3674 **(2019)**.

189. Lamaze, G. P., Chen-Mayer, H., Langland, J. K. & Downing, R. G. Neutron Depth Profiling with the New NIST Cold Neutron Source. *Surf. Interface Anal.* **25**, 217–220 **(1997)**.

190. Biersack, J. P., Fink, D., Henkelmann, R. & Müller, K. The use of neutron induced reactions for light element profiling and lattice localization. *Nucl. Instruments Methods* **149**, 93–97 **(1978)**.

191. Downing, R. G., Lamaze, G. P., Langland, J. K. & Hwang, S. T. Neutron depth profiling: Overview and description of NIST facilities. *J. Res. Natl. Inst. Stand. Technol.* **98**, 109–126 **(1993)**.

192. Oudenhoven, J. F. M., Labohm, F., Mulder, M., Niessen, R. A. H., Mulder, F. M. & Notten, P. H. L. In situ neutron depth profiling: A powerful method to probe lithium transport in micro-batteries. *Adv. Mater.* **23**, 4103–4106 **(2011)**.

193. Ziegler, J. F., Cole, G. W. & Baglin, J. E. E. Technique for determining concentration profiles of boron impurities in substrates. *J. Appl. Phys.* **43**, 3809–3815 **(1972)**.

194. Biersack, J. P. He profiles in various metals after implantation and thermal anneals. *Radiat. Eff.* **78**, 363–363 **(1983)**.

195. Fink, D., Biersack, J. P., Müller, M., Wang, L. H., Cheng, V. K., Kassing, R., Masseli, K., Weiser, M. & Kalbitzer, S. Depth distributions of megaelectronvolt ^{14}N implanted into various solids at elevated fluences. *Mater. Sci. Eng. B* **2**, 49–54 **(1989)**.

196. Révay, Z., Kudějová, P., Kleszcz, K., Söllradl, S. & Genreith, C. In-beam activation analysis facility at MLZ, Garching. *Nucl. Instruments Methods Phys. Res.* **(2015)**.

197. Werner, L., Trunk, M., Gernhäuser, R., Gilles, R., Märkisch, B. & Révay, Z. The new neutron depth profiling instrument N4DP at the Heinz Maier-Leibnitz Zentrum. *Nucl. Instruments Methods Phys. Res.* **911**, 30–36 **(2018)**.

198. Trunk, M., Wetjen, M., Werner, L., Gernhäuser, R., Märkisch, B., Révay, Z., Gasteiger, H. A. & Gilles, R. Materials science applications of Neutron Depth Profiling at the PGAA facility of Heinz Maier-Leibnitz Zentrum. *Mater. Charact.* **146**, 127–134 **(2018)**.

199. Werner, L., Trunk, M., Gernhäuser, R., Gilles, R., Märkisch, B. & Révay, Z. The new neutron depth profiling instrument N4DP at the Heinz Maier-Leibnitz

Zentrum. *Nucl. Instruments Methods Phys. Res. Sect. A Accel. Spectrometers, Detect. Assoc. Equip.* **911**, 30–36 **(2018)**.

200. Trunk, M. Monitoring Depth Profiles Using Cold Neutrons. *PhD Thesis, Technical University of Munich* **(2020)**.

201. Han, F., Westover, A. S., Yue, J., Fan, X., Wang, F., Chi, M., Leonard, D. N., Dudney, N. J., Wang, H. & Wang, C. High electronic conductivity as the origin of lithium dendrite formation within solid electrolytes. *Nat. Energy* **4**, 187–196 **(2019)**.

202. Ziegler, J. F. *Handbook of Helium Stopping Powers and Ranges in All Elements, Vol. 4*. Pergamon Press, New York **(1977).**

203. Janni, F., Force, A., Air, K. & Base, F. Proton Range-Energy Tables. *Atom Data Nucl. Data Tables* **27**, 147–339 **(1982)**.

204. Ziegler, J. F., Ziegler, M. D. & Biersack, J. P. SRIM - The stopping and range of ions in matter (2010). *Nucl. Instruments Methods Phys. Res.* **268**, 1818–1823 **(2010)**.

205. Lamaze, G. P., Chen-Mayer, H. H., Becker, D. a., Vereda, F., Goldner, R. B., Haas, T. & Zerigian, P. Cold neutron depth profiling of lithium-ion battery materials. *J. Power Sources* **119-121**, 680–685 **(2003)**.

206. Whitney, S., Biegalski, S. R., Huang, Y. H. & Goodenough, J. B. Neutron Depth Profiling Applications to Lithium-Ion Cell Research. *J. Electrochem. Soc.* **156**, A886–A890 **(2009)**.

207. Whitney, S. M., Biegalski, S. R. F. & Downing, G. Benchmarking and analysis of ^{6}Li neutron depth profiling of lithium ion cell electrodes. *J. Radioanal. Nucl. Chem.* **282**, 173–176 **(2009)**.

208. Nagpure, S. C., Downing, R. G., Bhushan, B., Babu, S. S. & Cao, L. Neutron depth profiling technique for studying aging in Li-ion batteries. *Electrochim. Acta* **56**, 4735–4743 **(2011)**.

209. Nagpure, S. C., Gregory Downing, R., Bhushan, B. & Babu, S. S. Discovery of lithium in copper current collectors used in batteries. *Scr. Mater.* **67**, 669–672 **(2012)**.

210. Nagpure, S. C., Mulligan, P., Canova, M. & Cao, L. R. Neutron depth profiling of Li-ion cell electrodes with a gas-controlled environment. *J. Power Sources* **248**, 489–497 **(2014)**.

211. Wetjen, M., Trunk, M., Werner, L., Gernhäuser, R., Märkisch, B., Révay, Z., Gilles, R. & Gasteiger, H. A. Quantifying the Distribution of Electrolyte Decomposition Products in Silicon-Graphite Electrodes by Neutron Depth Profiling. *J. Electrochem. Soc.* **165**, A2340–A2348 **(2018)**.

212. Zhang, X., Verhallen, T. W., Labohm, F. & Wagemaker, M. Direct Observation of Li-Ion Transport in Electrodes under Nonequilibrium Conditions Using Neutron Depth Profiling. *Adv. Energy Mater.* **5**, 1500498 **(2015)**.

213. Bach, T. C., Schuster, S. F., Fleder, E., Müller, J., Brand, M. J., Lorrmann, H., Jossen, A. & Sextl, G. Nonlinear aging of cylindrical lithium-ion cells linked to heterogeneous compression. *J. Energy Storage* **5**, 212–223 **(2016)**.

214. Buchberger, I. Electrochemical and structura linvestigations on lithium-ion battery materials and related degradation processes. *PhD Thesis, Technical University of Munich* **(2016)**.

215. Bommier, C., Leonard, D., Jian, Z., Stickle, W. F., Greaney, P. A. & Ji, X. New Paradigms on the Nature of Solid Electrolyte Interphase Formation and Capacity Fading of Hard Carbon Anodes in Na-Ion Batteries. *Adv. Mater. Interfaces* **3**, 1600449 (1–10) **(2016)**.

216. Bommier, C., Luo, W., Gao, W. Y., Greaney, A., Ma, S. & Ji, X. Predicting capacity of hard carbon anodes in sodium-ion batteries using porosity measurements. *Carbon N. Y.* **76**, 165–174 **(2014)**.

217. Lv, W., Wen, F., Xiang, J., Zhao, J., Li, L., Wang, L., Liu, Z. & Tian, Y. Peanut shell derived hard carbon as ultralong cycling anodes for lithium and sodium batteries. *Electrochim. Acta* **176**, 533–541 **(2015)**.

218. Ponrouch, A., Goñi, A. R. & Palacín, M. R. High capacity hard carbon anodes for sodium ion batteries in additive free electrolyte. *Electrochem. commun.* **27**, 85–88 **(2013)**.

219. Väli, R., Jänes, A. & Lust, E. Alkali-Metal Insertion Processes on Nanospheric Hard Carbon Electrodes: An Electrochemical Impedance Spectroscopy Study. *J. Electrochem. Soc.* **164**, E3429–E3437 **(2017)**.

220. Dahbi, M., Nakano, T., Yabuuchi, N., Fujimura, S., Chihara, K., Kubota, K., Son, J. Y., Cui, Y. T., Oji, H. & Komaba, S. Effect of Hexafluorophosphate and Fluoroethylene Carbonate on Electrochemical Performance and the Surface Layer of Hard Carbon for Sodium-Ion Batteries. *ChemElectroChem* **3**, 1856–1867 **(2016)**.

221. Dugas, R., Ponrouch, A., Gachot, G., David, R., Palacin, M. R. & Tarascon, J. M. Na Reactivity toward Carbonate-Based Electrolytes: The Effect of FEC as Additive. *J. Electrochem. Soc.* **163**, A2333–A2339 **(2016)**.

222. Ding, C., Nohira, T., Hagiwara, R., Fukunaga, A., Sakai, S. & Nitta, K. Electrochemical performance of hard carbon negative electrodes for ionic liquid-based sodium ion batteries over a wide temperature range. *Electrochim. Acta* **176**, 344–349 **(2015)**.

223. Petibon, R., Aiken, C. P., Sinha, N. N., Burns, J. C., Ye, H., VanElzen, C. M., Jain, G., Trussler, S. & Dahn, J. R. Study of Electrolyte Additives Using Electrochemical Impedance Spectroscopy on Symmetric Cells. *J. Electrochem. Soc.* **160**, A117–A124 **(2013)**.

224. Burns, J. C., Krause, L. J., Le, D.-B., Jensen, L. D., Smith, A. J., Xiong, D. & Dahn, J. R. Introducing Symmetric Li-Ion Cells as a Tool to Study Cell Degradation Mechanisms. *J. Electrochem. Soc.* **158**, A1417–A1422 **(2011)**.

225. Morasch, R., Suthar, B. & Gasteiger, H. A. Simple Way of Making Free-Standing Battery Electrodes and their Use in Enabling Half-Cell Impedance Measurements via µ -Reference Electrode. *J. Electrochem. Soc.* **167**, 100540 **(2020)**.

226. Beguin, F. & Frackowiak, E. *Carbons for electrochemical energy storage and conversion systems*. Crc Press, Boca Raton **(2009).**

227. Andre, D., Kim, S. J., Lamp, P., Lux, S. F., Maglia, F., Paschos, O. & Stiaszny, B. Future generations of cathode materials: An automotive industry perspective. *J. Mater. Chem. A* **3**, 6709–6732 **(2015)**.

228. Liu, Y., Zhu, Y. & Cui, Y. Challenges and opportunities towards fast-charging battery materials. *Nat. Energy* **4**, 540–550 **(2019)**.

229. Li, Z., Huang, J., Yann Liaw, B., Metzler, V. & Zhang, J. A review of lithium deposition in lithium-ion and lithium metal secondary batteries. *J. Power Sources* **254**, 168–182 **(2014)**.

230. Gallagher, K. G., Trask, S. E., Bauer, C., Woehrle, T., Lux, S. F., Tschech, M., Lamp, P., Polzin, B. J., Ha, S., Long, B., Wu, Q., Lu, W., Dees, D. W. & Jansen, A. N. Optimizing Areal Capacities through Understanding the Limitations of Lithium-Ion Electrodes. *J. Electrochem. Soc.* **163**, A138–A149 **(2016)**.

231. Nyman, A., Zavalis, T. G., Elger, R., Behm, M. & Lindbergh, G. Analysis of the polarization in a Li-ion battery cell by numerical simulations. *J. Electrochem. Soc.* **157**, 1236–1246 **(2010)**.

232. Harks, P. P. R. M. L., Mulder, F. M. & Notten, P. H. L. In situ methods for Li-ion battery research: A review of recent developments. *J. Power Sources* **288**, 92–105 **(2015)**.

233. Liu, D., Shadike, Z., Lin, R., Qian, K., Li, H., Li, K., Wang, S., Yu, Q., Liu, M., Ganapathy, S., Qin, X., Yang, Q. H., Wagemaker, M., Kang, F., Yang, X. Q. & Li, B. Review of Recent Development of In Situ/Operando Characterization Techniques for Lithium Battery Research. *Adv. Mater.* **31**, 1–57 **(2019)**.

234. Wandt, J., Jakes, P., Granwehr, J., Eichel, R. A. & Gasteiger, H. A. Quantitative and time-resolved detection of lithium plating on graphite anodes in lithium ion batteries. *Mater. Today* **21**, 231–240 **(2018)**.

235. Zinth, V., Von Lüders, C., Hofmann, M., Hattendorff, J., Buchberger, I., Erhard, S., Rebelo-Kornmeier, J., Jossen, A. & Gilles, R. Lithium plating in lithium-ion batteries at sub-ambient temperatures investigated by in situ neutron diffraction. *J. Power Sources* **271**, 152–159 **(2014)**.

Acknowledgements

The content of this thesis was accomplished between January 2017 and May 2020 at the Chair of Technical Electrochemistry at the Technical University of Munich (TUM) in the group of Prof. Dr. Hubert A. Gasteiger.

First of all I would like to thank my PhD supervisor

Hubert A. Gasteiger

for his commitment and truly excellent support during the past three years. In an enviable way, you managed to create a working atmosphere at our chair that not only encourages everyone to achieve the highest level of research and at the same time to have fun during work. You give technical input without restricting the development of own ideas and creativity. Your commitment to your employees, your enthusiasm for good, well-founded research, which deservedly enjoys a worldwide reputation, is probably unique in this form. In addition, there is perhaps only a very limited number of chairs that provides the individual PhD student such a wide range of technical equipment and know-how to build upon. Even if this might sound cheesy, it indeed was a privilege to work and learn in this group.

Next, I would also like to thank our secretary **Veronika Pichler** for her tireless support of all employees in organizational and administrative matters - be it the correction of business travel applications or incorrectly filled in time sheets, without you the chair would collapse after a few days under the burden of rejected business travel applications. In particular, I would also like to express my gratitude to **all of my PhD colleagues** and **other employees** for the very pleasant working atmosphere, the mutual support and all evening events that were regularly organized in our seminar room. Among them, I would especially like to highlight my office colleagues **Tanja Zünd, Daniel Pritzl, Qi He, Anne Berger, Burak Koyutürk and Simon Qian**, who had to endure my jokes and chatter for several years, and **Ana-Marija Damjanović** for the musical gigs we had together.

I would also like to acknowledge my **bachelor** and **research internship students Jervais Oscar Howes, Leon Richter,** and **Hien Nguyen** for their support, and above all my **master's student Philip Rapp** who contributed largely to the success of our NDP studies, and conducted most of the technical drawings. I enjoyed working together with you, also during our neutron beamtime in Washington, D.C, and our short trip to New York, including the 3:30 h list of musical classics. Moreover, I want to thank **Richard Holtzner, Dominik Reiter, and Philip Frisch** for providing me access to their synthesis infrastructure, and their expertise in distillations of all kind. I especially want to thank **Markus Trunk** for his support during planning and execution of our numerous NDP beamtimes at the neutron reactors FRM2 in Garching and the National Institute of Standard and Technologies (NIST) in Gaithersburg, USA – the glass of cheese balls will be unforgotten.

Furthermore, I want to give thanks to all my colleagues from the iwb, EES, and FRM2 working together with me in joint projects. Among them, I want to highlight **Patrick Schmitz, JB Habedank, Florian "Mode-ILK" Günter, Nicolas Billot, David Schreiner, Benedikt Stumper, Fabian Konwitschny, and Ludwig Kraft**.

Especially, I would like to thank my parents **Monika and Rudolf Linsenmann**, and my sister **Sandra with family** who not only supported me financially during my studies, but also with advice and action whenever necessary, constantly knowing that I could always rely on them, no matter what happens.

Last but not least, I would like to thank my good friends **Lukas Brenner and Sandro Belz** for their support and distraction from science, and **Marco Decker** and **Daniel Pritzl** for our heated discussions on stock investments at the regular's table.

7 Scientific Contributions

Articles

D. Schreiner, T. Zünd, F. Günter, L. Kraft, B. Stumper, **F. Linsenmann**, M. Schüßler, R. Wilhelm, A. Jossen, G. Reinhart, and H. A. Gasteiger, "Comparative Evaluation of LMR-NCM and NCA Cathode Materials in Multilayer Lithium-Ion Pouch Cells - Part I: Production, Electrode Characterization and Formation", *submitted*.

F. Linsenmann, D. Pritzl, and H.A. Gasteiger, "A Comparative Study of Lithium and Sodium Intercalation into Hard Carbon Using Impedance Spectroscopy", *J. Electrochem. Soc.*, 168, 010506 (**2021**).

F. Linsenmann, D. Pritzl, and H. A. Gasteiger, "A Reference Electrode for In Situ Impedance Measurements in Sodium-Ion Batteries", *J. Electrochem. Soc.*, 166 (15), A3668-A3674 (**2019**).

F. Linsenmann, M. Trunk, P. Rapp, L. Werner, R. Gernhäuser, R. Gilles, B. Märkisch, Z. Revay, and H. A. Gasteiger, "A Liquid Electrolyte-Based Lithium-Ion Battery Cell Design for Operando Neutron Depth Profiling", *J. Electrochem. Soc.*, 167 (15), 100554 (**2020**).

Y. Matsukawa, **F. Linsenmann**, M. A. Plass, G. Hasegawa, K. Hayashi, and T.-P. Fellinger, "The Use of Different Gas Sorption Techniques for the Evaluation of Hard Carbons as Anodes for Lithium- and Sodium-Ion-Batteries", *Beilstein Journal of Nanotechnology*, 11 (**2020**).

R. Holzner, A. Kaushansky, B. Tumanskii, P. Frisch, **F. Linsenmann**, and S. Inoue, "Isolation of a Relatively Air-stable, Bulky Silylgroup-Substituted, Neutral Silicon-Centered Radical", *European J. of Inorganic Chemistry*, 25, 2977-2981 (**2019**).

R. Jung, **F. Linsenmann**, R. Thomas, J. Wandt, S. Solchenbach, F. Maglia, C. Stinner, M. Tromp and H. A. Gasteiger, "Nickel, Manganese, and Cobalt Dissolution from Ni Rich NMC and Their Effects on NMC622-Graphite Cells", *J. Electrochem. Soc.*, 166 (2), A2625-A2635 (**2019**).

Articles in preparation

F. Linsenmann, P. Rapp, M. Trunk, J. Weaver, R. Gernhäuser, B. Märkisch, and H. A. Gasteiger, "Spatially- and Time-Resolved Detection of Lithium Plating During Fast-Charging of a Graphite-Based Lithium-Ion Battery".

Oral presentations

Lithium Quantification in Lithium-Ion Batteries Using *Operando* Neutron Depth Profiling / **F. Linsenmann**, P. Rapp, M. Trunk, R. Gernhäuser, R. Gilles, B. Märkisch, and H. A. Gasteiger, German Neutron Scattering Conference 2020, **Munich** (Germany), **2020**.

Spatially and Time-Resolved Investigation of Lithium Plating on a Graphite Electrode During Fast Charging Using *Operando* Neutron Depth Profiling (NDP) / **F. Linsenmann**, P. Rapp, M. Trunk, R. Gernhäuser, J.L Weaver, B. Märkisch, and H. A. Gasteiger, PRiME, **Honululu** (USA), **2020**.

Formation of the Solid Electrolyte Interphase on the Graphite Anode in Lithium-Ion Batteries – An Operando Neutron Depth Profiling Study / **F. Linsenmann**, M. Trunk, P. Rapp, L. Werner, R. Gernhäuser, R. Gilles, Z. Revay, B. Märkisch, and H. A. Gasteiger, 236th ECS Meeting (October 13th-17th), **Atlanta** (USA), **2019**.

In Situ Impedance Spectroscopy as an Analytical Tool in Sodium-Ion Batteries / **F. Linsenmann**, D. Pritzl, and H. A. Gasteiger, Munich School of Engineering Colloquium (August 1st), **Munich** (Germany), **2019**.

A Novel Reference Electrode for EIS Measurements in Sodium-Ion Batteries / **F. Linsenmann**, D. Pritzl, and H. A. Gasteiger, 235th ECS Meeting (May 26th-30th), **Dallas** (USA), **2019**.

Hard Carbons as Anodes for Lithium Ion Batteries – Towards a Commercial Use? / **F. Linsenmann**, T.P. Fellinger, and H. A. Gasteiger, Fraunhofer IWS (October 10th), **Dresden** (Germany), **2017**.

Poster presentations

Lithium-Ion Battery Materials' Characterization for Advanced Electrode Engineering Using Neutron Depth Profiling (NDP) / **F. Linsenmann**, P. Rapp, M. Trunk, L. Werner, R. Gernhäuser, B. Märkisch, R. Gilles, Z. Révay, and H. A. Gasteiger, Batterieforum 2020, Berlin, 2020.

In Situ EIS Study of the Sodiation of Hard Carbon Using a Novel Micro Reference Electrode / **F. Linsenmann**, D. Pritzl, and H. A. Gasteiger, Kraftwerk Batterie, Aachen, 2019.